THE GEOGRAPHY AND GEOLOGY OF THE 2009 VOLCANIC UNREST PERIOD AT HARRAT LUNAYYIR, SAUDI ARABIA

A thesis submitted for the degree of
Doctor of Philosophy at the
University of London

Azizah Aziz AlShehri

Rock Fractures and Fluid Flow research group
Department of Earth Sciences
Royal Holloway, University of London

May 2020

Declaration

I, Azizah Alshehri, hereby declared by me that the corresponding thesis work has been comprised by me only without any scope of deviation to such observation. The primary segment of the accompanying thesis composition is constituted by an assemblage of papers which have already been published in international journals. The researcher has been the person with sole responsibility regarding the authentication of the data and the publication of the same and the collection of such data through the entire discourse of the thesis formulation. The researcher is as well the sole proprietor of all of the tow of the collection of the tow research papers. The cover page of the thesis also exhibits the statements of contribution in this regard.

Signed

Dated

16/10/2019

Abstract

Recent volcano tectonic activity at Harrat Lunayyir, western Saudi Arabia has signaled a renewed geohazard. The year 2009, marked the occurrence of the most substantial recent activity resulting in a regional dyke that reached a level very close to the surface in Harrat Lunayyir; Western Saudi Arabia. This in turn, caused an evacuation of more than 40,000 residents of the area. This study presents new general numerical models on the local stresses induced by arrested dykes. The numerical results show that, for a given surface deformation, non-layered (half-space) models underestimate the dyke overpressure/thickness needed and overestimate the likely depth to the tip of the dyke. Also, as the mechanical contrast between the layers increases, so does the stress dissipation and associated reduction in surface stresses (and associated fracturing). The width of a graben, if it forms, should therefore be roughly twice the depth to the tip of the associated arrested dyke. When applied to the 2009 episode at Harrat Lunayyir, the main results are as follows. The entire 3-7 km wide fracture zone/graben formed during the episode is far too wide to have been generated by induced stresses of a single, arrested dyke. The dyke tip was arrested at only a few hundred meters below the surface, the estimated thickness of the uppermost part of the dyke being between about 6 and 12 m. For the inferred dyke length (strike dimension) of about 14 km. In order to study complex occurrences, which lead to natural hazards and monitor volcanic activities, remote sensing has been used. In order to study complex occurrences, which lead to natural hazards and monitor volcanic activities, remote sensing has been used. Monitoring and estimating the relative changes in surface temperatures as a means for detecting an impending dyke-fed eruption or, alternatively, dyke arrest at a shallow depth. An analysis of thermal (infrared) data with a focus on the spatial distribution of land surface temperatures over a longer period of observation may help reveal the link between volcanic activity and dyke propagation. Here, the land surface temperature changes in the center of Harrat Lunayyir were recorded when the 2009 dyke was propagating toward the surface. The spatial distribution of the land surface temperatures in the area indicated the segmentation of the dyke and suggested the segments were arrested at somewhat different depths below the surface. we also have been studied the spectral behaviors of different volcanic terrains 'TOA Reflectance' The goal is to characterize recent lava flows, and old lava flows based on their spectral reflectance properties. According to the mapping results, three identified basaltic flows erupted in the same area as most of the epicenters of the earthquake swarm are associated with the dyke emplacement in the spring-summer of 2009. More specifically, most of the earthquakes were located around the most recent basaltic flows.

Acknowledgements

Thanks is but one word, and behind it there is a lot of gratitude to all those whom these words cannot thank enough for their support. Each of their names engraved in my heart and my memory like the Acknowledgements in bold font at the top of this page. First of all I want to thank my supervisor, (Agust), for all the hard work, support and guidance. I learned from you the seriousness of working together with teamwork and the simplicity of your meticulous handling of every (volcanology) issue. A big thank you also goes to (Morayyea Alshahrani) who gave me all his experience in (Cartography and Survey science) with all generosity and kindness. He was a friend, guide and motivated in every time I was frustrated. I also want to thank warmly, Dr.Abdullah Al amri for his support and help. Thank you also to Yahya Alshehri, Dr. Abdullah Alshehri and Talal Alshafie who accompanied me from the beginning of the journey to its end. Thanks a lot to a Leader of Geography department Dr.Ali Alqarni and from geological survey; Adel Alsharif, Maher and Basem Aldahri for the great atmosphere, friendship and help. Thanks with no limits to my parents who supported me from the first day of my life until I completed my PhD thesis. I present them all my achievements. I learned from you the love of knowledge and strive to reach our goals. A big thank you also to my sisters and brothers, Sarah, Bathan, Azzah, Loulah, Nouf, Meshal and Mishael. I am lucky and happy because you are always around me with your support and love even when I am living abroad for a long time. Thanks to all my friends here in the UK and in Saudi Arabia, I do not even have to mention your names but i will never forget your support.

Contents

List of figures

List of tables

Table 5: Water well depths and temperatures (measured at ground surface level over the period of 2007‑2011)

Chapter 1: Introduction

1.1 Overview and Aims

An active volcano is a vent that transports magma and volatiles to the Earth's surface (Gudmundsson, 2019). The accumulation of volcanic materials around the vent gives rise to a small volcano. This is commonly a crater cone: a cinder or scoria cone or a spatter cone and similar structures. Volcanoes formed in single eruptions are referred to as monogenetic. Many of these are volcanic fissures composed of many spatter and cinder or scoria cones, single craters or cinder cones. Repeated eruptions through a single or, more commonly, multiple nearby vents lead to the accumulation of volcanic materials into a volcanic edifice. The volcanoes formed through multiple eruptions are considered polygenetic. Edifices can be formed by several types of polygenetic volcanoes, including shield volcanoes (basaltic edifices) and stratovolcanoes, which are also known as composite volcanoes. Well-known examples of shield volcanoes are the Mauna Loa and Kilauea, which form part of the Island of Hawaii. Another is Fernandina, which forms part of the Galapagos Islands. The well-known stratovolcanoes include Augustine in Alaska, Mount Fuji in Japan, Teide on Tenerife (Canary Islands) and Semeru in Indonesia (Gudmundsson, 2019).

Volcanoes are classified on the basis of three main elements: eruption style, edifice type and magma composition. To gain a good understanding of the behaviour of volcanoes, their eruptions and the generation of molten magma and its transportation through the Earth's crust, a knowledge of dyke emplacement, i.e. initiation, propagation and arrest, and magma chamber formation, are required (Brown, 1994; Fowler, 1989; Gudmundsson, 2012, 2019).

The present thesis focuses on the volcanic processes related to the tectonic movements and shifts in the Harrat Lunayyir regions under consideration. The purpose is to improve the understanding of dyke emplacement in volcanoes and, specifically, the 2009 dyke emplacement in the Harrat Lunayyir region. The mechanical and aspects and thermal effects on the host rocks are considered. The initial chapter of the present study contains an overview and summary of the field work. It also discusses the methods used to study the dykes.

1.2 Magma Chamber Initiation

A magma chamber is a reservoir in the Earth's crust into which molten magma is channelled from a deeper reservoir. It may be totally or partly molten (Gudmundsson, 2012; Maaloe & Scheie, 1982; Marsh, 1998). Some magma chambers are partly molten throughout their lifetimes. Others are totally molten in the beginning and become partly molten as they evolve (Gudmundsson, 2012). In particular, small sill-like chambers may be totally molten during their early stages of development.

Several recent studies have investigated the dynamical effects and geological consequences of the injection of a new supply of hot, relatively dense magma into a comparatively homogeneous magma chamber. If dense, the incoming magma may initially occupy a separate layer at the bottom of the magma chamber; however, over time, its density may equalise with that of the existing magma in the chamber. The two would then become intimately mixed (Huppert et al., 1980). Magma reservoirs located at shallow depths in the Earth's crust - commonly referred to as magma chambers - are most easily studied through the geophysical investigations of active volcanoes and the petrological and geochemical studies of erupted igneous rock or to fossil plumbing systems. Such studies have shown that as the magma cools, it undergoes chemical changes and becomes more fractionated over time in addition to providing information on the geometries and mechanics of the systems.

At various times, active magma chambers are replenished with supplies of fresh, usually hotter, magma from the deeper reservoirs in the Earth's crust or upper mantle (Huppert & Sparks, 1982). This places the rocks surrounding the magma chamber under pressure mainly because of the excess pressure in the chamber. When the rock fractures because of this pressure, a fraction of the magma is able to propagate as a dyke or an inclined sheet into the chamber roof and sometimes towards the surface (Gudmundsson, 2002, 2006; Jellinek & DePaolo, 2003; Macdonald, 1982). Magma compressibility is highly significant. Therefore, it must be considered in the estimations of the change of mass or the comparisons of the amount of magma that is being stored with the volume that has erupted (Gudmundsson, 2006; Johnson et al., 2000).

Recent advances have been made in the understanding of the hazards associated with dyke emplacement and, eventually, volcanic eruptions. Specifically, the internal processes in volcanoes during unrest periods are now better understood. In addition, the mechanics of

dyke propagation and arrest are being interpreted through geodetic and seismic measurements (Gudmundsson & Philipp, 2006; Gudmundsson, 2019). One of the most important and studied geodetic quantities is the volume of the ground surface uplift, the inflation and the integral of the vertical displacement over the deformed volcanic edifice (Johnson et al., 2000). This is a measure of the strain energy stored in the volcano during the unrest period (Gudmundsson, 2019).

A very important topic is the mechanisms behind the development of shallow magma chambers. Gudmundsson (1990, 2012) has suggested that a majority of chambers start as sills. Two conditions must then be fulfilled for a sill to develop into a magma chamber. The first is that the sill should be tens of metres thick. Second, it must be frequently replenished with magma through dykes to sustain a high temperature and to maintain the magma in a liquid state. This enables a chamber to grow and to develop and to inject the dykes and sheets (Gudmundsson, 1990, 2012; Gudmundsson et al., 2014).

1.3 Dyke Propagation, Deflection and Arrest

A dyke is a tabular body of igneous rock that is normally almost vertical or steeply inclined and cuts through the layers that constitute the volcano – that is, is discordant. A dyke is an intrusion. Specifically, it is formed by a magma-driven fracture. Dykes normally dissect or cut through the layers of the surrounding host rock, such as lava flows and pyroclastic layers, and are thus discordant. Originally, the word ‘dyke’ referred to the solidified rock in a fracture. However, phrases such as ‘dyke propagation’ and ‘dyke emplacement’ reflect the more recent use of this word to denote the propagating magma-driven fracture itself. ‘Dike’, the American spelling, is also used in British English; however, ‘dyke’ is exclusively British (Gudmundsson, 2017).

Volcanic eruptions are fed most commonly by dykes, as is observed in erupting volcanoes around the world (Cayol & Cornet, 1998; Gudmundsson, 2002, 2006; Sigmundsson, 2006). Most dykes and inclined sheets, however, do not reach the surface to erupt; rather, they become arrested, i.e. stop their propagation paths or stall, at various depths in the crust (Gudmundsson, 2002, 2003; Moran et al., 2011; Rivalta et al., 2015; Townsend et al., 2017). The conditions for dyke arrest have been studied in the field (Gudmundsson, 2002, 2003; Gudmundsson & Philipp, 2006; Tibaldi, 2015). They have also been examined through analogue models (Kavanagh et al., 2006), numerical models (Barnett & Gudmundsson, 2014; Gudmundsson & Philipp, 2006; Rivalta et al., 2015; Townsend et al.,

2017) and analytical models (Gudmundsson, 2011a, 2011b). An understanding of these conditions is critical to theoretical and applied volcanology.

Despite the available instrumentation for volcano monitoring, forecasting dyke propagation paths once a dyke has been initiated during magma chamber or reservoir rupture is still not possible. Therefore, reliable forecasts about (1) the likely path of the dyke: in particular, (2) the likelihood of the dyke's reaching the surface and erupting or, alternatively, (3) becoming arrested at some depth in the volcano cannot be made. Direct field studies of arrested solidified or 'fossil' dykes, as well as geodetic and seismic studies of dyke arrest during unrest periods, are vital for improving the understanding of dyke propagation and dyke-fed eruptions.

Many dyke arrests have been reported in recent decades. In some unrest periods, many dykes become arrested; however, at the end of the unrest period, one or more dykes will have reached the surface to erupt. A well-documented case is the unrest in Eyjafjallajökull in South Iceland for nearly two decades before the 2010 eruption. Between 1993 and 2010, four to five dyke injections became arrested, and some of the dykes changed into sills. However, in March 2010, a new dyke injection reached the surface and erupted (Sigmundsson et al., 2010). That many dykes and sills are exposed in the volcano suggests that such episodes are common (Gudmundsson, 2017, 2019). Many of the unrest periods with dyke injections, however, have not resulted in eruptions. One eruption happened in Tenerife in the Canary Islands in 2004 (Garcia et al., 2006; Gottsmann et al., 2006), and another in Harrat Lunayyir in western Saudi Arabia in 2009 (Baer & Hamiel, 2010; Pallister et al., 2010; Xu et al., 2016). The Harrat Lunayyir in western Saudi Arabia is the main topic in Chapter 3.

Hundreds of arrested dykes have been observed, and many of their tips have been studied in detail. Field studies have shown that while some dykes terminate within layers, most become arrested at the contacts between the rock layers or units: in particular, at the contacts between mechanically dissimilar layers (Gudmundsson, 2002, 2003). Some of these dykes become deflected into sills (e.g. Barnett & Gudmundsson, 2014; Casagli et al., 2009; Gudmundsson, 2011b; Kavanagh et al., 2015; Tibaldi, 2015; Tibaldi & Pasquarè, 2008). However, others become arrested upon meeting the contact.

There are three principal mechanisms by which dykes and other extension fractures or mode I cracks become arrested: (1) Cook–Gordon delamination, (2) stress barriers and (3) elastic mismatches. All of these mechanisms may operate simultaneously; however, the

Cook–Gordon delamination is most effective at shallow crustal depths. The other two mechanisms can operate at any depth. A detailed description of these mechanisms, including the appropriate references, has been provided by Gudmundsson (2011a, 2011b, 2019). The Cook–Gordon delamination mechanism implies that the contact that arrests the dyke is mechanically weak. Therefore, the tensile strength and, by implication, the shear strength (because of their relationship) is low. Around the dyke tip is a tensile stress field (Kavanagh et al., 2018). The highest tensile stress is orientated perpendicular to the dyke and serves to generate the dyke fracture. However, there is also a high dyke parallel tensile stress that, for a contact with a low tensile strength, could open the contact when the dyke tip is close to it. The opening of a contact, which has been observed in many numerical models of dyke emplacement (Gudmundsson, 2003, 2011a, 2019), is likely to occur in nature. When the dyke tip finally reaches the open contact, the tip then either becomes deflected along the contact to form a sill or stops altogether: i.e. it becomes arrested.

1.4 Significance of the Study and the Study Area

During the early Miocene (~25 Ma), the Arabian plate separated from Africa along the Red Sea and the Gulf of Aden rifts ~10–15 Ma prior to the beginning of the Arabia–Eurasia continental collision (Garfunkel, 1987; Garfunkel & Beyth, 2006; McQuarrie et al., 2003). Geologically, Arabia lies on a tectonic plate of its own, the Arabian Plate, which has been moving away from Africa and creating the Red Sea. The other plates in the vicinity of the Harrat Lunayyir are the Eurasian Plate in the east and the Anatolian Plate in the north. The formation of the Arabian Plate is believed to be related to the African Rift. At ~30 Ma, the rifting processes started in Afar, and the opening of the Red Sea was linked to the sinistral strike–slip displacements along the Gulf of Aqaba–Dead Sea transform fault system (Abdel Khalek et al., 1993; Bosworth et al., 2005; Morgan, 1998). It propagated both eastward and northward to form the Gulf of Aden and the Red Sea, respectively (Camp & Roobol, 1992; Cochran & Martinez, 1988). The understanding of the rift history of the Red Sea has evolved beyond the early ‘two-stage’ models that included two stages of ocean spreading (at 41–34 Ma and 5–4 Ma; Girdler & Styles, 1974) or two pulses of ‘initial’ or ‘early-stage’ rifting (at ~34 Ma and 25–21 Ma; Omar & Steckler, 1995) to the wide acceptance of the late Oligocene (28–24 Ma) as the initial formation of the Red Sea rift basins (Bosworth, 2015; Fig. 1.1).

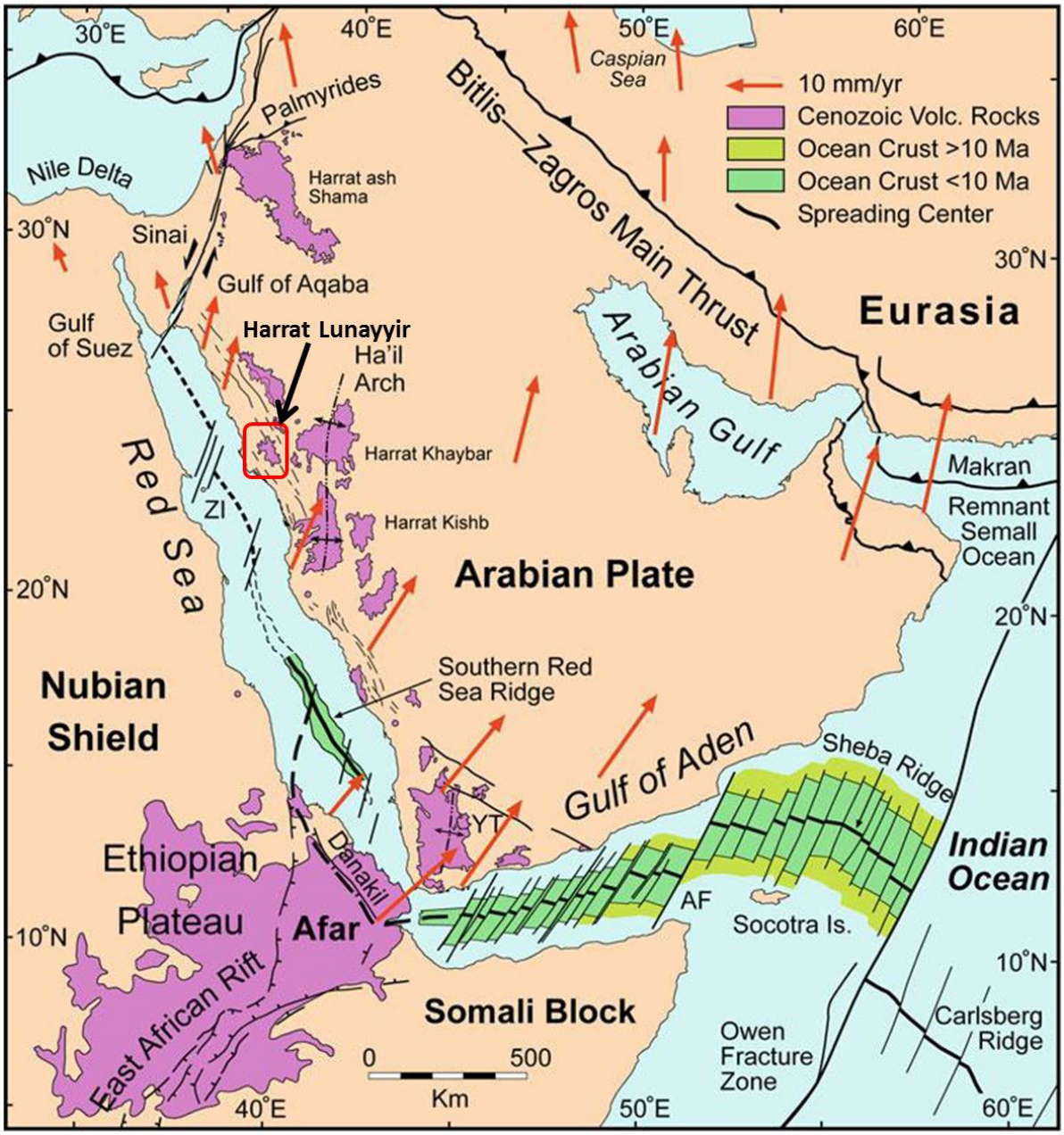

Figure 1.1: Tectonic features of the greater Red Sea rift system, including the northern Ethiopian (East African) rift, Afar and the Gulfs of Aden, Aqaba and Suez. Modified from Bosworth et al. (2015).

The Red Sea, an active rift system, was formed by the rifting of the Precambrian continental lithosphere beginning in the late Oligocene and continuing with the breakup and spreading of the seafloor (Roeser, 1975). The present rifting led to the expansion and propagation of the Red Sea from the south to the north. Currently, the Red Sea extends from 30° N, the northern limit of the Gulf of Suez, to 12.5° N, where it meets the Gulf of Aden. The total north–south length is ~2,250 km, and the maximum east–west width is ~354 km. The oceanic crust itself has a maximum width of ~100 km. The Red Sea could

be regarded as an excellent example of the early stages of ocean development through seafloor spreading (Bonatti et al., 2015). It has a continental scale rift system that stretches from the Dead Sea to Mozambique. This has led to the popularisation of the term 'Afro-Arabian rift system' by the geologists mapping its segments (Kazmin, 1977). During the spreading of the Red Sea, parts of the Arabian Shield became extended and thinned because of the associated formation of dyke swarms and volcanic fields, one of which is the Harrat Lunayyir (Genna et al., 2002; Hansen et al., 2013a, 2013b).

The Arabian Shield occupies one-third of the Arabian Peninsula. Its estimated area is 670,000–725,000 km^2 (Brown et al., 1978). The Arabian Shield is a part of a larger group, the Arabian–Nubian Shield, whose total estimated area is 2.7 × 106 km^2 (Johnson & Woldehaimanot, 2003; Rodgers et al., 1999). The upper part of the crust of the Arabian plate consists of a crystalline Precambrian basement, Phanerozoic sedimentary cover and Cenozoic flood basalt, such as that at Harrat Lunayyir (Stern & Johnson, 2010; Fig. 1.2). This is the section that occupies the northeast flank of the Red Sea, which includes the well-exposed highlands of Yemen and the central part of Saudi Arabia, i.e. Najd (Powers et al., 1963; Stern & Johnson, 2010). The geologic and topographic features of the western Arabian shield are different from those of the eastern platform. The shield has extensive Proterozoic basement exposures and little or no sedimentary cover. The surface exposures in the shield are composed of approximately 50% plutonic rock and 50% volcanic and sedimentary rock (Gettings et al., 1986) The platform is covered by as much as 10 km Phanerozoic sediment (Stoeser & Camp, 1985). Studies indicate that the platform crust stabilised at ~700 Ma. However, the shield crust stabilised ~150 Ma later after the shield had undergone several cycles of metamorphism, tectonism and plutonism (Gettings et al., 1986; Stern & Johnson, 2010).

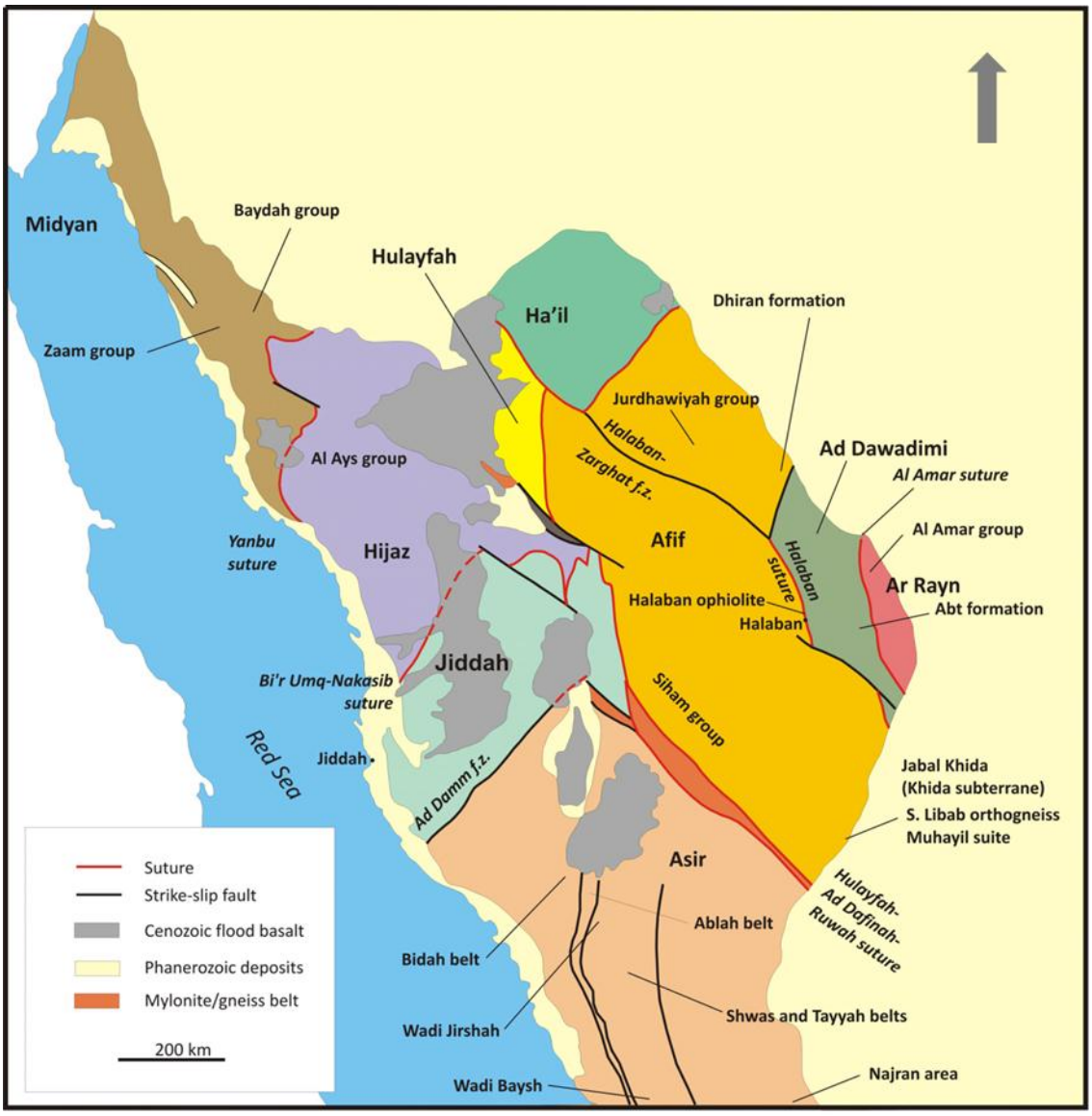

Figure 1.2: Locations of some of the main lithostratigraphic units and structures on a base map showing the tectonostratigraphic terranes and terrane boundaries in the Arabian shield in Saudi Arabia (modified from Johnson, 1998).

The average crustal thickness of the Arabian Shield is ~40 km (Al Damegh et al., 2005); however, the crust becomes thinner towards the Red Sea coast where the thickness is 23–25 km. A similar crustal thickness can be found in the Nubian Shield on the west side of the Red Sea: a thickness of 25–26 km in Egypt within 50 km of the coast of the Red Sea. Yet another similar phenomenon can be observed in the Nubian Shield, which is situated towards the western region of the Red Sea. Within Egypt, the thickness of the crust is 25–26 km, and this continues up to a distance of 50 km towards the coastal region of the Red Sea.

There are two distinct phases of volcanism within the Arabian plate. From 30–20 Ma, tholeiitic-to-transitional lavas were emplaced along the rift-parallel dykes extending throughout the length of the Red Sea rift flank. This was contemporaneous with the impingement of the Afar plume on the base of the African–Arabian plate. Since 12 Ma, transitional-to-strongly-alkalic lavas have been continuously emplaced along a north–south trend, the Makkah–Madinah–Nafud (MMN) line of volcanism, thereby forming the younger harrats (Camp & Roobol, 1992; Stern & Johnson, 2010). The common name 'harrats' refers mostly to the lava fields (Pint, 2006), which are also known as the Harrat Al-Shaqa.

These areas are among the smallest alkali basaltic lava fields generated during the Holocene. They are generally located towards the western margin of Saudi Arabia. Specifically, the coordinates for the fields are 25° 10′–25° 17′ N latitude and 37° 45′–37° 75′ E longitude. The lava field is located ~60 km from the eastern section of the Red Sea coastal regions and 150 km east of the central section of the Red Sea (Al Amri & Fnais, 2009; Al-Zahrani et al., 2013; Baer & Hamiel, 2010; Duncan & Al-Amri, 2013; Fig. 1.3).

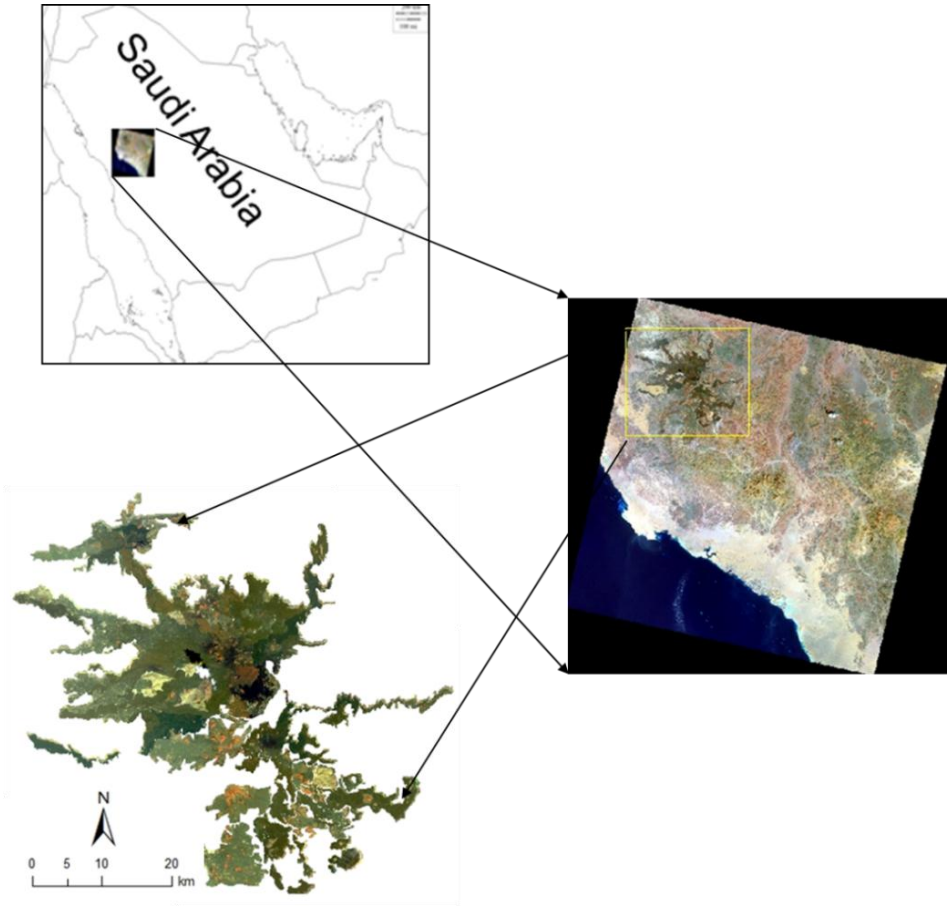

Figure 1.3: Location of Harrat Lunayyir.

Approximately 50 monogenetic craters of variously sized volcanic cones contributed to the formulation of this region (Baer & Hamiel, 2010). The basaltic lava flows can be characterised by two specific segments. The first is the Tertiary unit, the Jarad basalt, which is considerably older, and the second is the Quaternary unit, the Maqrah basalt, which is younger (Al Amri et al., 2012; Fig. 1.4).

The eastern, northern and southern sections of Harrat Lunayyir are formed by Precambrian rocks. The central section is composed of a variety of rocks, of which those from the Precambrian period are found only in isolated sections. The seismic and volcanic events in the Harrat Lunayyir began ~0.5 Ma ago (Duncan & Al-Amri, 2013). An informed estimation suggests that the most recent lava flows could have occurred ~5,000 years ago (Al-Amri et al., 2012). Thus, it can also be presumed that there could have been some recent eruptions in the region because a specific cone of craters was formed at a point ~1,000 years earlier, as indicated by Baer and Hamiel (2010).

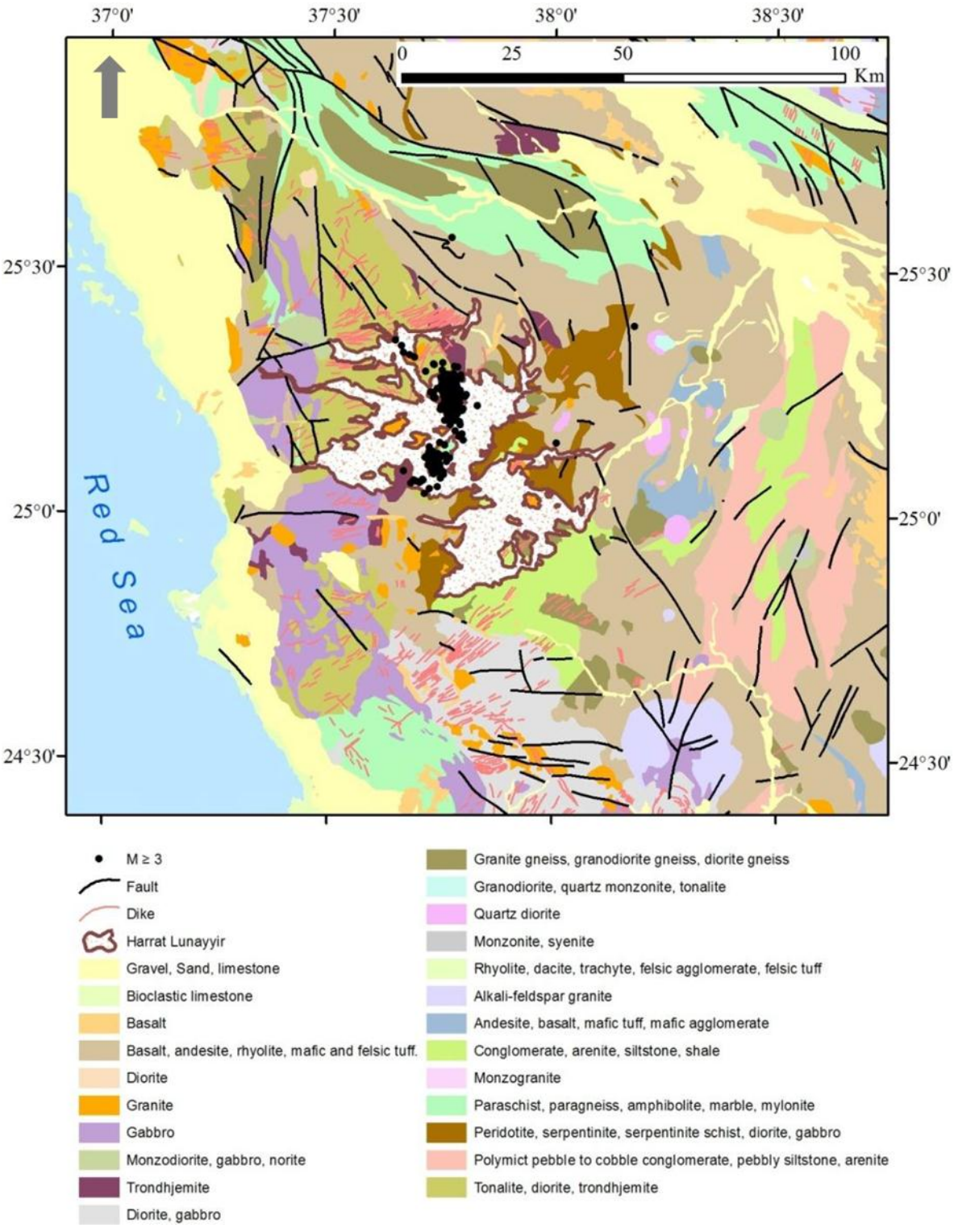

Figure 1.4: Geological setting around the Lunayyir area (modified from Al-Zahrani et al., 2013).

1.5 Research Problem`

Until recently, the prevalent perception about the Harrat Lunayyir was that it is inactive. This perception was derived from previous studies that suggested that the most recent eruption in the region had occurred at least 1,000 years ago. . In addition, the assumption

was that the eruption that preceded this eruption could have occurred at least 5,000 years ago. None of these dates can be ruled out, but recent volcano-tectonic events show clearly that the region is active.

In October 2007, the region experienced a volcano-tectonic episode. This was indicated by the earthquake swarm (Al-Amri & Al-Mogren, 2011; Mukhopadhyay et al., 2013; Zobin et al., 2013). This relatively limited earthquake swarm involved no more than 500 seismic events. The largest of these earthquakes registered at approximately magnitude M3.2. This series of events was indicative of a northwest–southeast-striking earthquake swarm. The focal depth of the earthquakes was greater than 10 km. This swarm did not give rise to any deformations or changes on the surface of the region (Xu et al., 2016). It culminated during the final days of May 2008.

Another volcano-tectonic episode began 18 April 2009, peaked 17–19 May and ended in July the same year (Al-Mahri et al., 2009; Baer & Hamiel, 2010; Koulakov et al., 2014; Pallister et al., 2010; Xu et al., 2016). Again, it was an earthquake swarm with a general northwest–southeast strike; however, it was located ~15 km northwest of the 2007 swarm. The 2009 swarm generated more than 30,000 recorded earthquakes. The most intense activity occurred 17–19 May, with a sequence of seven earthquakes of $M > 4$, the largest being M5.7 (Baer & Hamiel, 2010; Xu et al., 2016). The focal mechanisms of the $M > 4$ earthquakes indicated primarily normal faulting, some of which showed evidence of strike–slip components. The main episode came to an end in July 2009. Al-Zahrani et al. (2013) estimated the focal depth of the largest earthquake, M5.7, as 9 km. Most of the earthquakes were located at depths of 5–15 km. The overall strike was north-northwest–south-southeast (NNW–SSE; Xu et al., 2016). In addition to the earthquake swarm, there was extensive surface deformation during the 2009 episode. There was a broad area of uplift and extension. The area was ~2,000 km^2, the maximum uplift was ~0.4 m, and the extension was ~1 m (Pallister et al., 2010). The total NNW–SSE length of the uplifted area was 14–15 km. Subsequent studies have estimated the total extension at ~1.5 m across the deformation zone and the subsidence at a maximum of 0.8 m in the central part of a ‘graben’ that dissects the dome (Baer & Hamiel, 2010).

1.6 Research Objectives

1. To further assess the risks and hazards associated with the 2009 dyke emplacement in the research area. This assessment relies partly on the new estimates for the depth to the dyke tip when the dyke became arrested.

2. To estimate the general dimensions of the 2009 dyke.

3. To conduct a comprehensive numerical study of the dyke-induced surface stresses. In particular, to explore the effects of mechanical layering on the surface stresses and the resulting fracture pattern.

4. To formulate, through the use of remote sensing technologies, a rigorous estimation of the surface temperature variations in relation to the 2009 dyke emplacement.

5. To perform the unsupervised classification of the lava flows in Harrat Lunayyir through the use of remote sensing.

1.7 Previous Studies

Duncan and Al-Amri (2013) indicate that western Saudi Arabia has been the site of many volcanic eruptions. The most recent was ~1,000 years ago in Harrat Lunayyir. The current phase of volcano-tectonic activity in Harrat Lunayyir began more than 10 years ago, as has been confirmed by the Saudi Geological Survey measurements of the geothermal anomalies in the area. Duncan and Al-Amri (2013) also indicate that there were no differences or changes in the composition of the lava during the development of the present volcanic field. Al-Amri et al. (2012) estimated the eruption volumes for each of the volcanic units as follows: Quaternary upper Maqrah basalt (lacking erosion) Q5, 7.2 km^3; Q4, 11.5 km^3; Q3, 6.1 km^3; Q2, 4.3 km^3; Q1, 13.7 km^3; and T, 18.0 km^3. The authors also noted that the high seismic velocity region is partly related to the common intrusions and plutons in the crust. Their study discusses the various models that have been applied in an attempt to explain the upwelling activity in the Arabian Shield area. Some have associated the volcano-tectonic activity at Harrat Lunayyir with melt migration from the Afar mantle plume. Others have suggested the presence of a separate mantle plume upwelling beneath the Arabian Shield.

Baer and Hamiel (2010) suggest that the 2009 earthquake was caused by a magma-driven rifting episode. They used interferometric synthetic aperture radar (InSAR) measurements

and elastic modelling with seismic moment calculations to estimate the dimensions of the dyke (Fig. 1.5). The authors concluded that a 12 km-long dyke, which was controlling the deformation during the rifting event, dominated the far-field deformation. They also discovered that two normal faults dominated the near-field deformation. The study compared the geometric, structural and seismic characteristics of Harrat Lunayyir with the 2005 Dabbahu (Afar) and 2007 Gelai (Tanzania) events. Some similarities regarding the size (dyke and fault lengths, graben width) and geodetic moment were found at Harrat Lunayyir and Gelai (Tanzania). However, there were differences in their seismic or geodetic moment partitioning. There were also similarities between the 2005 Dabbahu event and Harrat Lunayyir in terms of size (thicker dyke and longer and narrower graben). On the basis of double difference tomography and data from the earthquakes from the 2009 swarm, Hansen et al. (2013b) focused on the P-wave velocity structure beneath Harrat Lunayyir. Their results suggest that unrest in the Arabian Shield region was partly the result of the tectonic processes along the Red Sea rift and the transform fault in the Gulf of Aqaba–Dead Sea.

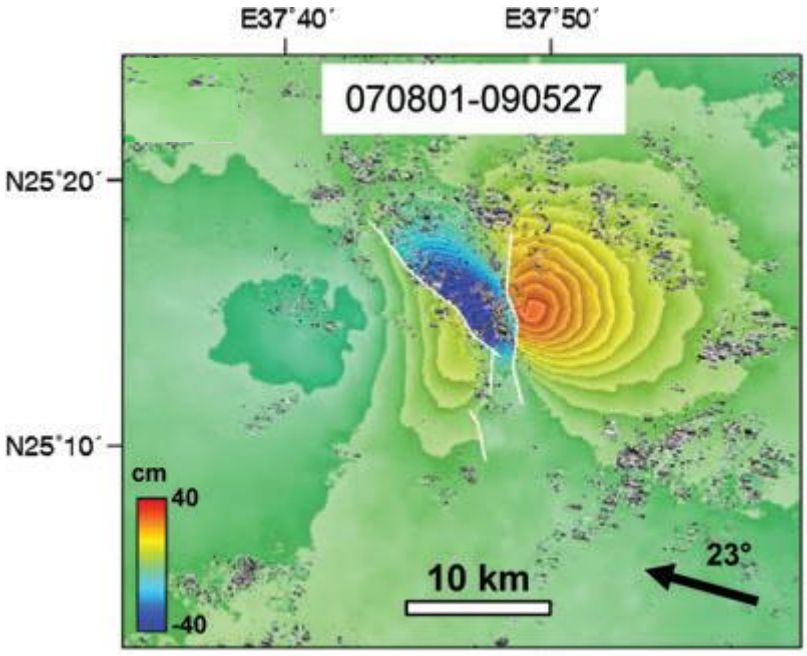

Figure 1.5: Envisat Advanced Synthetic Aperture Radar (ASAR) interferograms for the 2009 Harrat Lunayyir swarm period (Baer & Hamiel, 2010).

Hansen et al. (2013b) also found that a pronounced high-velocity anomaly at a depth of ~15 km included a shallower extension in the north-north-westerly direction. This region is considered very important because of the repeated magmatic intrusions. Moreover, as a result of the dyke emplacement in 2009, several shallow swarms occurred ~2–8 km beneath northern Harrat Lunayyir. Al-Zahrani et al. (2013) attributed the 2009 aftershocks that occurred in the northwest and parallel to the Red Sea axis to the largest aftershock. The normal fault is representative of this trend. These aftershocks happened subsequently at 5–10 km and 15–25 km beneath the Lunayyir area. The authors also noted that the main shock was at a depth of 9 km. The stresses associated with the aftershocks were characterised by heterogeneity, which was partly attributed to the repeated magmatic dyke intrusions that resulted from the main shock. While most of the energy was released with the aftershock, energy was also released directly in conjunction with the main shock.

Kenedi et al. (2013) focused on improving the understanding of the seismic hazards in Medina through a rigorous investigation of the previously documented tectonic events and earthquake swarms that occurred in Al-Madinah in 1256 A.D. An earthquake swarm occurred in Harrat Rahat in 1999, and a magmatic intrusion, i.e. failed eruption, took place

in Harrat Lunayyir in 2007, 2008 and 2009. The results of this study suggest the probability of the occurrence of significantly destructive volcanic eruptions in Harrat Rahat in the future. The study also shows that the volcanism in the Arabian Shield harrats was the result of dyke intrusions, as was seen in Harrat Lunayyir. A near-vertical shallow arrested dyke was observed by InSAR at a distance of 2 km beneath the surface. This initially resulted in a 3 km normal fault that grew to 8 km after the 19 May M5.7 earthquake. This was an indication of the continued addition of magma to the dyke. Al-Amri and Fnais (2009) concluded that the seismicity associated with the swarms that occurred on the eastern side of Harrat Lunayyir on 18 April 2009 was shallow. Koulakov et al. (2015) studied P- and S-wave velocities to identify the cause of a missed eruption, dyke arrest, in the Harrat Lunayyir basaltic field in 2009. They found a large seismic anomaly of high VP/VS ratio below 7 km depth coincides with the locations of more than 50 recent cinder cones with ages of older than 100 ka, and is interpreted as a steady-state magma reservoir. The study also found another seismic anomaly at depths below 15 km, which is interpreted as a conduit for fluids and melts from deeper sources.

1.8 Thesis Outline

Each chapter of this thesis can be considered to be part of an independent study. Some chapters are published papers, and others contain work that is in preparation for publication in scientific journals. Chapter 2 provides a comprehensive description and analysis of the methods used in the study. The conclusion in chapter 7 concludes the Problem and research objectives that have been solved throughout the project. The discussion in Chapter 6 includes a critical evaluation of the main findings and suggestions for future research. Chapters 3, 4 and 5 (results chapters) have been published, chapter 1 is presented as a stand-alone work with independent page numbers. Chapter 3, 4, 5 are presented in the printed format of the target journal. Chapter 2 presents the main methodological frameworks governing each independent study. This chapter is divided into two main sections related to the techniques used in the study: numerical and analytical studies, and remote sensing and geographic information systems (GIS).

The aim of Chapter 3 is to present the unsupervised classification of lava flows in Harrat Lunayyir, western Saudi Arabia. The classification was performed with remote sensing that used iterative self-organizing data analysis (ISODATA) algorithms. This technique allows the user to specify the number of classes into which the data are separated for clustering within each land cover. The author previously studied the spectral behaviour of different volcanic terrains in terms of top-of-atmosphere (TOA) reflectance. The goal is to characterise the recent and old lava flows on the basis of their spectral reflectance properties. To validate the classification, samples of the ISODATA classification results were obtained from the same sites. The sample was sent to Oregon State University for 40Ar/39Ar-based dating of the incremental heating structures. Incremental heating experiments allow examination of the step-wise release of Ar with increasing temperature for evidence of mantle-derived 40Ar.

Chapter 4 focuses on the monitoring and estimation of the relative changes in surface temperature to facilitate the detection of an impending eruption. Infrared observations could indicate the approaching dyke-related hazards. The observations can provide critical information for supporting potential disaster responds and emergency managers. Also, the approach here could facilitate response prioritisation, disaster assessment, mitigation planning and comprehensive risk assessment. The Land Surface Temperature (LST) is situated in the centre, which is shown in the surface temperature maps.

Chapter 5 presents new and general results on dyke-induced stresses in crustal segments composed of layers with contrasting mechanical properties. The focus is on new numerical models of dykes arrested with tips at various crustal depths. The dykes are hosted by rocks with mechanical properties ranging from elastic half spaces (uniform properties) to those with alternating stiff (high Young's modulus) and soft (compliant, low Young's modulus)

layers. The results are general; however, they are applied to the 2009 period of volcano-tectonic unrest in Harrat Lunayyir in Saudi Arabia. The numerical results and analytical models, together with field observations of the associated surface deformation, form the basis for new estimates of the dyke dimensions. In addition, there are new estimates of the depth to the arrested dyke tip below the surface and the surface deformation induced by the dyke inferred to have been emplaced during the 2009 episode.

Chapter 6 integrates all of the key findings and critically evaluates the methods and techniques used throughout the study. The possible avenues for expanding the work and insights on future research directions are also discussed.

Chapter 7 warps up the research, It Includes answers to the research questions.

Chapter 2: Methodologies

2.1. Introduction

2.1.1 Overview

Many numerical methods have been developed to simulate dyke emplacement and arrest (e.g. Al Shehri and Gudmundsson, 2018; Gudmundsson, 2006; Rivalta et al., 2015). The most commonly used is the finite element method (FEM), which was used in this study. It is described in detail by Logan (2002). The FEM is considered a particularly useful means of analysing stress, has been used in various applications (Kulhawy, 1973). In this type of analysis, a set of elements connecting the joints or nodal points represents the continuous body. It is possible to compute the stresses and strains and displacements of the nodal points of each element on the basis of the stress–strain characteristics of the element material and the loading More specifically, the stresses and strains within the elements can be calculated once the displacements of each nodal point are known (Bathe, 2014). A problem can be presented physically as an actual structure or a component of a structure that has been subjected to a particular load. The FEM can be used for problem-solving: typically for problems that do not have an analytical closed-form solutions. Thus, the method is numerical rather than analytical. This type of approach is necessary because many engineering and related geology problems are real and complicated and cannot be adequately addressed by analytical methods. For example, mathematical theories of elasticity and the engineering strength of materials are useful for calculating the strains and stresses of a bent beam from an analytical perspective. However, neither of these approaches is appropriate for investigating the performance of a car suspension system during vehicle cornering. Similarly, layered beams, or a layered crustal segment or a part of a volcano, even for simple loadings generate stresses and displacements that are too complex to be solved analytically.

The FEM has been widely adopted in several fields, including fluid mechanics, heat conduction, electrostatics and vibration (Modlen et al., 2010) as well as in volcanotectonics. Specifically, the present study uses COMSOL Multiphysics, a numerical cross-platform finite-element multiphysics simulation software (www.comsol.com). The software can manage problems involving structures, heat conduction, fluid transport, and other types of physics, engineering, and geological problems.

There are three critical stages in the formulation of numeric modelling (Andrew, 2008). The first is the pre-processing phase during which the model is defined by utilisation, and the applications of the environmental factors are considered. These can be better understood and explained in relation to the design formation for the elaboration of the model's structural details. This can be completed inside the program or accomplished via specialised software packages. Utilisation can occur subsequently. This geometric portrayal is then segmented into components and nodes, framing a mesh composed of the elements. The nodes on this mesh are the focal points that highlight, for example, the calculated displacements, stresses and strains.

The second phase can be envisaged as the analysis of the accumulated data gleaned from the models. Appropriate properties, e.g. the values of Young's modulus and Poisson's ratio used for the layers in the model, are then used to define the model behaviour under loading. The third is the post-processing phase. The focus is the visualisation of the findings through the use of charts, images, graphical interfaces and numerical formats. For example, the stresses inside the model are represented by curves that illustrate the stress magnitudes. In addition, stresses and displacement at the surface above an arrested dyke can be presented in the post-processing phase. The likely location of tension fractures and faults can be inferred from the known strengths of the crustal rocks, specifically the tensile and shear strength.

2.1.2 Thesis Models

As was indicated above, the finite-element COMSOL Multiphysics software (www.comsol.com) was used for performing a general analysis of the local stresses associated with dykes, with specific application to the inferred 2009 arrested dyke. All of the models were created in a two-dimensional regime, as is standard for dyke modelling. The models were created with sufficient length and width, 15 km × 15 km, to ensure that the edge effects would be negligible. The models were fastened in the corners, as indicated by the crosses, to avoid rigid-body rotation and translation. Boundary conditions are commonly applied to the edges of models to simulate far-field tectonic stresses (see the 2D model in Fig. 2.1). The assumed tectonic situation is of the type normally associated with dyke emplacement in a rift zone. A free surface is the boundary condition applied to the upper edge of the model to allow free movements/displacements without a constraint so as

to simulate the ground (the Earth's) surface. In solid mechanics and geology, a free surface is, like here, a solid in contact with air or water, i.e. a surface free from shear stresses.

In all of the models, the only loading was an internal magmatic overpressure (driving pressure) of 6 MPa. A higher overpressure was not used because of the assumption that the dyke is basaltic and that this overpressure would be within the range of the typical in situ tensile strength of the rocks. Magmatic overpressure in a dyke is determined by the following equation (Gudmundsson, 2011a):

$$p_o = p_e + (p_r - p_m)gh + \sigma_d \tag{1}$$

where p_e is the excess magmatic pressure, that is, the pressure in the source chamber in excess of σ_3, p_r is the average host-rock density, p_m is the average magma density, g is acceleration caused by gravity, h is the dip dimension of the dyke and σ_d is the differential stress (i.e. the difference between the maximum, σ_1, and the minimum, σ_3, principal stress) in the host rock where the dyke in question is located.

The second term on the right-hand side of Eq. (1) is the buoyancy term. In the uppermost 1–3 km of the crust in almost all volcanic areas, the average rock density is 2,500–2,600 kg/m^{-3}. In contrast, basaltic magma have a density of 2,650–2,800 kg/m^{-3} (e.g. Al Shehri and Gudmundsson, 2018). It follows that in the uppermost part of the crust, the buoyancy of basaltic magmas is often potentially negative. The ascent of magma is normally accompanied by gas expansion which makes the magma lighter, i.e. less dense. Gas expansion and density reduction are commonly observed in acid magma at depths of many kilometres (Gonnermann and Manga, 2013); however, for basaltic magma, such as that in the 2009 dyke at Harrat Lunayyir, much of the gas exsolution takes place at very shallow depths. In Hawaii, for example, gas exsolution in basaltic magmas occurs primarily in the uppermost few hundred metres of the feeder or conduit (Greenland et al., 1985, 1988). Similarly, direct observations of dykes, sills and inclined sheets in deeply eroded lava piles and central volcanoes have revealed only small, rather infrequent vesicles formed by expanding gas at depths exceeding several hundred kilometres below the original surface of the volcanic zone or central volcano. In contrast, some feeder dykes contain large vesicles that are close to the surface (Galindo and Gudmundsson, 2012).

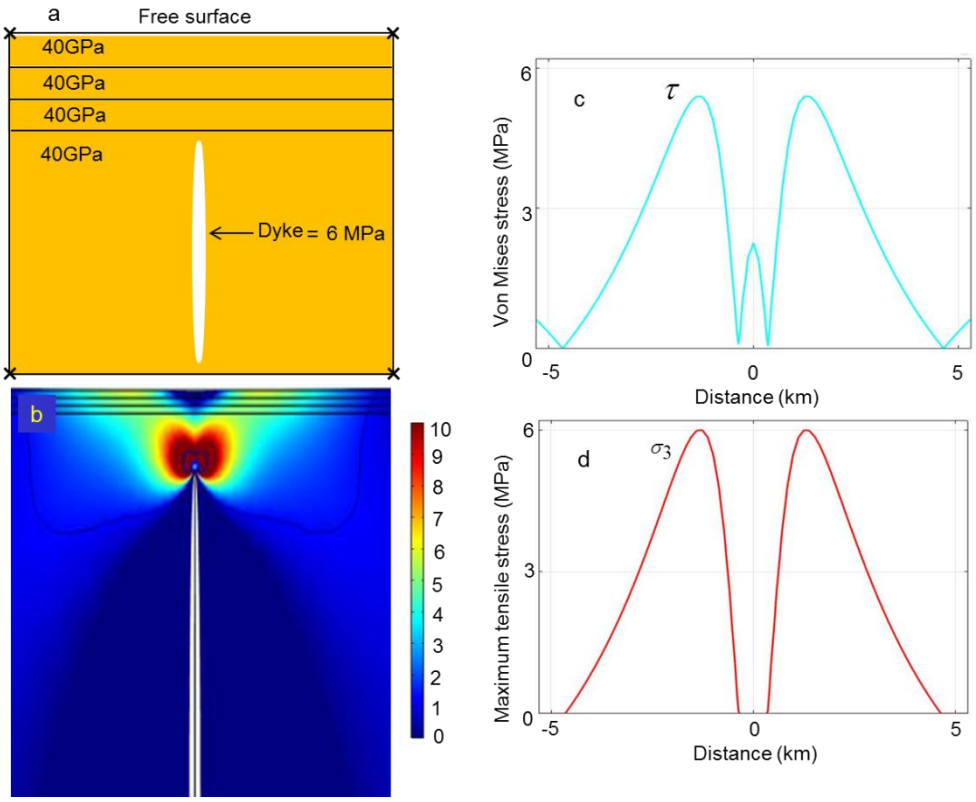

Figure 2.1: Numerical model of a dyke arrested with a tip at the depth of 1,000 m below the Earth's surface. The magmatic overpressure is 6 MPa, and Poisson's ratio of all the rock layers is 0.25. Each of the top 3 layers is 100 m thick. The top 3 layers and the main rock unit hosting the dyke have the same Young's modulus: 40 GPa. Thus, this is effectively an elastic half-space model. a: Schematic of the model. The thickness of the layers and the height of the dyke are not to scale. b: Maximum principal tensile stress, σ_3, in megapascals. The stresses shown here and in subsequent models range from 0 (blue) to 10 MPa (red). This range, 0–10 MPa, was chosen because the maximum in situ tensile strength of crustal rocks is 9 MPa and mostly 5–6 MPa. Thus, tensile stresses above 10 MPa can normally not be reached in the crust (Gudmundsson, 2011a). The dip dimension (height) of the dike in all the models is 9–10 km. c: The von Mises shear stress at the Earth's surface. d: Maximum principal tensile stress, σ_3, at the Earth's surface.

A higher overpressure was not used because of the assumption that the dyke is basaltic. Thus, in a continental crust, for a basaltic dyke the buoyancy term may not add much overpressure to the excess pressure at the time of magma chamber or reservoir rupture (Eq. 1). In all of the models, the lower tip (bottom) of the dyke was at a depth of ~10 km; however, the upper tip (or top) was at depths of 0.3 km, 0.5 km and 1 km below the surface.

As was discussed by Al Shehri and Gudmundsson (2018), the dip dimension of the 2009 dyke might have been as large as 15–20 km. However, for the purpose of modelling the effects of shallow layering on surface stresses, the 10 km dip dimension used in this study

is appropriate. In the first models, the crust has the same uniform properties. This is supported by the fact that all the indicated layers have the same Young's modulus (40 GPa in this study). Therefore, the first models represent elastic half-spaces, which are still used most commonly to model the surface stresses and deformations associated with volcanic unrest periods (Dzurisin, 2006; Segall, 2010). For the models presented in this study, all the layers and units had the same Poisson's ratio, 0.25, which is the most common ratio for rocks (Gudmundsson, 2011a). In comparison to the variations in Young's modulus or stiffness, those in the Poisson's ratio of rocks are generally small enough (normally a factor of $\leq$2) to be negligible. The former may easily vary by two, or sometimes even three, orders of magnitude in any volcanic zone or volcanic edifice.

In the later models, realistic layering was achieved with Young's modulus in different layers ranging from 1 GPa for soft layers to 40 GPa for stiff layers. While this range was presumably smaller than the actual range in layers such as those hosting Harrat Lunayyir, it serves the purpose of illustrating the effects of reasonable layering on surface stresses and the likely fracture formation induced by arrested dykes, such as that in 2009. In the layered models, each of the layers constituting the uppermost part of the crust was 100 m thick. This thickness remained constant in all the models. Moreover, in all the models, the lowermost layer or unit hosted most or all of the dyke. (Depending on the shallowness of the dyke tip, the top part of the dyke may penetrate some of the shallow layers in some of the models.)

The Young's moduli of these shallow layers were derived from the seismic data; thus, the dynamic Young's modulus was calculated on the basis of the velocities of the seismic waves (Jaeger and Cook, 1979). The dynamic moduli were 27 GPa for two of the layers and 17 GPa for the surface layer. The layer or unit hosting (most of) the dyke had a dynamic Young's modulus of 40 GPa. These values were based primarily on the seismic velocities recorded in Harrat Lunayyir. They were also within the range of the laboratory-determined Young's moduli for granites and other typical continental rocks (Gudmundsson, 2011a) and thus reflect more general conditions. The later layered models used still more realistic layering in which comparatively soft layers with Young's moduli of 1–3 GPa formed part of the crustal segment.

The 100 m layer thickness was somewhat arbitrary in that it generally reflects 'seismic layers', i.e. groups of layers with similar seismic or mechanical properties. Although some sedimentary layers and some lava flows, such as pahoehoe, may reach a thickness of

100 m and more, this thickness should be interpreted here as being mechanical or seismic rather than lithological. In all the models, the layering (and lack of layering in the first models) was included to illustrate the assumed general structure of the crust. The layers are shown in Part A of each model figure, which also provides the Young's modulus of each layer. The location of the dyke tip, however, is not changed in Part A of the figures (e.g., Fig. 2.1; cf. Al Shehri and Gudmundsson, 2018). The dyke is always shown at the same location because the main aim is to illustrate the layering. Part B of the figures shows the exact location of the dyke tip, which, in some of the later models, penetrated the lowermost of the top three to four layers. The early models had three layers above the thick layer or unit that hosts (most of) the dyke. In the later models, however, an additional layer (coloured white in all the models) with a Young's modulus or stiffness of 1 GPa was included. An in situ Young's modulus of 1 GPa is common in many compliant pyroclastic and sedimentary rocks (Gudmundsson, 2011a). For example, many soil, sediment and scoria layers between lava flows have similar or lower Young's moduli.

Here, the layer was assumed to have the same thickness as the other layers, namely 100 m. There are certainly layers much thinner than 100 m in most crustal segments. Some are mere metres or even tens of centimetres thin. However, to illustrate the principles that control dyke-induced surface deformation, the thickness used here for the seismic/mechanical top layers was appropriate. In the absence of more detailed knowledge regarding the actual layering of the Harrat Lunayyir crust to which these models were applied, these thicknesses were considered suitable (the soft layers were added in the later models) particularly because the main mechanical effect of a layer lies not in its thickness but, rather, its softness or compliance. In these models, the depth of the 1 GPa layer was varied to explore the effect of the depth on the dyke-induced surface stresses and associated deformation.

2.2. Remote Sensing and Geographic Information System

2.2.1 Overview

Remote sensing is an efficient method for the analysis of volcanoes and volcano-related activity and products. Every type of instrument and methodology available for collecting data from the Earth's surface, monitoring and supervising the parameters involved in the essential processes, and managing the data can be used (Bryant et al., 1990; Colwell, 1983; Eidenshink & Hass, 1992; Nicholson et al., 1990). Remote sensing can be defined in

several ways. According to Colwell (1966), the most common definition is ‘performing reconnaissance from a distant position’. Another description refers to fact that remote sensing uses methodologies and procedures to obtain information about any object from a distance without the need for direct contact between the measuring elements and the object itself (Fischer et al., 1976). The energy that radiates from a distant object is measured, and this information is used to calculate the properties and physical dimensions of the object, along with the environment immediately surrounding the object. As indicated by Moore (1979), remote sensing is therefore recognised as being both a technique to generate primary data and a scientific process to use as a tool.

Remote sensing is being applied much more widely in geological studies, and its effectiveness and reliability when compared with traditional approaches, such as field mapping, is being increasingly acknowledged (Head et al., 2012). For example, it is used to map geological phenomena, such as volcanoes and lava flows, and to provide spectral, spatial and temporal coverage for the volcanoes and earthquake zones around the world. Remote sensing allows for the detection and measurement of electromagnetic radiation through the use of a remotely located device (Shen et al., 2008). The spectral reflectance and wavelengths of EM were the most important parameters that were measured in the present study.

Remote sensing is particularly important in the monitoring of volcanic activity, especially in cases involving InSAR and thermal studies (Nicolas et al., 2008). The energy produced by EM can be measured with sensors that detect the energy that strikes them at specific wavelengths. Remote sensors can be airborne, ground-based or space-based, the most frequently used method for classifying lava flows (Crown & Ramsey, 2016). Factors such as surface roughness, permittivity or conductivity determine whether lava will reflect or scatter a signal (OSU, 2015). One crucial aspect in the classification and monitoring of lava flows is surface reflectivity, defined by D’Alessandro (2006) as the ratio of reflected power to direct power. Several of the image processing methods through which lava flows are described in the succeeding sections.

Most geographic occurrences on the Earth’s surface are monitored by satellites. Satellite sensing instruments are capable of using optical datasets to map geographic events (OSU, 2015). Although satellites are largely reliable, mapping can be adversely affected by heavy cloud cover; therefore, the data must be gathered from multiple satellite sources over several days to obtain a clear picture of events (US Geological Survey, 2008). Landsat

imagery is frequently used for unsupervised classification because of the increasing number of Landsat satellites monitoring the Earth's surface and atmosphere. Landsat satellites obtain and record image data spectra by using operational land imagers (OLIs) and thermal infrared sensors (TIRSs): nine visible and shortwave infrared band spectra and two longwave thermal bands (Shen et al., 2008). The three image resolution criteria are spectral, spatial and radiometric resolutions.

2.2.2 Thermal mapping

Remote sensing technology has revolutionised the mapping and monitoring of natural hazards and risks, including fault zones, volcanic activity and other important geological events. Satellite imagery is an important tool for gathering data to improve the understanding of volcanoes and the associated natural phenomena. Several studies have highlighted the importance of the observation and investigation of thermal energy emissions from high-temperature events and structures, such as volcanoes, to gain a deeper understanding of geological occurrences (Barnie & Oppenheimer, 2015; Harris et al., 1997; Tralli et al., 2005).

Another remote sensing technique for evaluating the surface temperature of specific areas is thermal infrared (TIR) technology, which is also used to investigate and to monitor volcanic eruptions, volcano-tectonic events and the tremors and earthquakes associated with such events. TIR has been used extensively in the field for at least two decades. In brief, all objects that could possess a temperature greater than absolute zero emit thermal energy in the infrared band, and this can be measured with TIR technology. Infrared energy emission sensors can detect emissions from all artificial and natural objects on any landscape on the Earth. This includes water, vegetation, soil, the sun, rocks and life forms, such as animals and humans, all of which emit infrared-based electromagnetic and thermal radiation. This energy can then be measured by remote TIR sensors. Objects within the infrared energy band are undetectable by the human eye. The limit for the human eye is light beams in the 400–700 nm range; therefore, changes or measurements in the thermal energy emissions outside this spectrum cannot be detected. Jensen (2007) indicates that the human eye is sensitive to only 3.0–14 μm within the infrared energy range and 700 nm–3.0 μm in the infrared reflective index range. Consequently, humans cannot process information optically from the reflective infrared band or perceive information from the thermal energy emitted from the infrared spectrum.

Because the data are collected in remote sensing mode, there is no risk associated with the infrared evaluation process. This low risk has led researchers and scientists to intensify their efforts to discover and to investigate these types of signals because they are the markers of current and imminent volcanic activity around the world. Geological activities, including volcanoes, frequently emit much heat. Therefore, remote sensing, such as TIR, tends to be used for monitoring and mapping the changing surface temperatures in all regions of the world. This technology is essential for detecting and evaluating consistent volcano activity patterns because of the possible precursor signals (Haselwimmer & Prakash, 2013; Realmuto & Worden, 2000; Tralli et al, 2005; Vaughan et al., 2005).

Heat sensors are often embedded in satellites to facilitate the detection of heat variation. Such satellites include the Landsat Thematic Mapper (TM)/Enhanced Thematic Mapper (ETM), Moderate Resolution Imaging Spectroradiometer (MODIS), Advanced Very-High-Resolution Radiometer (AVHRR), National Oceanic and Atmospheric Administration (NOAA) and Advanced Spaceborne Thermal Emission and Reflection Radiometer (ASTER). The current study is closely related to the process of deriving thermal bands from Landsat and LST, e.g. band 6 from ETM+, across different time periods. In view of the objectives of the Harrat Lunayyir-based research, we obtained three separate images from the United States Geological Survey (USGS) server (Earthexplorer.usgs.gov).

ArcGIS 10.1 and ERDAS IMAGINE 2015 software, which can enable the further identification of the images, are commonly used in the interpretation of the data pertaining to surface temperatures. Landsat imagery was also used in the current study. Specifically, the thermal bands related to band 6 of ETM+ were downloaded. The ETM+ bands and those from dataset band 6 were preferred because they are brighter and could thus facilitate the assessment of the area through photographic images. The region under investigation does not have significant amounts of vegetation. The axis, rows and thermal constants associated with the developments in the area are typically determined by the metadata from the thermal bands. The perspectives from the various algorithm-based operational processes that were used are presented in Table 2. The land surface temperature is one such indicator.

Acquisition date	Satellite / Sensor	Path	Band	Spatial resolution
17 the March 2007	Landsat ETM+	147	6	60 Meter
03 the March 2008	Landsat ETM+	147	6	60 Meter
22 the March 2009	Landsat ETM+	147	6	60 Meter
26 the June 2009	Landsat ETM+	147	6	60 Meter
23 the July 2009	Landsat ETM+	147	6	60 Meter
26 the August 2009	Landsat ETM+	147	6	60 Meter
25 the March 2010	Landsat ETM+	147	6	60 Meter
12 the March 2011	Landsat ETM+	147	6	60 Meter

Table 2.1: Metadata and Acquisition date of Landsat 7.

2.2.3 Data Preparation

The activity involved in the primary phase of the processing of the imagery obtained from the satellite images, also known as the pre-processing stage, concerns the strips that can become apparent in images acquired after 2003. These strips generally need to be completely removed via ERDAS IMAGINE 2015, a focal analysis tool-based software package. The strips are in fact generated by the malfunctions associated with the correction of the scanning lines (Fig. 2.2).

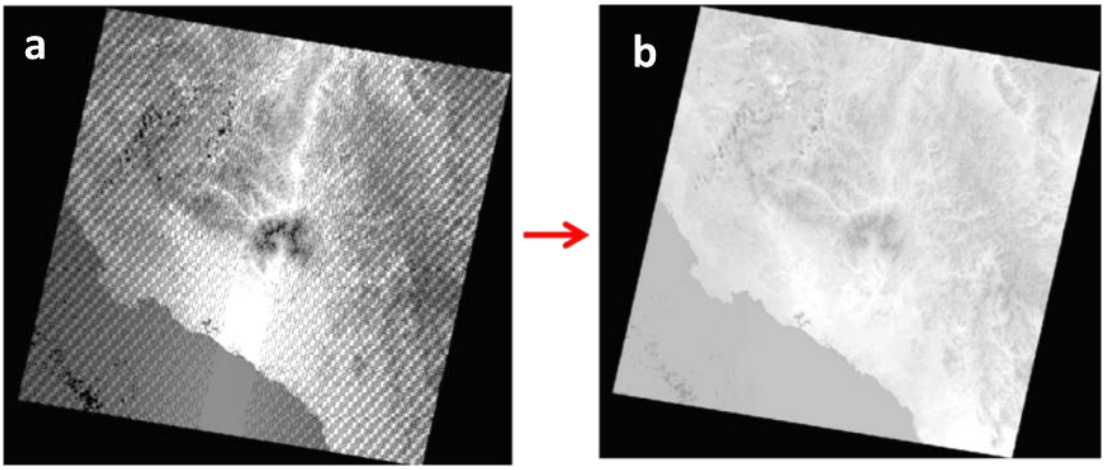

Figure 2.2: The primary phase of the processing of the imagery obtained from satellite images. a: Landsat 7 June 2009 image of Harrat Lunayyir before the removal of the strips. b: Image after the removal of the strips.

2.2.4 Conversion to Radiance

The remote sensing mechanism gathers the digital numbers (DNs), which can be converted to LST values through a technique designed for radiometric corrections and modifications. The data resulting from this step can then be contrasted with the existing data. The sensors' radiance, which relates to the wavelength regions, can be stored and kept within the gathered and compared DNs. Specially designed quantification systems can subsequently be used to process the DNs. The facilitation of data processing and storage is the main benefits of this approach. The DN-based values have no physical units; therefore, these values must be transformed into tangible radiances. The formula developed for the transformation of DNs into spectral radiance measures is known as ETM+DN, and the values are typically 0–255 (Fig. 2.3).

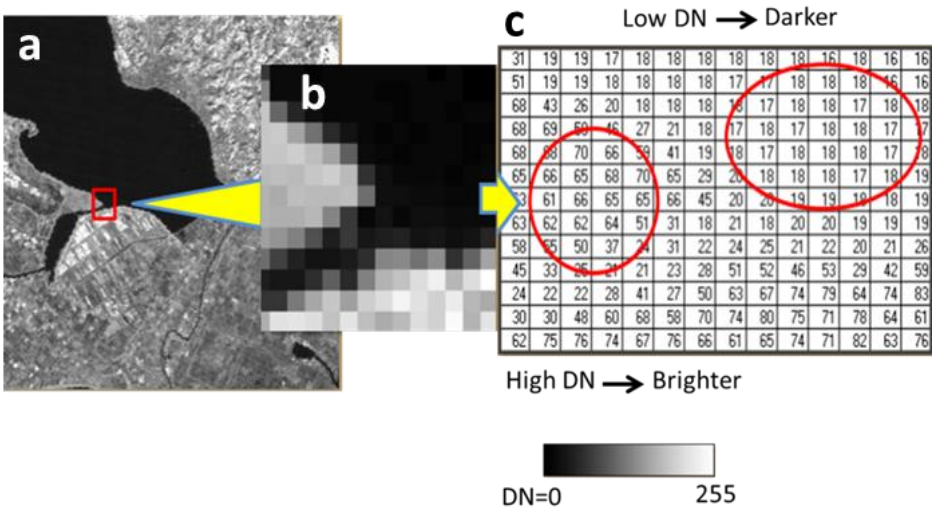

Figure 2.3: Conversion to radiance. a: The red square shows the location on the satellite image. b: The location after zooming in. c: This illustrates the digital number of each pixel. (Lwin, 2008).

$$L_{\lambda} = Grescale \times Qcal + Brescale \tag{2}$$

This is also expressed as:

$$L_2 \equiv \frac{(LMAX_2 - LMIN_2)}{(QCALMAX - QCALMIN) \times (QCAL - QCALMIN) + LMIN_2} \tag{3}$$

Here, Lλ = spectral radiance at the sensor's aperture in watts/(meter squared × ster × μm), Grescale = rescaled gain (the data product "gain" contained in the Level 1 product header or ancillary data record) in watts/(meter squared × ster × μm) /DN, Brescale = rescaled bias (the data product "offset" contained in the Level 1 product header or ancillary data record) in watts/(meter squared × ster × μm), QCAL= the quantized calibrated pixel value in DN, LMINλ = the spectral radiance that is scaled to QCALMIN in watts/(meter squared × ster × μm), LMAXλ = the spectral radiance that is scaled to QCALMAX in watts/(meter squared × ster × μm), QCALMIN= the minimum quantized calibrated pixel value (corresponding to LMINλ) in DN = 1 for LPGS products, = 1 for NLAPS products processed after 4/4/2004 ,= 0 for NLAPS products processed before 4/5/2004, QCALMAX= the maximum quantized calibrated pixel value (corresponding to LMAXλ) in DN = 255.

The Landsat 8 metadata contain all of the ancillary data required to calibrate the data to the radiances.

CPF_FILE_NAME = "L7CPF19991001_19991123_12"

GROUP = MIN_MAX_RADIANCE

LMAX_BAND1 = 191.600

LMIN_BAND1 = -6.200

LMAX_BAND2 = 196.500

LMIN_BAND2 = -6.400

LMAX_BAND3 = 152.900

LMIN_BAND3 = -5.000

LMAX_BAND4 = 157.400

LMIN_BAND4 = -5.100

LMAX_BAND5 = 31.060

LMIN_BAND5 = -1.000

LMAX_BAND61 = 17.040

LMIN_BAND61 = 0.000

LMAX_BAND62 = 12.650

LMIN_BAND62 = 3.200

LMAX_BAND7 = 10.800

LMIN_BAND7 = -0.350

LMAX_BAND8 = 243.100

LMIN_BAND8 = -4.700

END_GROUP = MIN_MAX_RADIANCE

GROUP = MIN_MAX_PIXEL_VALUE

QCALMAX_BAND1 = 255.0

QCALMIN_BAND1 = 1.0

QCALMAX_BAND2 = 255.0

QCALMIN_BAND2 = 1.0

QCALMAX_BAND3 = 255.0

QCALMIN_BAND3 = 1.0

QCALMAX_BAND4 = 255.0

QCALMIN_BAND4 = 1.0

QCALMAX_BAND5 = 255.0

QCALMIN_BAND5 = 1.0

QCALMAX_BAND61 = 255.0

QCALMIN_BAND61 = 1.0

QCALMAX_BAND62 = 255.0

QCALMIN_BAND62 = 1.0

QCALMAX_BAND7 = 255.0

QCALMIN_BAND7 = 1.0

QCALMAX_BAND8 = 255.0

QCALMIN_BAND8 = 1.0

END_GROUP = MIN_MAX_PIXEL_VALUE

2.2.5 Conversion from Spectral Radiance to Temperature

The ETM+ band 6 imagery can be transformed for increased effectiveness regarding the physical dimensions for the existing variables from the spectral radiance. Under the presumption of the factor of unity emissivity, such imagery can be effectively used for evaluating the Earth's atmospheric temperatures obtained through the satellites. The formula for transformation and conversion is as follows:

$$T = \frac{K2}{In\left(\frac{K1}{L_\lambda} + 1\right)} \quad (4)$$

Where T = effective at-satellite temperature in Kelvin, K2 = calibration constant 2 from , K1= calibration constant 1 from, L= spectral radiance in watts/(meter squared × ster × μm) (Table. 2.2).

ETM+ Thermal Band Calibration Constants		
	Constant 1- K1 watts/(meter squared × ster × μm)	Constant 2 - K2 Kelvin
Landsat 7	666.09	1282.71

Table 2.2: ETM + Thermal Band Calibration Constants.

2.2.6 Conversion from Kelvin to Celsius scale

Because the temperature was estimated in Celsius, the results obtained from Equation 4 were converted to Celsius. The formula-based conversion method can be described with the formula B6 − 273.15. Here, B6 is the result obtained from Equation 2, which is

expressed on the Kelvin scale. This enabled the inference and development of the temperature outline map.

2.2.7 Data Processing and Analysis

The ArcGIS Spatial Analyst provides spatial analysis and investigation tools. It also offers tools for model formulation and displays for generating data from both raster (cell-based) and feature (vector) units. The capacities of Spatial Analyst are segmented into classifications and specific groups that feature interrelated functionalities. The knowledge of these classifications facilitates the identification of the most appropriate devices and tools for a study. The table located in the final segment of the study provides a list of the available effective instruments and tools. The particular functionality of each is included.

There are a few measures that needed to be used to fully access the functionalities of Spatial Analyst. Through geoprocessing, tasks in the Spatial Analyst inventory of instrumentation can be managed with the Tool dialog box and the Python programming language. The variables involved are the interactive command line interface and the written content, such as that in the scripts. Models can also be used. Conventional activities and work processes using map algebra and polynomial mathematics can likewise be performed in the Python environment. Raster calculators can be used for entering straightforward and simplified algebra-based map data to produce the raster output extents (ESRI, 2016).

2.2.8 Extraction of the Study Area

The extraction tools and devices can facilitate the extrication of the necessary cell substrates from a raster through the use of the cell characteristic, locations or spatial areas. This can further be explained by noting that the values for the cells regarding their specific locations can be obtained through the use of the tables and the feature point-based classifications (ESRI, 2016; Fig. 2.4).

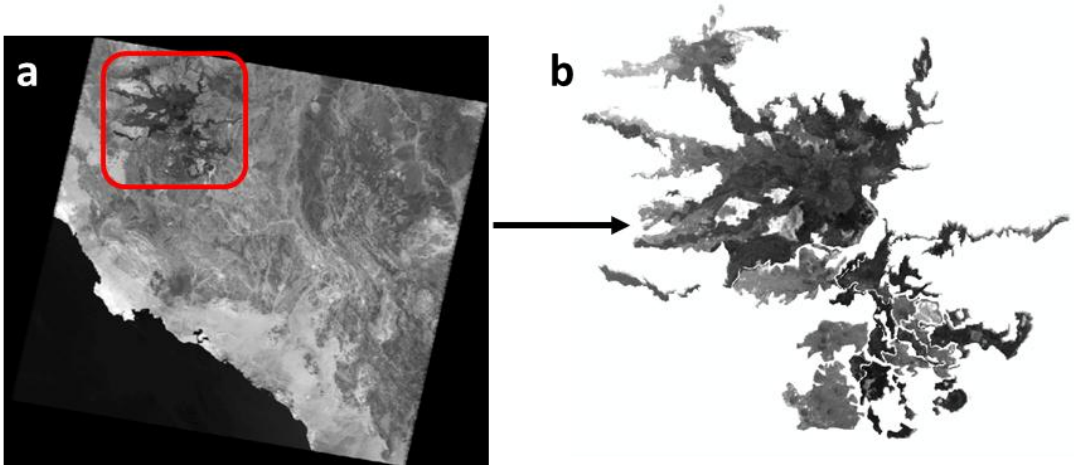

Figure 2.4: Extraction of the study area. a: The red square shows the lava flow border in Harrat Lunayyir. b: Harrat Lunayyir after extraction.

2.2.9 Calculation of the Land Surface Temperature

The map algebra instrument was identified as the most effective method and instrument for performing the spatial analysis. It can lead directly to the creation of specific expressions on the basis of the delineations of the algebra-based information. With the Raster Calculator tool, the formulation and operation of the Map Algebra data expressions can be performed to create the final output for the datasets related to the raster. The LST equation is presented below with the appropriate inputs (Fig. 2.5).

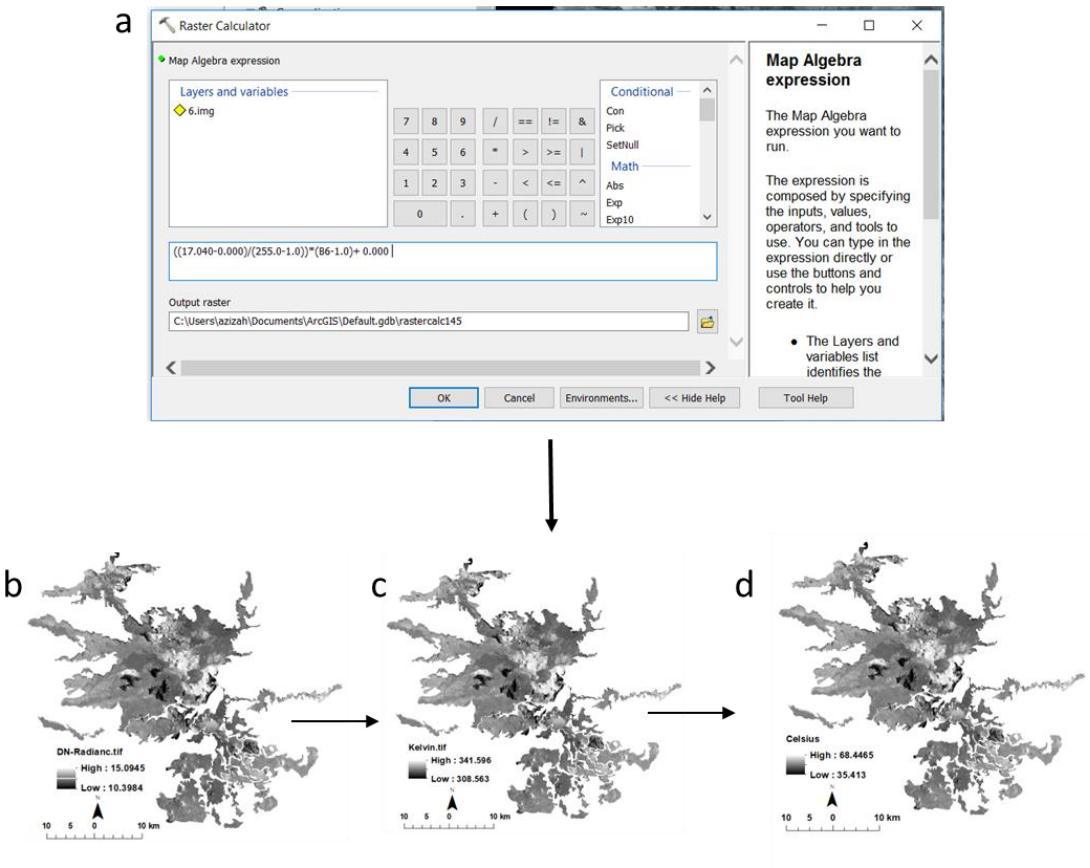

Figure 2.5: Calculation of the land surface temperature. a: Map Algebra tool for performing spatial analysis, the land surface temperature equation has been demonstrated through the proper inputs. b: The digital numbers obtained through the remote sensing mechanism could then be transformed into the radiance. c: Conversion from spectral radiance to the Kelvin scale. d: Conversion from the Kelvin to the Celsius scale.

2.2.10 Unsupervised Slassification

The best way to view the images is to crop them, leaving the region around the studied lava flow visible. This method allows for faster and more precise classification because of the lower number of pixels to be assessed and classified into groups (Head et al., 2012). This method can also be used to determine the number of unimodal spectral classes and to identify their locations. The migrating means clustering (MMC) classifier is a widely used method in unsupervised classification (Crown & Ramsey, 2016). The unsupervised classification of lava flows can be achieved through the use of digital image processing software, such as ArcGIS and ERDAS IMAGINE that include spatial analysis tools. Lahar flows, flooding and other related natural phenomena are commonly described through the MMC algorithm (Joyce et al., 2008). The current study used the ISODATA.

2.2.10a Iterative Self-Organizing Data Analysis Technique

The ISODATA is one of the most important and widely used algorithms in unsupervised clustering. This processing method is a necessary step in the effective classification of images obtained from satellite platforms. Spectral reflectance is derived from a variety of wavebands for the identification of the characteristics of multidimensional clusters and their associated spaces. The results of the classification then need to be analysed to ensure validity. These data are considered indispensable to the understanding of the geological activity under study and the clusters of lava attributes. The actual numerical extents and the nature of the composition of classes must be determined by the classification approaches, which need to be wholly unsupervised. The extents must be unrelated to the previously developed conceptions regarding the structure of the geological landscape under investigation.

ISODATA-based analyses, which also facilitate the determination of the number of classes that may be included, enable the extensive detailing and classification of the obtained data (de Alwis et al., 2007). The following tasks are performed during each iteration of the algorithm at a high level. Points are designated to their closest cluster centres, which are revised to become the centroid of all the points assigned to them. The clusters with a very small number of points are deleted, and those with a large number of points that fit specific criteria are split. The small clusters that fulfil other criteria are combined. The algorithm continues with these iterations until the number of iterations reaches a user-defined value (Fig. 2.6).

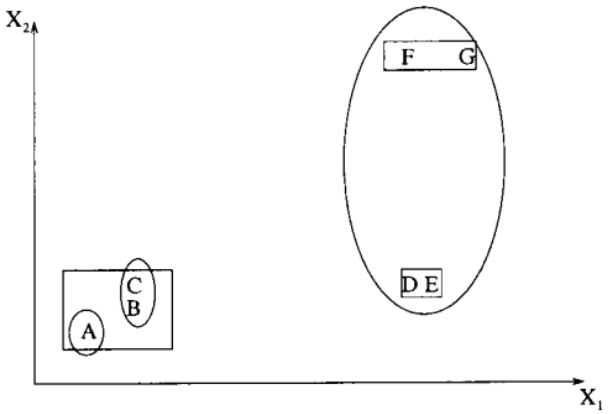

Figure 2.6: The iterative self-organizing data analysis (ISODATA) procedure. Through the ISODATA, Clusters (A) and (B, C) were first merged into one cluster because of the small distance between their centroids. The cluster (D, E, F, G), which had a large variance, was split into two clusters: (D, E) and (F, G) (Jain et al, 1999).

For the present study, the USGS website allowed the use of an image from the Landsat 8 OLI data (LC81710432017063LGN00), Path 171 Row 043. The image had minimal cloud cover. The data were collected on 4 March 2017, and the images taken during this time were identified as the data products of the Level 1 digital number. The data were acquired from zipped Georeferenced Tagged Image File Format (GeoTIFF) files representing systematically terrain-corrected data (L1T). The analysis, interpretation and elucidation of the data obtained from the files required that specific steps be followed. There are two parts to the advanced digital processing of the images. The first requires the subsetting of the images to establish the required area of study. Imagery upgrading and enhancement strategies can then be used during image development and interpretation in order to organise the relevant data.

The L8 Observatory satellite, which is the result of a complex design process, performs a 705 km sun-synchronous orbit in a cycle that is repeated every 16 days. The L8 satellite orbits the Earth once every 98.9 minutes. The satellite contains two sensors: the TIRS built by the NASA Goddard Space Flight Center (GSFC) and the Operational Land Imager (OLI) built by BATC. The TIRS and the OLI can simultaneously image each scene; however, they can also be used independently in the event of a problem with a sensor. Under normal conditions, the sensors operate by scanning the Earth and making observations at a nadir-positional location that is optimised through the orbital circulation

path of the Worldwide Reference System-2 (WRS-2), which is synchronised with the sun. Nevertheless, significant and specific imaging can still be performed from an off-nadir position. Each sensor can be used to obtain much more advanced and improved technical measures than is possible with the previously mentioned Landsat equipment. According to Zanter (2016), the L8 Observatory directly references the spacecraft, as well as the integration of the sensors.

2.2.10b Spectral reflectance

When electromagnetic radiation and objects located on the Earth's surface interact, considerable variations in the reflection of energy and light, the absorption process and energy transmission can be observed. D'Alessandro (2006) asserted that this process also reflects the reciprocal interaction of the objects and the energy generated around them. Depending on the characteristics of the objects, significant fluctuations in the amount of energy that is reflected, absorbed or transmitted can occur during such a process (Bernard, 2013). Thus, several complications must be considered when distinguishing between two phenomena occurring on the surface of the planet within the available spectral zones. The variations in these spectral zones could provide differential measures for the identification of specific objects. These factors reflect the wide range of interactions that can facilitate the identification of the physical characteristics of an object under study: from light- and composition-based perspectives. The following equation can thereby be extrapolated from the conservation of energy:

$$\mathrm{E}_r + \mathrm{E}_\tau + \mathrm{E}_a \equiv 1, \tag{5}$$

where E_r is the light reflected back from the surface of the object, E_t is the light transmitted through the object, and E_a is the light absorbed by the object. Each is a function of the wavelength. This leads to the realisation that the reflected waves are primarily those that are neither absorbed nor transmitted. Regarding the observations that can be determined through an examination of the laws of reflection, the light will be reflected from a surface at an angle equal to the incident angle (Farrier, 2006).

The study under consideration emphasised the properties of reflectance. The aspects related to the study topic were dependent on the primary evaluation of the roughness at the

surface of the object. A close comparison can be made with the wavelength of the emitted electromagnetic radiation, which can be observed by focussing on the object. The two relevant primary measures of reflectance were diffuse and specular reflectance (Joyce et al., 2008). Diffuse reflectance is observable on rough surfaces, and specular reflectance is emitted from less rough or are mostly smooth or flat surfaces (Fig. 2.7).

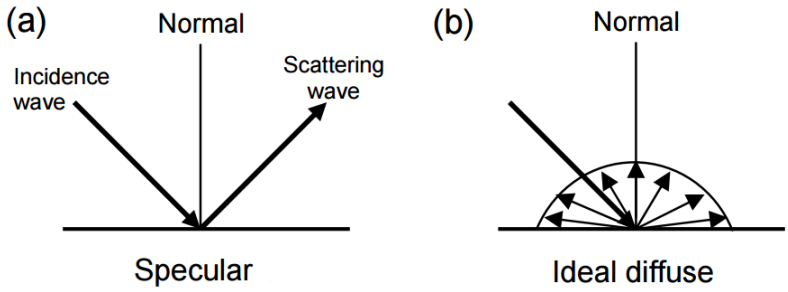

Figure 2.7: Reflection models. a: Specular reflectance. b: Diffuse reflectance (Farrier, 2006).

Radiometric corrections were performed to determine the measure of reflectance that could be observed at the surface of the object. This process was important for the successful conversion of the data derived from the digital images. The images, which were gathered mostly through satellite imagery, were used in the calibration of the quantities and physical dimensions associated with the surface conditions of the planet Earth.

Atmospheric correction, the removal of atmospheric effects, was performed to recover the surface reflectance (which portrays the surface properties) from the remotely detected imagery. The radiometric and atmospheric corrective strategies are explained below.

2.2.10c Conversion to top-of-atmosphere reflectance

The information available from the USGS website facilitated the conversion of the data from the OLI band to TOA reflectance. The emphasis was on planetary reflectance; thus, the reflectance rescaling coefficients provided in the product metadata (MTL) file were applied. The resulting equation could then be used to effectively convert the DN values to TOA reflectance values to facilitate the analysis of the OLI data (Zanter, 2016).

$$\rho\lambda' = M_\rho \times Q_{cal} + A_\rho \quad (6)$$

where:

$p\lambda'$ = TOA planetary reflectance without correction for solar angle.

M_ρ = Band specific multiplicative rescaling factor from metadata.

A_ρ = Band-specific additive rescaling factor from the metadata.

Q_{cal} = Quantized and calibrated standard product digital number (DN).

Note that $p\lambda'$ is not true TOA Reflectance, because it does not contain a correction for the solar elevation angle. The conversion to true TOA Reflectance is as follows:

$$\rho\lambda = \frac{\rho\lambda'}{\cos(\theta)} = \frac{\rho\lambda'}{\sin(\theta)} \quad (7)$$

where:

$\rho\lambda$ = TOA planetary reflectance.

θ = Solar Elevation Angle (from the metadata, or calculated).

Chapter 3

Unsupervised classification of lava flows in Harrat Lunayyir using remote sensing and GIS

Arabian Journal of Geosciences

Azizah Al Shehri and Agust Gudmundsson

https://doi.org/10.1007/s12517-019-4707-3

Statement of contribution:

The origin idea, methodology, computation and creation of models were developed by AA.
Fieldwork by AA
Writing the initial draft was made by AA and later critical review and commentary from co-author
All illustrations were prepared by AA, with later adjustments and modifications from co-author.
Interpreted data and discussions were done by AA and specifically critical revision from co-author.

Arabian Journal of Geosciences (2019) 12:522
https://doi.org/10.1007/s12517-019-4707-3

COMMENT

Unsupervised classification of lava flows in Harrat Lunayyir using remote sensing and GIS

Azizah Al Shehri[1] · Agust Gudmundsson[1]

Received: 25 April 2019 / Accepted: 31 July 2019

Abstract
Mapping of lava flows based on remote sensing data of high accuracy has become a common tool for exploring volcanic eruptions in greater detail. Mapping data based on remote sensing data provides information on the location and flow direction of lava flows as well as their areas and enables the localisation of volcanic vents—valuable knowledge for pre- and post-eruption volcanic activity and behaviour estimations. The current research seeks to expand the understanding of the volcanic and tectonic processes in Harrat Lunayyir, Saudi Arabia. In view of this, remote sensing data was classified using iterative self-organising data analysis technique (ISODATA) algorithms. The aim of the classification is to identify spectral top-of-atmosphere (TOA) reflectance values to distinguish layers of old and recent lava flows based on differences. As a result, three distinct basaltic units were identified to have the following ages: 15.1 ± 6.1 ka (4%), 15.0 ± 8.4 ka (6%), and 14.6 ± 23.1 ka (10%). The differences in the calculated areas of the lava flows as mapped based on the remote sensing data and earlier modelling are captured and identified in relation to the local geomorphologic and geologic structures. The differences can be partly explained as being related to a considerable weathering of the observed geological formations at 800–1600 nm, with reflectance of 12%. The limitation of the methodology relates to the lack of accurate geochronological timeline, that is, an inability to identify accurate age of the samples.

Keywords ISODATA · Morphology classification · Remote sensing · Top-of-atmosphere (TOA)

Introduction

The factors that affect the flow of lava and its morphology include its rheological properties, the rate of discharge or effusion, the topography, in particular the slope, and the external environment in which the flow of lava takes place. As the lava flows, its temperature falls, which affects its rheology (Griffiths 2000; U.S. Geological Survey 2008). The most important rheological properties of lava include the yield strength, viscosity, crystal fraction, composition, and vesicularity (Loughlin et al. 2014). Yield strength is strongly dependent upon the lava's temperature.

Mapping to delineate the nature of the expansion of lava flows and flow fields is directly associated with factors such as the improved understanding and identification of vents, including their locations, as well as lava-flow volumes. Moreover, forecasting possible hazards and risks associated with lava flows can only be performed through obtaining information concerning the geographical position and direction of these flows (Trusdell 1995). Estimation of the volume of lava can be performed by utilising a combination of the information derived from the areas of lava flow with that derived from the measurements of the thickness of the flow of lava, which can be observed in the field (Shaw and Swansond 1970; Self et al. 1997; Crown and Baloga 1999).

In the last two decades, researchers have studied Holocene volcanic events and mapped the distribution of associated lava at several locations, including some of the world's most volcanically active regions. For example, Rossi (1997) and Rossi and Gudmundsson (1996) mapped lava flows in Iceland, Head et al. (2012) mapped lava flows in Central Africa, and

Editorial handling: Abdullah M. Al-Amri

✉ Azizah Al Shehri
azizahzz@yahoo.com

Agust Gudmundsson
rock.fracture@gmail.com

[1] Department of Earth Sciences, Royal Holloway University of London, Egham, UK

Published online: 11 August 2019

Guest et al. (1987) and Calvari et al. (Calvari and Pinkerton 1999) mapped lava flows in Mt. Etna, while Murcia et al. (2013) studied lava flows in the Harrat Rahat region of Saudi Arabia. Most of these studies employed field mapping techniques to gather data. While field measurements and analysis are accurate, they are also time-consuming and laborious, particularly when lava flows are extensive (Cashman et al. 1998; Crown and Ramsey 2016). One viable alternative mapping method, which is potentially as reliable and accurate, and certainly more efficient, is remote sensing.

Urban landscape planning has many benefits in terms of the environment. Urban landscape planning means making decisions about the future situation of urban land. In this case, it is necessary to predict how the land has changed over time and the effects of natural factors and human activities on the land. In this way, successful and sustainable landscape planning studies can be achieved. Land cover and green area change related to urban area and its immediate surroundings were determined: Land use change is due to human activities and natural factors. Land cover is one of the most important data used to demonstrate the effects of land use changes, especially human activities. Production of land use maps can be done by using different methods on satellite images. Some studies have produced land cover maps of the controlled classification technique over Landsat satellite imagery. By using land cover maps, the changes in urban development and green areas over time have been evaluated. At the same time, the relationship between changes in the land cover over time and changes in the urban population has been (Cetin 2015; Cetin 2016a, 2016b; Cetin et al. 2018; Kaya et al. 2018).

Remote sensing technology for geological surveys is a rapidly developing field and has been cited as a highly reliable alternative to traditional approaches such as field mapping (Head et al. 2012). It provides spatial, spectral, and temporal coverage for both the monitoring and geological mapping of broad regions of volcanic terrain. In the supervised classification of volcanic morphology, image processing is guided by the user to specify morphological classes of interest. The user defines areas of the mapped region that are known to be representative of a particular volcanic cover type for each class of interest. The software then determines the spectral signature of the pixels within each specified area and uses this information to define the mean and variance of the classes in relation to the entire imaged region. Each pixel in the image is then assigned, based on its spectral signature, to the class it most closely matches. In unsupervised classification, image processing software classifies an image based on natural groupings of the spectral properties of the pixels, without the user specifying how any portion of the image should be classified. Conceptually, unsupervised classification is similar to cluster analysis, where observations (pixels) of the same values or value ranges are assigned to the same classes. For example, Shen et al. (2008) used a remotely located device to detect and measure electromagnetic radiation (EM). The most important parameters of such radiation are the wavelengths and spectral reflectance of resulting EMs. More often than not, satellite images are used in both supervised and unsupervised classification. In these cases, the wavelength spectrums for an object are represented as bands.

Remote sensing has been applied in the mapping of lava flows some time ago (James et al. 2009; Harris et al. 2011; Dietterich et al. 2012; Kubanek et al. 2015; Slatcher et al. 2015). Recent studies reveal that several types of satellite images can be used for mapping, including radar, thermal infrared, and optical images (Bonne et al. 2008; Millington et al. 2012; Nicolas et al. 2008; Tarquini and Favalli 2011). Bymes et al. (Byrnes et al. 2004) used remote sensing technology to characterise the surface morphology of Mauna Ulu in Hawaii. They employed ASTER and MASTER (multispectral) techniques to map and interpret lava emplacement. Their survey concluded that pahoehoe lava flows have a higher reflectance than ‘a’a lava flows. One reason for this is pahoehoe crystalline structure providing a greater reflective surface. Pahoehoe is more crystalline than A ā; due to its slow moving nature, it is able to cool slower due to heat being retained at depth within the flow, thereby allowing the formation of larger crystals.

The present paper aims to present the results of the remote sensing–based classification of flows of lava at Harrat Lunayyir in western Saudi Arabia (Fig. 1). This classification was performed in an unsupervised manner through the utilisation of remote sensing data based on ISODATA algorithms. This technique is effective in that it outlines the number of different classifications in which the data obtained can be categorised. The purpose was to form data clusters within each of the areas of land coverage. The study of the behaviours of spectrums being emitted from various volcanic regions, which is known as ‘TOA Reflectance’, also forms an element of the present research. The objective here is to consistently outline the various categories and characteristics of both recent and old flows of lava through an evaluation of the properties of spectral reflectance. The validation of these classifications has been performed through sampling, which involved the results of the ISODATA classification.

Study area

Harrat Lunayyir is located in the western part of the Arabian Plate, which is situated in close proximity to the African Plate, being separated from it by the Red Sea rift zone. A Proterozoic shield constitutes the core of the western part of the Arabian Plate. The major tectonic changes that formed the macrotectonic structures in the area occurred during the African Rift formation. Thus, the Red Sea and the Gulf of Aden formed at around 25 Ma ago (Stern and Johnson 2010).

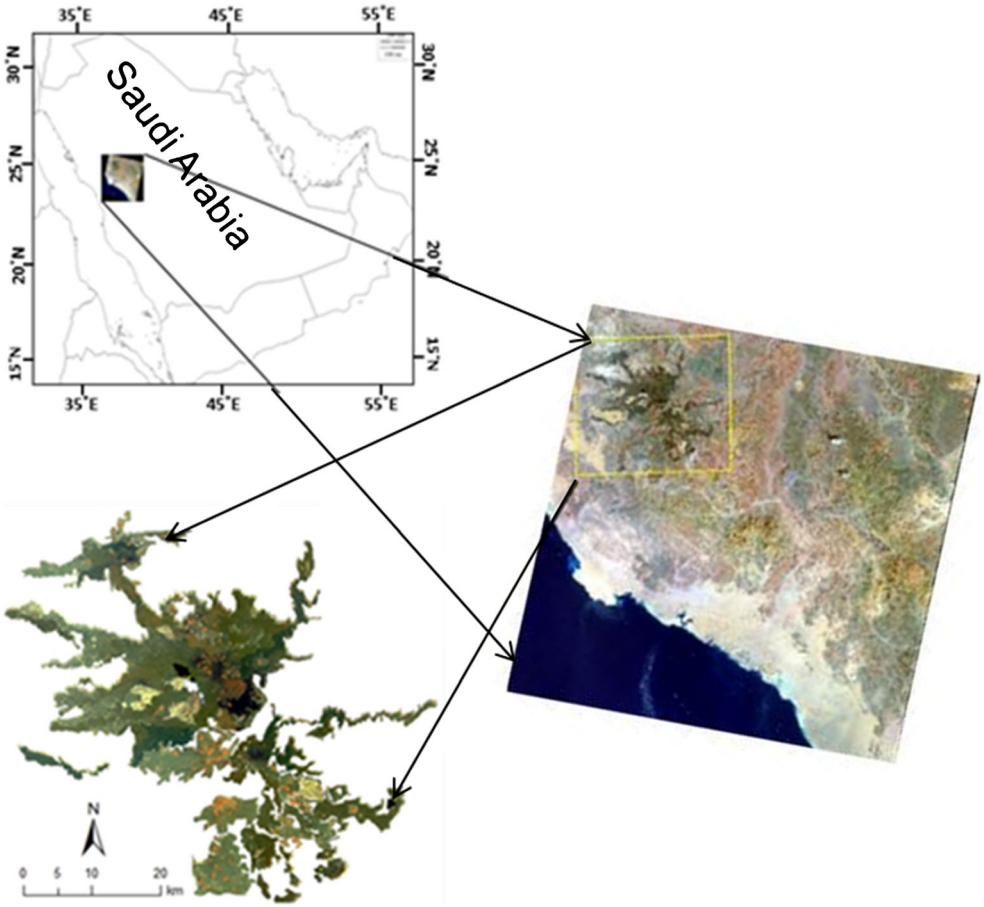

Fig. 1 Location map for the Harrat Lunayyir volcanic field, western Saudi Arabia

Throughout the process of the spreading of the Red Sea, which has been active over the past 30 million years, some parts of the Arabian Shield became extended along the Red Sea rift boundary (Bailey 2009). This process was accompanied by continental collision between the Arabian and Euro-Asian Plates, which has been taking place since the Miocene (Hansen et al. 2013). The result of these processes was active deformation and magma generation that created the conditions for the formation of volcanic fields within the areas adjacent to rifting zone (Al Damegh et al. 2005; Rodgers et al. 1999).

The main geological structures that constitute the Arabian Shield in the area of interest include pre-Cambrian crystalline rocks, Phanerozoic sedimentary rocks, and Cenozoic flood basalts. Harrat Lunayyir is one of those fields that represent an instance of Cenozoic flood basalts. The average crustal thickness of the shield is around 40 km (Al Damegh et al. 2005) with a tendency to decreased thickness towards the Red Sea. Thus, in the areas around Harrat Lunayyir, crustal thickness is as little as 23 km. A similar degree of crust thickness can also be observed in the Nubian Shield, which is situated towards the western region of the Red Sea. Within Egypt, the thickness of the crust is 25–26 km, and this continues up to a distance of 50 km towards the coastal region of the Red Sea.

During the Cenozoic period, there was considerable volcanic activity in the western section of the Arabian Plate. This activity took place during two principal episodes. The first was during a period from around 20 to 30 Ma ago, while the later one began 12 Ma ago and continues to this day (Camp and Roobol 1992). The common name of *harrats* is mostly attributed to the fields of lava (Pint 2006). These are also known as the Harrat Al-Shaqa. These areas are amongst the smallest alkali-basaltic fields of lava generated during the Holocene and are generally located towards the western margin of Saudi Arabia. More specifically, the location of the field is at the coordinates of 25° 10′–25° 17′ N latitude and 37° 45′–37° 75′ E longitude. The field of lava is located approximately 60 km from the eastern section of the Red Sea coastal regions and 150 km to the east from the central section of the red sea (Al Amri and Fnais Al-Amri and Fnais 2009; Baer and Hamiel 2010; Al-Zahrani et al. 2013; Duncan and Al-Amri 2013) (Fig. 1).

The region of Harrat Lunayyir is characterised by the alkali-olivine-basalt lava flows that formed during the Cenozoic geological period (Duncan and Al-Amri 2013). This region, and its formation period, involved approximately 50 monogenetic craters of volcanic cones of various measures (Baer and Hamiel 2010). There are two specific segments that

could characterise the basaltic flows of lava. The first is the Tertiary unit, which is considerably older (Jarad basalt), and the second is the Quaternary unit, which is comparatively younger and is also known as Maqrah basalt, according to Al Amri et al. (Al-Amri et al. 2012) (Fig. 2).

The eastern, northern, and southern sections of Harrat Lunayyir are composed of Precambrian rocks. The central section of the region is composed of a multiplicity of rocks, of which only isolated sections have rocks from the Precambrian period as their constituents. The seismic as well as the volcanic events of Harrat Lunayyir began approximately 0.5 Ma ago (Duncan and Al-Amri 2013). An informed estimation suggests that the flows of lava that occurred most recently could have taken place approximately 5000 years ago (Al-Amri et al. 2012). In this respect, it could also be presumed that some recent eruptions could have taken place in the region, since a specific cone of craters was formed here approximately 1000 years earlier, as pointed out by Baer and Hamiel (2010).

Methodology

Nicolas et al. (2008) observe that the use of remote sensing is invaluable in volcanic monitoring. Sensors are devices that record the amount of electromagnetic radiation energy that strikes them at a specific wavelength range. Remote sensing can be accomplished from air-borne and space-borne platforms. Crown and Ramsey (2016) suggest that space-borne platforms are the most widely used in the unsupervised classification of lava flow. The scattering or reflection of an energy signal by lava flows is dependent on a number of factors, including conductivity, permittivity, and surface roughness (OSU 2015). Surface reflectivity is the ratio of reflected power to direct power and is critical in the monitoring and classification of lava flows (D'Alessandro 2006).

Satellites are the principal remote-sensing instruments used by geoscientists to monitor geographic data on the Earth's surface. Satellites map events use optical instruments (OSU 2015). Despite the general reliability of this technology, cloud cover can hinder satellite mapping. As a result, it is essential that users utilise satellite imagery from various sources gathered over an extended period (U.S. Geological Survey 2008). Landsat imagery is widely used in unsupervised classification, owing to the large number of Landsat satellites that have increased coverage of the Earth's surface.

Digital image classification techniques

Bernard (2013) reports that digital image classification techniques are the main tools used in grouping pixels to represent land-cover features. The main purpose of remote sensing is the interpretation of observed data and classification of features. Pixels are the smallest units of an image that are used in classification (Nicolas et al. 2008). As such, images are classified according to the reflectance statistics of their pixels. There are two major image classification techniques, namely unsupervised and supervised classifications (Head et al. 2012). In practice, supervised image classification involves the input from the user, who classifies objects in correspondence with the features known or observable in the satellite imagery, while unsupervised image classification is automated and performed by software. A brief description of unsupervised classification is provided below.

According to Bonne et al. (2008), the unsupervised classification of images entails the clustering of pixels according to their reflectance properties (Fig. 3). Users then determine the number of clusters to be generated and the bands to be used (Millington et al. 2012). This information represents an input into image classification software, which uses clustering algorithms to identify clusters with morphological features. This approach is most effective in instances where no sample sites

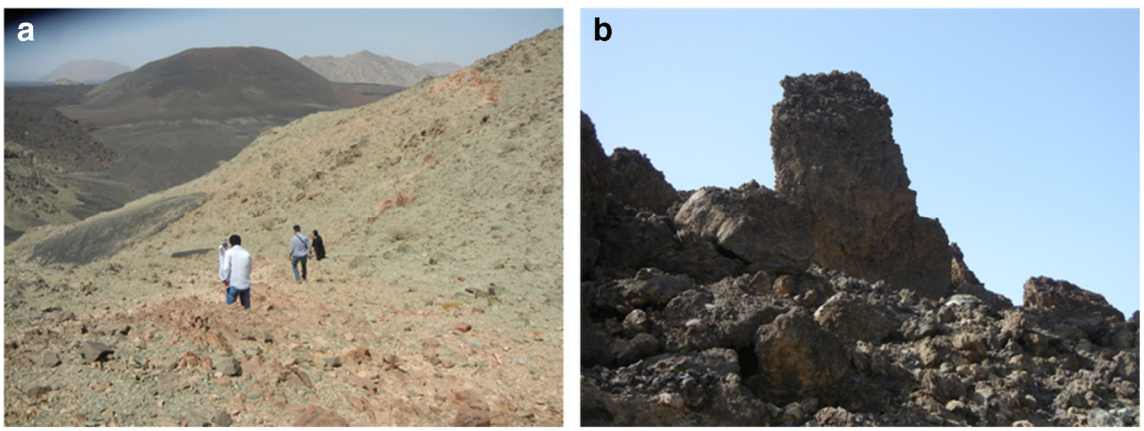

Fig. 2 Volcanic geology of the Harrat Lunayyir volcanic field. **a** Volcanic ash partly covering a hill. **b** Basaltic lava flow of Quaternary age (Maqrah basalt)

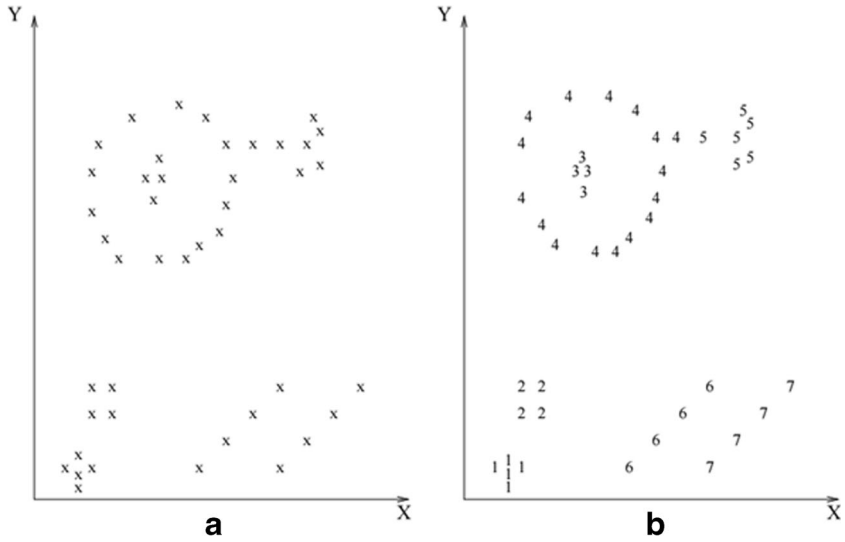

Fig. 3 Digital image classification techniques. Input patterns are shown in (**a**), and the desired clusters are shown in (**b**). Clusters assigned the same label (Jain et al. 1999)

exist (Nelson 2016). In summary, image analysis algorithms identify related pixels and group them into different classes without any human guidance whatsoever. Joyce et al. (2008) report that unsupervised clustering is a fundamental tool in image processing, particularly for remote sensing and geoscience applications.

General overview

It is advisable to crop the chosen images to include the area around the lava flow of interest in order to permit accurate and faster classification, since fewer pixels will need to be evaluated and grouped into classes under these circumstances (Head et al. 2012). This procedure can be used to determine the location and number of unimodal spectral classes. One common approach in unsupervised classification is the migrating means clustering classifier (MMC) (Crown and Ramsey 2016). Digital image processing software, such as the spatial analysis tool in ARC GIS Imagine, is used for the unsupervised classification of lava flows. The migrating means clustering algorithm is widely used in describing flooding and lahar flow, amongst a host of other phenomena (Joyce et al. 2008). In this paper, we use the iterative self-organising data analysis technique (ISODATA).

ISODATA

One of the most significant and extensively used algorithms that perform unsupervised clustering is ISODATA. This procedure is a general process of application that is necessary to perform the classification of satellite-based imagery. A multiplicity of wavebands is used to derive spectral reflectance for the purpose of identifying the attributes of multidimensional clusters and the spaces associated with them. The classification results must then be analysed from the perspective of the researchers. The information that these researchers possess can be understood to be integral regarding the geological structure or process under consideration; this is also significant regarding the understanding of the nature of various clusters of lava attributes. The methods of classification, which must be completely unsupervised, need to be able to identify the actual numerical extents as well as the nature of the composition of classes that cannot be related to the previously formulated conceptions regarding the structure of the geological landscape under consideration.

Techniques involving ISODATA-based analysis make it possible to reach the required level of details with identification of the number of additional classes (de Alwis et al. 2007). The algorithm of the data classification can be described in the following steps: (1) data points are assigned in accordance with the closest cluster centres; (2) the positions of cluster centres are amended so that they become centroids for the set of data points assigned to them; and (3) splitting of clusters with an abnormally large set of points and merging smaller clusters (Fig. 4).

Landsat 8 OLI data (LC81710432017063LGN00)

One image of Landsat 8 OLI data (LC81710432017063LGN00), Path 171 Row 043, which did not have much cloud cover, was made available by the website of the United States Geological Survey (USGS) for this study. The data collection took place on 4 March 2017, and the resulting acquisition of the images could be identified as the data products of the level 1 digital number. The acquisition process of the data was undertaken in the format of the zipped georeferenced tagged image file format (GeoTIFF) files, representing systematically terrain-corrected data (L1T). A number of processes needed to be utilised for the analysis, interpretation, and elucidation of the obtained data. The

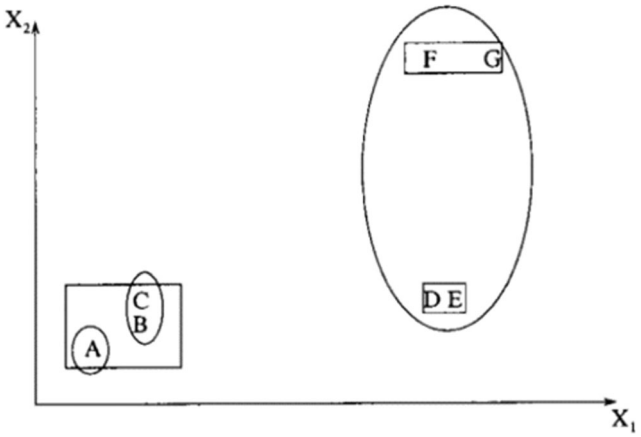

Fig. 4 ISODATA techniques. Merging the clusters (A) and (B, C) into one cluster since distance between their centroids is small and then splitting the cluster (D, E, F, G), which has a large variance, into two clusters (D, E) and (F, G) (Jain et al. 1999)

advanced digital processing of images can be sorted into two parts. The first involves the sub-setting of the images, which is performed to acquire the zone of study interest. Thereafter, imagery enhancement and upgrading strategies can be used in the process of image development and interpretation with the aim of separating out valuable data.

The L8 Observatory satellite was constructed using an intricate design process with the purpose of having a 705-km, sun-synchronous orbit and a cycle of repetition of 16 days in length. The L8 completely orbits the Earth every 98.9 min. L8 carries a two-sensor payload: the OLI was built by the BATC, while the TIRS was built by the NASA GSFC. Every scene can be automatically imaged by both the OLI and TRS in a simultaneous manner; however, both are also capable of being utilised independently should any problem occur in one of the sensors. During the operations that can be undertaken under normal conditions, the sensors can scan and observe the Earth at a nadir-positional location that is optimised through the orbital circulation path of the sun-synchronous Worldwide Reference System-2 (WRS-2). Both of these sensors can be utilised to achieve greater improvements and advancements in technical measures relative to the previous Landsat equipment. The L8 Observatory is a direct reference to the spacecraft, along with the integration of both of the sensors (Zanter 2016).

Spectral reflectance

General overview

The interaction between the electromagnetic radiation and the objects situated on the Earth's surface can lead to significant variations in the absorption process, reflection of light and energy, and the transmission of energy. This entire process is also indicative of the reciprocity amongst the generated energy and the objects (D'Alessandro 2006). The amount of the energy that can be transmitted, absorbed, or reflected in such a process can also fluctuate considerably according to the differences in the physical conditions and typology of the objects (Bernard 2013). There are therefore certain complications involved in distinguishing two separate phenomena that may be observed on the surface of the Earth involving the available spectral zones. The variations in these spectral zones can provide differential measures of undertaking such identifications of specific objects. These aspects are closely reflective of the various interactions that can highlight the differential physical characteristics associated with the light and the physical composition–based elements of the object being viewed. The following equation can thereby be extrapolated from the principle of the conservation of energy:

$$E_r + E_\tau + E_\alpha = 1 \quad (1)$$

where E_r is the light reflected back from the surface of the object, E_τ is the light transmitted through the object, and E_α is the light absorbed by the object; each is a function of wavelength. It follows that the reflected waves are primarily those that neither get absorbed nor transmitted. From the laws of reflection, it also follows that light is reflected from a surface at an angle equal to the incident angle (Farrier 2006).

The present study emphasises the properties of reflectance. The aspects related to the study topic depend on the primary evaluation of the roughness at the surface of the object; this can be closely compared with the wavelength of the emitted electromagnetic radiation, which can be observed through focusing on the object. The two primary measures of reflectance relevant in this study are diffuse and specular reflectance (Joyce et al. 2008). Diffuse reflectance is observable at rough surfaces, while specular reflectance is that emitted from surfaces that are comparatively less rough, or that are mostly smooth or flat (Fig. 5).

Radiometric corrections were performed to determine the measure of reflectance that could be observed at the surface of the object. This process is important for converting the data derived from the digital images in a successful manner. The images are mostly gathered through satellite imagery and are utilised in the calibration of the quantities and physical dimensions associated with the surface conditions on Earth. Moreover, atmospheric correction is made to recover the surface reflectance (which portrays the surface properties) from

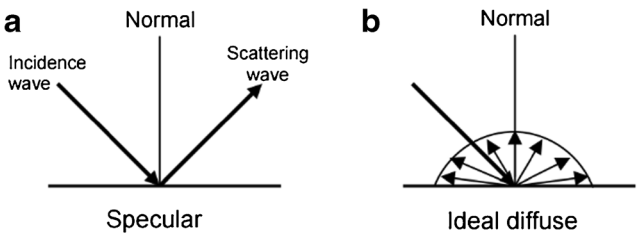

Fig. 5 Reflection models. **a** Specular reflectance. **b** Diffuse reflectance (Farrier 2006)

remotely detected imagery by removing atmospheric effects. The strategies by which radiometric and atmospheric corrective actions are performed are clarified below.

Conversion to TOA reflectance

Based on information available from the USGS website, the data from the OLI band can be converted to top-of-atmosphere (TOA), or top of the atmosphere reflectance. The emphasis here is on planetary reflectance using the reflectance rescaling coefficients provided in the product metadata file (MTL file). The resulting equation can be applied to effectively convert the DN values to TOA reflectance values to facilitate the analysis of the data regarding OLI (Zanter 2016).

$$\rho\lambda' = \mathrm{M}_\rho \times Q_{cal} + \mathrm{A}_\rho \quad (2)$$

where $\rho\lambda'$ = TOA planetary reflectance without correction for solar angle, M_ρ = band-specific multiplicative rescaling factor from metadata, A_ρ = band-specific additive rescaling factor from the metadata, and Q_{cal} = quantised and calibrated standard product digital number (DN).

Note that $\rho\lambda'$ is not the true TOA reflectance, because it does not contain a correction for the solar elevation angle. The conversion to true TOA reflectance is through the following equation:

$$\rho\lambda = \frac{\rho\lambda'}{\cos(\theta)} = \frac{\rho\lambda'}{\sin(\theta)} \quad (3)$$

where $\rho\lambda$ = TOA planetary reflectance, and θ = solar elevation angle (from the metadata or calculated).

Landsat 8 OLI spectral endmember selection

In this method, spectra are selected from the images for specific areas. These regions are generally familiar to the image interpretation personnel due to their experience with previous research and field studies. The collected endmember points regarding the age groups of the lava are four points.

This spectral endmember point can be a specific spectral signature related to any surface cover of absolute measure that is visible in the satellite-derived images. This could represent individual categories, which are utilised to either classify or determine any aspect within the individual images (Fig. 6). Such uncontaminated, pure spectral endmembers are usually defined under either idealised in situ or laboratory conditions. Under such conditions, reflectance spectra may be obtained through the application of a portable spectrometer that focuses only on a single surface. At the point when in situ estimations become unrealistic, spectral endmembers can likewise be obtained from "pure" features in the imagery. The choice of such endmembers from the image itself can be carried out on the basis of prior knowledge regarding the occurrence of materials imaged in the scene. Manual selection from image data assumes spectral homogeneity.

Sample collection and processing

This section describes the rock samples collected at the site that were used in the current study. Initially, three volcanic rock samples were submitted to Oregon State University for analysis using the $^{40}Ar/^{39}Ar$ geochronological determination method. The samples were collected to represent the basaltic rocks in the study area. In terms of their composition, these samples are consistent with the amphibole-bearing rocks typical for the area; e.g., the trace components found in the basaltic rocks in the area are associated with the type of continental magmatism processes typical to the Arabian Shield.

The selection of the samples was based on the geological maps of the area. These show fine-grained basanites, alkali olivine basalt, and trachy basalts (Duncan and Al-Amri 2013). The groundmass of the sample rocks comprises largely glass and augite with minor olivine (Duncan and Al-Amri 2013). According to Al-Amri et al. (2012), in a study using an extended set of samples, the plateau ages of the samples showed significant variances.

Following the methodology developed by Duncan and Keller (2004), the sample rocks were processed and sieved to obtain the fractions of 300–600 nm size. The groundmass was separated from the phenocrysts and cleaned by acid leaching (Duncan and Al-Amri 2013). Thereafter, the sample units were cleaned and dried. The samples underwent irradiation in a dummy fuel rod in the reactor's central ring at 1 MW (Duncan and Keller 2004).

Results and discussion

TOA reflectance

Weather and climate conditions influence surface weathering of lava flows and affect their reflectivity. Lavas on Harrat Lunayyir have undergone different forms of surface alteration, but primarily oxidation-based chemical weathering processes. The lava flows have erupted at different times—they are of different age—and this was analysed through spectral reflectance measurements using Landsat 8 in the range of 435–2300 nm (Fig. 7).

The elements constituting the spectral information vary considerably with the morphological attributes and the age of the lava flows. In Fig. 8, the common features of the reflectance spectra are illustrated based on the shape of the spectral curves. A noticeable sharp increase in reflectance at 435–500 nm for all the studied lava flow with reflectance of 12% was observed, while the maximum shifts were identified in shorter wavelengths for lava flows 2, 3, and 4. The steepest part of the reflectance curves in the visible blue band area of

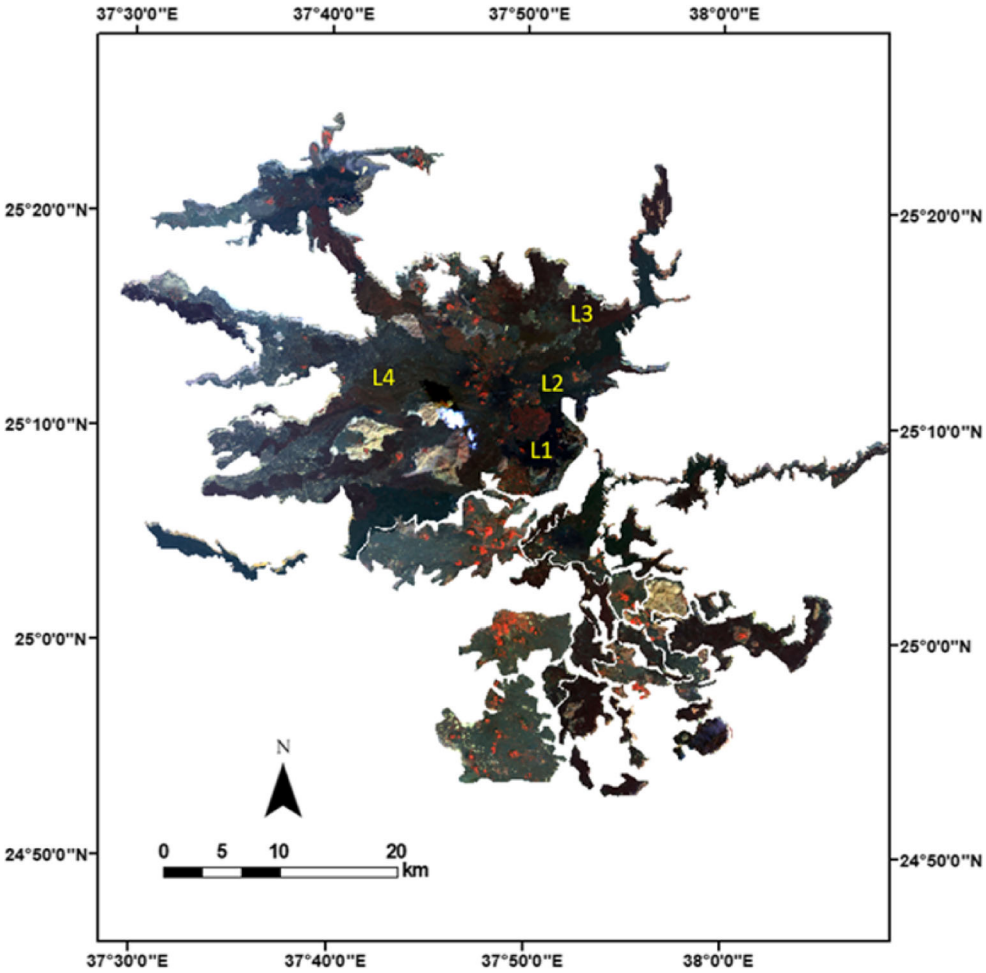

Fig. 6 Spectral endmember points were collected from Landsat 8 OLI False colour (bands combination 7, 4, 1)

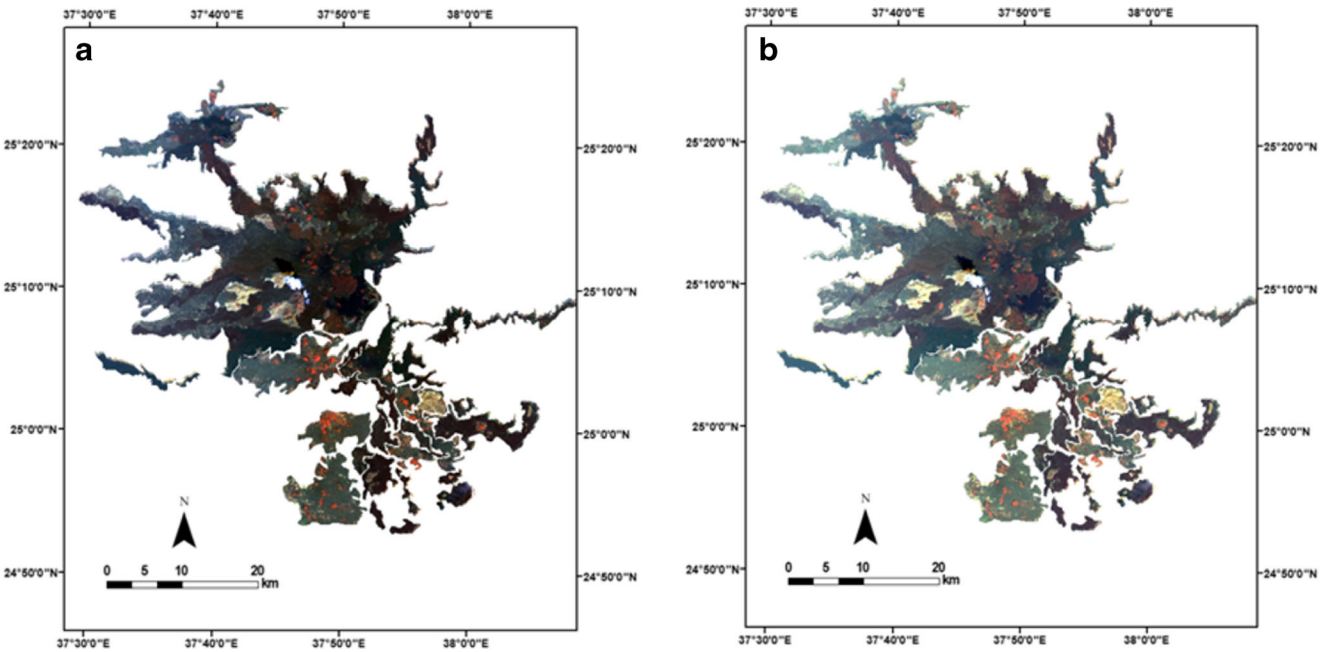

Fig. 7 Conversion to TOA reflectance. **a** Landsat 8 OLI image before conversion to TOA reflectance. **b** Image after conversion to surface reflectance

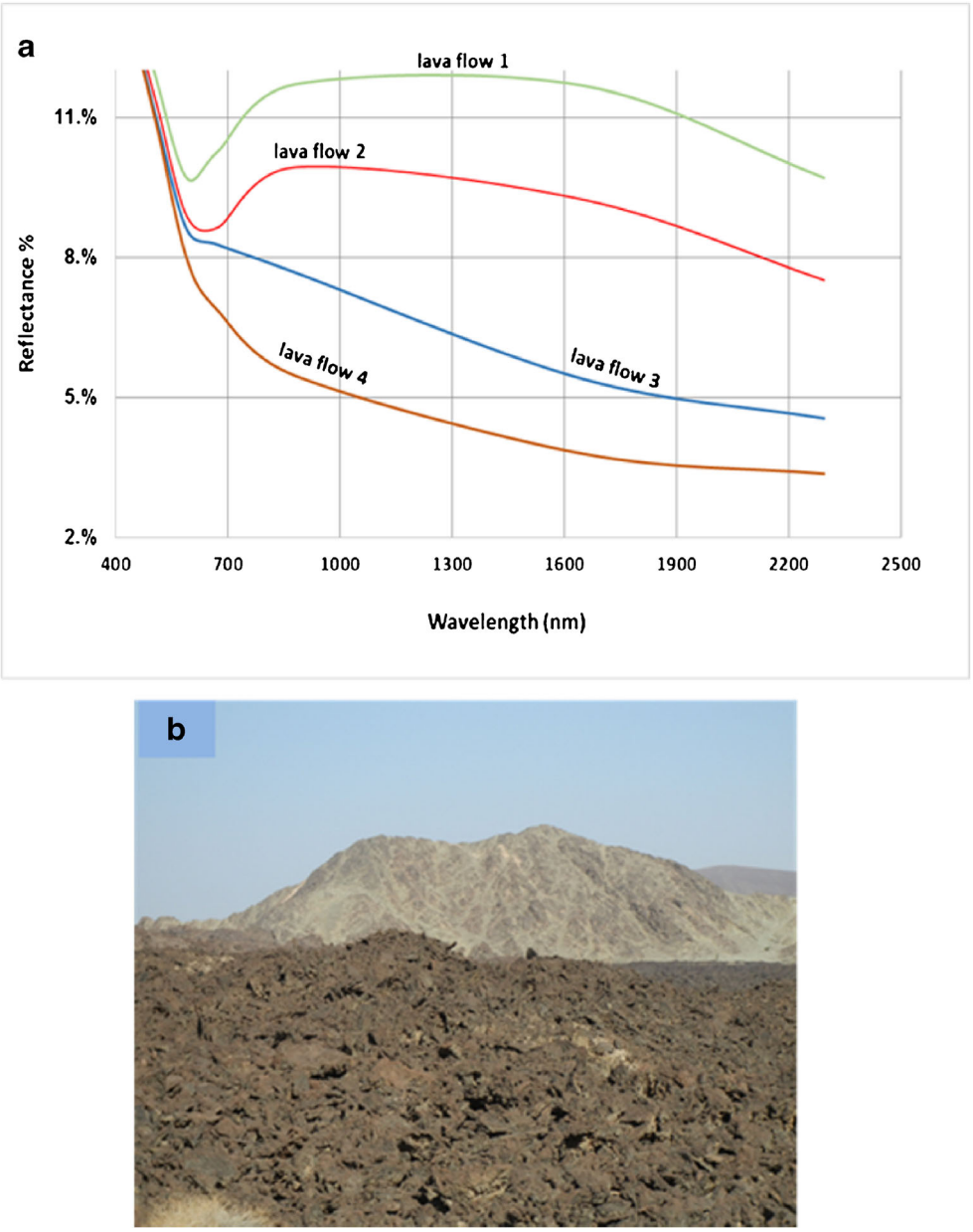

Fig. 8 Reflectance spectra. **a** Reflectance spectra of old and recent lava flows. **b** Note that lava flow 1, which has been subject to significant surface oxidation, attains high reflectance values especially in the near-infrared region

the visible range spectrum occurs at 452 nm. The reflectance curves are very flat for lava flows 1 and 2, apart from a noticeable decrease in reflectance from 1900 nm onwards. However, there is a gradual and sustained reflectance decrease in lava flows 3 and 4 beginning from the end of the visible range. We observe that for lava flow 1, there is a higher reflectance at 800–1600 nm at a rate of around 12%. A similar sustained rate can be seen for lava flow 2, albeit at a slightly reduced reflectance of around 9 to 10%.

Lava surfaces with a complete absence of any lichen (a simple slow-growing plant that typically forms a low crustlike, leaflike, or branching growth on rocks, walls, and trees) show low and flattened reflectance spectra, expanding in the visible segment and diminishing in the infrared segment of the spectrum. This flattening is generally more evident in older lava flows, which have been subject to considerable surface oxidation (of iron). In particular, the slope of the reflectance curve from the blue to the red range of the spectrum increases as oxidation increases, a spectral feature useful for defining an oxidation index that can be used to quantify the relative degree of the oxidation of lava surfaces.

ISODATA classification

The analysis of imagery regarding the trends of reflectance and colour is average measures and can be caused by a number of factors, including the weathering of glass, oxidation of iron elements, and the gradual development of plant life and

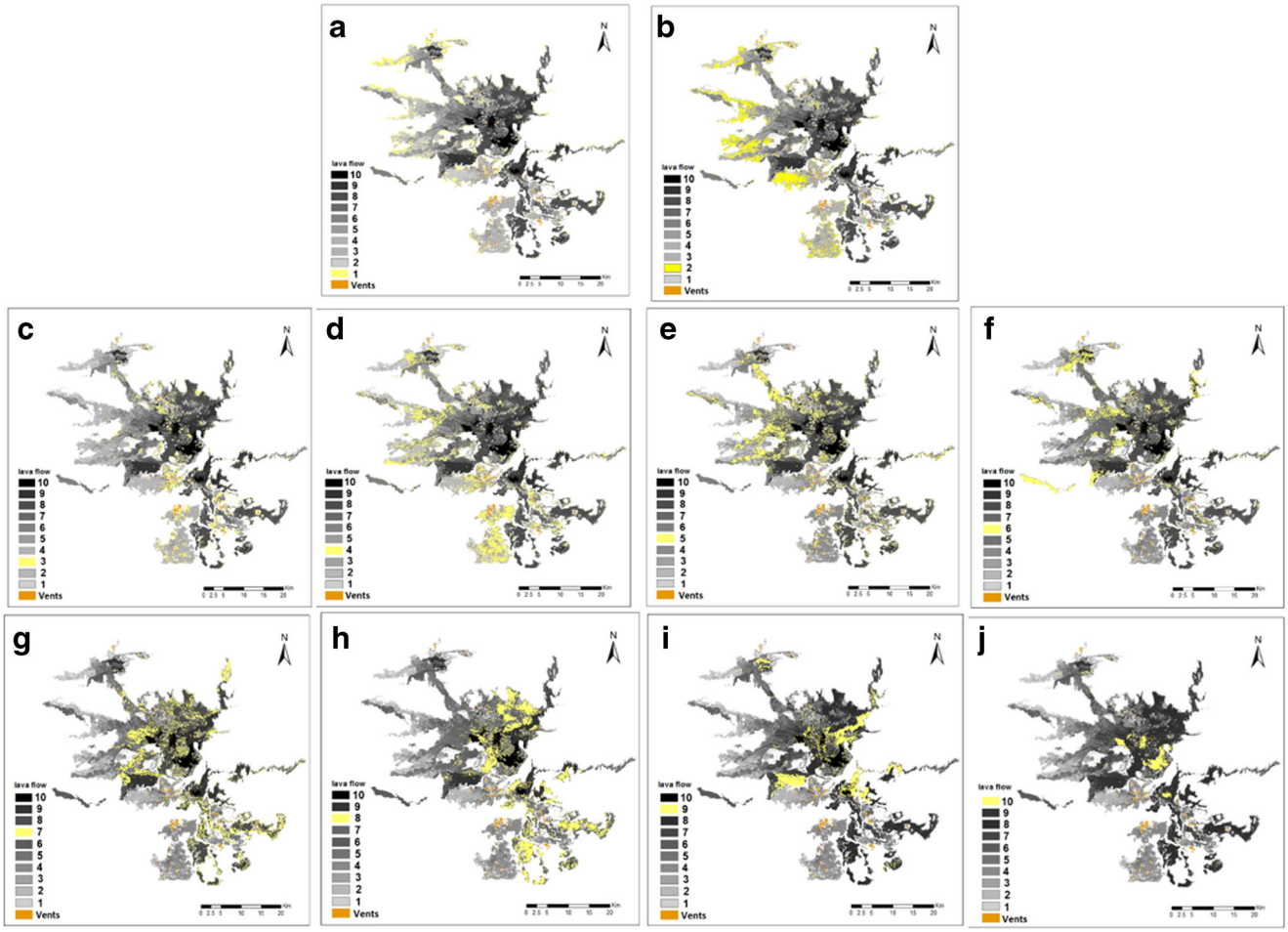

Fig. 9 Classification results of the ISO cluster method. **a** (class 1 represents old eruption) then **b** (class 2); **c** (class 3)...etc. **j** (class 10) in the legend shows the most recent lava flow

vegetation upon the uppermost crust of the lava flow. We use ten classes for the age classification of the lava flows. We also used geological maps to identify the basement rock types on which the lava flows were erupted.

The TOA reflectance (Figs. 7 and 8) was utilised as a key to both classify the lava and to choose the number of classes. We examined different numbers of classes and found that the best number that gave us the cluster of the youngest lava was number 10. As can be seen in Fig. 10, the classification results were found to be the same as those of the TOA reflectance. Accordingly, we give the oldest lava flow as 'class 1' sequentially with the rest of the classes (Fig. 9).

Accuracy assessment

To validate the classification, we sampled from the sites of the ISODATA classification (classes 10-9-8) (Fig. 9) for analysis at the Oregon State University for ^{40}Ar-^{39}Ar incremental heating age determinations (Fig. 10; Table 1). The accuracy of the unsupervised classification results is benchmarked to the output of the supervised classification, which is done with

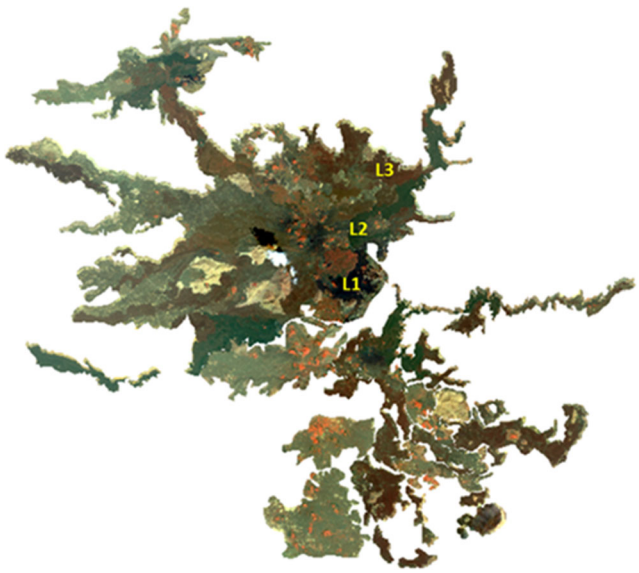

Fig. 10 Sample locations of lavas from Harrat Lunayyir, NW Saudi Arabia

Table 1 Location of samples for lavas from Harrat Lunayyir, NW Saudi Arabia

Sample number	Type of material	Longitude (°E)	Latitude (°N)
L1	Whole rock	37.846	25.150
L2	Whole rock	37.853	25.195
L3	Whole rock	37.882	25.256

reference to the knowledge of local geographic/geological features. Firstly, we gather training data from the field. This approach requires a priori knowledge of the geographical/geological features under investigation. Here, the analysts must have extensive knowledge of the lava flows, their formation, and subsequent weathering, as such information is critical in obtaining appropriate training data.

The placement of infrastructure such as pipelines, roads, and railways is highly dependent on the rock outcrops in an area. For this reason, the supervised classification of lava flows is vital. Some of the techniques employed include, but are not limited to, band ratios, synthetic aperture radar (SAR), linear spectrum unmixing, and vegetation masking. Geologists can detect a variety of variables, such as soils and lava flows (Egorov et al. 2015).

^{40}Ar-^{39}Ar incremental heating method

The precise dating of lava flows is crucial for understanding the characterisation of volcanic fields, which is itself essential for the reliable reconstruction of past events that shaped the topography of the fields (Walsh 2006). Different methods are used to date lava flows in order to determine the relative ages of past volcanic events. In this study, we have relied on the ^{40}Ar-^{39}Ar incremental heating method (McDougall and Harrison 1999) to assign ages to lava flows.

The Quaternary age of Harrat Lunayyir was indicated by a K-Ar date reported by Camp and Roobol (1992). Al-Amri et al. (2012) attempted to investigate the chronostratigraphy of Harrat Lunayyir using the ^{40}Ar-^{39}Ar method on six basaltic flows. Their results confirm the overall Quaternary (mostly late Pleistocene) age of the lava field, yet the age spectra are virtually indistinguishable within the lack of atmospheric argon ratios. Furthermore, the authors resorted to forcing the inverse isochron through the 295.5 value, which makes the results model ages rather than reliable age estimates.

Duncan and Al-Amri (2013) reported ^{40}Ar-^{39}Ar ages for 18 new samples from the six volcano-stratigraphic units mapped in the Harrat Lunayyir volcanic field (Al-Amri et al. 2012). One of their samples yielded a plateau age of 1.21 ± 0.13 Ma, which is considerably older than all other age estimates. The isochron for this particular sample has an age of 970 ± 29 ka, with an initial ^{40}Ar/^{36}Ar composition of 312 ± 4, thus indicating the presence of excess ^{40}Ar, which renders this age invalid for the purpose of delineating the eruptive sequence. All other ages were considered acceptable and indicate an overall continuous volcanic activity from about 600 ka to the present, with putative peaks of activity at ~ 400 ka and ~ 200 ka. The relatively uniform spread of ages rules out any significant hiatus in volcanic activity.

Fig. 11 Location of young lava place sample (L1)

In this study, we obtained samples from the same sites of the ISODATA classification results (class 10-9-8) (Fig. 9) and analysed the three youngest flows at the Oregon State University in the Argon Geochronology Laboratory (Fig. 11). The results are as follows:

- L1: plateau age 15.1 ± 6.1 ka (2 s.d. error) (Fig. 12a), which represents quaternary upper basalt (stratigraphic unit Qm5), historic to late prehistoric lava flows and scoria cones. The subunit comprises the products of four eruption sites of black scoria cones with lava flows (Al-Amri et al. 2012) surrounded by black air-fall ash covering adjacent Precambrian basement hills protruding through the lava field. One of these sites is believed to have erupted as recently as the tenth century (Al-Amri et al. 2012).

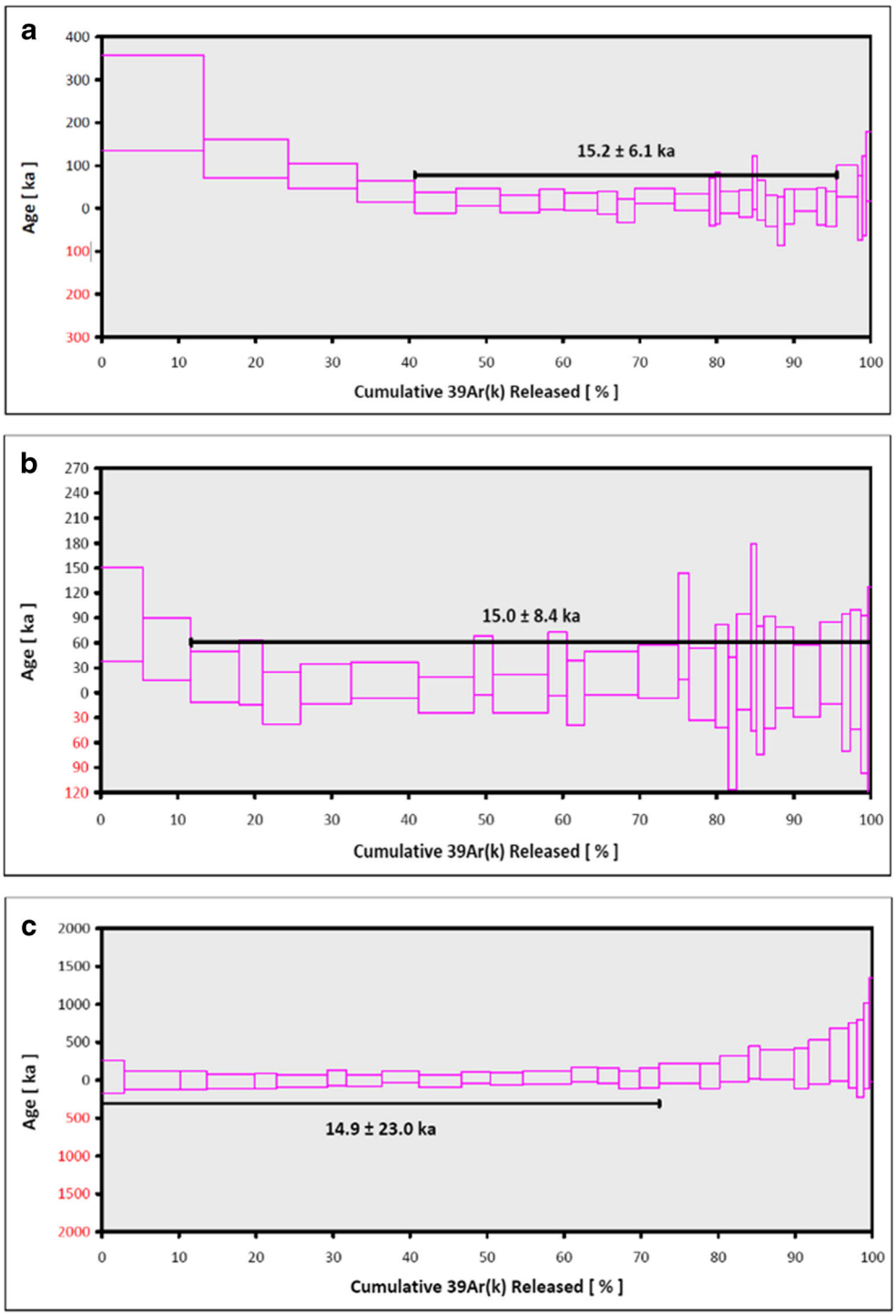

Fig. 12 Representative age spectra (plateaus) derived from $^{40}Ar/^{39}Ar$ incremental heating experiments on Harrat Lunayyir basaltic lavas. **a** represents location 1 (L1, plateau age 15.1 ± 6.1 ka); **b** represents the result of location 2 (L2, plateau age 15.0 ± 8.4 ka), and **c** represents the result of location 3 (L3, plateau age 14.6 ± 23.1 ka)

Table 2 ^{40}Ar-^{39}Ar incremental heating method L1, L2, and L3 lava flows

Sample	Plateau age (ka)	2σ error (ka)	MSWD	Initial $^{40}Ar/^{36}Ar$
L1	15.2	6.1	0.67	295.50
L2	15.0	8.4	0.47	291.75
L3	14.9	23.0	0.38	287.03

- L2: plateau age 15.0 ± 8.4 ka (2 s.d. error) (Fig. 12b). This represents prehistoric lava flows (stratigraphic unit Qm4), with prehistoric lava flows and scoria cones, lacks erosion, and having dust ponds 3 m in diameter. Dust ponds can be defined as fine-grained deposits in topographic lows transported and sorted by intense localised electric fields acting on charged dust or by impact-induced shaking. A very black colour was observed on the aerial photographs and satellite image.
- L3: plateau age 14.6 ± 23.1 ka (2 s.d. error) (Fig. 12c); non-eroded lava flows (correspond to the stratigraphic unit Qm3): non-eroded lava flows, slight gullying on scoria cones, dust ponds up to 100 m in diameter; Qm2: eroded lava flows and scoria cones, surface structures on flows such as flow ridges intact, but erosional rivulets are present. Scoria cones have distinct gullies and dust ponds are up to 400 m in diameter.

The obtained ages are characterised be exceptionally well-developed plateaux and comprising 55–72% of the ^{39}Ar released.

The age discrepancy between the inverse isochron of L1 and the other ages is probably related to the presence of relic ^{40}Ar, as manifested by the descending age pattern of the first four steps, which contain about 40% of the released ^{39}Ar. Such an inherited component would have the undesirable effect of shifting the isochron line towards an older age (Kuiper 2002), a fact exacerbated by the clustering of data points very close to the $^{36}Ar/^{40}Ar$ axis. This same feature was observed by Duncan and Al-Amri (2013), which they attributed to the presence of small amount of excess ^{40}Ar, probably in olivine xenocrysts not completely removed.

In the current study, we identified spectral top-of-atmosphere (TOA) reflectance values to distinguish layers of old and recent lava flows based on differences. As a result, three distinct basaltic units were identified to have the parameters shown in the table below (Table 2). For this dataset, the temperature ranges fall in the same area as for the Ar testing and meet the plateau age criteria. On the other hand, the distribution of the TOR data is not homogenous in this sample set.

The value of the mean square of weighted deviates (MSWD) does not exceed the analytical value for the sample, which means that the scatter points of the sample set are consistent with the analytical model (isochronic relationship is established across the dataset).

Geographic distribution of the lava flows

The identification of basaltic units that are related to different typologies was facilitated by the conversion of the reflectance

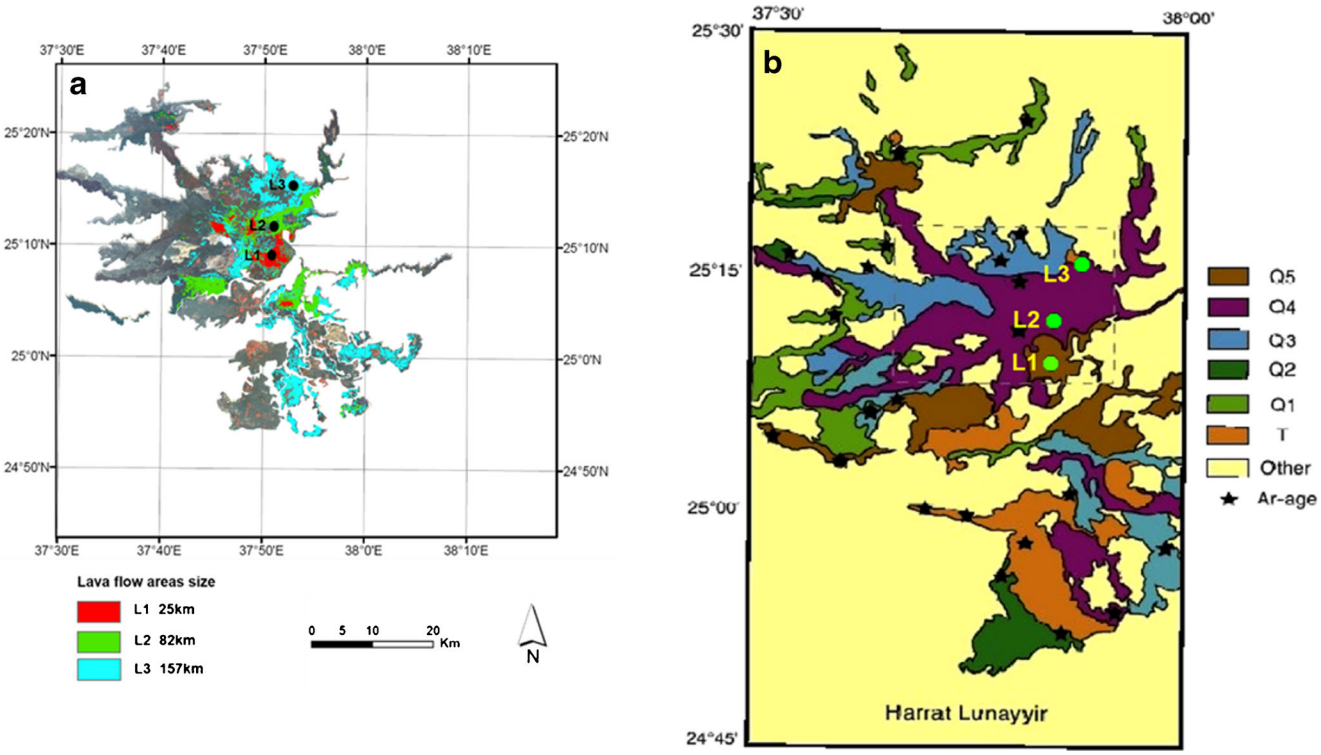

Fig. 13 **a** Remote sensing output with lava flow areas identified. **b** Resulting map by Al-Amri et al. (2012)

values into radiance values. The low reflectance value is a characteristic of basaltic flows in the visible spectrum. The Landsat band ratios were employed to distinguish volcanologic units (ration band 5 to band 4, band 7 to band 6).

In contrast to the findings of Al-Amri et al. (2012), who found two major basaltic units—Jarad, the older Tertiary unit, and Upper Maqrah, younger Quaternary unit—with the application of remote sensing data processing, three basaltic typologies were discerned and mapped by red, pink, and turquoise colours (Fig. 13). We therefore identify three lava flows in accordance with their relative position at the timescale (the identification of exact age is not possible using this methodology, which is a limitation of the study):

- L1 – the most recent lava flows; as seen in Fig. 13. They occupy the central part of the Harrat Lunayyir basaltic field being enclaved into the area of volcanic cones. The total area occupied by these basaltic units is 25 km^2.
- L2 – the lava flows of intermede age that cover the peripheral zones of the epicentre and stretch over a total area of 82 km^2.
- L3 – the oldest lava flows, which occupy an area of 157 km^2 and have a NW-SE direction in alignment with localisation of the dyke (direction of its intrusion); also notably represented around the volcanic cones area.

From the map in Fig. 13a, it is evident that all three lava flows are clustered in the enclave around the volcanic cones; this relatively small cluster of 18 km^2 is constituted of 72% L3, 20% L2, and 8% L1 areas. This clustering towards the epicentre area may suggest that three separate volcanic events happened independently of each other. Based on this, we conclude that the area has been the site of magmatic activity over a longer period than suggested in previous research (Al-Amri et al. 2012). This is in line with recent research findings suggesting

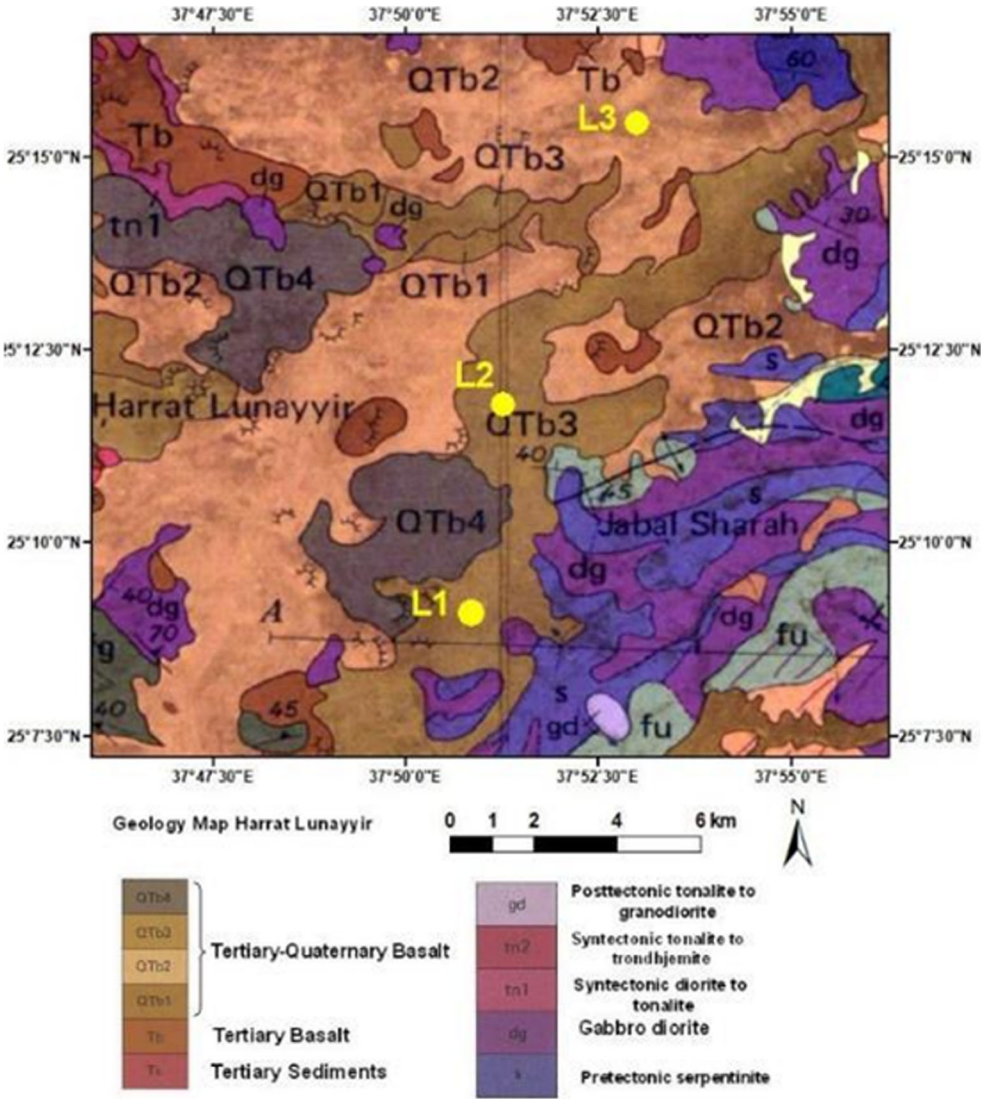

Fig. 14 Geologic map of Harrat Lunayyir

that the 2009 dyke became arrested at a shallow depth (Al Shehri and Gudmundsson 2018).

According to the mapping results, three identified basaltic flows erupted in the same area as most of the epicentres of the earthquake swarm are associated with the dyke emplacement in the spring-summer of 2009 (Al Shehri and Gudmundsson 2018). More specifically, most of the earthquakes were located around the perimeter of the L1 (the most recent basaltic flows). This can be associated with the peculiarities of Harrat Lunayyir's geomorphology. The geomorphology of the harrat is rather restrictive, with higher (up to 800-m elevation) terrain forms located along the perimeter of the area.

In order to make more robust inferences about the geological connections, it is necessary to juxtapose the mapped basaltic units with a geologic map of the area (Fig. 14). This enables us to identify the geochronological types to which the L1, L2, and L3 lava samples belong. In contrast to Al-Amri et al. (2012) findings, we find the three samples being related to three different Tertiary-Quaternary basaltic units, where samples have larger variance in terms of their age. This is attributed to differences in methodology and the described above characteristics of the area's geomorphology. With fields being adjacent and enclaved in the limited area, the remote sensing data provides a more accurate spatiality of the magmatic intrusion processes.

Besides high clustering of both 2009 earthquake swarms and the young basaltic lava flows, the mapping also makes the northwest-southeast strike of the dyke clearly (Fig. 13a, b) observable. The determinant behind that could be the slope effect—which is localised in consistency with fault direction. This may be the basis to conclude the presence of the persistent upward magmatic movement before the swarms as well as the correlation between the volcanic events and dyke intrusion.

Conclusions

The main aim of this paper has been to improve our understanding of the spatial distribution of volcanic processes in the Harrat Lunayyir area. To achieve this, the current study employed the unsupervised classification of remote sensing inputs from Landsat 8, identifying different generations of lava flows in Harrat Lunayyir, western Saudi Arabia. The accurate dating of lava flows is important if we are to understand the eruptive nature of volcanoes and volcanic fields. There are many technical details to be worked out in order to be able to date flows accurately using satellite techniques. We have used numerical classification methods to identify the number of classes into which the data is separated for clustering within each land cover.

The utilisation of ISODATA for the segmentation of the remote sensing data has also been made. The algorithm for performing unsupervised classification was obtained from the GIS package raster (ArcInfo). The characteristics of spectral reflectance regarding volcanic materials, which could be widely observed at the zone of analysis at Harrat Lunayyir, have been investigated, and the resultant classifications of the examined region have been spectrally classified. The data was derived through an analysis involving the counting of the pixels of randomly selected regions. This suggests that the most elevated measures of reflectance value could be exhibited by the older flows of lava. The reason for this could be related to the weathering of the same within 800–1600 nm with a rate of 12%. In contrast, the lava flow, which is considerably younger in geological age, has been analysed to contain a reflectance measure of lesser intensity and a rate of 9 to 10%.

Acknowledgements AAS thanks Morayyea Al-Shahrani, president of the General Commission of Survey, for the helpful suggestions. She also thanks Adel Alsharif, Basim al Dahri, Abdullah Al-Amri, Nabil El-Masry, Maher Al Dahry, Bob Duncan, and Saad al Mogrin for various helpful suggestions and information in connection with this work.

References

Al Damegh K, Sandvol E, Barazangi M (2005) Crustal structure of the Arabian plate: new constraints form the analysis of teleseismic receiver functions. Earth Planet Sci Lett 231:177–196

Al Shehri A, Gudmundsson A (2018) Modelling of surface stresses and fracturing during dyke emplacement: application to the 2009 episode at Harrat Lunayyir, Saudi Arabia. J Volcanol Geotherm Res 356:278–303

Al-Amri Am, Fnais M (2009) Seismo-volcanic investigation of 2009 earthquake swarms at Harrat Lunayyir (Ash Shaqah), Western Saudi Arabia. Int J Earth Sci Eng, India

Al-Amri A, Fnais M, Abdel-Rahman M, Al-Dabbagh M (2012) Geochronological dating and stratigraphic sequences of Harrat Lunayyir, NW Saudi Arabia. Int J Phys Sci 7:2791–2805

Al-Zahrani H, Fnais M, Al-Amri A, Abdel-Rahman K (2013) Tectonic framework of Lunayyir area, Northwest Saudi Arabia through aftershock sequence analysis of 19 May, 2009 earthquake and aeromagnetic data. Int J Phys Sci 7:5821–5833

Baer G, Hamiel Y (2010) Form and growth of an embryonic continental rift: InSAR observations and modelling of the 2009 western Arabia rifting episode. Geophys J Int 182:155–167

Bailey G (2009) The Red Sea, coastal landscapes and hominin dispersals. In: Petraglia MD, Rose JI (eds) The Evolution of Human Populations in Arabia. Springer, Dordrecht, p 15–37

Bernard B (2013) Homemade ashmeter: a low-cost, high-efficiency solution to improve tephra field-data collection for contemporary explosive eruptions. J Appl Volcanol 2:1–9

Bonne K, Cascone M, Njome S, Ranst E, Suh E (2008) A new approach to assess long-term lava flow hazard and risk using GIS and low-

cost remote sensing: the case of Mount Cameroon, West Africa. Int J Remote Sens 29:6537–6562

Byrnes J, Ramsey M, Crown D (2004) Surface unit characterization of the Mauna Ulu flow field, Kilauea volcano, Hawaii, using integrated field and remote sensing analyses. J Volcanol Geotherm Res 135: 169–193

Calvari S, Pinkerton H (1999) Lava tube morphology on Etna and evidence for lava flow emplacement mechanisms. J Volcanol Geotherm Res 90(3–4):263–280

Camp E, Roobol J (1992) Upwelling asthenosphere beneath western Arabia and its regional implications. J Geophys Res 97(15):255–15,271

Cashman K, Pinkerton H, Stephenson J (1998) Introduction to special section: long lava flows. J Geophys Res Solid Earth 103(B11): 27281–27289

Cetin M (2015) Using GIS analysis to assess urban green space in terms of accessibility: case study in Kutahya. Int J Sust Dev World Ecol 22(5):420–424

Cetin M (2016a) Sustainability of urban coastal area management: a case study on Cide. J Sustain For 35(7):527–541

Cetin M (2016b) Determination of bioclimatic comfort areas in landscape planning: a case study of Cide coastline. Turkish J Agric Food Sci Technol 4(9):800–804

Cetin M, Zeren I, Sevik H, Cakir C, Akpinar H (2018) A study on the determination of the natural park's sustainable tourism potential. Environ Monit Assess 190(3):167

Crown A, Baloga M (1999) Pahoehoe toe dimensions, morphology, and branching relationships at Mauna Ulu, Kilauea volcano, Hawaii. Bull Volcanol 61:288–305

Crown A, Ramsey S (2016) Morphologic and thermophysical characteristics of lava flows southwest of Arsia Mons, Mars. J Volcanol Geotherm Res:1–16

D'Alessandro W (2006) Human fluorosis related to volcanic activity: a review. Environ Toxicol Trans: Biomed Health 10

De Alwis D, Easton Z, Dahlke H, Philpot W, Steenhuis T (2007) Unsupervised classification of saturated areas using a time series of remotely sensed images. Hydrol Earth Syst Sci 11:1609–1620

Dietterich HR, Poland MP, Schmidt DA, Cashman KV, Sherrod DR, Espinosa AT (2012) Tracking lava flow emplacement on the east rift zone of Kīlauea, Hawai 'i, with synthetic aperture radar coherence. Geochem Geophys Geosyst:13(5

Duncan R, Al-Amri A (2013) Timing and composition of volcanic activity at Harrat Lunayyir, western Saudi Arabia. J Volcanol Geotherm Res 260:103–116

Duncan RA, Keller RA (2004) Radiometric ages for basement rocks from the Emperor Seamounts, ODP Leg 197, Geochem Geophys Geosyst 5, Q08L03. https://doi.org/10.1029/2004GC000704

Egorov V, Hansen C, Roy P, Kommareddy A, Potapov V (2015) Image interpretation-guided supervised classification using nested segmentation. Remote Sens Environ 165:165–147

Farrier, L., 2006. Influence of surface roughness on the specular reflectance of low gloss coatings using bidirectional reflectance measurements. Air Force Research Laboratory. Thesis, OH 45433-7750

Geological Survey US (2008) Understanding volcano hazards and preventing volcanic disasters: a science strategy for the volcano hazards program. USGS, New York

Griffiths R (2000) The dynamics of lava flows. Research School of Earth Sciences, the Australian National University, Canberra, Australia. Annual Reviews 32:477–518

Guest JE, Kilburn CRJ, Pinkerton H, Duncan AM (1987) The evolution of lava flow-fields: observations of the 1981 and 1983 eruptions of Mount Etna, Sicily. Bull Volcanol 49(3):527–540

Hansen S, DeShon H, Moore-Driskell M, Al-Amri A (2013) Investigating the P wave velocity structure beneath Harrat Lunayyir, northwestern Saudi Arabia, using double-difference tomography and earthquakes from the 2009 seismic swarm. J Geophys Res Solid Earth 118:4814–4826

Harris A, Steffke A, Calvari S, Spampinato L (2011) Thirty years of satellite-derived lava discharge rates at Etna: implications for steady volumetric output. J Geophys Res Solid Earth 116(B8)

Head M, Maclean L, Carn A (2012) Mapping lava flows from Nyamuragira volcano (1967–2011) with satellite data and automated classification methods. Geomat, Nat Haz Risk 4:119–144

Jain A, Murty M, Flynn P (1999) Data clustering: a review. ACM Comput Surv 31:3

James MR, Pinkerton H, Applegarth LJ (2009) Detecting the development of active lava flow fields with a very-long-range terrestrial laser scanner and thermal imagery. Geophys Res Lett 36(22)

Joyce, K., Samsonov, S., Jolly, G., 2008. Satellite remote sensing of volcanic activity in New Zealand. Auckland. https://doi.org/10.1109/USEREST.2008.4740346, IEEE

Kaya E, Agca M, Adiguzel F, Cetin M (2018) Spatial data analysis with R programming for environment. Hum Ecol Risk Assessment: An International Journal:1–10. https://doi.org/10.1080/10807039.2018.1470896

Kubanek J, Richardson JA, Charbonnier SJ, Connor LJ (2015) Lava flow mapping and volume calculations for the 2012–2013 Tolbachik, Kamchatka, fissure eruption using bistatic TanDEM-X InSAR. Bull Volcanol 77(12):106

Kuiper YD (2002) The interpretation of inverse isochron diagrams in 40Ar/39Ar geochronology. Earth Planet Sci Lett 203(1):499–506

Loughlin S, Sparks S, Brown K, Jenkins F, Vye-Brown C (2014) Global volcanic hazards and risk. Cambridge University Press, Bristol

McDougall I, Harrison TM (1999) Geochronology and Thermochronology by the 40Ar/39Ar Method, Oxford University Press, Oxford

Millington C, Saunders W, Francis N, Webster N (2012) Simulated volcanic ash imagery: a method to compare NAME ash concentration forecasts with SEVIRI imagery for the Eyjafjallajökull eruption in 2010. J Geophys Res 117

Murcia, H., Smith, I., Lindsay, M., Niedermann, S., Cronin, J., 2013. The potential use of cosmogenic nuclides for dating in Harrat Rahat. Conference: Vorisa Scientific Meeting, Jeddah, KSA

Nelson, A., 2016. Volcanic hazards and prediction of volcanic eruptions. Tulane University. http://www.tulane.edu/~sanelson/Natural_Disasters/volhaz&pred.htm

Nicolas S, Astrid G, Minoru U, Zarah S (2008) Preliminary results of lava flow mapping using remote sensing in Piton de la Fournaise. La Réunion island. https://doi.org/10.1109/USEREST.2008.4740339. IEEE

OSU. 2015. How do volcanoes affect the atmosphere and climate? Retrieved November 20, 2016, from Oregon State University: http://volcano.oregonstate.edu/how-do-volcanoes-affect-atmosphere-and-climate

Pint J (2006) Vulcanospeleology in Saudi Arabia. In: Vulcanospeleology in Saudi Arabia. UIS Commission on Volcanic Caves

Rodgers J, Walter R, Mellors J, Al-Amri M (1999) Lithospheric structure of the Arabian Shield and Platform from complete regional waveform modelling and surface wave group velocities. Geophys J Int 138:871–878

Rossi M (1997) Morphology of the 1984 open-channel lava flow at Krafla volcano, Northern Iceland. Geomorph 20:95–112

Rossi M, Gudmundsson A (1996) The morphology and formation of flow-lobe tumuli on Icelandic shield volcanoes. J Volcanol Geotherm Res 72:291–308

Self, S., Thordarson, T., Keszthelyi, L., 1997. Emplacement of continental flood basalt lava flows. In Large igneous provinces: continental, oceanic, and planetary Flood Volcanism, J.J. Mahoney, M.F. Coffin (Eds.), 381–410

Shaw, R., Swansond, A., 1970. Eruption and flow rates of flood basalts. In Proceedings, second Columbia River basalt symposium, E.H. Gilmour, D. Stradling, 271–299

Shen, C., Juang, C., Tsai, L., 2008. Remote sensing stream flow and soil moisture by using reflected GPS signals Li & L2 observation and Doppler shifts with an integrated GPS receiver. Conference, Charlston, SC, USA

Slatcher N, James M, Calvari S, Ganci G, Browning J (2015) Quantifying effusion rates at active volcanoes through integrated time-lapse laser scanning and photography. Remote Sens 7(11):14967–14987

Stern R, Johnson P (2010) Continental lithosphere of the Arabian Plate; a geologic, petrologic, and geophysical synthesis. Earth-Sci Rev 101: 29–67

Tarquini S, Favalli M (2011) Mapping and DOWNFLOW simulation of recent lava flow fields at Mount Etna. J Volcanol Geotherm Res 204: 27–39

Trusdell F (1995) Lava flow hazards and risk assessment on Mauna Loa volcano, Hawaii. Mauna Loa revealed: structure, composition, history, and hazards. Geophys Monogr Ser 92:327–336

Walsh D (2006) Relative dating of volcanic flows on a back-arc strato-volcano, London http://frontiersabroad.com/wp-content/uploads/2012/09/Daniel-Walsh.pdf

Zanter, K., 2016. Landsat 8 (L8) data users handbook. Department of the Interior U.S. Geological Survey. Version 2.0

Chapter 4

Thermal mapping of the 2009 dyke emplacement at Harrat Lunayyir, Saudi Arabia

Arabian Journal of Geosciences

Azizah Al Shehri and Agust Gudmundsson

https://doi.org/10.1007/s12517-019-4774-5

Statement of contribution:

The origin idea, methodology, computation and creation of models were developed by AA.
Writing the initial draft was made by AA
All illustrations were prepared by AA, with later adjustments and modifications from co-author.
Interpreted data and discussions were done by AA and specifically critical revision from co-author.

Arabian Journal of Geosciences
https://doi.org/10.1007/s12517-019-4774-5

ORIGINAL PAPER

Thermal mapping of the 2009 dyke emplacement at Harrat Lunayyir, Saudi Arabia

Azizah Al Shehri[1] · Agust Gudmundsson[1]

Received: 13 June 2019 / Accepted: 4 September 2019

Abstract
The 2009 seismic episode at Harrat Lunayyir signalled a renewed geohazard and resulted in a regional dyke that propagated to a very shallow depth (a few hundred metres) below the surface. Since then, there has been an extensive research debate over the potential links between the volcanic/intrusive activity and tectonic processes, particularly because the earthquake swarm and dyke propagation did not eventually result in an eruption. The current study seeks to estimate the relative changes in surface temperatures as a means for detecting an impending dyke-fed eruption or, alternatively, dyke arrest at a shallow depth. An analysis of thermal (infrared) data with a focus on the spatial distribution of land surface temperatures over a longer period of observation may help reveal the link between volcanic activity and dyke propagation. Here, the land surface temperature changes in the centre of Harrat Lunayyir were recorded when the 2009 dyke was propagating toward the surface. The spatial distribution of the land surface temperatures in the area indicated the segmentation of the dyke and suggested the segments were arrested at somewhat different depths below the surface.

Keywords Dyke emplacement · Dyke arrest · Surface temperature · Volcanic hazard · Remote sensing

Introduction

Volcanoes pose a significant threat to human life and property through their extensive lava flow from effusive volcanic eruptions as well as pyroclastic flows and falls from explosive volcanic eruptions that altogether may create far-reaching hazards in the surrounding environment (Alberico et al. 2010). Considering the significance of these hazards, there has been extensive research over the past few decades aimed at exploring effective methods for the monitoring of volcanic activities (IUCN 2009). Monitoring systems are of great importance in terms of providing adequate warning of imminent potential disasters related to active volcanoes. Volcanic activity is usually controlled by processes that take place in the depths of the Earth's lithosphere, particularly in the magma reservoirs, and, thus, there are several challenges related to the monitoring of active volcanoes and interpreting volcanic unrest episodes (Noguchi et al. 2011; Pyle et al. 2015; Al Shehri and Gudmundsson 2018; Gudmundsson 2019). Volcanic eruptions result in the transfer of heat from erupted lava flows and pyroclastic layers as well as from eruption columns that extend into the atmosphere. Additional environmental and tectonic processes associated with volcanoes include gas emission, earthquakes, and surface deformation (Harris 2013; Murphy et al. 2013; Noguchi et al. 2011; Pyle et al. 2015; Gudmundsson 2019).

The Red Sea Rift is one of the few areas in the world in which the processes of continental rifting and splitting actively take place and intraplate volcanism occurs, with a range of volcanic risk episodes observed in the western part over the last few decades (Bailey 2009; van der Zwan et al. 2013). The Red Sea Rift may be considered the most recent example of the early stages of ocean development via sea-floor spreading. This makes the areas within and adjacent to the rift particularly suitable for exploring volcanotectonic structures, dyke and fault patterns, and the inter-relation between structural, sedimentary, tectonic, and volcanic processes. Volcanic fields and dyke swarms formed along the eastern margin of the rift, predominantly during the Red Sea spreading as a result of a series of volcanic eruptions (Genna et al. 2002; Hansen et al. 2013a, b).

Responsible Editor: Abdullah M. Al-Amri

✉ Azizah Al Shehri
azizahzz@yahoo.com

[1] Department of Earth Sciences, Royal Holloway University of London, Egham, UK

Published online: 08 October 2019

One of the most recent and significant volcanotectonic episodes occurred in Harrat Lunayyir, a young basaltic lava field located in the northwestern part of Saudi Arabia and adjacent to the central part of the Red Sea in 2009. This volcanotectonic activity was primarily characterised by an intense earthquake swarm that occurred between April and June 2009, with more than 30,000 earthquakes taking place over the period of 3 months. It produced far-reaching consequences for the socioeconomic status of the region despite its limited direct damage and considering the area is quite remote and no eruption took place. As a result of the episode, the Saudi Arabian government had to evacuate 40,000 residents from the town of Al Ays, which is located in the path of lava flows from the potential volcanic fissure that would have formed if the dyke had reached the surface. The predominant interpretation based on both the earthquake data and geodetic data is that a near-vertical dyke of magma made its way from a great depth but then stopped at ~ 2 km beneath the surface, which induced most of the earthquakes in the swarm (Jónsson et al. 2010). More recent studies, however, conclude that the dyke became arrested at much shallower depths, namely, several hundred metres below the surface, indicating a significantly greater hazard than previously estimated (Al Shehri and Gudmundsson 2018). The arrest of the dyke at a shallower depth is likely to be the factor in the observed tension fractures and normal fault formation at the surface. Another important research question behind why the dyke's movement was arrested at such a shallow depth—a topic analysed in many papers and of great interest and importance to volcanotectonic and hazard studies (e.g., Gudmundsson 2002, 2003).

In order to study the complex volcanic processes that lead to eruptions and other natural hazards as well as to monitor volcanic activities, remote sensing techniques have been extensively applied. Specifically, satellite images provide key data for understanding volcanic behaviour and registering thermal emissions from high-temperature events (Barnie and Oppenheimer 2015; Harris et al. 1997; Tralli et al. 2005). The fact that this data is acquired remotely makes these processes relatively risk-free, meaning this method is particularly well-suited to studying the precursor signals of changing volcanic activity patterns. Additionally, thermal infrared (TIR) remote sensing of land surface temperature has been used in the past 20 years to monitor and explore volcanic processes and activity. TIR remote sensing is a significant tool in terms of mapping and monitoring the temperature of the surface; therefore, it could be used to identify increased volcanic activity by examining precursor signals (Haselwimmer and Prakash 2013; Realmuto and Worden 2000; Tralli et al. 2005; Vaughan et al. 2005). TIR data can provide a simultaneous and synchronous view of temperature changes in a given landscape, overcoming the limitations specific to meteorological or land-surveying data. Remote sensing TIR is generally used to monitor and map the surface temperature in various regions, as volcanic and other natural processes can release substantial amounts of heat. Therefore, the increase of volcanic activity signals can be both detected and measured with such types of technology and through the evaluation of precursor signals (Haselwimmer and Prakash 2013; Tralli et al. 2005; Vaughan et al. 2005). Nevertheless, recent studies have indicated a currently limited employment of TIR data due to the prevailing use of low-resolution satellite images (Sobrino et al. 2008). The present project addresses this phenomenon by using Landsat 7 satellite images, a split-window algorithm of land surface temperatures, and threshold methods for heat emission measurement (Fig. 1). Despite the disadvantages of Landsat 7, which has only one thermal band, this method of emissivity measurement meets the project objective of capturing surface temperature anomalies.

Thermal mapping based on satellite data is a valuable tool that produces a temporal and spatial interpretation of baseline thermal activity to identify thermal anomalies. Thermal mapping has been a common practice in the study of thermal patterns exhibited during volcanic eruptions (Ramsey and Flynn 2004). The primary advantage of this method is that it enables the retrieval of a greater number of spatial details. More conventional methods, such as meteorological monitoring, are characterised by a lack of a spatial dimension. A focus on spatiality is particularly important to this project since it aims to establish the relationship between the tectonic and volcanic components. A juxtaposition of thermal maps using the data from tectonic observations, also acquired through remote sensing, is hypothesised to be a suitable method for identifying any further relationships between these phenomena, thus addressing the research gaps discussed above.

This paper focuses on monitoring and estimating changes in surface temperature during the 2009 dyke emplacement in Harrat Lunayyir, Saudi Arabia, in order to examine how this method can be used to detect a potential dyke-fed eruption through significant temperature deviations. Overall, this method could provide critical information related to the support of disaster response and emergency management. The results also provide a foundation for response prioritisations and disaster assessment as well as informed mitigation planning and thorough risk assessments.

Methodology

The methodological framework employed in the current paper involved extending upon the recent research findings from the Harrat Lunayyir dyke emplacement episode by adding more extensive spatial components (Al-Amri and Fnais 2009; Baer and Hamiel 2010; Hansen et al., 2013; Al-Zahrani et al. 2013). First, the geological settings and hypotheses regarding volcanic and seismic activity in the area were reviewed to construct a basis for the empirical framework. Second, through the

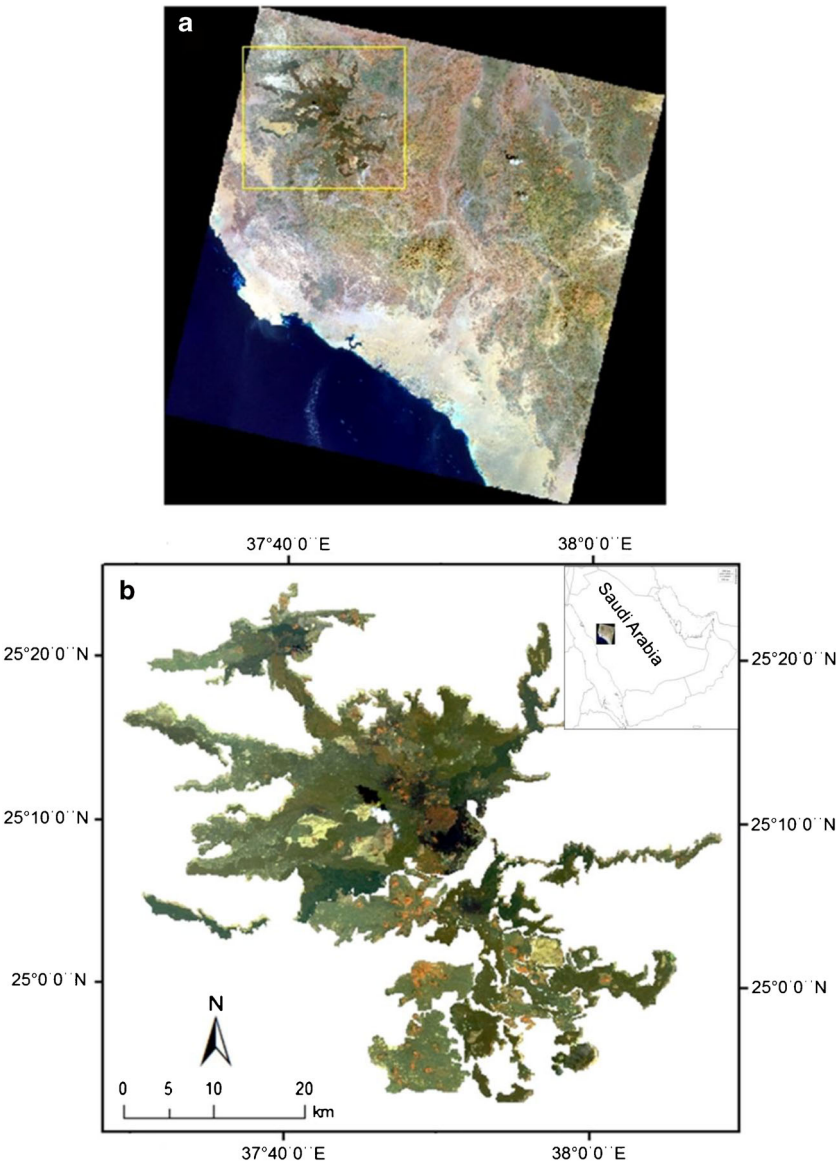

Fig. 1 **a** Satellite image (Landsat 7) identifying the area of interest. **b** Harrat Lunayyir borders

processing of remote sensing data, the major spatial configurations of both volcanic and seismic processes were identified using spatial density mapping and spatial alignment. Third, thermal mapping was conducted based on Landsat 7 satellite images, which helped plot the distribution of heat anomalies across the periodical timescale. This allowed for the connection of the spatial density and alignment analysis findings to the land surface heat distribution patterns. The resulting surface temperature maps were then further related to the previous hypotheses about the 2009 dyke intrusion and analysed using spatial analysis techniques.

Geological setting of Harrat Lunayyir

In order to provide a methodology applicable to the scope of this project, the major geological and geomorphological characteristics of the area of interest were identified. Harrats, also known as Cenozoic basaltic lava fields, are commonly found in the Arabian Shield (Fig. 2). These fields are predominantly composed of alkali olivine basalt (Koulakov et al. 2014) and tholeiitic basalt (Al-Amri and Fnais 2009) lava flows. Harrat Lunayyir is located in the western region of the Arabian Plate and is composed of Neogene and Quaternary basaltic lava flows that cover the Neoproterozoic basement (Koulakov et al. 2014). Lunayyir is one of the youngest Harrats in the region, exhibiting a more diverse composition. According to studies conducted by Al-Amri et al. (2012), in terms of geostructural composition, Harrat Lunayyir is represented by two different basalt age groups: older Neogene basalts and younger Quaternary basalts (Fig. 2b). The Quaternary basaltic lava flows are common in the western region of the Arabian Shield and formed during the Red Sea spreading, which has been occurring since the Miocene period (Al-Amri and Al-Mogren 2011). The older Neogene basalts are characterised by scoria cones,

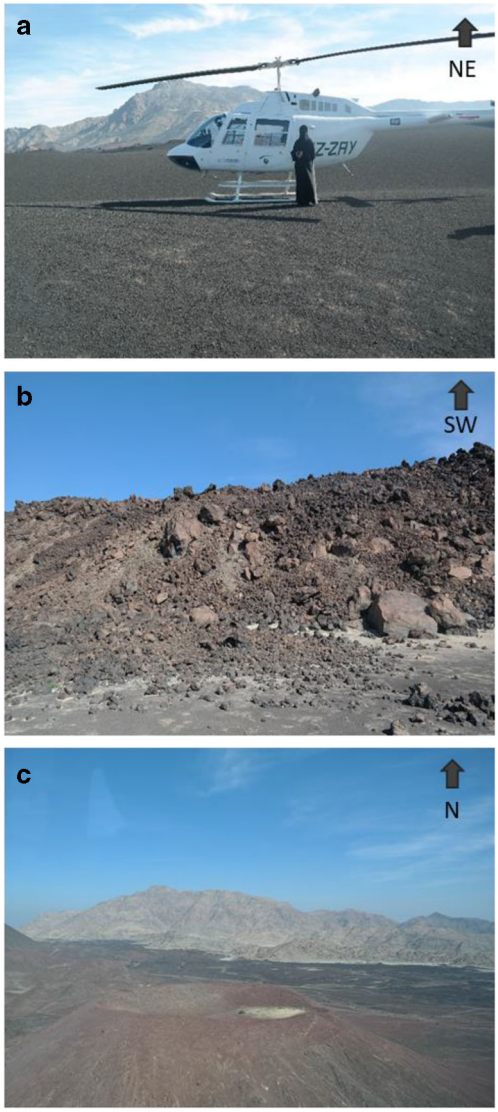

Fig. 2 Landscape features representing typical volcanic structures located in the southeastern part of the Harrat Lunayyir field. **a** Ground-level view of the volcanic scoria rocks in the northeast of Harrat Lunayyir (position: 24° 21′ 21.2″ N; 39° 46′ 55.3″ E). **b** Basaltic lava flows of the Quaternary age, southwestern part of Harrat Lunayyir (position: 24° 12′ 9.1″ N; 39° 52′ 41.6″ E) **c** Typical scoria cone with a cater formation, northern most part of the Harrat Lunayyir field (position: 24° 23′ 4.5″ N; 39° 49′ 59.02″ E, towards north)

which are significantly eroded to the extent of having indistinct crater formation (Fig. 2a). The basaltic layers rest directly on the Precambrian Arabian Shield (Al-Amri and Al-Mogren 2011; Al-Amri and Fnais 2009), while some Precambrian formations are also exposed in the central parts of the field. The volcanic deposits at Harrat Lunayyir are not radiometrically dated, although a number of studies have indicated a possible eruption that occurred in the tenth century (Zobin et al. 2013). Moreover, signs of recent volcanic activity have been identified through the examination of the geomorphic features of the deposits, including pristine vent structures and unweathered lava surfaces (Pallister et al. 2010; Zobin et al. 2013).

Dyke intrusion and other hypotheses

The initial monitoring data obtained in the region demonstrated that the observed magmatic intrusion, or dyke propagation, was continuous throughout the earthquake swarm (Pallister et al. 2010). The bulk of research on these earthquake swarms and their associated surface deformation indicated that the primary surface deformation might be partly associated with dyke propagation at a shallow depth and that the earthquake epicentres resided beneath the morphologically young volcanic crater cones (Pallister et al. 2010). According to Mukhopadhyay et al. (2013), the vertical dyke propagation initiated at crustal depths and exhibited a 5-day peak period (15–20 May 2009). After this peak, the volcanic activity was seen to gradually diminish. During the intrusion process, the dyke propagated to more shallow crustal levels, which may have contributed to a portion of the meter-scale fault slip on the western graben-bounding faults (Mukhopadhyay et al. 2013; Pallister et al. 2010).

Zahran et al. (2009), relying on a range of geodetic monitoring data, registered seismotectonic observations

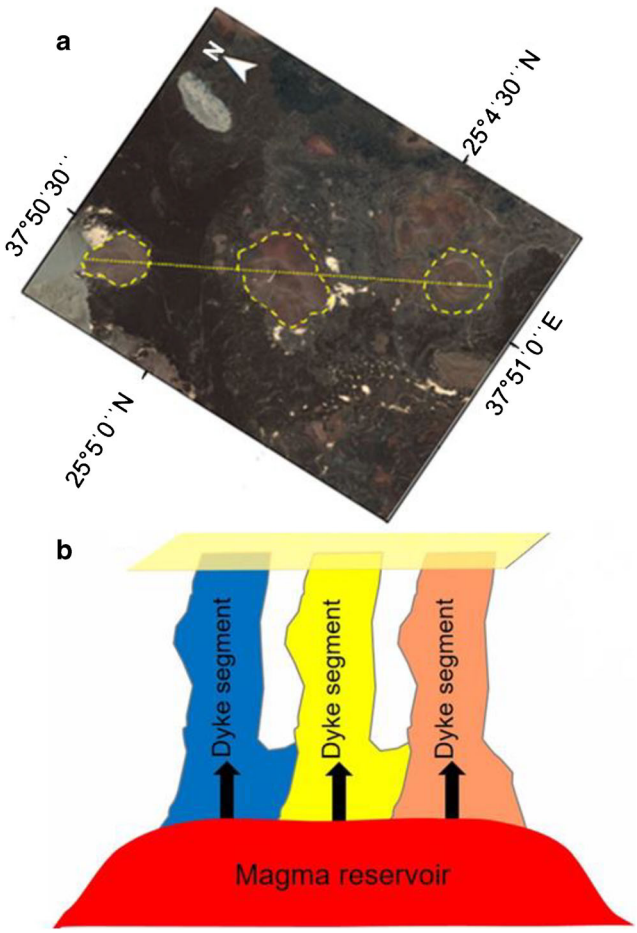

Fig. 3 **a** Data adopted from the Landsat satellite images of eruption points and centres developed by the segmented dyke. **b** Schematic representation of the possible feeder-dyke to the cinder cones in (**a**)

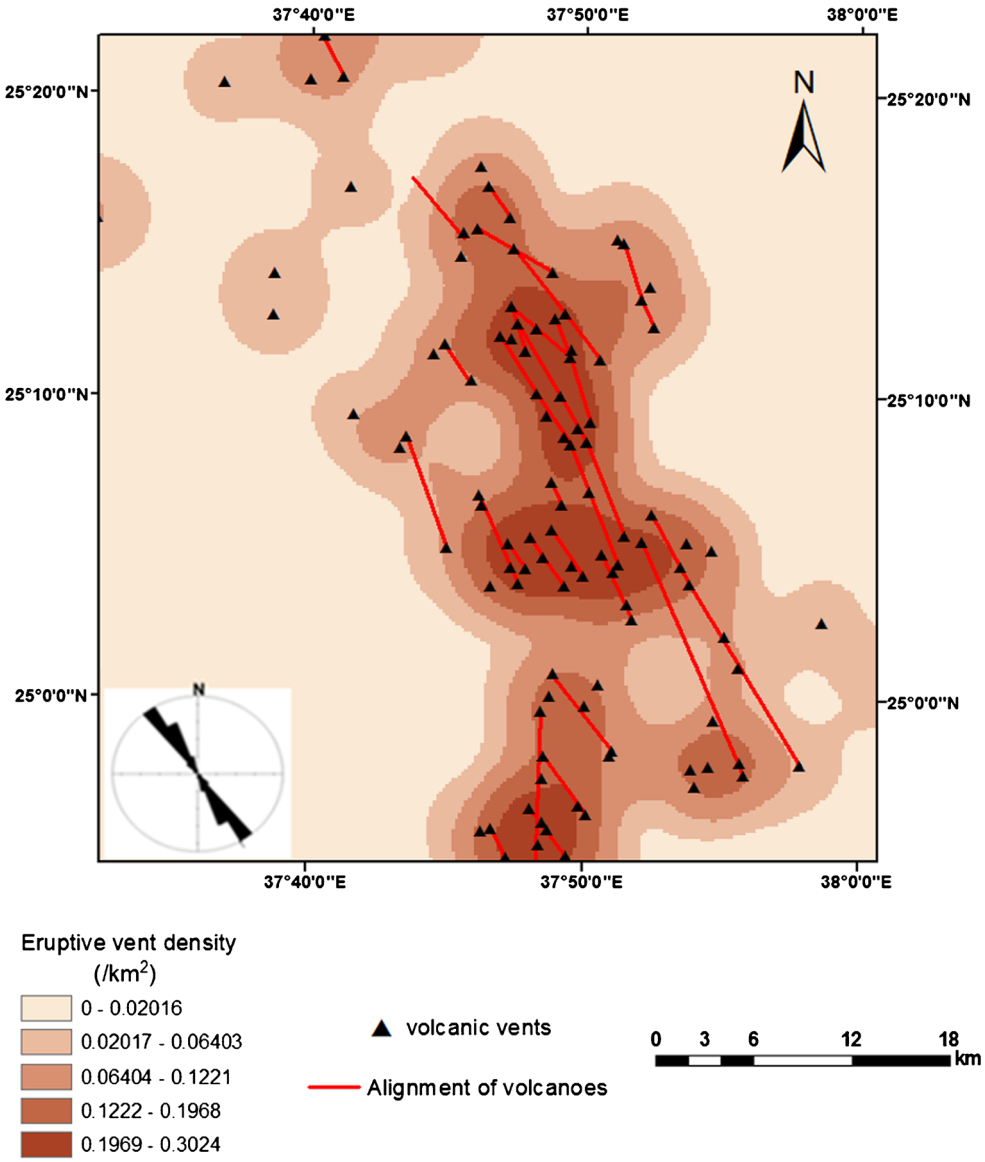

Fig. 4 Harrat Lunayyir density map of monogenetic volcanoes/eruption points. Around 104 eruption points are mapped; the majority of which are lava flows and cinder cones. The spatial alignments of volcanoes have also been plotted using the rose diagrams for data taken from the satellite images. The data plotted also show the zone of maximum density of vents

corroborating the dyke intrusion hypothesis. This data indicated that there was a 3-km-long surface rupture in the central area of the harrat, which had been extending prior to May 2009. InSAR data demonstrated that there was an uplift and 1-m extension following the peak of the earthquake swarm, which corresponded to the first hypothesis, specifically in terms of stalled eruption, namely, an arrested dyke (Zahran et al. 2009). There are three major mechanisms through which dyke arrest occurs: stress barrier, elastic mismatch, and Cook–Gordon delamination (Gudmundsson 2011a, b, and 2019). The Cook–Gordon delamination mechanism implies that whatever contact that arrests the dyke is mechanically weak and has low tensile strength, so it opens up by the dyke-parallel tensile stress induced by the propagating dyke (Gudmundsson 2011a, b; Kavanagh et al. 2018). The opening of a contact is observed in many numerical models on dyke emplacement (Gudmundsson 2003, 2011a, 2019). When the dyke tip finally reaches the open contact, the tip becomes either deflected along the contact to form a sill or, alternatively, stops altogether (i.e., is arrested) (Gudmundsson 2003, 2011a).

Most dykes become arrested at various depths in the crust rather than ever reaching the surface (Gudmundsson 2002, 2003; Moran et al. 2011; Rivalta et al. 2015; Townsend et al. 2017) (Fig. 3). Previous models (Baer and Hamiel 2010; Pallister et al. 2010) have inferred that dyke intrusion is based on the fact that seismic events in the area tended to form a linear structure oriented toward the southern part of the harrat. In light of this, Koulakov et al. (2014) modelled the distributions of P-wave to S-wave velocities in the area and concluded that it is not possible to directly confirm whether the dyke intrusion took place in 2009. Based on their research and

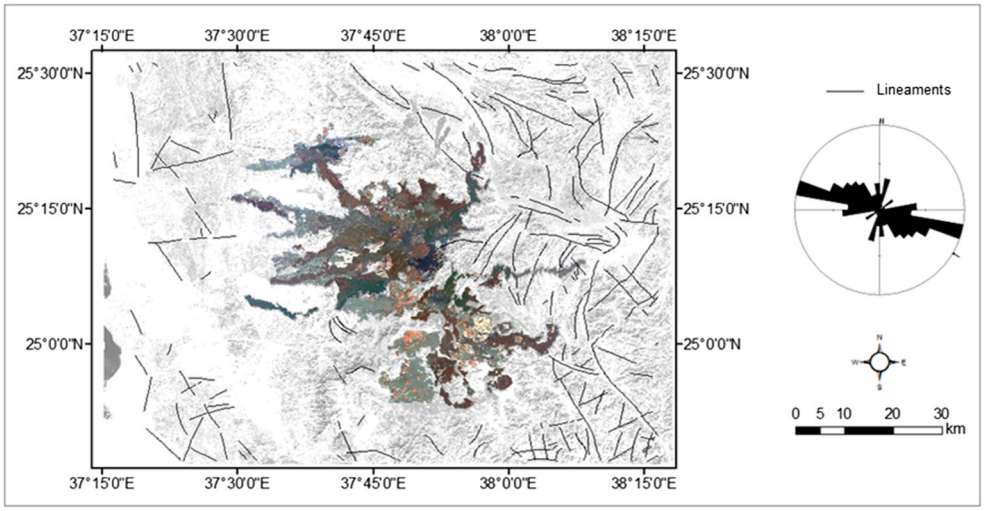

Fig. 5 Lineaments, mostly normal faults, in Harrat Lunayyir. The direction of the faults has also been plotted using the rose diagrams

further attempts to develop seismic tomography models, an alternative hypothesis emerged, which assumes a buried fault may have caused the tectonic displacements that resulted in the linear structure of the events distribution (Koulakov et al. 2014). However, the earthquake swarm and thermal effects were more in-line with dyke emplacement, which is the model accepted by the present study and discussed in detail by Al Shehri and Gudmundsson (2018).

Spatial density mapping

Figure 4 shows the density map of 104 volcanic eruption points and volcanic vents, which have been identified and mapped. These are mostly crater, spatter, or cinder (scoria) cones, either existing alone or as parts of volcanic fissures or lava flows. Arc Map 10.1 was used to plot the volcanic vents, while the shape files of the volcanoes were imported into Arc Map 10.1. With the aid of the density maps, the frequency of eruption centres could be assessed in the neighbourhood surrounding each raster cell. Specifically, the neighbourhood is the area around each cell centre and the total of all eruption points divided by the total area of the neighbourhood.

The spatial density map was drawn with the help of ArcGIS 10.1, has a radius of approximately 18.5 km, and focuses on producing a generalised output raster. The addition of lineaments (e.g., proposed volcanic fissures) in this map took place with the help of Harrat Lunayyir raster images. There is an evident clustering of eruption points and vents, as indicated by the contours (Fig. 4). In addition, it has been suggested that a number of eruption points and crater cones form parts of volcanic fissures whose northwest trend is the same as that of the proposed 2009 dyke. The major density subzone present in the central area of Harrat Lunayyir is mostly composed of lava shields and scoria cones, which majorly contribution to

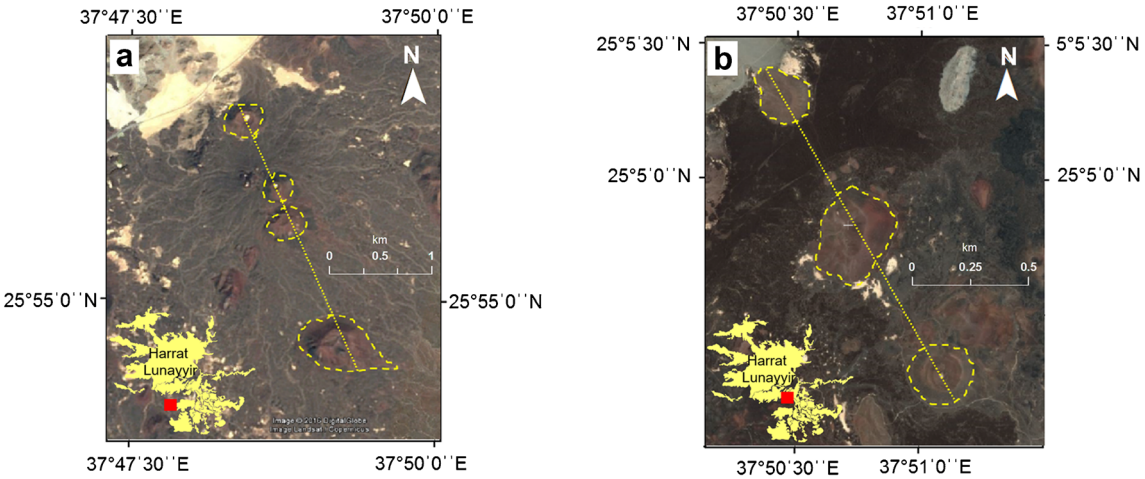

Fig. 6 Landsat 7 satellite images showing the spatial alignment of eruption points/monogenetic volcanoes in the central part of Harrat Lunayyir. The crater cones are presumably fed by a dyke. The maps also provide the location of the volcanic eruptions

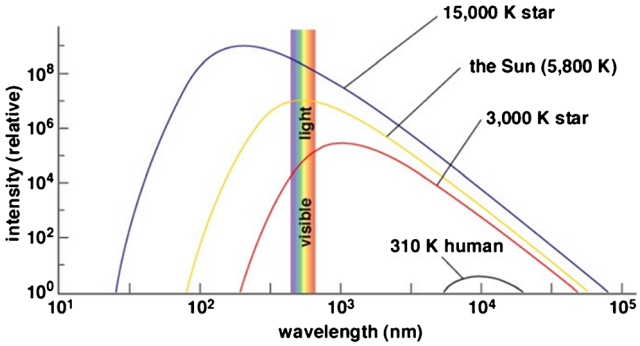

Fig. 7 The thermal radiation emitted by several reference objects. Hotter objects have smaller peak wave lengths and sharper curves (Wellons 2007)

eruption sites. The figure also shows that the lowest eruption point frequency is concentrated in the form of a cluster in the southwestern region.

Spatial alignment of volcanic eruptions

Volcanic vent alignment is evident in the assessed satellite imagery, which exhibits at least three volcanic cones traced on ArcGlobe 10.1 and saved in polyline shape files (.shp). These files were exported into ArcGIS 10.1 and juxtaposed with the lineament's locations (Fig. 4). Identification of the alignments was based on the Hough transform method algorithm and automatically calculated using the geosimulation capacity of the software. The algorithm behind this method is based on the transformation of the linear data in a Cartesian plane into points in a parameter plane, calculating the length and angle between any line of vent alignment origin and the coordinate system. Each alignment is marked by orientation, length, and edge coordinates. The volcanic fissures, which were inferred from the volcanic alignments, have also been highlighted (Figs. 5 and 6). When more than one configuration is possible, the elongated caters can be used to highlight the general inferred fissure trend, following a standard method (Paulsen and Wilson 2009). The strikes of the elongated vents then coincide with corresponding strikes of the volcanic fissure. Using the GEOrient software, rose diagrams could also be produced, which helped identify the volcanic fissures in the NNE–SSW or NNW–SSE trends that dominate the volcanic region along with the presence of some small subsets like the N–S subsets.

The rose diagram of around 84 tension fractures and normal faults associated with the dyke-induced earthquake swarm in 2009 (Al-Zahrani et al. 2013) are also shown in Fig. 5. In terms of the two main sets of fracture strikes, the main strikes NNW–SSE, whereas the smaller one strikes NNE–SSW.

Table 1 Metadata and acquisition dates of Landsat 7

Acquisition date	Satellite/sensor	Path	Band	Spatial resolution
17 March 2007	Landsat ETM+	147	6	60 m
03 March 2008	Landsat ETM+	147	6	60 m
22 March 2009	Landsat ETM+	147	6	60 m
26 June 2009	Landsat ETM+	147	6	60 m
23 July 2009	Landsat ETM+	147	6	60 m
26 August 2009	Landsat ETM+	147	6	60 m
25 March 2010	Landsat ETM+	147	6	60 m
12 March 2011	Landsat ETM+	147	6	60 m

Thermal mapping of Harrat Lunayyir

Thermal infrared (TIR) technology is a remote sensing approach that has been utilised to evaluate the surface temperature of targeted regions as well as to monitor and investigate volcanotectonic events, volcanic eruptions, intrusions, and any associated earthquakes and tremors. Satellite images have major potential to gain more information about volcanic eruptions and the behavioural aspects related to such natural phenomena. In addition, the investigation and observation of thermal energy emissions from high-temperature events such as eruptions or shallow intrusions are also considered to be of paramount significance in this field (Barnie and Oppenheimer 2015; Harris et al. 1997; Tralli et al. 2005).

Thermal infrared (TIR) technology is a remote sensing approach that has been utilised to evaluate the surface temperature of targeted regions as well as to monitor and investigate volcanotectonic events, volcanic eruptions, intrusions, and any associated earthquakes and tremors. TIR has been an operational standard for the past 20 years. Generally speaking, thermal energy in the infrared band is emitted from each object at a temperature above absolute zero. Thus, vegetation, soil, rock, water, and living beings emit infrared band–based thermal and electromagnetic radiation, which can in turn be measured and evaluated using infrared energy emission–detection sensors. The human eye is incapable of detecting any measurement or change in thermal energy emissions in the infrared energy band, as it can only detect light beams in the 400- to 700-nm range and remains sensitive only within this spectrum. Moreover, the sensitivity of the human eye is generally restricted to the infrared reflective index range of 700 nm–3.0 μm and the infrared energy range of 3.0–14 μm (Jensen 2007). Thus, it is not possible for the human eye to process the reflective infrared band or thermal energy emanating in the infrared spectrum (Fig. 7).

Some satellites have sensors for the purpose of heat detection, such as Landsat TM/ETM, NOAA AVHRR ASTER, and MODIS. The current study employed the Landsat 7 series with a ETM+ sensor (Table 1) to derive thermal bands related to Landsat and land surface temperatures (LST), such as band

Table 2 ETM+ thermal band calibration constants (NASA 2018)

	Constant 1—$K1$ (watts/(m^2 × sr × μm))	Constant 2—$K2$ (Kelvin)
Landsat 7	666.09	1282.71

6 from ETM+, for various durations. The objectives of this Harrat Lunayyir–based study resulted in the obtainment of three different images from the USGS server (earthexplorer.usgs.gov), which could be further identified using ERDAS IMAGINE 2015 and ArcGIS 10.1 software. These two approaches have been utilised to help understand the collected surface temperature data.

The downloaded bands are part of the thermal bands, specifically band 6 of ETM+. The bands of ETM+ and those of dataset band 6 are generally favoured owing to their enhanced brightness, which can help facilitate the study of this region via photographs. This region is devoid of any significant vegetation cover, and the metadata of the thermal bands is generally used to determine the rows, axis, and thermal constants related to such developments in the region.

Theoretical basis for the method

Conversion to radiance

Landsat thermal data is transformed into a set of mosaic images, and then any obtained digital numbers can be transformed into LST (land surface temperature) values through any method used for radiometric modifications and corrections. The data is generated in a manner that allows for a comparison with the previously available data (Table 1). The radiance of the sensors, which is related to the regions of the wavelength, can then be preserved and stored within the collected and compared digital numbers (DNs). These DNs can then be quantified through the utilisation of systems that have been specifically designed for such purposes. The primary benefits of this involve both the processing and storage of data. The absence of physical units or other such information associated with DN-based values means that such values need to be converted into tangible radiances.

The resulting values of ETM+ DN, which is a specific formula utilised for the purpose of converting the DNs into *spectral radiance measures*, will generally fall between 0 and 255.

$$L_\lambda = Grescale \times Qcal + Brescale \tag{1}$$

This can also be designated as follows:

$$L_2 \equiv \frac{(LMAX_2 - LMIN_2)}{(QCALMAX - QCALMIN) \times (QCAL - QCALMIN) + LMIN_2} \tag{2}$$

Here Qcal is the quantified calibrated pixel value in DN, LMINλ is the spectral radiance scaled to QCALMIN in (W/(m^2 × sr × μm)), LMAXλ is the spectral radiance scaled to QCALMAX in (W/(m^2 × sr × μm)), QCALMIN is the minimum quantised calibrated pixel value (corresponding to LMINλ) in DN, QCALMAX is the maximum quantised calibrated pixel value (corresponding to LMAXλ) in DN = 255 (NASA 2018).

Conversion from spectral radiance to temperature

Landsat ETM+ Band 6 imagery can be transformed and altered to become more effective than spectral radiance or brightness temperature. On the assumption of unity emissivity, such imagery can be effectively utilised to evaluate Earth–atmosphere system temperatures obtained by satellites. The formula of transformation and conversion is as follows:

$$T = \frac{K2}{\mathrm{In}\left(\frac{K1}{L_\lambda} + 1\right)} \tag{3}$$

where T is the effective at-satellite temperature in Kelvin, $K1$ and $K2$ are calibration constants, and L_λ is the spectral radiance as defined in Eq. 2 (Table 2) (NASA 2018).

Conversion from degrees Kelvin to degrees Celsius

Since the temperature will be estimated in degrees Celsius, the results obtained from Eq. 3 can be converted into degrees Celsius. The formula-based method for such a conversion can be described using the formula B6-273.15. Here, B6 is the result obtained from Eq. 2, which is expressed in degrees Kelvin. In this manner, the temperature outline map can be inferred and developed.

Heat transfer model

The heat transferred via electromagnetic radiation is referred to as 'thermal radiation'. Infrared radiation is a sub-category of thermal radiation and can also transfer heat; consequently, it is frequently referred to as 'heat radiation'. However, only a fraction of the infrared radiation spectrum is actually able to carry heat (Wellons 2007; Da Wen 2010). While all matter with a temperature greater than 0°K (absolute zero) will emit electromagnetic radiation, either the radiant flux density or the rate of energy flow per unit area and the spectral composition of this radiation is dependent upon the temperature of the

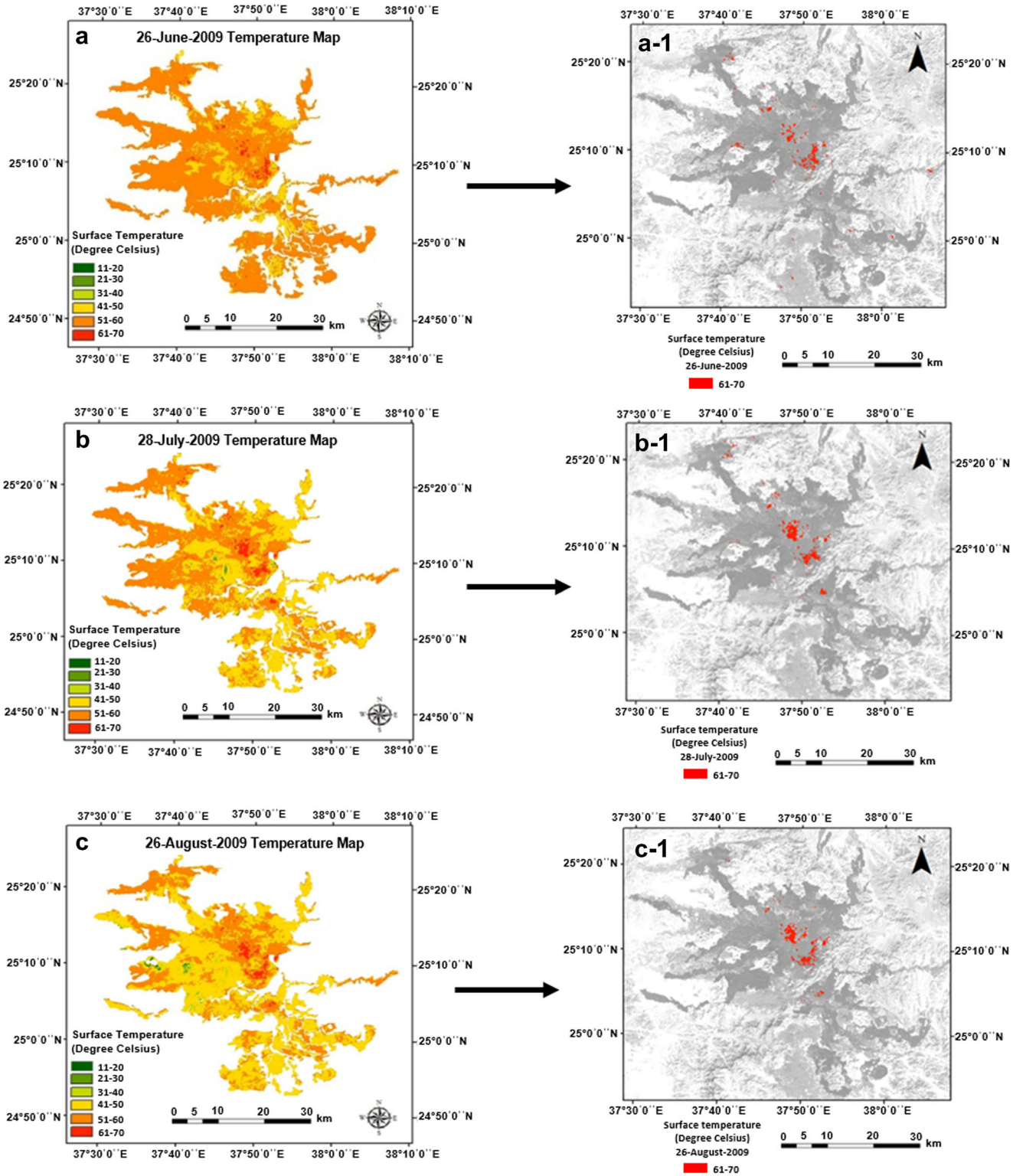

Fig. 8 2009 surface temperature map in degree Celsius. **a**–**c** Absolute temperature plots for the whole region during June, July, and August 2009. The red colour in (a-1, b-1, and c-1) highlights the anomalously hot regions

emitting matter (Blackett 2017). Thermal radiation is also capable of directly transferring heat over long distances (e.g., the Earth continuously receives thermal radiation from the Sun). As a consequence of the wave nature of radiation and the Earth's atmosphere, a proportion of the energy received will be reflected back, while some may be transmitted further and

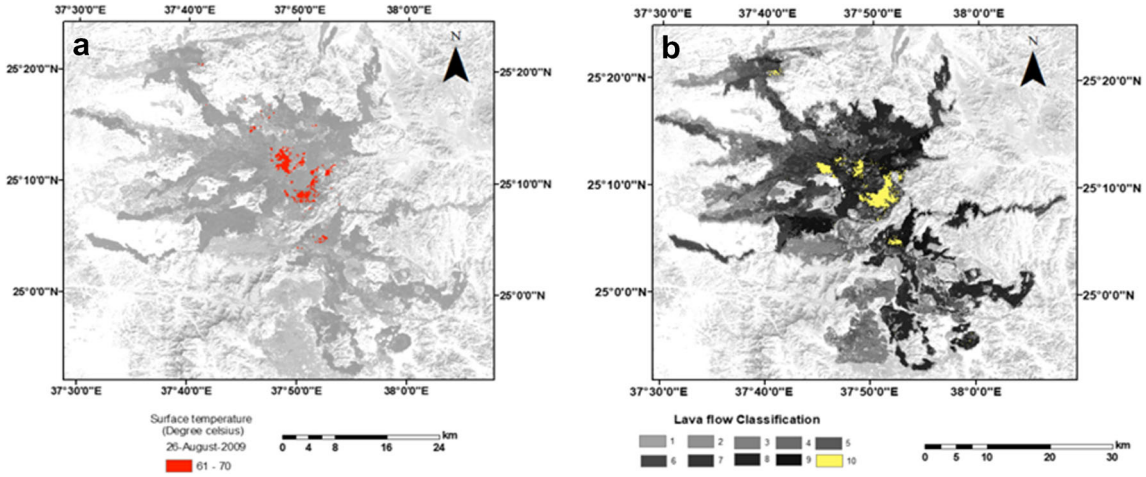

Fig. 9 **a** August 2009 surface temperature map in degree Celsius; the red colour indicates the temperature. **b** Unsupervised classification of Harrat Lunayyir lava flows (Al Shehri and Gudmundsson 2019). You can see the location of the high surface temperature 'a' located in the same area of new lava flow 'b. class 10'

the remainder absorbed. Only the latter results in the direct heating of the matter. The percentage of reflected, absorbed, and transmitted heat is dependent on the nature of the matter, the surface characteristics of the matter, and the wavelength of the incipient radiation (Da Wen 2010). The Stefan–Boltzmann law states that the radiant flux density generated by an object is directly proportional to the fourth power of that object's surface temperature (Boya 2004) (i.e. the greater the temperature of an object, the greater the total energy it will emit).

Temperatures associated with volcanic features are subject to wide variations. While newly erupted basaltic lavas may have a temperature range of 1050 to 1200 °C for basaltic lavas and komatiite may be as high as 1600 °C (Gudmundsson 2019), the temperatures associated with lava lakes can be as

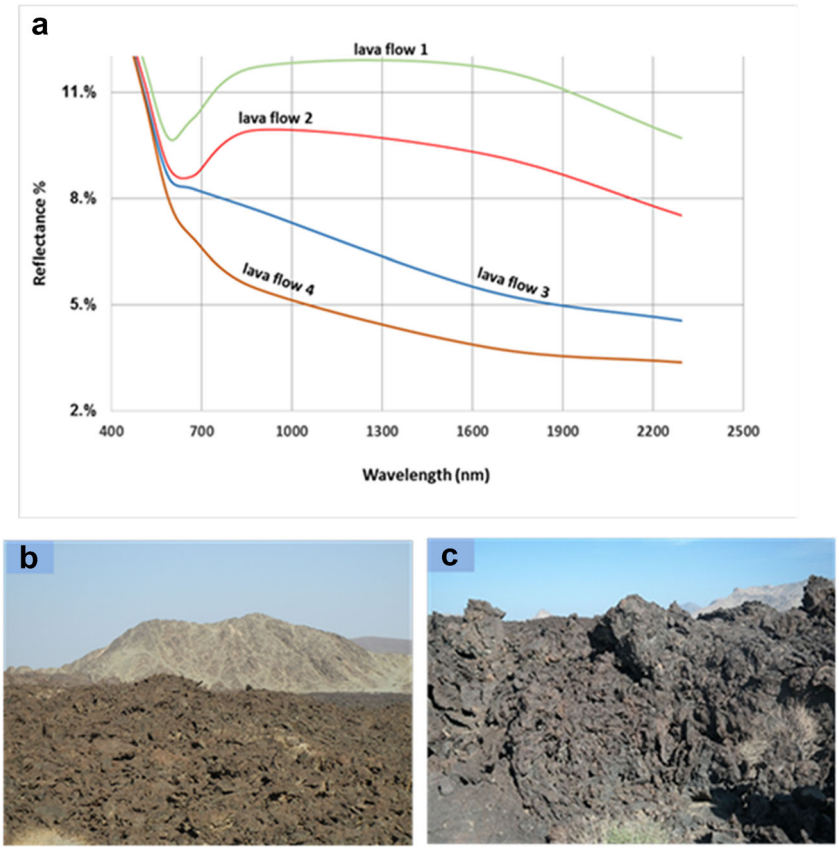

Fig. 10 **a** Reflectance spectrum of the old and young lava flows. **b** An old lava flow affected by significant surface oxidation attains high reflectance values in the near infrared region. **c** A typical Quaternary basaltic lava flow (Upper Maqrah) (Al Shehri and Gudmundsson 2019)

Table 3 Mean temperatures from grids

Month/year	2007	2008	2009	2010	2011
March	35.7	37.4	42.8	40.3	36.6
June			58.4		
July			55.5		
August		49.5	47.7		
December	38.9				

high as 1473 °C, and cooler active surfaces may only reach 673 °C (Oppenheimer and Yirgu 2002. At such temperatures, the primary radiant emissions are derived from the thermal infrared (TIR), middle infrared (MIR), and shortwave infrared (SWIR) regions of the electromagnetic spectrum.

Results

Volcanotectonic signals indicative of a potential dyke-fed eruption in Harrat Lunayyir commenced on 18 April 2009, peaked between 17 and 19 May, and ended in July that same year (Baer and Hamiel 2010; Koulakov et al. 2014; Pallister et al. 2010; Al Shehri and Gudmundsson 2018). The dyke eventually became arrested at a few hundred metres below the ground surface, with the dyke's top section thickness estimated to be between 6 and 12 m (Al Shehri and Gudmundsson 2018). The strike–dimension (e.g., horizontal length) of the dyke was estimated to be 14 km, giving a length/thickness ratio of between 2400 and 1200, a common value for regional dykes.

For the thermal monitoring and modelling of the arrested dyke, the digital number (DN) values from the image were converted to a radiance value and then into degrees Celsius. Thermal maps for March, June, July, and August 2009 were prepared in order to monitor the progress associated with temperature increases. It is important to note that the temperatures of 60–70 °C in June, July, and August 2009 (Fig. 8) were detected in a region of young lava flow. The lavas were also mostly vesicular and porous. Climatic conditions impacted surface weathering and, consequently, the texture of the lava flows. Lava on Harrat Lunayyir was subject to various kinds of surface alteration, such as chemical oxidation caused by weathering. Spectral reflectance measurements of the basaltic lava flow on Harrat Lunayyir were taken, and lava flow surfaces of varying ages were subject to methodical measurement via Landsat 8 over the range 435–2300 nm (Al Shehri and Gudmundsson 2019). Young lava exhibited reflectance values of approximately 4% as a consequence of minimal weathering, which indicated that a small proportion of the radiation was reflected, while some were transmitted, and the remainder was absorbed. However, only the absorbed energy is relevant to the heating of the lava flow units (Figs. 9 and 10).

Table 4 Mean monthly surface air temperature, Harrat Lunayyir

Month/year	2007	2008	2009	2010	2011
March	22.2	25.1	22.7	25.6	23.6
June	29.7	31.1	30.9	32.5	31.2
July	31.9	31.8	32	32.8	32.5
August	32.6	31.8	32.2	34.5	31.9
December	22.2	22.4	21.9	23	21.9

The temperature anomalies were identified based on the normalisation of the neighbourhood pixel brightness values. First, the baseline surface temperature series data, which included averages of the characteristics displayed by the pixel during the 5-year period of observation (2007–2012), were estimated and georeferenced for given mapping units. This helped identify the statistical threshold for the brightness values for the given neighbourhood of pixels. Second, the resulting series was obtained by dividing the central values in the normalised series. Based on this calculation, the acquired surface temperature distribution values were treated as anomalous if they exceeded 60.7°.

The mapped surface temperature measurements of around 51–60 °C obtained in March were found to be highly variable throughout the years 2007, 2008, 2009, 2010, and 2011 (Tables 3 and 4; Fig. 11). However, this was not indicative of an absence of seismic swarm in 2007, in October 2007, a volcanotectonic episode in the region commenced and was typified by an earthquake swarm (Al-Amri and Al-Mogren 2011; Mukhopadhyay et al. 2013; Zobin et al. 2013). Additionally, a swarm of more than 500 earthquakes began in October 2007 and ended in May 2008, indicating an origin with a NW–SE strike at a depth greater than 10 km. No surface deformation was correlated with this occurrence (Xu et al. 2016).

However, the seismic swarm that occurred from October 2007 to May 2008 may be considered a precursor to the main swarm that occurred during the dyke emplacement between April and July 2009. This precursor swarm has been interpreted as a deep-seated reservoir subject to inflation and potential rupture (Koulakov et al., 2015). During reservoir inflation, the reactivation of fractures, especially faults in the reservoir roof, would typically result in earthquakes. Furthermore, in regard to the swarm of 2009, the extent of coverage increased toward the northern portion of the Harrat and there are other inferred segments of the dyke. It is therefore anticipated that a number of other dyke areas will assume the same direction as the 2009 extinction fracture; however, all such areas have been arrested at different sub-surface depths (Fig. 12c).

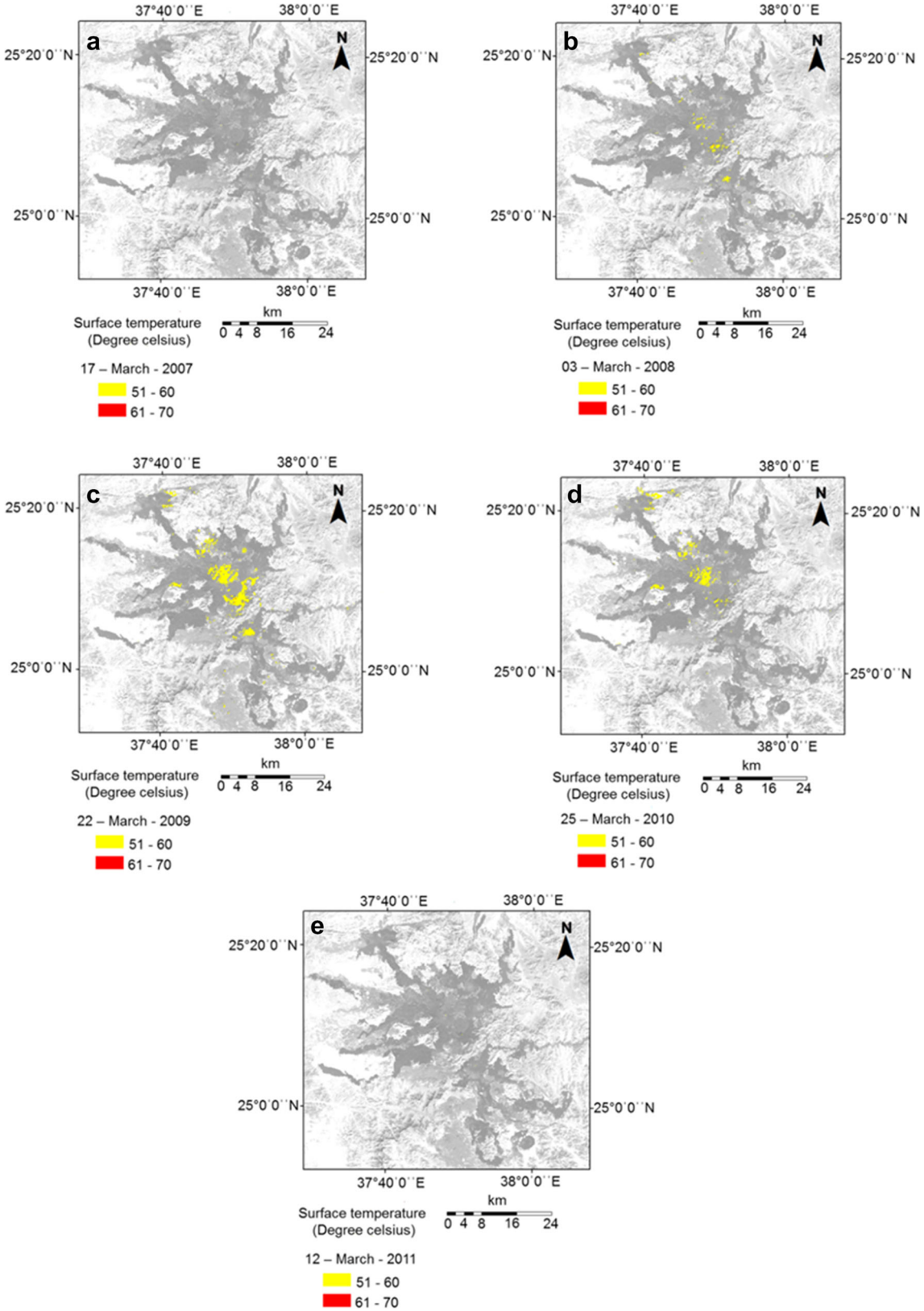

Fig. 11 March 2007, 2008, 2009, 2010, and 2011 surface temperature maps (degree Celsius); the yellow colour indicates the temperature anomalies

To achieve a more comprehensive presentation of the spatial–temporal distribution of LST for several subsequent periods (using the month March of each subsequent year), Fig. 11 reveals the range of the temperature

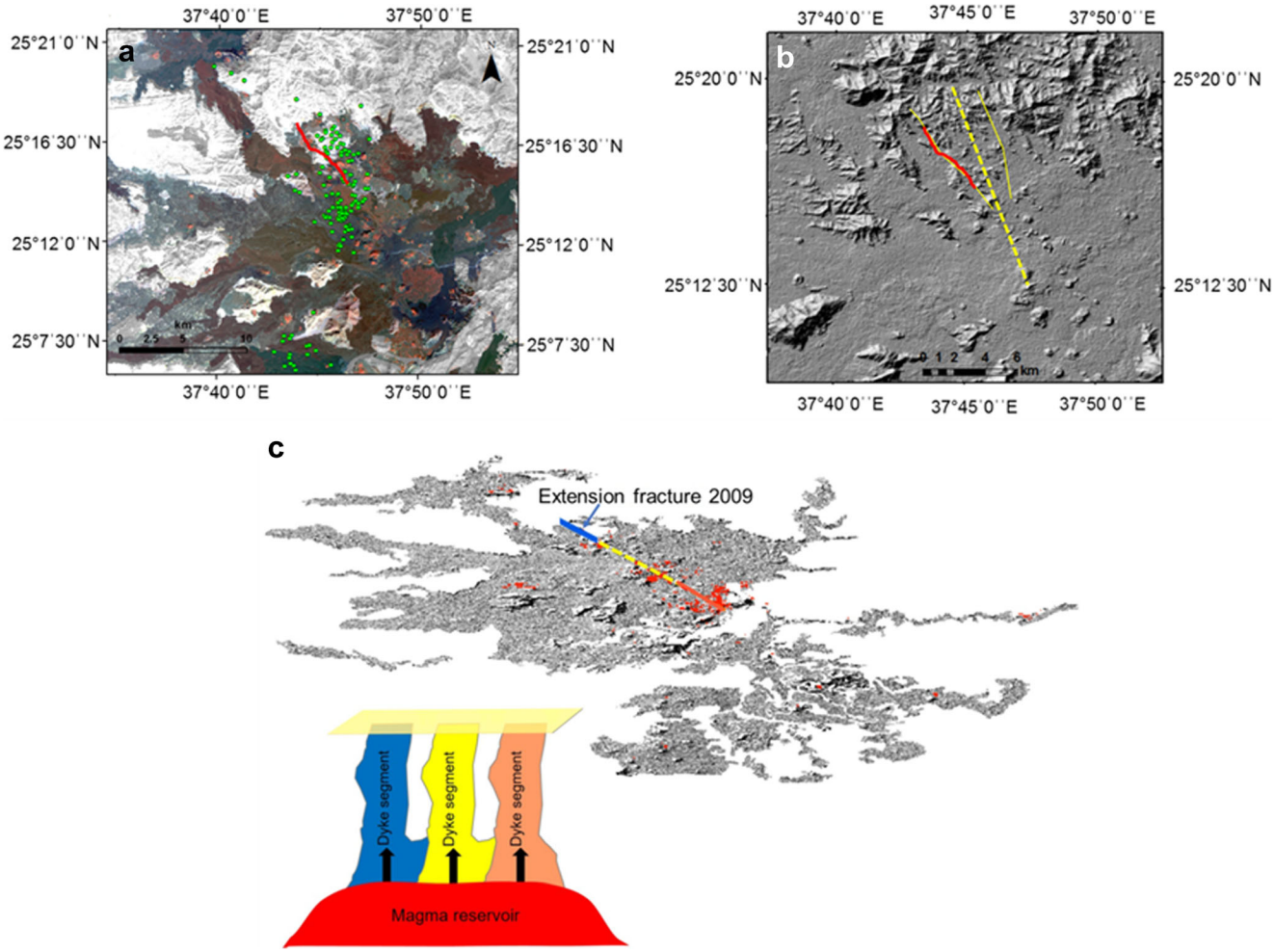

Fig. 12 Landsat 7 image of Harrat Lunayyir. **a** From the SGS website, the probable epicentre locations for the 7 May–15 August 2009 seismic events are shown as green circles, whereas the extension fracture is represented by a red line. **b** The dashed yellow line represents the projection line of the dyke direction at depth (modified after Baer and Hamiel 2010; Pallister et al. 2010); the red and yellow solid lines are the projections of the other inferred segments of the dyke. **c** Dyke segments arrested at different depths along the extension fracture of 2009

over the Harrat Lunayyir range—from 51 to 60 °C. The high temperature coincides with areas of maximum tectonic deformation (e.g., extensive fracture formation) (Fig. 12). Spatial density analysis and LST revealed that heat emission spikes can be observed throughout the years regardless of whether earthquakes, or any sort of seismic activity, had occurred or not. However, there is a statistically significant correlation between the density of heat and the seismic period timescale.

The analysis of the tectonic processes over the same periods of observation reveals insignificant levels of correlation between the surface temperatures and seismic intensity. The main cluster of seismic intensity formed in the southwestern part of the Harrat Lunayyir was not linked to any post- or pre-activity temperature increase. The epicentre locations reveal the general direction of the fracturing process toward the northern central area, which is in-line with previous research results (Pallister et al. 2010). Notably, the cluster of temperature anomalies in the southern central part were seen to have intensified in the period following the earthquake swarm. These patterns most likely reflect the emplacement of a very shallow dyke intrusion.

Discussion

TA thorough interpretation of the heat anomalies and variability in land surface temperature based on the remote sensing data is limited due to certain other factors (geothermal, hydrothermal, and geomorphological) behind temperature variations as well as characteristics of the remote sensing data. Hence, there are a number of factors that must be taken into account when acquiring and analysing thermal maps. These factors include the following:

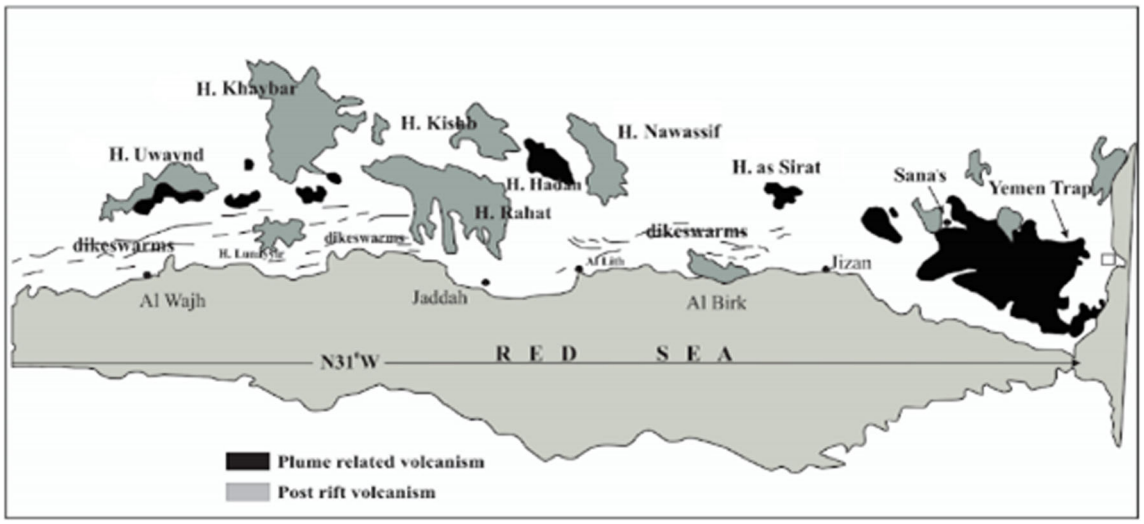

Fig. 13 Map of the geothermal system of the Red Sea Rift area (Chandrasekharam et al. 2016)

1. Spatial resolution. The TIR band of the ETM+ satellite sensor has a spatial resolution of 60 m, whereas the other six multispectral bands have a spatial resolution of 30 m, and the panchromatic band (or band 8) has a spatial resolution of 15 m (Galiano et al. 2011). A major difficulty commonly encountered in evaluating the accuracy of thermal surveys is the disparity between the spatial scale of the remote sensing measurements and contemporaneous ground truth measurements (Vlassova et al. 2014).
2. Atmospheric effects. Further research should be directed toward the incorporation of InSAR and other methods of atmospheric correction into volcanic activity monitoring systems that use remote sensing data. Additional complications related to aerial or orbital measurements of surface radiance to actual surface

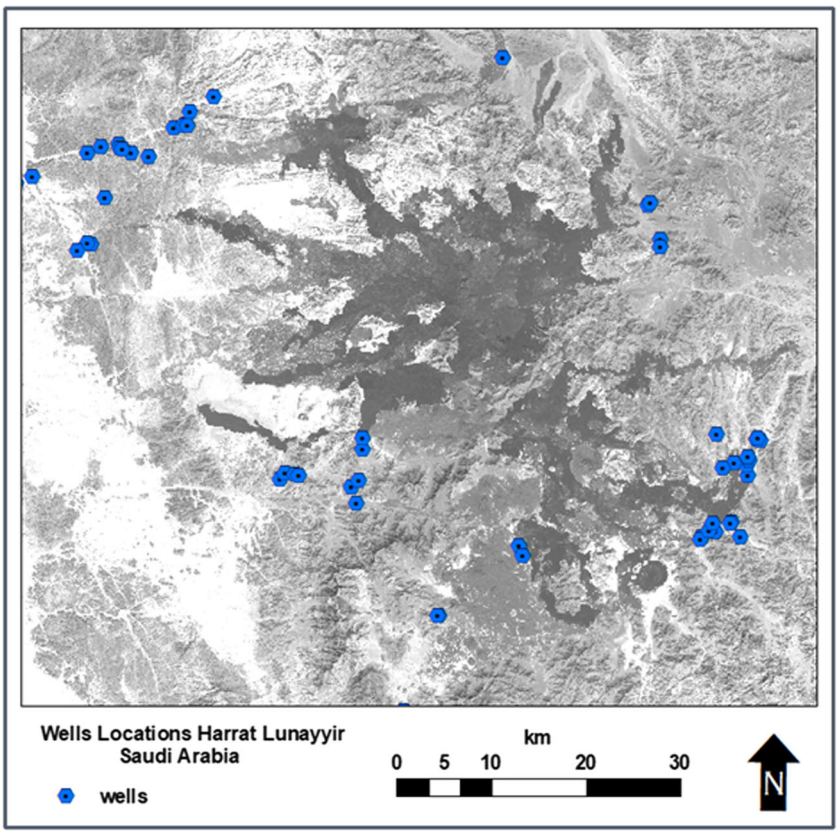

Fig. 14 The map of the hot water wells identified over the period of observation (2007–2011)

Table 5 Water well depths and temperatures (measured at ground surface level over the period of 2007–2011)

Well	Depth (m)	Temperature (°C)									
		2007		2008		2009		2010		2011	
		Mar	July	Mar	Nov	May	Oct	Jun	Oct	Feb	Sep
1	43	28.9	28.4	27	28.5	28.4	27.6	26.6	28.6	28.3	28.3
2	53	29.5	30	21.1	29.2	29.3	29.3	29.2	29.2	29.3	29.2
3	80	29.7	30.3	30.8	30.2	30.3	30.5	29.6	30.8	30	30.5
4	70	27.6	29.6	27.7	28.1	28.3	29.2	26.5	28.3	27	28.6
5	43	31.3	31.8	31.3	31.7	31.8	32	31.5	31.8	31.1	31.6
6	15	27.7	30	25.3	27.6	28.8	29.7	26.5	29.4	26.4	29.5
7	20	30.2	30.2	26.6	28.8	28.8	27.8	27.5	30	27.7	29.9
8	19	25.1	28.4	25.4	30	26.4	30.1	28.2	30.4	29.6	30.8
9	22	30.8	31.6	28.2	29	31.4	30.4	28.2	30.4	27.3	30.8
10	20	30.9	31.9	31.2	30.8	31	31.3	29.5	31.2	31	31.2
11	10	30.9	31.2	27.3	31.2	31.7	31.3	30.5	31.5	31.6	31.7
12	15	30.2	29.2	25.6	27.7	28.7	28.1	26.1	28.7	26.2	28.4
13	15	26.7	31.2	27.2	28.6	29.3	30.5	26	31.2	26.2	31.1
14	50	28.4	29.8	24.5	29.7	29.2	29.9	29.1	30.2	29.3	30.1
15	49	31.3	32.7	32.1	32.5	32.8	32.6	31.9	32.9	32.5	33
16	35	32	32.6	31.5	32.5	32.2	32.5	31.6	32.8	31.9	32.7
1	43	30.1	31.1	29.6	31	30.4	31	30	31.3	30.4	31.2
17	38	32	32.9	32.3	32.4	32.6	32.7	32.3	33.1	32.3	33
18	22	22.8	26.6	25	26.6	25.9	26.5	24.6	27.9	23.5	27.2
19	26	24.5	27.5	24.5	20.8	26.8	27.2	24.9	27.7	25.6	27.6
20	71	29.5	29.5	29.8	29.6	30	30.4	29.4	29.5	29.8	30.6
21	25	24.4	25.8	25	25.5	25.3	25.9	24.3	26.4	24.6	26.5
22	26	16.9	26.4	24.8	27.3	26.1	26.6	25.4	26.9	25.6	27.1
23	80	28	28.5	27.4	29.7	28.6	28.9	27.8	29.2	28.4	29.2
24	22	30	30	29	29	28.7	28.8	28.7	28.7	30.9	32.7
25	82	23	23.5	25	23.8	28.8	23.8	23.2	23.9	23.3	23.9
26	62	30.6	30.5	27.6	30.5	30.6	30.5	30.6	28.5	30.1	30.7
27	70	30.2	30.5	30.5	30.5	30.4	30.5	30.5	30.5	30.7	30.7
28	75	30.7	30.9	28.5	30.8	30.8	30.8	30.7	30.6	30.9	31.4
29	63	30.5	30.5	30.3	30.6	30.5	30.6	30.5	30.5	30.7	30.7
30	70	30.7	30.5	28.9	30.7	30.6	30.5	30.5	30.2	30.7	30.5
31	45	28.2	29.1	26.6	29	29.1	29.4	28.3	29.5	28.4	29.6
32	35	30.1	31.5	30.2	31.4	31.8	32.1	31.8	32.2	31.5	32.4
33	41	32.9	32.7	31.5	32.1	31.7	31.8	31.4	31.9	30.7	31.8
34	41	31.8	32.3	29.3	32	32	32.2	31.8	32.3	31.9	32.2
35	50	32.4	33	28.8	32.7	32.1	32.6	32.6	32.3	31.8	32.8
36	10	26.2	29.9	27.6	27.6	28.2	28.8	25.3	29.8	26.8	29.7
37	15	31.2	31.5	25.8	27.9	28.1	28	26.6	29.5	25.5	29.4
38	15	31.4	32.5	30	29.4	32	32.4	31.5	32.1	29.6	31.3
39	10	27.8	30.4	24.8	27.1	29.5	30.1	29.3	31	28.3	30.3
40	20	29.5	31.5	29.3	31.1	30.1	30.7	28.2	31.9	27.6	30.9
41	30	28	29.7	25.3	28	27.5	28.5	26.8	29	26.6	28.8
42	26	29.1	29.7	27.3	30	29.3	29.6	28.2	30	28	29.9
43	30	30.6	30.6	26.6	30.1	31.5	30.7	31	30.5	30.7	31.6
44	12	28.2	30.7	22.6	29.2	29.5	29.9	26.8	31	28.3	31.4

Table 5 (continued)

Well	Depth (m)	Temperature (°C)									
		2007		2008		2009		2010		2011	
		Mar	July	Mar	Nov	May	Oct	Jun	Oct	Feb	Sep
45	40	26.2	28	24	37.3	28	28.4	26.8	29	26.4	29.5
46	40	28.2	29.2	25.4	28.4	28.3	29.3	27.5	29.5	27.3	30.1
47	30	29.2	29.3	26.8	29.3	28.6	29	28.1	28.2	28	28.5
48	20	26.6	28.5	24	28.1	28	28.6	28.3	29	26.9	29.1
49	48	30.2	30.7	27	29.7	30	29.9	29.1	30	29.3	29.9
50	48	27.7	27.6	25	27.7	27.7	27.6	27.6	27.7	27.8	28.1
51	44	27.1	27.2	26	27.3	27.1	27.1	26.8	27	25.7	26.9
52	50	26.3	28.2	21.5	27.9	27.8	28	26.1	32	26.2	28.5
53	27	31.3	32.2	23	29.6	29.6	29.4	27.4	30	27	28.8
54	33	27.7	24.9	20	27.9	27.8	27.9	27.4	28.5	28	28.5

temperatures must be introduced to address these factors. This is particularly true for space-borne sensors with large fields of view that conduct regional surveys over ground swaths of hundreds of kilometres or more (Hammerle et al. 2017).

3. Emissivity. This is the ratio of energy emitted from a particular body to that radiated from a perfect emitter (a blackbody) at the same temperature and wavelength (Blackett 2017). The energy emitted by the Earth is related to the temperature and emissivity of the objects or materials within a pixel on the ground (Becker and Liang Li 2009; Galiano et al. 2011). Emissivity quantifies the radiating efficiency of a surface. An object with an emissivity of 1.0 is a perfect emitter, emitting radiation with 100% efficiency; all other objects emit with less efficiency, with the consequence that the apparent (or radiance) temperature of such objects, if measured remotely, is less than the true kinetic temperature of the object (Blackett 2017) (Vlassova et al. 2014).

In addition to the aforementioned factors, there is a need to account for different explanations for the land surface temperature variation observed via remote sensing data. These temperature variations may be partly due to differences in solar activity and terrain influence. In the case of Harrat Lunayyir, the tectonic activity component can be a residual component after accounting for volcanotectonic activity and terrain influence. The significant scatter pattern of the heat anomalous pixels in the developed surface temperature maps indicates the segmentation of the dyke and forms a linear configuration. The spatial alignment between the volcanic vent and temperature anomalous areas indicates a correlation between the observed thermal variation and volcanotectonic activity, that is, the inferred dyke emplacement.

Another major consideration is the hydrothermal regime of the region. The active geothermal systems are located in the central and southern parts of the Arabian Shield. However, even in the north and north-central parts closer to the Red Sea Rift, active thermal springs have been found (Fig. 13). Based on previous studies (Chandrasekharam et al. 2015, 2016) of the geothermal regime, issuing temperatures associated with these springs are in the range of 31–55 °C but may reach up to 70 °C during summer periods. Another geothermal factor contributing to heat anomalies is the high heat input from post-orogenic granites, which are common in the Harrat Lunayyir area. The clusters of heat anomalies located in the outskirts of the Harrat might be the result of heat flow generation due to the process of magma movement at shallower levels.

The map shown in Fig. 14 indicates that the hot water wells in the Lunayyir area are preferentially located along the margins of the basaltic field, but they are typically restricted to the margins of the lava flows. This pattern is in agreement with the regional characteristic of hot springs found in the vicinities of the basaltic fields along the cataclastic zone (Lashin et al. 2015). These hot water wells are characterised by low charge, but individual heat flows may radiate long distances. The maximum depth of the hot wells is 80 m (Table 5). At this depth, permeable components are likely to include tension fractures and normal faults oriented toward the centre of the field. The hot water wells of this crustal part are also characterised by low resistance as a result of Table 1. The far-distance heat emanating from the centre of the field that can flow is also reflected in the two mapping datasets (Figs. 8 and 11), with the heat anomalies clustered toward the centre of the field and the hot water wells located alongside the margin.

Future research objectives highlight the need for a variety of activities, including in situ field studies on bulk emissivity and the thermal inertia of surface cover materials. An empirical analysis of high spectral and spatial resolution imagery is needed to evaluate the utility of thermal infrared measurements for mapping variations in the emissivity of natural surfaces. This is also specifically necessary to evaluate trade-offs between increased resolution and decreased signal-to-noise. In future research, atmospheric effects can be accounted for within localised areas through the use of upward-viewing, ground-based radiometers.

Conclusions

The current study examined the relationship between the relative changes in surface temperatures 'LST' and seismic–tectonic activities and provided new insights into the spatiotemporal relationship between volcanic and tectonic processes in the area. Through the employment of the methodology of thermal mapping and spatial density mapping of volcanic vents (primarily crater cones and small lava shields), the land surface temperature changes in the centre of Harrat Lunayyir were recorded when the 2009 dyke was propagating toward the surface. The obtained results are in agreement with previous research findings indicating the northwest–southeast direction of the dyke system and the normal fault formation.

This paper focused on monitoring and estimating relative changes in surface temperatures as a means for detecting an impending dyke-fed eruption or, alternatively, dyke arrest at a shallow depth, which consequently provides an understanding of the point at which a particular hazard event ('fissure eruptions') is most likely to occur. This provides critical information that supports disaster responders and emergency management. Consequently, this helps provide the foundation for response prioritisations, disaster assessment, informed mitigation planning, and thorough risk assessments. Therefore, infrared observations may increase understanding about a volcano's activity status and reveal incoming changes in activity.

A strong correlation was found between dyke intrusion and LST. The variety of surface temperature values in the past several years based on the thermal energy response. Consequently, this study was beneficial in that it can help protect the lives of those residing close to danger zones by suggesting necessary courses of action to take before a disaster occurs in the future.

Acknowledgements AAS thanks Morayyea Al-Shahrani, President of the General Commission of Survey for the helpful suggestions. She also thanks Abdullah Al-Amri Adel Alsharif, Basim al Dahri, Maher Al Dahry, Ali Al Shehri, and Numan Muhammd for various helpful suggestions and information in connection with this work.

References

Al Shehri A, Gudmundsson A (2018) Modelling of surface stresses and fracturing during dyke emplacement: application to the 2009 episode at Harrat Lunayyir, Saudi Arabia. Volcanol Geotherm Res 356: 278–303

Al-Amri AM, Al-Mogren SM (2011) Seismo-volcanic investigation of the current activity in Harrat Lunayyir, Al-Madinah Al-Munawwarah area. Final report. King Saud University, Riyadh, pp 1–184

Al-Amri A, Fnais M (2009) Seismo-volcanic investigation of 2009 earthquake swarms at Harrat Lunayyir (Ash Shaqah), Western Saudi Arabia. Int J Earth Sci Eng, October issue, 1–18.

Al-Amri A, Fnais M, Abdel-Rahman K, Mogren S, Al-Dabbagh M (2012) Geochronological dating and stratigraphic sequences of Harrat Lunayyir, NW Saudi Arabia. Int J Phys Sci 7:2791–2805. https://doi.org/10.5897/IJPS12.178

Alberico I, Petrosino P, Lirer L (2010) Volcanic hazard and risk assessment in a multi-source volcanic area: the example of Napoli city (Southern Italy). Nat Hazards Earth Syst Sci 11:1057–1070. https://doi.org/10.5194/nhess-11-1057-2011

Al-Zahrani H, Al-Amri AM, Abdel-Rahman K, Fnais M (2013) Aftershock sequence analysis of 19 May 2009 earthquake of Lunayyir lava flow, northwest Saudi Arabia. Int J Phys Sci 8:277–285

Baer G, Hamiel Y (2010) Form and growth of an embryonic continental rift: InSAR observations and modelling of the 2009 western Arabia rifting episode. Geophys J Int 182:155–167

Bailey G (2009) The Red Sea, coastal landscapes and hominin dispersals. In: Petraglia MD, Rose JI (eds) The evolution of human populations in Arabia. Springer, Dordrecht, pp 15–37

Barnie T, Oppenheimer C (2015) Extracting high temperature event radiance from satellite images and correcting for saturation using independent component analysis. Remote Sens Environ 158:56–68

Becker F, Liang Li Z (2009) Surface temperature and emissivity at various scales: definition, measurement and related problems. Remote Sens Rev 12:225–253

Blackett M (2017) An overview of infrared remote sensing of volcanic activity. J Imaging 3:13. https://doi.org/10.3390/jimaging3020013

Boya L (2004) The thermal radiation formula of Planck (1900). Universidad de Zaragoza, Zaragoza

Chandrasekharam D, Lashin A, Al Arifi N, Al Bassam AA, Varun C (2015) Evolution of geothermal systems around the Red Sea. Environ Earth Sci 73(8):4215–4236

Chandrasekharam D, Lashin A, Al Arifi N, Al-Bassam AM (2016) Red Sea geothermal provinces. CRC Press

Da Wen C (2010) Investigation of steel emissivity behavior: examination of multispectral radiation thermometry emissivity models. Int J Heat Mass Transf 53:2035–2043

Galiano R, Igúzquiza P, Olmo C, Sánchez R (2011) Increasing the spatial resolution of thermal infrared images using cokriging. Procedia Environ Sci, Elsevier 3:117–122

Genna A, Nehilg P, Le Goff E, Guerrot C, Shanti M (2002) Proterozoic tectonism of the Arabian Shield. Precambrian Res 117:21–40

Gudmundsson A (2002) Emplacement and arrest of sheets and dykes in central volcanoes. J Volcanol Geotherm Res 116:279–298

Gudmundsson A (2003) Surface stresses associated with arrested dykes in rift zones. Bull Volcanol 65:606–619
Gudmundsson A (2011a) Deflection of dykes into sills at discontinuities and magma-chamber formation. Tectonophysics 500:50–64
Gudmundsson A (2011b) Rock fractures in geological processes. Cambridge University Press, Cambridge
Gudmundsson A (2019) Volcanotectonics: understanding the structure, deformation, and dynamics of volcanoes. Cambridge University Press, Cambridge
Hammerle A, Meier F, Heinl M, Egger A, Leitinger G (2017) Implications of atmospheric conditions for analysis of surface temperature variability derived from landscape-scale thermography. Int J Biometeorol 61:575–588
Hansen E, Puckett E, Keller R, Brueseke E, Bulen L, Mertzman A, Finegan A, McCleery A (2013a) Intra-plate magmatism related to opening of the southern Iapetus Ocean: Cambrian Wichita igneous province in the Southern Oklahoma rift zone. Lithos. 174:57–70
Hansen E, DeShon R, Driskell M, Al-Amri M (2013b) Investigating P-wave velocity structure beneath Harrat Lunayyir, north western Saudi Arabia, using double-difference tomography and earthquakes from the 2009 seismic swarm. J Geophys Res 118:4814–4826
Harris A (2013) Thermal remote sensing of active volcanoes: a user's manual. Cambridge University Press, Cambridge 736
Harris L, Blake S, Rothery A, Stevens F (1997) A chronology of the 199 to 1993 Etna eruption using AVHRR data: implications for real time thermal volcano monitoring. J Geophys Res 102:7985–8003
Haselwimmer C, Prakash A (2013) Thermal infrared remote sensing of geothermal systems. Remote Sens Digit Image Process 17:453–473
IUCN (2009) In: IUCN (ed) World Heritage Volcanoes, Gland 70
Jensen J (2007) Remote sensing of the environment: an Earth resource perspective, 2nd edn. Pearson Prentice Hall, Upper Saddle River
Jónsson, S., Pallister, J., McCausland, W., El-Hadidy, S., 2010. Dyke Intrusion and Arrest in Harrat Lunayyir, western Saudi Arabia, in April-July 2009. Geophysical Research Abstracts, 12, 7704.
Kavanagh J, Burns A, Hazim S, Wood E, Martin S, Hignett S, Dennis D (2018) Challenging dyke ascent models using novel laboratory experiments: implications for reinterpreting evidence of magma ascent and volcanism. Volcanol Geotherm Res 354:87–101
Koulakov I, El Khrepy S, Al Arifi N, Sychev I, Kuznetsov P (2014) Evidence of magma activation beneath the Harrat Lunayyir basaltic field (Saudi Arabia) from attenuation tomography. Solid Earth 5: 873–882
Koulakov, I., El Khrepy, S., Al-Arifi, N., Kuznetsov, P., & Kasatkina, E., (2015) Structural cause of a missed eruption in the Harrat Lunayyir basaltic field (Saudi Arabia) in 2009. Geology. 43:395–398
Lashin A, Al Arifi N, Chandrasekharam D, Al Bassam A, Rehman S, Pipan M (2015) Geothermal energy resources of Saudi Arabia: country update. In Proceeding, World Geothermal Congress
Moran C, Newhall C, Roman C (2011) Failed magmatic eruptions: late-stage cessation of magma ascent. Bull Volcanol 73:115–122
Mukhopadhyay B, Mogren S, Mukhopadhyay M, Dasgupta S (2013) Incipient status of dyke intrusion in top crust– evidences from the Al-Ays 2009 earthquake swarm, Harrat Lunayyir, SW Saudi Arabia. Geomat Nat Haz Risk 4:30–48
Murphy W, Wright R, Oppenheimer C, Souza Hilho R (2013) MODIS and ASTER synergy for characterizing thermal volcanic activity. Remote Sens Environ 131:195–205
NASA (2018) Landsat 7 science data users handbook. Nasa.Gov
Noguchi T, Ohno N, Hattori K, Oyama K (2011) Detection of thermal changes possibly associated with volcanic activity and discrimination of faint changes from MODIS. J Asian Earth Sci 41:467–475
Oppenheimer C, Yirgu G (2002) Thermal imaging of an active lava lake: Erta 'ale volcano, Ethiopia. Int J Remote Sens 23:4777–4782
Pallister J, McCausland W, Jónsson S, Lu Z, Zahran H, El-Hadidy S, Aburukbah A, Stewart I, Lundgern P, White R, Moufti M (2010) Broad accommodation of rift-related extension recorded by dyke intrusion in Saudi Arabia. Nat Geosci 3:705–712
Paulsen T, Wilson T (2009) Structure and age of volcanic fissures on Mount Morning: a new constraint on Neogene to contemporary stress in the West Antarctic Rift, southern Victoria Land, Antarctica. Geol Soc Am 121:7–8
Pyle D, Mather T, Biggs J (2015) Remote sensing of volcanoes and volcanic processes: integrating observation and modelling – introduction. Remote Sensing of Volcanoes and Volcanic Processes: Integrating Observation and Modelling. Geol Soc Lond Spec Publ 380:1–13
Ramsey MS, Flynn LP (2004) Strategies, insights, and the recent advances in volcanic monitoring and mapping with data from NASA's Earth Observing System. J Volcanol Geotherm Res 135(1-2):1–11
Realmuto J, Worden M (2000) The impact of atmospheric water vapor on the thermal infrared remote sensing of volcanic sulfur dioxide emissions: a case study from the Pu'u 'O'o vent of Kilauea Volcano, Hawaii. J Geophys Res 21:497–421
Rivalta E, Taisne B, Bunger P, Katz F (2015) A review of mechanical models of dyke propagation: schools of thought, results and future directions. Sci. Direct. Tect Phys 638:1–42. https://doi.org/10.1016/j.tecto.2014.10.003
Sobrino JA, Jiménez-Muñoz JC, Sòria G, Romaguera M, Guanter L, Moreno J, Plaza A, Martínez P (2008) Land surface emissivity retrieval from different VNIR and TIR sensors. IEEE Trans Geosci Remote Sens 46(2):316–327
Townsend R, Pollard D, Smith P (2017) Mechanical models for dikes: a third school of thought. Tectonophysics. 703-704:98–118
Tralli D, Blom R, Zlotnicki V, Donnellan A, Evans D (2005) Satellite remote sensing of earthquake, volcano, flood, landslide and coastal inundation hazards. ISPRS J Photogramm Remote Sens 59:185–198
van der Zwan FM, Augustin N, Devey CW, Bantan R, Kwasnitschka T (2013) New insights into volcanism and tectonics in the Red Sea Rift. Geophys Res Abstr 15:EGU2013-7188 EGU General Assembly
Vaughan G, Hook J, Ramsey S, Realmuto J, Schneider J (2005) Monitoring eruptive activity at Mount St. Helens with TIR image data. Geophys Res Lett 32:1–4
Vlassova L, Pérez-Cabello F, Mimbrero MR, Llovería RM, García-Martín A (2014) Analysis of the relationship between land surface temperature and wildfire severity in a series of Landsat images. Remote Sens 6(7):6136–6162
Wellons M (2007) The Stefan-Boltzmann law. Physics Department, The College of Wooster, Wooster
Xu W, Jonsson S, Corbi F, Rivalta E (2016) Graben formation and dike arrest during the 2009 Harrat Lunayyir dike intrusion in Saudi Arabia: insights from InSAR, stress calculations and analog experiments. J Geophys Res 121. https://doi.org/10.1002/2015JB012505
Zahran M, Mccausland A, Pallister S, Lu Z, El-hadidy S, Aburukba A, Schawali J, Kadi K, Youssef A, Ewert W, White A, Lundgren P, Mufti M, Stewart C (2009) Stalled eruption or dike intrusion at Harrat Lunayyir, Saudi Arabia? Am Geophys Union 13:E-2072
Zobin V, Al-Amri A, Fnais M (2013) Seismicity associated with active, new-born and re-awakening basaltic volcanoes: case review and the possible scenarios for the Harrat volcanic provinces, Saudi Arabia. Arab J Geosci 6:529–541

Chapter 5

Modelling of surface stresses and fracturing during dyke emplacement: Application to the 2009 episode at Harrat Lunayyir, Saudi Arabia

Journal of Volcanology and Geothermal Research

Azizah Al Shehri and Agust Gudmundsson

https://doi.org/10.1016/j.jvolgeores.2018.03.011

Statement of contribution:

The origin idea, methodology, computation and creation of models were developed by AA.
Fieldwork by AA
Writing the initial draft was made by AA and later critical review and commentary from co-author
All illustrations were prepared by AA, with later adjustments and modifications from co-author.
Interpreted data and discussions were done by AA and specifically critical revision from co-author.

Journal of Volcanology and Geothermal Research 356 (2018) 278–303

Contents lists available at ScienceDirect

Journal of Volcanology and Geothermal Research

journal homepage: www.elsevier.com/locate/jvolgeores

Modelling of surface stresses and fracturing during dyke emplacement: Application to the 2009 episode at Harrat Lunayyir, Saudi Arabia

Azizah Al Shehri, Agust Gudmundsson *

Department of Earth Sciences, Royal Holloway University of London, Egham, UK

ARTICLE INFO

Article history:
Received 24 August 2017
Received in revised form 18 February 2018
Accepted 16 March 2018
Available online 20 March 2018

Keywords:
Dyke propagation
Dyke arrest
Surface deformation
Grabens
Crustal stresses
Numerical models

ABSTRACT

Correct interpretation of surface stresses and deformation or displacement during volcanotectonic episodes is of fundamental importance for hazard assessment and dyke-path forecasting. Here we present new general numerical models on the local stresses induced by arrested dykes. In the models, the crustal segments hosting the dyke vary greatly in mechanical properties, from uniform or non-layered (elastic half-spaces) to highly anisotropic (layers with strong contrast in Young's modulus). The shallow parts of active volcanoes and volcanic zones are normally highly anisotropic and some with open contacts. The numerical results show that, for a given surface deformation, non-layered (half-space) models underestimate the dyke overpressure/thickness needed and overestimate the likely depth to the tip of the dyke. Also, as the mechanical contrast between the layers increases, so does the stress dissipation and associated reduction in surface stresses (and associated fracturing). In the absence of open contacts, the distance between the two dyke-induced tensile and shear stress peaks (and fractures, if any) at the surface is roughly twice the depth to the tip of the dyke. The width of a graben, if it forms, should therefore be roughly twice the depth to the tip of the associated arrested dyke. When applied to the 2009 episode at Harrat Lunayyir, the main results are as follows. The entire 3–7 km wide fracture zone/graben formed during the episode is far too wide to have been generated by induced stresses of a single, arrested dyke. The eastern part of the zone/graben may have been generated by the inferred, arrested dyke, but the western zone primarily by regional extensional loading. The dyke tip was arrested at only a few hundred metres below the surface, the estimated thickness of the uppermost part of the dyke being between about 6 and 12 m. For the inferred dyke length (strike dimension) of about 14 km, this yields a dyke length/thickness ratio between 2400 and 1200, similar to commonly measured ratios of regional dykes in the field.

1. Introduction

Most volcanic eruptions occur when a magma-filled fracture is able to propagate from its source to the surface. In many central volcanoes (composite volcanoes/stratovolcanoes and collapse calderas) the source is a shallow magma chamber, in which case the local stress field may favour inclined (cone) sheets rather than vertical dykes. In areas of rifting outside central volcanoes, however, the regional stress field controls the magma propagation path. In rift zones the minimum principal compressive stress σ_3 is normally horizontal and parallel with the spreading or rifting vector. Since all magma-filled fractures generally form perpendicular to the σ_3 it follows that the greater parts of magma paths tend to be vertical dykes.

Most dykes (and inclined sheets) do not reach the surface to erupt but rather become arrested (stop their propagation path, stall) at various depths in the crust (Gudmundsson, 2002, 2003; Moran et al., 2011; Rivalta et al., 2015; Townsend et al., 2017). The conditions for dyke arrest have been studied in the field (Gudmundsson, 2002, 2003; Gudmundsson and Philipp, 2006; Tibaldi, 2015) and through analogue models (Kavanagh et al., 2006), numerical models (Gudmundsson and Philipp, 2006; Barnett and Gudmundsson, 2014; Rivalta et al., 2015; Townsend et al., 2017), and analytical models (Gudmundsson, 2011a, 2011b). Understanding these conditions is of fundamental importance in theoretical and applied volcanology. Despite all the available instrumentation for volcano monitoring, we still cannot forecast dyke-propagation paths once a dyke has been initiated during magma-chamber/reservoir rupture. It follows that we cannot make reliable forecasts as to (i) what the likely path of the dyke is going to be and, in particular, (ii) whether or not the dyke is going to reach the surface and erupt or, alternatively, (iii) become arrested at some depth in the volcano. Direct field studies of arrested solidified or 'frozen' dykes, as well as geodetic and seismic studies of dyke arrest during unrest periods, are of great importance for improving our understanding of dyke propagation and dyke-fed eruptions.

There have been many reported dyke arrests in recent decades. In some unrest periods many dykes have become arrested while at the end of the unrest period one or more dykes have reached the surface

* Corresponding author.
E-mail address: rock.fractures@googlemail.com. (A. Gudmundsson).

https://doi.org/10.1016/j.jvolgeores.2018.03.011
0377-0273/

to erupt. A well-documented case of this type is the unrest in the volcano Eyjafjallajökull in South Iceland for nearly two decades before its 2010 eruption. During the period 1993 until 2010 there were 4–5 dyke injections that became arrested, some of the dykes changing into sills, until in March 2010 a new dyke injection reached the surface and erupted (Sigmundsson et al., 2010). Many dykes and sills are exposed in the volcano, suggesting that episodes of this kind are common (Gudmundsson, 2017). Many unrest periods with dyke injections, however, have not resulted in eruptions. One happened in Tenerife, Canary Islands, in 2004 (Garcia et al., 2006; Gottsmann et al., 2006), and another one in Harrat Lunayyir in western Saudi Arabia in 2009 (Baer and Hamiel, 2010; Pallister et al., 2010; Xu et al., 2016). This latter one is the main topic of the present paper.

This paper has two aims. The first is to present new and general results on dyke-induced stresses in crustal segments with contrasting mechanical properties. Here the focus is on new numerical models on dykes arrested with their tips at various crustal depths and hosted by rocks with mechanical properties that range from elastic half spaces (uniform properties) to those with alternating stiff (high Young's modulus) and soft (compliant, low Young's modulus) layers. The results are completely general, but are here applied to the 2009 volcanotectonic unrest period in Harrat Lunayyir in Saudi Arabia (Figs. 1 and 2). The second, and main, aim is thus to use the numerical results, as well as some analytical models together with field observations of the associated surface deformation, to make new estimates of the dimensions, the depth to the tip at arrest, and contribution to surface deformation of the

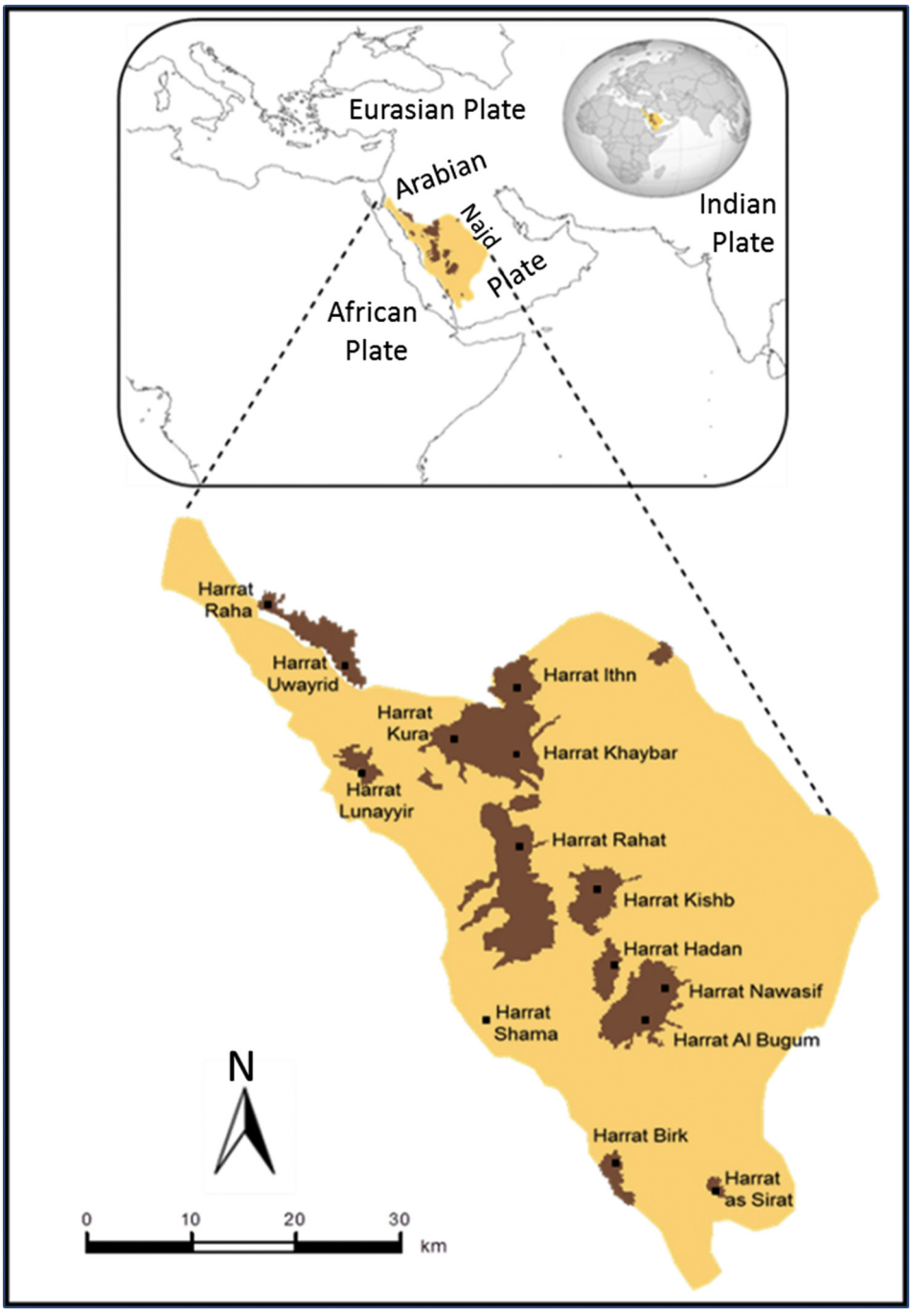

Fig. 1. Main Cenozoic lava fields (referred to as harrats) in western Saudi Arabia (their location in a wider geographic context is on the inset). Modified from a map of the SGS (https://www.sgs.org.sa, 2011).

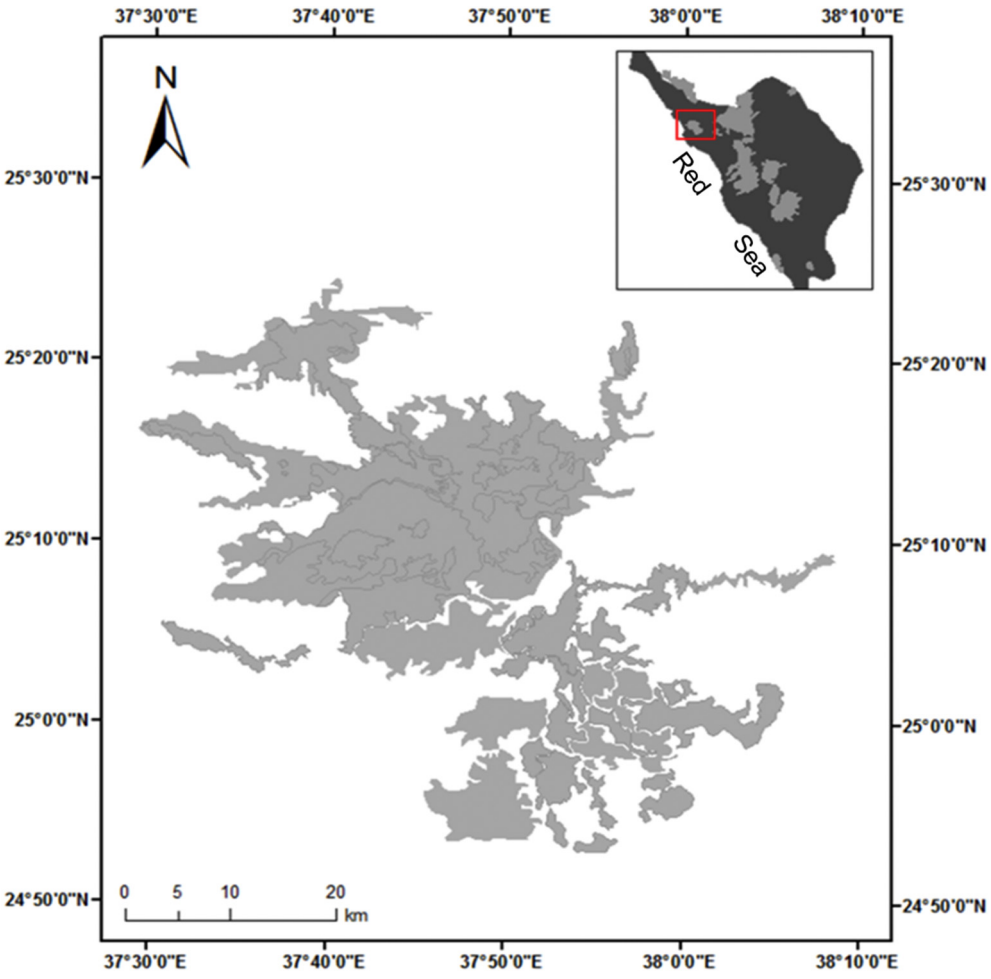

Fig. 2. Details of the Harrat Lunayyir volcanic field. On the inset, the location of the field within the fields shown in Fig. 1.

dyke inferred to have been emplaced during the 2009 episode. We also put the dyke propagation and arrest in Harrat Lunayyir into general context of arrested dykes, their dimensions, and aspect (length/thickness) ratios, as obtained in direct field studies. Furthermore, we explain the likely conditions for the 2009 dyke arrest in Harrat Lunayyir and the implications of the results for volcanic hazards. For understanding the 2009 episode, we first provide brief outline of the geological setting of the Harrat Lunayyir, as well as a short overview of its volcanic geology.

2. Regional geological setting

The Harrat Lunayyir forms a part of the Arabian Plate, which is adjacent to the African Plate, with several other plates being nearby (Fig. 1). The eastern part of the Arabian Plate consists of a late Proterozoic shield (Genna et al., 2002) which is bounded to the southwest by the African Plate, the Red Sea rift separating the plates. The other plates in the area are the Eurasian Plate, in the east, and the Anatolian Plate, in the north. The Arabian Plate was generated by the African Rift that led to the formation of the Red Sea and the Gulf of Aden during a rifting episode which began about ~25 Ma ago (Stern and Johnson, 2010).

The Red Sea is considered an active rift zone that emerged from a weakness formed during continental rifting in the pre-Cambrian era (Cochrna and Karner, 2007; Bailey, 2009). The present rifting led to the expansion and propagation of the Red Sea from the south to the north. Currently, the Red Sea extends from 30° N (the north limit of the Gulf of Suez) to 12.5° N (where it meets the Gulf of Aden), with a total north-south length of about 2250 km and a maximum east-west width of about 354 km – the oceanic crust itself being of maximum width of about 100 km. The Red Sea may be regarded as an excellent example of the early stages of ocean development through sea-floor spreading. The Gulf of Aqaba-Dead Sea Transform Fault represents another major tectonic element in the area. During spreading of the Red Sea, parts of the Arabian Shield have become extended and thinned (as discussed below) with associated formation of dyke swarms and volcanic fields, one of which is the Harrat Lunayyir (Genna et al., 2002; Hansen et al., 2013a, 2013b).

The Arabian Shield itself occupies one-third of the Arabian Peninsula with an estimated area ranging from 670,000 km^2 to 725,000 km^2 (Brown et al., 1978). The Arabian Shield it is a part of a larger group referred to as the Arabian-Nubian Shield whose total area is around 2.7×10^6 km^2 (Rodgers et al., 1999; Johnson and Woldehaimanot, 2003). Precambrian crystalline rocks, Phanerozoic sedimentary rocks, and Cenozoic flood basalts (such as at Harrat Lunayyir) constitute the uppermost part of the western part of the Arabian Shield. This is the part that occupies the northeast flank of the Red Sea, including the well-exposed highlands of Yemen and the central part of Saudi Arabia, Najd (Powers et al., 1963; Stern and Johnson, 2010) (Fig. 1). The average crustal thickness of the Arabian Shield is about 40 km (Al Damegh et al., 2005), but the crust becomes thinner towards the coast of the Red Sea where the thickness is 23–25 km. Similar crustal thicknesses occur in the Nubian Shield on the west side of the Red Sea, the thickness being 25–26 km in Egypt within 50 km of the coast of the Red Sea

(Hosny and Nyblade, 2014). The crustal thickness in the eastern part of the Arabian Shield is much greater than in the western part (Camp and Roobol, 1992; Stern, 2008). Duncan and Al-Amri (2013).

Close to the volcanic areas of the Arabian Shield is the Afar Triangle, a depression generated by the Afar Triple Junction (Waltham, 2005) where the rift zones of the Red Sea, the Gulf of Aden, and the East African Rift meet (Keir et al., 2011). The crustal spreading is at the rate of 1–2 cm/year across each of the arms or legs of the Triangle. The Triangle is also the site of a hot spot, and widely regarded as the surface expression of a deep mantle plume (Hansen et al., 2013a, 2013b).

3. Volcanic geology of the Harrat Lunayyir

The western part of the Arabian Plate has been volcanically active during the Cenozoic. The activity has been largely confined to two episodes: one happened from 30 to 20 Ma ago while the other began some 12 Ma ago and is still continuing (Camp and Roobol, 1992). The cumulative area covered by these relatively young volcanic materials is about 80,000 km^2. The lava fields themselves are commonly known as 'Harrats' (Pint, 2006). Harrat Lunayyir (also known as Harrat Al-Shaqa) is one of smallest and youngest of the alkali basaltic Holocene lava fields in western Saudi Arabia. More specifically, the lava field is located northwest of the city of Medina (Al-Madinah Al Munawwarah in Arabic) between latitudes 25° 10′–25° 17′ N and longitudes 37° 45′–37° 75′ E. The lava field is somewhat elongated in the northwest-southeast direction and located about 60 km east of the nearby coast of the Red Sea or, alternatively, some 150 km east of the Red Sea spreading centre (Al Amri and Fnais, 2009; Baer and Hamiel, 2010; Al-Zahrani et al., 2013; Duncan and Al-Amri, 2013) (Fig. 2).

Harrat Lunayyir is characterised by Cenozoic alkali-olivine-basalt lava flows (Duncan and Al-Amri, 2013) and about 50 monogenetic crater cones (Baer and Hamiel, 2010). The basaltic lava flows in the area have been divided into 'an older Tertiary unit (Jarad basalt)' and 'a younger Quaternary unit (Maqrah basalt)' by Al Amri et al. (2012) (Fig. 3). Precambrian rocks are exposed in the northern, southern, and eastern parts of Harrat Lunayyir, while in the central part the Precambrian rocks form only isolated outcrops (Duncan and Al-Amri, 2013). Volcanic activity in Harrat Lunayyir began about 0.5 Ma ago. The youngest lava flows in the field are generally regarded as about 5000 year old (Al-Amri et al., 2012). Eruptions in the area, however, may be more recent, since there is some evidence that one of the crater cones was formed about 1000 years ago (Baer and Hamiel, 2010).

4. The 2007 and 2009 volcanotectonic episodes

Harrat Lunayyir was until recently considered inactive. As indicated above, the last eruption in the area is at least 1000 years old and more likely 5000 years old. However, in October 2007 a volcanotectonic episode began in the area, characterised by an earthquake swarm (Al-Amri and Al-Mogren, 2011; Mukhopadhyay et al., 2013; Zobin et al., 2013). The earthquake swarm was comparatively small, including about 500 earthquakes, the largest one being of moment magnitude M3.2. The swarm came to an end in May 2008. The swarm indicates a source with a northwest-southeast strike and located at depth in excess of 10 km. No surface deformation was associated with this episode (Xu et al., 2016).

Another volcanotectonic episode began 18 April 2009, reached its peak 17–19 May, and came to an end in July the same year (Al-Mahri et al., 2009; Baer and Hamiel, 2010; Pallister et al., 2010; Koulakov et al., 2014; Xu et al., 2016). Again, there was an earthquake swarm with a general northwest-southeast strike, but the swarm was located some 15 km to the northwest of the 2007 swarm. The 2009 swarm generated over 30,000 recorded earthquakes, peaked in its intensity 17–19 May with a sequence of 7 earthquakes of M > 4, including the largest earthquake during the episode, of M5.7 (Baer and Hamiel, 2010; Xu et al., 2016). The focal mechanisms of the M > 4 earthquakes indicate

Fig. 3. Volcanic geology of the Harrat Lunayyir volcanic field. a. Basaltic lava flow of Quaternary age (Maqrah basalt). b. Basaltic lava flow of Tertiary age (Jarad basalt). c. An irregularly shaped basaltic dyke, light coloured (people standing on the dyke). d. Volcanic ash partly covering a hill. The thickness of the nearby pahoehoe lava flow is a few tens of centimetres.

primarily normal faulting, some of which showed evidence of strike-slip components. The main episode came to an end in July 2009. Al-Zahrani et al. (2013) estimate the focal depth of the largest earthquake, M5.7, as 9 km. Most of the earthquakes were located at depths of 5–15 km and had an overall strike of NNW-SSE (Xu et al., 2016).

In addition to the earthquake swarm, there was extensive surface deformation during the 2009 episode (Figs. 4–7). There was, first, a broad area of uplift and extension, the area being about 2000 km^2 with a maximum uplift of about 0.4 m and an extension of about 1 m (Pallister et al., 2010). The total NNW-SSE length of the uplifted area is 14–15 km (cf. Fig. 4). Subsequent studies suggest a total extension of about 1.5 m across the deformation zone, and a subsidence of a maximum of 0.8 m in the central part of a 'graben' that dissects the dome (Baer and Hamiel, 2010). Doming normally generates tensile and shear stresses in the surface layers, as is well known from analytical models (e.g., Gudmundsson, 1987, 1999), and the same applies to general spreading (e.g., Gudmundsson, 2017). These stresses, in turn, may reach the tensile or shear strength of the rocks so as to generate tension fractures and/or normal faults. While regional doming, possibly combined with general spreading, very likely contributed to the observed fracture formation during and prior to the 2009 episode, the focus here is on the dyke-induced stresses and fracture formation. As indicated above, the particular aim is to understand how much of the fracture pattern could have been generated by dyke-induced stresses and how deep the dyke tip would have to be to generate the fractures. Following the established tradition, we use the word 'graben' for the general surface deformation of the 2009 episode. Later in the paper, however, we discuss in which way, if any, the actual deformation can be regarded as a classical graben structure.

4.1. Surface fractures

In addition to the uplift and general extension, there was considerable fracture development, particularly close to the centre of the uplift or dome. The fractures are of two main types: tension fractures (Figs. 5–6) and normal faults (Fig. 7). The tension fractures and normal faults that formed or became reactivated during the volcanotectonic episode reach cumulative lengths of up to 8 km (Figs. 4–6; cf. Baer and Hamiel, 2010; Pallister et al., 2010). While the rupture was still clearly seen during our field studies in 2015 and 2016, in the sedimentary

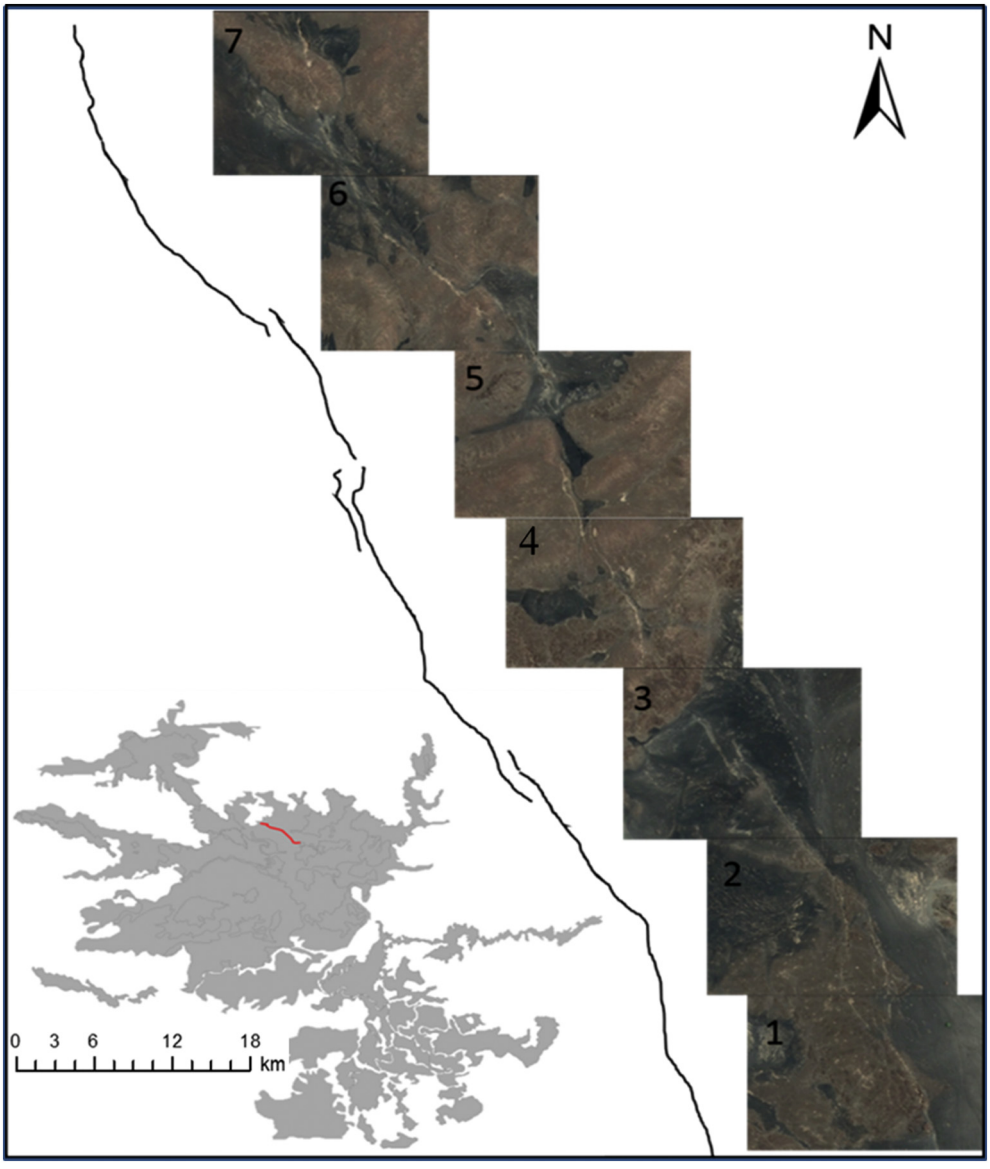

Fig. 4. Image and sketch of a part of one of the main faults on the western side of the fracture zone/graben formed during the 2009 episode. The total length of the fault part seen here is about 2.5 km. The inset in the left lower corner shows the length of the entire fault and its location within Harrat Lunayyir.

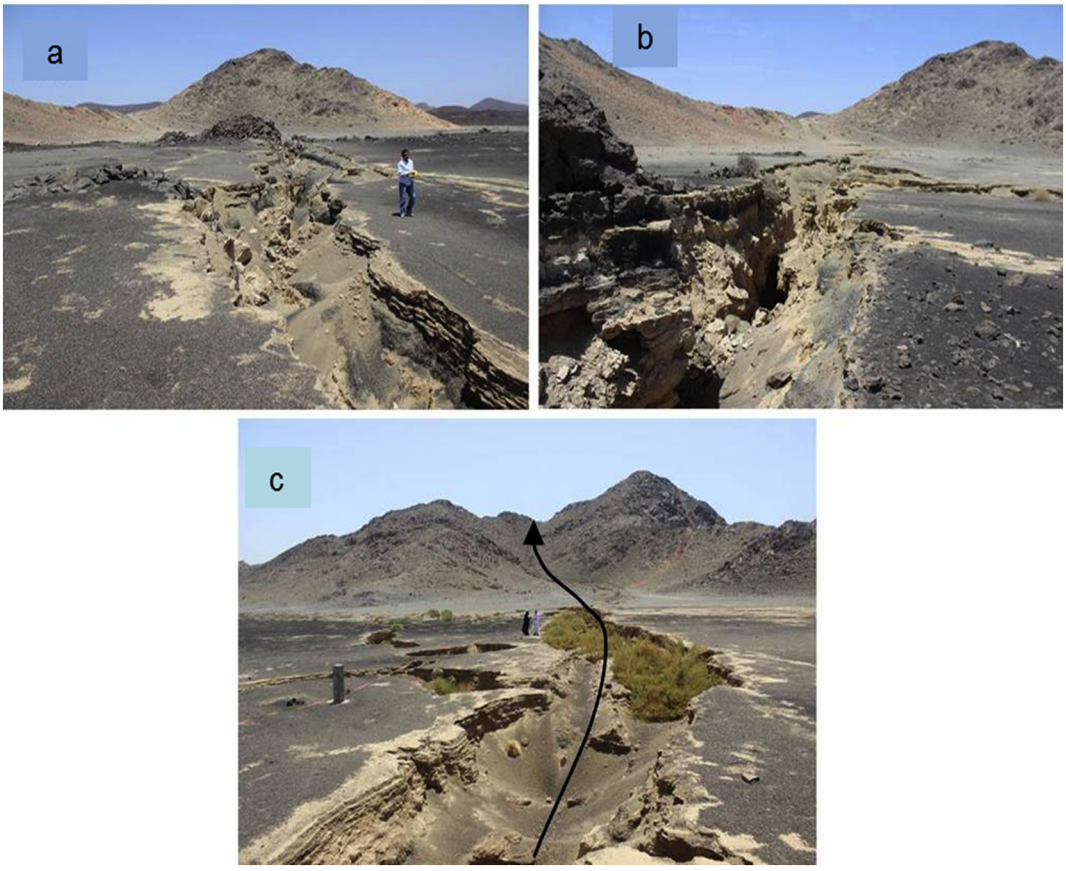

Fig. 5. Tension fractures at the western side of the fracture zone/graben, generated during the 2009 episode. a. The tension fracture cutting through pyroclastic and sedimentary rocks and lava at the surface, with irregular walls and considerable collapse. The person provides a scale. b. Close-up of part of the tension fracture in a. The maximum opening at the surface is a few metres, but partly due to collapsed walls c. Tension fracture dissecting pyroclastic and sedimentary rocks. The overall strike of the fracture, indicated schematically by an arrow, is north-northwest (cf. Fig. 8). The persons provide a scale.

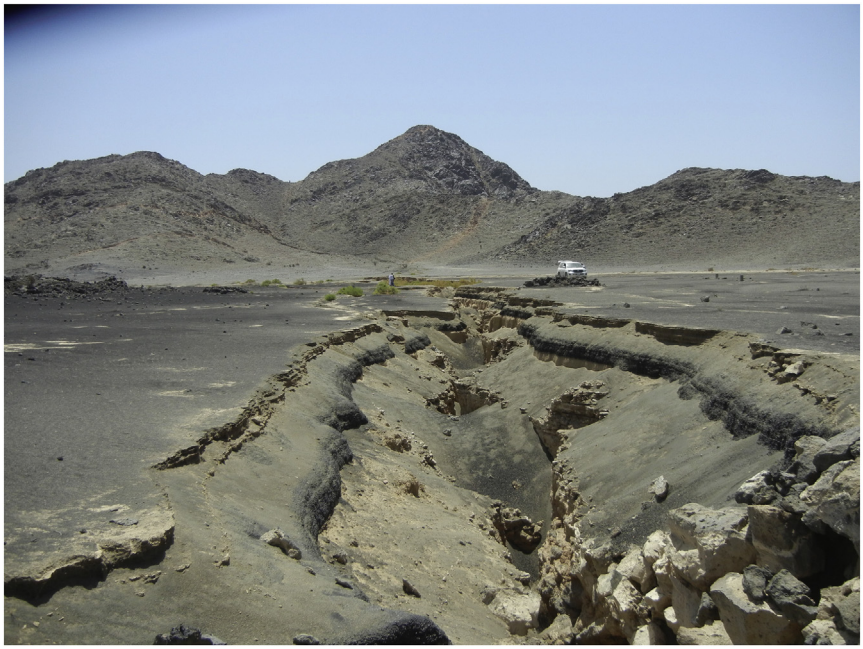

Fig. 6. Close-up of a northwest-striking tension fracture dissecting pyroclastic and sedimentary rocks at the western side of the fracture zone/graben generated during the 2009 episode. In these compliant layers, there is considerable collapse, so that opening at the surface appears much greater than the real opening (seen in the deepest exposed part of the fracture). The car and the person provide a scale.

Fig. 7. Mixed-mode fracture, an open normal fault, generated during the 2009 episode and dissecting sedimentary rocks at western side of the fracture zone/graben, generated during the 2009 episode. The trace of the fracture is curved, a common geometry of normal faults and tension fractures in mechanically weak rocks. The overall strike is northwest. Where the person is kneeling, the maximum throw is about 0.9 m while the opening is about 0.4 m. The people and the car provide a scale.

and tephra layers subsequent collapses and erosion make it difficult to estimate the openings accurately (Figs. 5–7). The field data, however, show that many of the fractures that constitute the rupture zone are pure tension fractures rather than normal faults (Figs. 5–6). Normal-fault displacement was, however, seen on some of the fractures (Fig. 7). The most accurately measured displacement in the field was made during the episode (in June 2009) by Pallister et al. (2010) where they measured a normal fault along part of its 8-km-long surface rupture. Their results show an open or gaping normal fault with a vertical displacement or throw of 0.78 m and opening (aperture) of 0.45 m. The fault wall is vertical (Fig. 7). This fault is thus clearly a mixed-mode (mode I and mode II) fault formed at the surface in absolute tension – similar to numerous mixed-mode fractures in the pahoehoe lava flows in the rift zone of Iceland (Gudmundsson, 2017). Other throw measurements at the western boundary of the area (graben) yield 0.6 m, whereas pure tension fractures at the eastern boundary show openings (apertures) of tens of centimetres (Jonsson, 2012). The tensional axes inferred from focal mechanism during the episode strike mostly ENE-WSW (Pallister et al., 2010) and thus roughly perpendicular to the tension fractures and open normal faults seen in the field (Figs. 4–7).

Our fracture studies focused primarily on the western part of the graben. What is most noticeable in the parts that we studied are large tension fractures (Figs. 5–6). While these have collapsed since their formation, it is clear from the deeper parts that the openings range from tens of centimetres to about one metre (Fig. 6). The fracture walls on either side are at the same elevation, which shows that there is no normal-fault component in these fractures, and there is also no evidence of strike-slip. The fractures are thus pure tension fractures or mode I cracks. We observed numerous tension fractures along the western side of the graben, but also some normal faults (Fig. 7). Jonsson (2012) confirmed that during the earthquake swarm the fractures formed on the eastern side of the graben were primarily tension fractures.

All the observations of surface fracturing during the 2009 volcanotectonic eposide thus show that tension fractures were the most common, but that there were also some small normal faults. The normal faults were mostly confined to the western side of the graben whereas tension fractures formed both on the western and eastern sides. The surface deformation, however, was not confined to the graben boundaries since many fractures formed inside the graben (Fig. 8).

Clearly, the detailed fracture pattern in Fig. 8a does not show a great resemblance to that in Fig. 8b. In Fig. 8a the white lines show the 'InSAR-determined faults', whereas the fracture pattern in Fig. 8b was derived from 'differential coherence maps', with black lines showing incoherent lineaments for the entire rifting episode and white lines for the period 27 May to 1 July 2009 (Baer and Hamiel, 2010). In Fig. 8b there are two main sets of fractures: a set of NW-striking fractures found at both sides of the graben, and then a set of roughly N-striking fractures, found primarily at the eastern side of the graben – although one such fracture occurs at the north end of the fracture set at the western side of the graben. The overall strike of the NW-set along the western side is roughly 315° whereas the common general strike of the N-striking fractures on the eastern side is about 352°. Thus, the angle between the two sets is about 37°. However, when individual fractures shown on Fig. 8b are measured, they range in strike from about 305° (northwest) to about 25° (north-northeast), yielding a maximum acute angle between the fractures of some 80°. Since the fractures are all thought to have formed during the 2009 episode, it is clear that they must have been subject to widely different local stresses, part of which may relate to the inferred dyke emplacement during the episode.

4.2. Comparison of earthquake swarms in 2007 and 2009

The general interpretation of the 2009 earthquake swarm is that it was, partly at least, triggered by dyke propagation (Baer and Hamiel, 2010; Pallister et al., 2010; Hansen et al., 2013a, 2013b; Xu et al., 2016). While no earthquake migration was observed, the interpretation that at least part of the swarm was associated with a dyke that failed to reach the surface – that is, became arrested – is plausible and one that we take as a basis for our analysis.

We interpret the data provided in the cited papers as follows:

- The seismic swarm in October 2007 may be seen as a precursor to the main swarm associated with subsequent dyke emplacement in April–July 2009. We interpret the precursor so that a deep-seated reservoir was subject to inflation and possibly rupture. During inflation of a reservoir, reactivation of fractures, particularly faults, in its roof would normally generate earthquakes.
- There are, however, remarkable differences between the October 2007 swarm and the April–July 2009 swarm. These differences

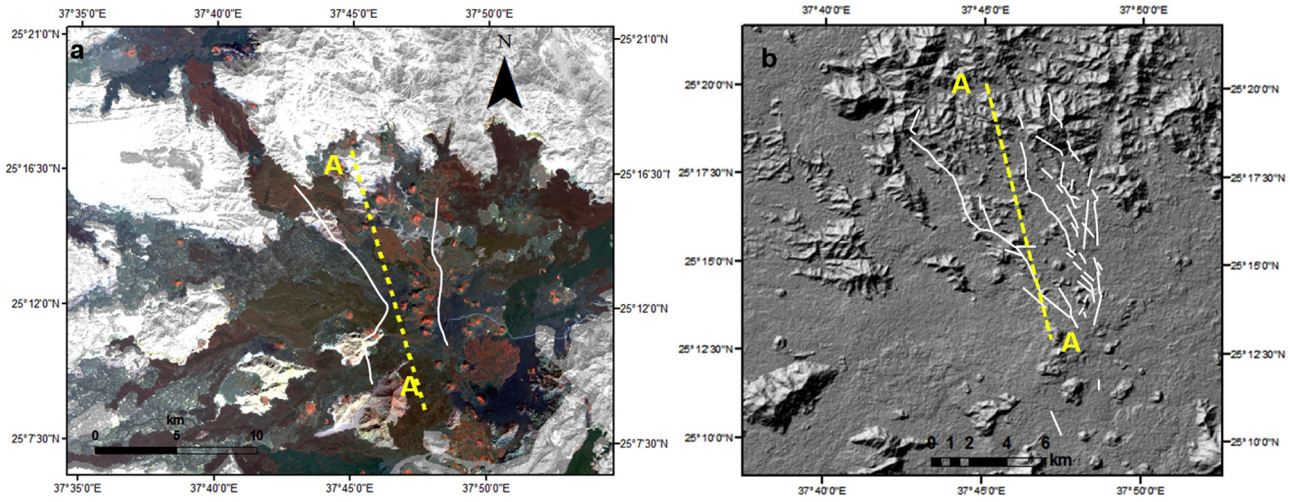

Fig. 8. Main fractures generated or reactivated during the 2009 episode in relation to the projected strike and strike dimension (length) of the associated dyke. a. The principal active/new fractures during the 2009 episode in relation to the surface projection of the inferred dyke, broken line A to A′, and the lava field of Harrat Lunayyir. Notice the difference in strike between the dyke and the fractures, particularly the main fractures (tension fractures and normal faults) at the western margin of the fracture zone/graben. b. Detailed map of the fracture pattern generated during the 2009 episode. Notice the variety in fracture strike in comparison with the inferred dyke strike and the broad system of (tension) fractures at the eastern side of the fracture zone/graben. In this interpretation, the projection of the dyke dissects some of the fractures at the western side of the fracture zone/graben.
Data from Baer and Hamiel (2010).

include a different location (including depth), number of earthquakes, and surface effects. (a) The October 2007 swarm generated only about 500 recorded earthquakes and was mostly some 15 km to the south-east of the April–July 2009 swarm which generated about 30,000 recorded earthquakes. (b) The October 2007 swarm was generally much deeper than the April–July 2009 swarm. In particular, the earthquakes of the October 2007 swarm were mostly located deeper than about 10 km, and many reached depths of 25–30 km. (c) By contrast, although the deepest earthquakes of the April–July 2009 swarm reach depths of 25–30 km, the great majority of the earthquakes are shallower than 20 km, and very many occurred at depths between 10 km and the surface. (d) In contrast to the April–July 2009 swarm, there was no recorded surface deformation during the October 2007 swarm.

- There are also certain similarities between the swarms. One is that they occur in basically the same area, even if not at the same location. Another is that both can be interpreted as being partly associated with apparently steep-dipping structures (between about 55° and 65°) to the east (Xu et al., 2016, Fig. 2). However, for both swarms this apparent dip may be an illusion because of the way the earthquakes concentrate in certain layers. In case of the October 2007 swarm, the dip can, in fact, be interpreted in various ways, and there is clear concentration of earthquakes at depths of about 10–15 km, 20–24 km, and 27–30 km. As for the April–July 2009 swarm, similar concentrations of earthquakes occur at depths of 2–8 km (although many earthquakes reach the surface), and 12–17 km (although some earthquakes occur at depths of 20–30 km).
- The concentration of earthquakes at certain depth intervals in the crust is very common and relates normally to stiff (high-Young's modulus) units or layers. Thus, during loading of the crust, the stiff units or layers concentrate much more stress (either in tension or compression) than the more compliant or softer layers. The lateral spread in earthquakes in the uppermost part of the crust during the April–July 2009 episode and 10–15 km and 27–30 km depth in the October 2007 episode may thus be attributable to the crustal layers or units at these depths being stiffer than adjacent units. Another interpretation is that some of the laterally spread earthquakes may be located in the roof of a magma reservoir – as is commonly observed during unrest and dyke injections (e.g., Becerril et al., 2013). But in the present cases, neither swarm has a distribution in space that is easily interpreted as roof failure due to magma-pressure changes (inflation) of a reservoir. We therefore think it is more likely that many of the earthquakes, particularly in the April–July 2009 swarm, relate to dyke emplacement.

4.3. Dyke emplacement

The data on the October 2007 swarm are too limited to allow us to decide whether or not there was any dyke emplacement. But contrast, the data, presented above and below, suggests that there was dyke emplacement during the April–July 2009 earthquake swarm. The focus here is on the 2009 swarm.

A swarm of earthquakes of this kind is typically associated with dyke emplacement. It is then the magmatic pressure within the dyke that triggers many of the fault-slips that generate the earthquakes. Focal mechanisms of the larger events ($M > 4$) indicate mostly normal faulting with some strike-slip components. This is in contrast to the earthquakes generated during the dyke emplacement in Bardarbunga in Iceland 2014 where most of the earthquakes were strike-slip (Agustsdottir et al., 2016). Strike-slip and some reverse slip (Gudmundsson et al., 2008) are expected in the walls of a dyke, since they become subject to horizontal compressive stress due to the magmatic overpressure of the dyke, which in turn induces shear stresses on some of the existing fractures, particularly joints. Since many of the earthquakes during the 2009 swarm, by contrast, seem to be associated with normal faulting, this may indicate two basic processes:

a. Much of the faulting may occur ahead of an upward-propagating dyke tip. In the 'process zone' around the dyke tip extension fracturing and normal faulting is common (Gudmundsson, 2011a). In this zone, normal-fault earthquakes are commonly generated by slips on existing fractures, many of which are cooling joints in the lava pile. Some dykes also use existing, steeply dipping normal faults as parts of their paths, in which case slip on an existing normal fault would be facilitated by the dyke-magma entering the fault plane (Gudmundsson, 2011a). The macroscopic dyke-fracture itself, however, is primarily an extension fracture (mode I crack) and thus does not generate classical double-couple earthquakes.
b. Part of the fault slip may be generated on existing normal faults, presumably buried by younger layers before the 2009 episode and thus

not seen earlier in the field or on aerial photographs. When the earthquake swarm is used to infer the dip – irrespective of the points discussed above as to concentration of earthquake in particular layers or units – then the overall dip would be about 65°E. It is possible that many of the earthquakes were associated with the western boundary faults of the graben. However, in case slip on the fault was triggered by the magmatic overpressure of the dyke, one would rather expect strike-slip or reverse faulting on the main boundary fault, as is commonly inferred and observed where dyke enter existing grabens (Gudmundsson and Loetveit, 2005; Gudmundsson et al., 2008).

Normal faulting and dyke emplacement are the most common large-scale processes associated with rifting worldwide. This is understandable since both are attributable to extension, that is, to the relative tension which dominates in rift zones. The processes may operate simultaneously; that is to say, dyke injection and normal faulting may both occur without necessarily one triggering the other. Normal faulting is common without dyke emplacement, such as in sedimentary basins, and most dykes become arrested without generating any large-scale normal faults or grabens. In fact, field studies in Iceland show clearly that where normal faults are common in parts of palaeo-rift zones, dykes are comparatively rare, and vice versa (Forslund and Gudmundsson, 1991). This is because there is essentially constant spreading rate in rift zones, so that if much of the spreading is accommodated by normal faulting then less will be accommodated by dykes, and vice versa. The general rule is, however, that the contribution of dykes to the overall spreading at plate boundaries everywhere varies positively with increasing crustal depth (e.g., Gudmundsson, 2002).

As indicated above, one of the unsolved issues with the 2009 episode is whether or not the inferred dip of the earthquake swarm is real or an artefact. We have already explained how it may be an artefact due to stress concentrations in layers and units of different stiffness. If, however, the dip is real and about 65°, then we should be able to relate the dip to the two main processes discussed above. For the second process, there is no problem in doing so since a dip of about 65° is a common dip of normal faults in continental areas.

For the first process, however, we would have to explain why the dyke triggering much of the normal faulting did not follow a vertical path but rather path dipping 65°. For a magma reservoir of either a sill-like or dome-like geometry, as appear to be the most common shapes (Gudmundsson, 2012, 2017), horizontal tension related to rifting would normally result in subvertical trajectories of the maximum principal compressive stress, σ_1. As is well known, dyke propagation paths tend to follow the trajectories of σ_1 and, thereby, being perpendicular to the trajectories of the minimum compressive (maximum tensile) principal stress, σ_3. However, if the main loading is internal magmatic excess pressure, then the trajectories of σ_1 become generally curved away from the reservoir, and may dip by as much as 65°, particularly above and beyond the marginal parts of the reservoir (Gudmundsson, 2002).

It is thus possible to explain the dip of the 2009 earthquake swarm in various ways. Not only as a result of crustal layering and variation in local stresses – which may certainly play a role and contribute to the dip being, partly at least, and artefact – but also as a direct consequence of either a major normal fault (the western boundary fault of the graben) or a dyke injected from the marginal parts of the source reservoir whose loading is then primarily internal magmatic excess pressure. In what follows, we assume that the earthquake swarm was largely, or primarily, the result of dyke injection and propagation towards the surface. The focus in the models is on understanding better the potential surface effects of such a dyke and trying to estimate as well as may be the likely depth of the tip of the dyke at the time of arrest. This latter is of very great importance when assessing the hazard in the area, and has implications for hazard and risk assessments in volcanic areas in general.

5. Dyke arrest

Most dykes become arrested. Hundreds of arrested dykes have been observed, and many tips of such dykes studied in detail. Field studies show that while some dykes terminate within layers, most dykes become arrested at contacts between rock layers or units; in particular, at contacts between mechanically dissimilar layers (Figs. 9–12; Gudmundsson, 2002, 2003). Some of these dykes become deflected into sills (e.g. Tibaldi and Pasquarè, 2008; Casagli et al., 2009; Gudmundsson, 2011b; Barnett and Gudmundsson, 2014; Tibaldi, 2015), whereas others become arrested on meeting the contact (Figs. 9–12).

There are three principal mechanisms by which dykes (and other extension fractures or mode I cracks) become arrested: (1) Gook-Cordon delamination, (2) stress barrier, and (3) elastic mismatch. All the mechanisms may operate simultaneously, but the Gook-Cordon delamination is most effective at shallow crustal depths. The other two mechanisms can operate at any depth. A detailed description of these mechanisms, including appropriate references, is given by Gudmundsson (2011a, 2011b), so only a brief discussion is provided here.

The Cook-Gordon delamination mechanism implies that the contact that arrests the dyke is mechanically weak. By this we mean that the tensile strength (and, by implication, the shear strength also, because

Fig. 9. Basaltic dyke arrested in a vertical section in Tenerife (Canary Islands). The host rock by comparatively soft (compliant) pyroclastic rock. The dyke becomes arrested at its contact with much stiffer (higher Young's modulus) inclined sheet, as forecasted by the elastic mismatch mechanism of dyke arrest. The maximum thickness of the dyke is about 0.8 m. There are no dyke-induced extension fractures or faults at the tip. The person provides a scale.

Fig. 10. Subvertical basaltic dyke arrested in a vertical section in Tenerife. The main host rock is a pyroclastic layer (red-pink) on top of which is a basaltic lava flow (black-blue). The dyke becomes arrested roughly at the contact between the pyroclastic layer and the lava flow. More specifically, on meeting the contact, the dyke abruptly becomes much thinner (its maximum thickness is 0.26 m at the bottom of the 3.7 m tall exposure) and tapers away to its tip. The length of the yellow steel tape parallel with the lowermost right margin of the dyke is 1 m. There are no dyke-induced extension fractures or faults at the tip. The arrest mechanism here is most likely a stress barrier.

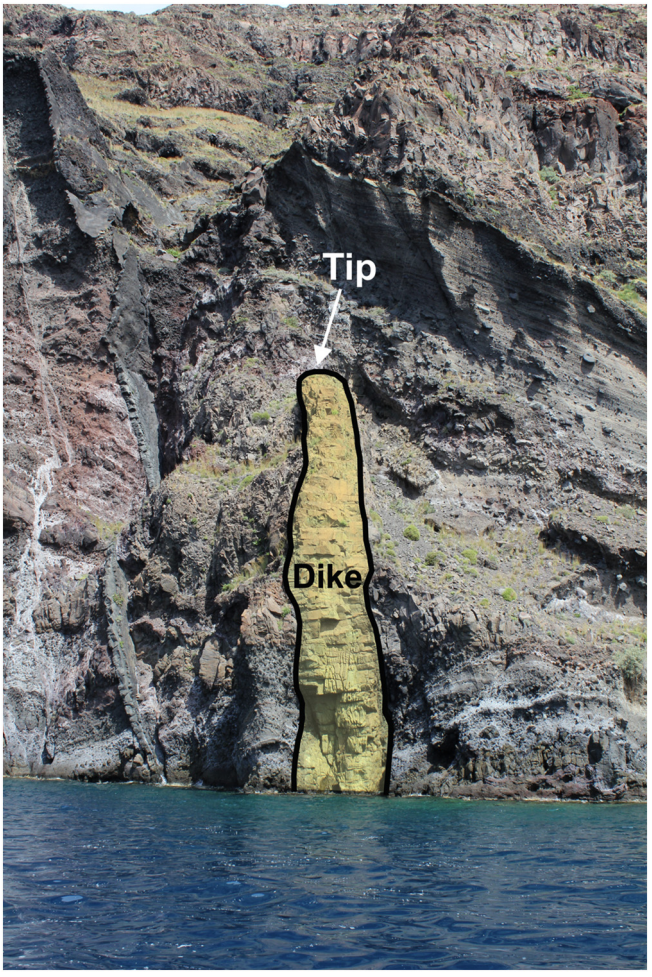

Fig. 11. Arrested dyke in the caldera wall of Santorini (Greece). The dyke is arrested at the contact between layers of pyroclastic rock. The grain size of the layers changes abruptly at the contact, and thereby their mechanical properties. The maximum dyke thickness at sea level is about 2 m. The arrest mechanism here is most likely elastic mismatch.

these are related) is low. Around the dyke tip there is a tensile stress field. The highest tensile stress is orientated dyke-perpendicular, and operates to generate the dyke fracture. But there is also a high dyke-parallel tensile stress which, for a contact with a low tensile strength, may open up the contact when the dyke tip is close to it. Opening of a contact is observed in many numerical models of dyke emplacement (Gudmundsson, 2003, 2011a) and is likely to occur in nature. When the dyke tip finally reaches the open contact, the tip then becomes either deflected along the contact to form sill or, alternatively, stops altogether, that is, becomes arrested.

Stress barrier is a layer or unit where the local stress field is unfavourable for a particular type of fracture propagation. For a vertical dyke, a stress barrier is a layer/unit where the compressive stress perpendicular to the projection of the dyke path/plane up into the layer/unit is either the maximum or the intermediate principal compressive stress, that is, σ_1 or σ_2, both being compressive. Since a dyke is an extension fracture, a mode I crack, it propagates along a path whose direction is parallel with σ_1 and σ_2 and perpendicular to the minimum compressive (maximum tensile) principal stress σ_3. Thus, once a vertical dyke tip approaches and tries to enter a layer where σ_1 and σ_2 are horizontal and σ_3 thus vertical, the dyke must either deflect into a sill or become arrested altogether. Stress barriers form in various ways, but perhaps the most common in volcanic rift zones is that earlier dyke injections have resulted in a 90° flip of the principal stresses because of their

Fig. 12. Arrested basaltic dyke in the lava pile of East Iceland. At the base of the photograph the dyke is about 2 m thick, but gradually thins towards its tip. The host rock is basaltic lava flows with scoria and soil layers (red) in-between. The arrest mechanism here is most likely a stress barrier, located in the layers above the tip of the dyke. On meeting a stress barrier, a dyke commonly thins before either stopping its propagation altogether (as here) or deflecting into a sill.

magmatic overpressure which compresses the surrounding rock horizontally. For example, consider a dyke with an overpressure of 15 MPa propagating through a layer where, originally, the principal stresses are $\sigma_1 = 50$ MPa, $\sigma_2 = 45$ MPa, and $\sigma_3 = 40$ MPa. Following the dyke emplacement the horizontal stress close to the dyke, initially $\sigma_3 = 40$ MPa, becomes $40 + 15 = 55$ MPa, and thus the largest compressive stress, that is, σ_1. Thereby, the layer, temporarily, becomes a stress barriers to subsequent vertical dyke propagation. Given that the crustal segment hosting the layer constitutes a part of a rift zone, the high horizontal stress of 55 MPa is eventually relaxed (through spreading) and the state of stress flips back to the original. Slip on the boundary faults of a graben may also generate stress barriers to dyke propagation (Gudmundsson, 2011a).

Elastic mismatch is a name given to the mechanism where deflection and arrest are primarily controlled by the contrast – the mismatch – in elastic properties of the layers on either side of a contact, in relation to the elastic properties of the contact itself (He and Hutchinson, 1989; Hutchinson, 1996; cf. Gudmundsson, 2011a, 2011b). More specifically, the probability of a dyke becoming deflected into a sill or arrested at a contact is related to the Dundurs elastic extensional mismatch parameter α_D (He and Hutchinson, 1989; Hutchinson, 1996):

$$\alpha_D = \frac{E_1 - E_2}{E_1 + E_2} \tag{1}$$

where E is the plane-strain extensional Young's modulus (stiffness). Arrest or deflection of a dyke, or an extension (mode I) fracture in general, on meeting a contact is encouraged when the Young's modulus of the layer hosting the fracture (E_2) and below the contact is lower than that of the layer above the contact (E_1). The probability of dyke arrest at a contact varies positively with increasing elastic mismatch or difference between E_1 and E_2, that is, with increasing Dundurs parameter (Gudmundsson, 2011a, 2011b). More specifically, arrest of a dyke or its deflection into a sill is more likely when the layer above the contact (E_1) has a higher Young's modulus than the layer below the contact (E_2).

While field observations show that most dykes are arrested at layer contacts (Figs. 9–11) and other discontinuities such as faults, some dyke simply taper away in layers presumably where the overpressure gradually decreases. Commonly, this happens when the dyke tip approaches a contact where the stress field is unfavourable; for example, a contact with a layer that acts as a stress barrier (Fig. 12). Part of the reason for dykes tapering away in vertical sections is decrease in magmatic overpressure or driving pressure for a dyke propagating through rocks of an average density less than that of the dyke magma. This is particularly the case for basaltic dykes propagating through low-density pyroclastic and sedimentary rocks. The decrease in magmatic overpressure is then due to negative buoyancy.

Magmatic overpressure in a dyke is given by (Gudmundsson, 2011a):

$$p_o = p_e + (\rho_r - \rho_m)gh + \sigma_d \tag{2}$$

where ρ_r is the average host-rock density, ρ_m is the average magma density, g is acceleration due to gravity, h is the dip dimension of the dyke, and σ_d is the differential stress (the difference between the maximum (σ_1) and the minimum (σ_3) principal stress) in the host rock where the dyke is studied. The second term on the right-hand side of Eq. (2) is the buoyancy term. In the uppermost 1–3 km of the crust in almost all volcanic areas, the average rock density is 2500–2600 kg m^{-3} whereas a basaltic magma may have density between 2650 and 2800 kg m^{-3}. It follows that, in the uppermost part of the crust, buoyancy for basaltic magmas is commonly potentially negative. During ascent of magma, there is normally gas expansion which makes the magma lighter, that is, of less density. While gas expansion and density reduction is common in acid magma to depths of many kilometres (Gonnermann and Manga, 2013), much of the gas exsolution in basaltic magma takes place at very shallow depths. In Hawaii, for example, gas exsolution in basaltic magmas occurs primarily in the uppermost few hundred metres of the feeder/conduit (Greenland et al., 1985, 1988). Similarly, direct observations of dykes, sills, and inclined sheets in deeply eroded lava piles and central volcanoes show only small and rather infrequent vesicles (formed by expanding gas) at depths exceeding several hundred below the original surface of the volcanic zone/central volcano. Some feeder-dykes, by contrast, contain large vesicles close to the surface (Galindo and Gudmundsson, 2012).

Thus, density decrease of basaltic magma due to gas exsolution is most likely to occur very close to the surface, mostly in feeder-dykes, and does thus normally not much affect the potential negative buoyancy term in Eq. (2). It follows that, commonly, for basaltic dykes injected from shallow magma chambers, the only driving pressure in Eq. (2) is the excess pressure p_e in the chamber. That pressure is roughly equal to the tensile strength of the walls or, normally, the roof of the magma chamber. The tensile strength of most rocks is between 0.5 and 9 MPa, the most common values being 2–4 MPa. Thus, the excess pressure at the time of magma-chamber rupture and dyke injection may, depending on the variation in tensile strength, vary by a factor of 2–3, and very rarely by a factor of 6–9.

When the only driving pressure of basaltic dykes injected from many shallow magma chambers is the excess pressure, of the order of megapascals, the driving pressure or overpressure gradually decreases as the dyke propagates towards the surface. The decrease in overpressure is then partly because of decline in the excess pressure in the source chamber as magma flows out of it and up the dyke. This decline may be described as follows (Gudmundsson, 2016):

$$p(t) = p_e\left(1 - e^{-\left(\frac{V_{er}}{Qt} - 1\right)}\right) \tag{3}$$

where $p(t)$ is the excess-pressure variation in the magma chamber as a function of time, p_e is, as before, the excess pressure at the time of magma-chamber rupture and dyke injection (roughly equal to the in-situ tensile strength), V_{er} is the dyke volume (or, in case of an eruption, the combined dyke and eruptive volume), and Qt is the magma volume (in m^3) that flows out of the chamber during the time interval t. Clearly, the exponent has the units of m^3/m^3 and is thus dimensionless. Eq. (3) indicates an exponential decrease in excess pressure in the source chamber during the eruption and/or dyke injection until the excess pressure approaches zero, that is, $p(t) \rightarrow 0$, when the bottom of the feeder closes, and the magma flow out of the chamber comes to an end.

A dyke injected from a shallow magma chamber under a very low excess magmatic pressure, say 1 MPa, and propagating through low-density crustal rocks may thus stop on its propagation path simply because the overpressure declines to zero. This would apply primarily if the magma chamber is (a) comparatively small, say with a volume of 20–30 km^3 or less and (b) very shallow, say with a roof at a depth of 1–2 km. Many dykes and, in particular, inclined sheets are seen to taper away in dense sheet swarms associated with such shallow chambers in Iceland and in ophiolites (e.g., Gudmundsson, 2002).

Several other mechanisms suggested for dyke arrest are, based on field observations and theoretical studies, likely to be of minor importance. Thus, it has been suggested that down-bending of the crustal segment on which a volcanic edifice rests generates local stresses that may arrest dykes (Rivalta et al., 2015). There is plenty of evidence of down-bending or sagging of crustal layers in the volcanic zones of Iceland, below volcanic edifices and in the volcanic zones in general, with no known effects as to dyke arrest. Similarly, down-bending of the lithosphere below large volcanic edifices such as in Hawaii has no known effects as to dyke arrest. If down-bending of crustal layers due to piling up of new eruptive material was a major factor here in arresting dykes, then no large edifices could form in the first place here. Generally, volcano spreading and divergent-plate boundary spreading counters any such effects and the magma chambers stay in close to lithostatic

equilibrium with the host rock through most of their lifetimes (except during unrest periods). An edifice takes thousands or tens of thousands of years to form, and the potential down-bending due to the load of each lava flow/pyroclastic layer is normally so small as to have hardly any stress effects that could result in dyke arrest.

Similarly, it is commonly suggested that cooling or solidification of the dyke results in its arrest (e.g. Rivalta et al., 2015). However, for dykes injected from shallow magma chambers the rate of propagation is commonly 0.1–1 m s^{-1} and they would normally reach the surface, in case they were feeders, before any significant cooling would take place. Furthermore, even if solidification of the dyke tip would occur – as, for example, if the tip would meet significant amount of groundwater – the solidified tip has the same tensile strength, or slightly lower, than that of the host rock. Thus, so long as there is any magmatic overpressure in the dyke, a temporarily solidified tip should not stop the propagation any more than the host rock would.

Based on the considerations above, we conclude that dyke arrest is primarily controlled by mechanical layering and local stresses along the potential path of the dyke. Given that the 2009 dyke at Harrat Lunayyir most likely generated tension fractures at the surface, and yet became arrested, mechanical layering is the most likely explanation for the dyke's arrest. Which brings us to the surface deformation associated with the dyke emplacement, in particular the formation and depth of the tension fractures.

6. Tension fractures and normal faults

The surface deformation associated with the 2009 dyke emplacement is primarily reflected in the formation or reactivation of tension fractures and normal faults (Figs. 4–8). Tension fractures can only reach a certain depth; if they try to propagate to greater depths they must change into normal faults. This theoretical result follows from Griffith's crack theory, and is supported by actual field observations in active rift zones and fossil rift zones (Gudmundsson, 2011a, 2017).

The two-dimensional Griffith criterion for fracture initiation in the tensile regime is given by:

$$\text{If } \sigma_1 < -3\sigma_3 \text{ then } \sigma_3 = -T_0 \tag{4}$$

Here, σ_1 is the maximum principal compressive stress, σ_3 is the minimum principal compressive stress, and T_0 is the tensile strength of the host rock. On substituting $-T_0$ for σ_3 in the inequality (4), we obtain:

$$\sigma_1 - \sigma_3 < 4T_0 \tag{5}$$

It follows from inequality (5) that the stress difference for the failure criterion in the tensile regime to apply cannot exceed $4T_0$. Using the following equation:

$$\sigma_1 = \rho_r g d \tag{6}$$

where ρ_r is the host-rock density, g is the acceleration due to gravity, and d is the fracture depth (dip dimension), the maximum depth d_{max} that a large-scale tension fracture can reach (by definition, in the absence of internal fluid overpressure) is

$$d_{\max} = \frac{3T_0}{\rho_r g} \tag{7}$$

If the tension fracture propagates to greater depth than given by Eq. (7), it must change into a normal fault.

As an example, if the average density of the uppermost part of the crust of 2500 kg m^{-3}, as is common in continental areas, the maximum depth of the tension fractures in Figs. 4 and 5 (other tension fractures are shown by Jonsson, 2012) ranges between about 60 m (for the lowest possible in-situ tensile strength of 0.5 MPa) and 1100 m (for the highest possible tensile strength of 9 MPa). These are extreme tensile-strength values, however. Most commonly, the in-situ tensile strengths of rocks, based on direct measurements through hydraulic fracturing, are 2–3 MPa (Gudmundsson, 2011a). These values are also similar to those obtained by theoretical strain considerations for the rocks in the present area, namely 1–3 MPa, by Jonsson (2012). Thus, using 2–3 MPa as the tensile strength, the most likely maximum depths of the tension fractures in the area would be between 244 and 367 m.

It follows that the absolute tension during the 2009 episode is unlikely to have reached greater depths than about 370 m. Given the uncertainty in the values used, we could set this upper limit for the absolute tension at a depth of about 400 m. The tension fractures may, of course, be much shallower than this; but they very unlikely to be deeper. These analytical results also mean that significant tensile stress must be at the surface; more specifically the tensile stress that the surface must be at least 2 MPa, if we assume that 2 MPa is the in-situ tensile strength. The theoretical tensile stress, however, should normally be expected to exceed the in-situ tensile strength for fracture formation and must be maintained to some depth – at least some tens of metres and, preferably, hundreds of metres so as to generate the tension fractures. Thus, if the dyke-induced tensile stress at the surface is only 2–3 MPa and diminishes at a shallow depth, such a dyke is unlikely to have generated the tension fractures at the surface. And it is even less likely to have triggered slip on existing, or the formation of new, normal faults. While discussing the numerical results below, we assume that the tensile stresses at the surface, for fracture initiation at the surface, must have, theoretically, reached several mega-pascals. As we shall also see in the numerical models below, there are further constraints on the mechanics of fracture formation, if triggered by dyke emplacement, in that while normal faulting and tension fractures occurred at the western boundary of the 'graben', only tension fractures were generated at the eastern boundary during the 2009 episode.

7. Numerical models

We used the finite-element software Comsol Multiphasic (www.comsol.com) for a general analysis of the local stresses associated with arrested dykes, with application to the inferred arrested 2009 dyke. All the models are fastened in the corners, as indicated by crosses (Fig. 13a), so as to avoid rigid-body rotation and translation. In all the models the only loading is internal magmatic overpressure (driving pressure) of 6 MPa (cf. Eq. (2)). This value is within the range of a typical in-situ tensile strength of rocks (Gudmundsson, 2011a). We do not use a higher overpressure because we assume the dyke to be basaltic, so that, in a continental crust like here, the buoyancy term may not add much overpressure to excess pressure at the time of magma-chamber or reservoir rupture (Eq. (2)). In all the models, the lower tip (bottom) of the dyke is at the depth of about 10 km, whereas the upper tip or top is at depths of 0.3, 0.5, and 1 km below the surface. As indicated above the dip dimension may be 15–20 km but for the purpose of modelling effects of shallow layering on surface stresses, the dip dimension used here is appropriate.

In the first models, the crust has the same uniform properties. This is shown by all the indicated layers having the same Young's modulus (here 40 GPa). This means that the first models are elastic half-space models, as are still the most commonly used to model surface stresses and deformation associated with volcanic unrest periods (e.g., Dzurisin, 2006; Segall, 2010). For the models presented in this paper, all the layers and units have the same Poisson's ratio, namely 0.25, which is the most common ratio for rocks (Gudmundsson, 2011a). Variations in Poisson's ratio of rocks are generally very small (normally by a factor of 2 or less) so as to be negligible in comparison with the variation in Young's modulus or stiffness; the latter may easily vary by 2 orders of a magnitude in any volcanic zone/volcanic edifice, and sometimes by 3 orders of a magnitude. In later models, we have realistic layering with Young's modulus in different layers ranging from 1 GPa, for soft layers, to 40 GPa for stiff layers. This range is presumably

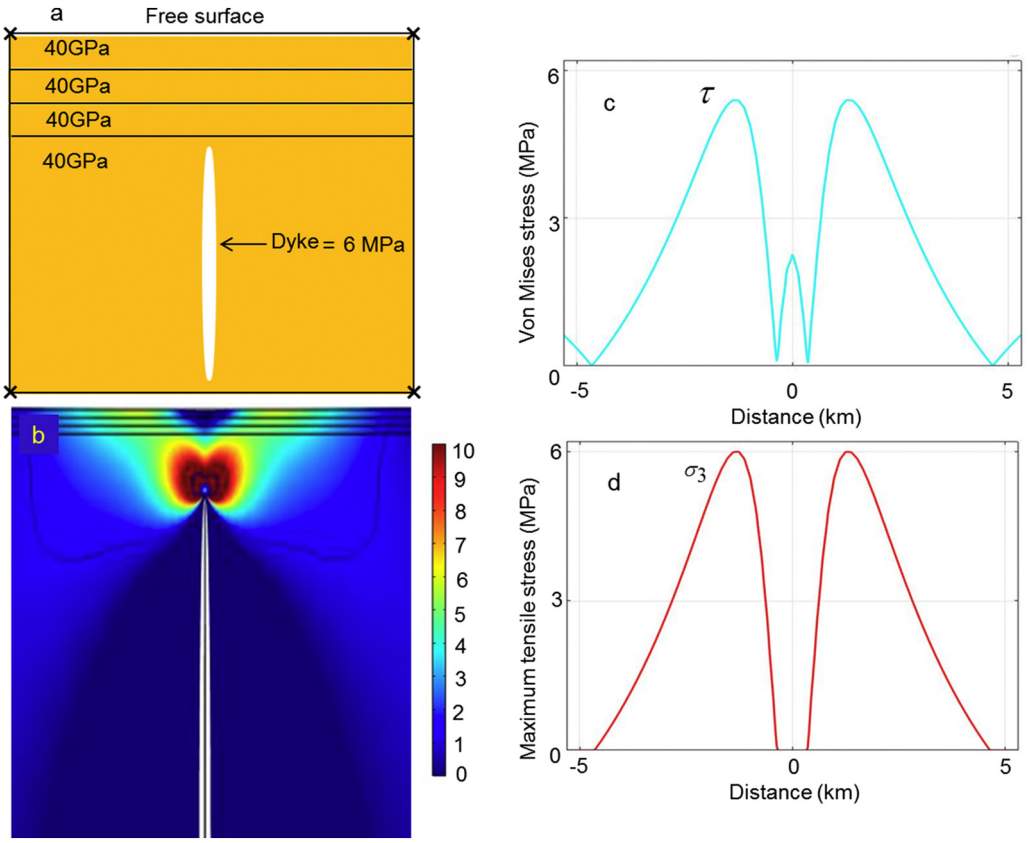

Fig. 13. Numerical model of a dyke arrested with a tip at the depth of 1000 m below the Earth's surface. The magmatic overpressure is 6 MPa and Poisson's ratio of all the rock layers is 0.25. Each of the 3 top layers is 100 m thick. All the 3 top layers, as well as the main rock unit hosting the dyke, have the same Young's modulus of 40 GPa. Thus, this is effectively an elastic half-space model. a. Schematic setup of the model. The thickness of the layers and the height of the dyke are not to scale. b. Maximum principal tensile stress, σ_3, in mega-pascals. The stresses shown here, and in subsequent models, range from 0 (blue) to 10 MPa (red). This range (0–10 MPa) is chosen so because the maximum in-situ tensile strength of crustal rocks is 9 MPa, and mostly 5–6 MPa, so that tensile stresses above 10 MPa can normally not be reached in the crust (Gudmundsson, 2011a). The dip dimension (height) of the dike in all the models is between 9 and 10 km. c. von Mises shear stress at the Earth's surface. d. Maximum principal tensile stress, σ_3, at the Earth's surface.

smaller than the actual range in crustal segments such as that hosting Harrat Lunayyir, but serves the purpose of illustrating the effects of reasonable layering on surface stresses and likely fracture formation induced by arrested dykes such as the one in 2009.

In the layered models, each of the layers that constitute the uppermost part of the crust is 100 m thick. This thickness remains constant in all the models. Also, in all the models the lowermost layer or unit hosts most or all of the dyke. (Depending on how shallow the dyke tip is, the top part of the dyke penetrates some of the shallow layers in some of the models.) Young's modulus of these shallow layers derives from seismic data, where we calculate the dynamic Young's modulus based on the velocities of the seismic waves (Jaeger and Cook, 1979). The dynamic moduli are 27 GPa for two of the layers and 17 GPa for the surface layer. The layer or unit hosting (most of) the dyke has a dynamic Young's modulus of 40 GPa. These values are primarily based on seismic velocities in Harrat Lunayyir, but are within the range of laboratory determined Young's moduli for granites and other typical continental rocks (Gudmundsson, 2011a) and thus reflect more general conditions. In later layered models we use still more realistic layering, where comparatively soft layers, with Young's modulus of 1–3 GPa, form part of the crustal segment. The layer thickness of 100 m is somewhat arbitrary in that it would generally reflect 'seismic layers', that is, groups of layers with similar seismic/mechanical properties. Some sedimentary layers and some lava flows, such as pahoehoe, may reach 100 m thickness, but here this thickness should be interpreted as mechanical/seismic rather than lithological.

In all the models, we show the layering (and lack of layering in the first models) to illustrate the assumed general structure of the crust. The layers are shown in the a-part of each model figure, which also gives the Young's modulus of each layer. The location of the dyke tip, however, is not changed in the a-parts of the figures; the dyke is there always shown at the same location because the main aim of the a-parts is to show the layering. The b-parts of the figures show the exact location of the dyke tip, which in some of the later models penetrates the lowermost of the 3–4 top layers.

The early models have 3 layers above the thick layer or unit hosting (most of) the dyke. In the later models, however, we have added one layer which is white in all the models and with a Young's modulus or stiffness of 1 GPa. In-situ Young's modulus of 1 GPa is common among many compliant pyroclastic and sedimentary rocks (Gudmundsson, 2011a). For example, many soil, sediment, and scoria layers between lava flows have similar or lower Young's moduli. Here we assume the layer to be of the same thickness as the other layers, namely 100 m. In most crustal segments there are certainly layers much thinner than 100 m – some as thin as metres or tens of centimetres – but for the purpose of illustrating the principles that control dyke-induced surface deformation the thickness used here for the seismic/mechanical top layers is appropriate. In the absence of detailed knowledge of the actual layering of the crust of Harrat Lunayyir – to which these models are applied - these thicknesses are suitable (we add the soft layers in the later models), in particular because the main mechanical effect of a layer does not lie in its thickness but rather in its softness or compliance. In the

models, we vary the depth of the 1GPa layer so as to explore the effect its depth would have on the dyke-induced surface stresses and associated deformation.

In the first model (Fig. 13) the dyke tip is arrested at 1 km depth below the surface. Here all the layers have the same Young's modulus, 40 GPa, so that the modelled crust is analogous to a homogeneous and isotropic elastic half space, a type of model still very common in volcano-deformation studies. The results (Fig. 13c, d) show that the surface shear stress and tensile stress reach close to 6 MPa. Both stresses are large enough to have the potential of generating or initiating fractures at the surface. We think, however, that the dyke became arrested at much shallower depth, at about 500 m or perhaps as little as 300 m below the surface. This follows partly from the analytical considerations above, and is used as a basis in many of the numerical models below. We therefore may two other elastic half-space models with the dyke tip at, first, the depth of 500 m (Fig. 14) and, then, at the depth of 300 m (Fig. 15). The results (Figs. 14–15) show that the surface stresses reach up from 10 to 12 MPa, for 500 m tip depth, up to 17–18 MPa, for 300 m tip depth.

In these models the stiffnesses (Young's modulus) of some of the layers are unrealistically high. This applies, in particular, to the surface layer; 40 GPa is far too high for the surface layers in Harrat Lunayyir, where a dynamic modulus of 10–20 GPa would be more reasonable for some of the surface layers, with the static modulus much lower, as discussed below. But for an elastic half-space model such as this one, there must be a uniform Young's modulus, and 40 GPa is reasonable to the average stiffness of the part of the crustal segment dissected by the dyke. Thus, even if the surface stresses reach something like 17 MPa, the high stiffness of the surface layers (which tends to raise the stresses) is unrealistic, making the calculated stress values unrealistic as well.

In the next model (Fig. 16) the crust is layered in the simplest possible way. There are 3 layers that constitute the uppermost part (300 m) of the crust. Two have a Young's modulus of 27 GPa, and the surface layer a Young's modulus of 17 GPa. These values, also used in subsequent models, are based on the considerations of the dynamic mechanical layering in Harrat Lunayyir, discussed above. These are likely to be crude average dynamic values. The unit hosting the dyke is, as before, with a stiffness of 40 GPa. The results (Fig. 16) show that for dyke arrested with a tip at 1 km depth and the simplest type of layering, the induced maximum theoretical tensile and shear stresses at the surface are only about 2 MPa, and thus generally too small to generate fractures, either tension fractures or normal faults.

Even when the dyke tip is arrested at the depth of 500 m, for the same layering, the surface stresses are so low as to be unlikely to generate surface fractures (Fig. 17). In fact, it is only when the dyke tip has reached the very shallow depth of 300 m that the surface stresses become high enough so as to have a chance of generating fractures (Fig. 18). Here the surface stresses reach 9–10 MPa. These stresses are certainly high enough to generate tension fractures. Whether initiated tension fractures might change into small normal faults would then depends on the depths to which they could propagate. In the model in Fig. 18 the tensile stresses are comparatively high to depths in excess of 300 m (the red zones in part b) so that, based on the conclusions in Section 6, some of the tension fractures might change into normal faults.

The models above, Figs. 16–18, while mechanically perfectly valid, are geologically perhaps not as realistic as such models can be made. In all crustal segments there are compliant or soft layers (with low Young's modulus) in-between stiffer layers. This applies particularly to volcanically active areas where soft pyroclastic, sediment, and soil layers are common in-between stiffer units such as lava flows. Such layers are known to have very great effects on the local stresses induced

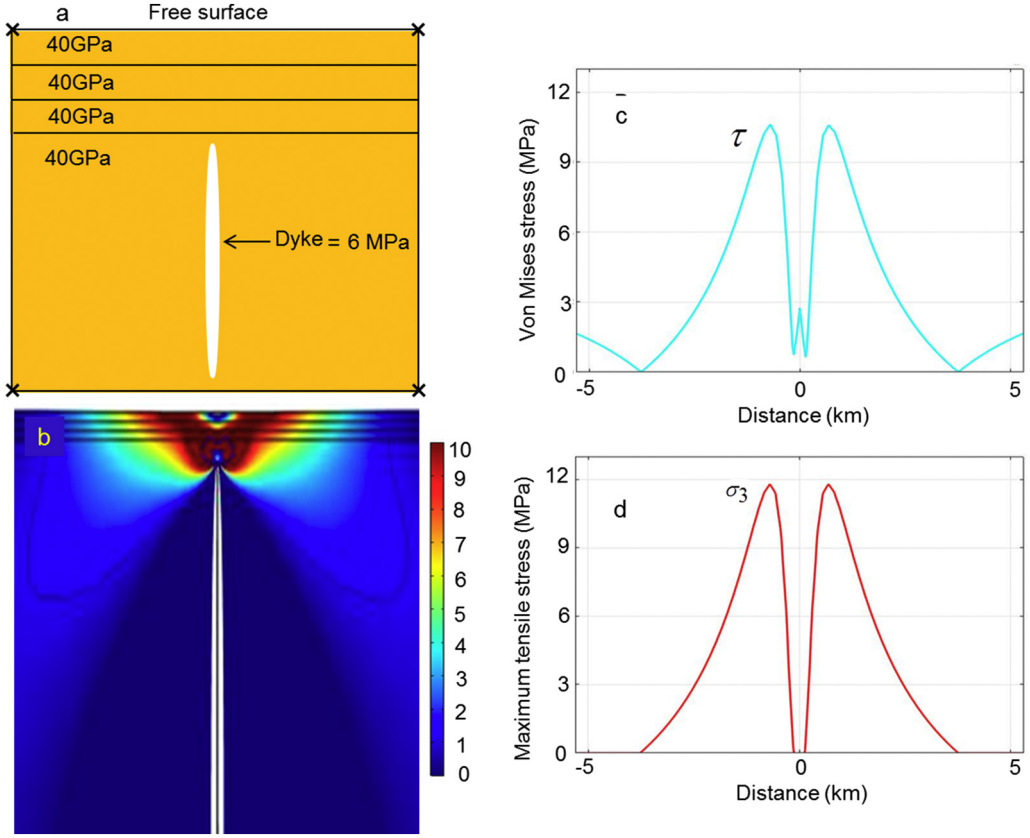

Fig. 14. Numerical model of a dyke arrested with a tip at the depth of 500 m below the Earth's surface. The magmatic overpressure is 6 MPa and Poisson's ratio of all the rock layers is 0.25. Each of the 3 top layers is 100 m thick. All the 3 top layers, as well as the main rock unit hosting the dyke, have the same Young's modulus of 40 GPa. Thus, this is effectively an elastic half-space model. a. Schematic setup of the model. The thickness of the layers and the height of the dyke are not to scale. b. Maximum principal tensile stress, σ_3, in mega-pascals (range shown 0–10 MPa). c. von Mises shear stress at the Earth's surface. d. Maximum principal tensile stress, σ_3, at the Earth's surface.

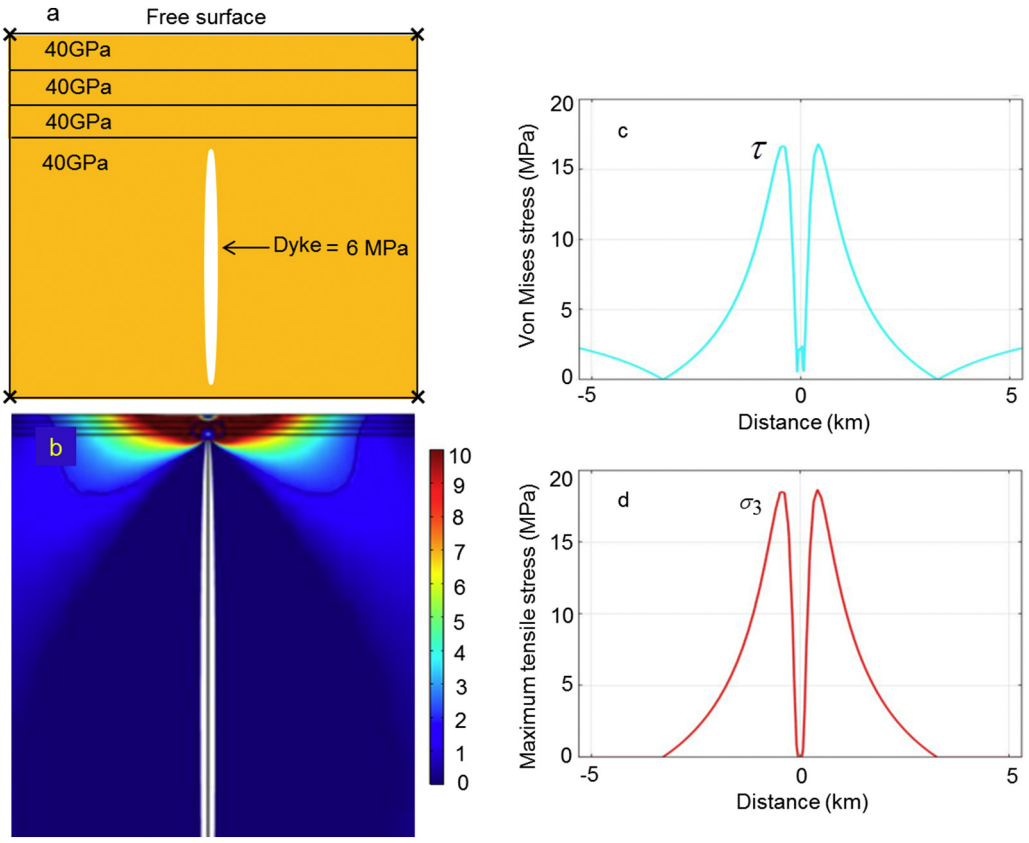

Fig. 15. Numerical model of a dyke arrested with a tip at the depth of 300 m below the Earth's surface. The magmatic overpressure is 6 MPa and Poisson's ratio of all the rock layers is 0.25. Each of the 3 top layers is 100 m thick. All the 3 top layers, as well as the main rock unit hosting the dyke have the same Young's modulus of 40 GPa. Thus, this is effectively an elastic half-space model. a. Schematic setup of the model. The thickness of the layers and the height of the dyke are not to scale. b. Maximum principal tensile stress, σ_3, in mega-pascals (range shown 0–10 MPa). c. von Mises shear stress at the Earth's surface. d. Maximum principal tensile stress, σ_3, at the Earth's surface.

by dykes (Gudmundsson, 2002, 2003). The detailed crustal layering in Harrat Lunayyir is unknown, but must certainly include soft layers. In addition, the surface layer in the western part of the graben, where we studied the fractures in the field (Figs. 3–7), is partly compliant pyroclastics, with a Young's modulus of the order of a few giga-pascal (rather than 17 or 40 GPa used in the models above). On the eastern side of the graben, however, some of the tension fractures occur in comparatively stiff granitic rocks (Jonsson, 2012).

In order to take soft layers into account, and explore their effects on the dyke-induced stresses, we made several models with a single soft layer, 100 m thick and with a stiffness of 1 GPa. Such stiffness would be typical of many soft or compliant pyroclastic and sedimentary layers – many of which could, in fact, be much softer (Gudmundsson, 2011a). In the models we, as before, vary the depth of the dyke tip below the surface – the three depths considered are 1000 m, 500 m, and 300 m. But, in addition, we vary the location, that is, the depth of the soft layer itself from being with the top at the depth of 100 m, to being with the top a depth of 300 m. The results show that varying the depth of the soft layer has comparatively little effect on the surface stresses, which are the stresses of greatest interest here. We therefore show only the results where the soft layer is at the maximum depth, 300 m, except for the last model of this kind, where the surface of the soft layer is at 100 m depth.

The first model (Fig. 19) shows the stresses induced by a dyke whose tip is arrested at 1 km below the surface. The model shows very clearly the great effects of the soft layer on the crustal stresses. In particular, the soft layer basically suppresses all stresses, so that very low stresses are transmitted across the layer. The surface stresses (Fig. 19c,d) are well below 2 MPa, even if the surface layer at 17 GPa is still stiff. It follows from the low surface stresses that neither tension-fracture formation nor normal faulting is likely. The next model is identical except for the depth to the dyke tip, which is here at 500 m (Fig. 20). Even if the dyke tip is here very close to the surface, the surface stresses are still very low, the maximum being around 3 MPa. Thus, even at such a shallow dyke-tip depth, much dyke-induced surface fracturing is unlikely.

We did not make a model with the dyke tip at 300 m depth for this layering, because then the tip of the dyke would have entirely penetrated the soft layer, thereby making its effect on the stress field minimal. Instead, we show here the dyke tip at 300 m depth, but the soft 1 GPa layer is with a top at 100 m depth below the surface, that is, the soft layer is the second layer from the surface (Fig. 21). The stress-suppressing effects of the soft layer are still very noticeable. Nevertheless, because the dyke tip is so close to the surface, the maximum dyke-induced surface stresses reach just over 8 MPa. These stresses would normally be able to initiate tension fractures and normal faults.

In all the models presented above, the surface layer has stiffness or Young's modulus of 17 GPa. This value, like that of other moduli here, is primarily based on seismic velocity considerations, that is, it is a dynamic modulus. While dynamic moduli are very suitable for the propagation of an earthquake rupture – whose rate is similar to that of an S-wave, that is, several kilometres per second – for dyke propagation static moduli are normally much more appropriate. This follows because dyke propagation rates are of the order of metres per second or less and thus many orders of magnitude slower than the velocities of seismic ruptures for which dynamic moduli are appropriate. The difference between static and dynamic Young's modulus varies from zero to a factor of about 13, and is normally highest at shallow depth in active areas (Gudmundsson, 2011a). This follows because at shallow depth in active areas the fractures (e.g. cooling joints) and cavities (pores, vesicles), and contacts are normally not yet filled with secondary minerals, and discontinuities and cavities of all kind lower the static modulus but have much less effect on the dynamic modulus.

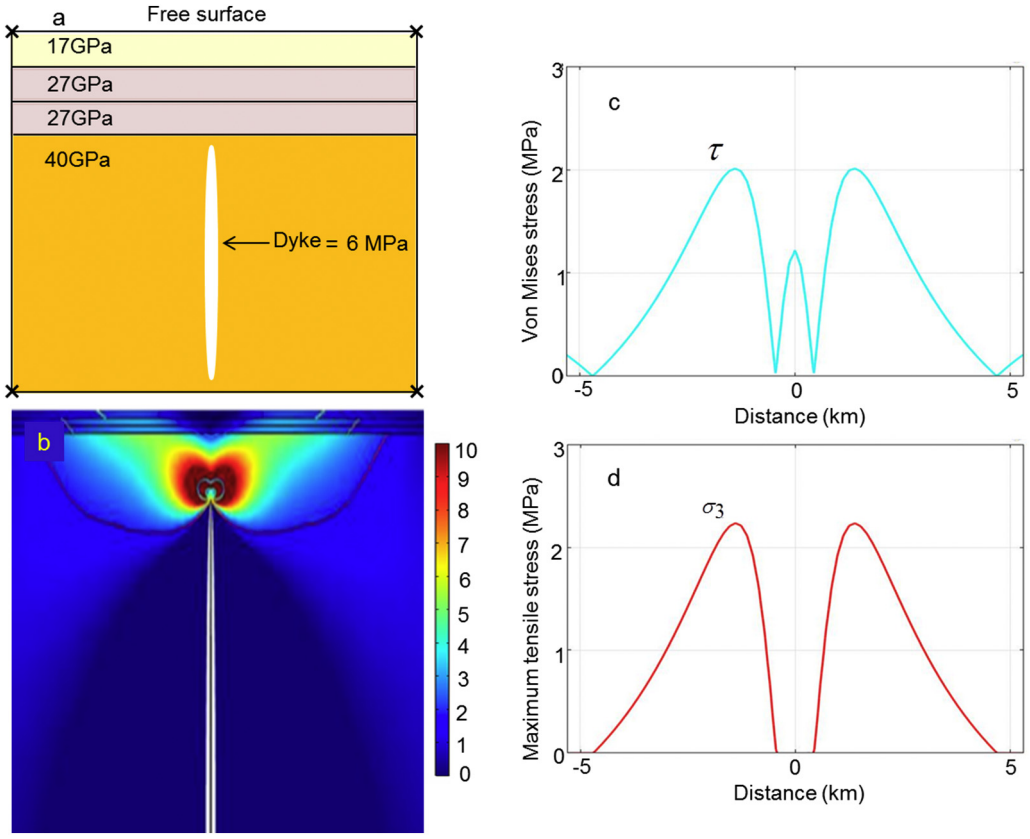

Fig. 16. Numerical model of a dyke arrested with a tip at the depth of 1000 m below the Earth's surface. The magmatic overpressure is 6 MPa and Poisson's ratio of all the rock layers is 0.25. Each of the 3 top layers is 100 m thick. The surface layer has Young's modulus of 17 GPa, followed by two layers with a Young's modulus of 27 GPa. The unit or layer hosting the dyke has a Young's modulus of 40 GPa. a. Schematic setup of the model. The thickness of the layers and the height of the dyke are not to scale. b. Maximum principal tensile stress, σ_3, in mega-pascals (range shown 0–10 MPa). c. von Mises shear stress at the Earth's surface. d. Maximum principal tensile stress, σ_3, at the Earth's surface.

Considering also the soft surface layers seen on many of the photographs (Figs. 3–8), we decided to run several models with a comparatively soft or compliant surface layer. In these models, the surface layer has a Young's modulus of 3 GPa. This is similar to that of many comparatively compliant layers, such as young lava flows, pyroclastic layers, and sedimentary layers (Gudmundsson, 2011a). We also include the earlier soft layer, 1GPa. For the first two models, the 1GPa layer is the fourth from the top, that is, with a top surface at the depth of 300 m, so as to be in agreement with the models above (Figs. 19 and 20). In the last model, however, where the dyke tip is at the depth of 300 m, the 1GPa layer is with its top surface at 100 m depth, as in the model in Fig. 21.

The results of the first model with this layering has a dyke tip at 1000 m depth and shows that very little stress reaches the surface (Fig. 22). The maximum tensile and shear stresses at the surface are only about 0.4 MPa, and would normally not result in any fracture formation. Very similar results are obtained for a dyke tip at 500 m depth. The surface stresses are about 0.7 MPa and thus generally too low to generate either tension fractures or normal faults. In the last model, the dyke tip is at a depth of 300 m so that the 1GPa layer is with a top at 100 m depth. Even if the dyke tip is only 300 m below the surface, the surface stresses are low – just about 2 MPa (Fig. 24). Some minor surface fracturing is possible, but major tension fractures and normal faults are unlikely to be generated in this stress field.

8. Dimensions of the 2009 dyke

The dimensions of the dyke inferred to have been emplaced during the 2009 episode can be estimated using various methods. The main methods that have been used are the distribution of associated earthquakes and geodetic data. Several estimates have been made. Baer and Hamiel (2010) give the dyke strike dimension or length as 12 km, the maximum dyke thickness as 2.5 m, and the dyke dip dimension or depth as about 10 km. However, they also use dyke segments with cumulative dip dimension of 15 km. The projection line of the hypocentres of the earthquakes, primarily associated with the dyke emplacement, during the 2009 episode is about 17 km long (Baer and Hamiel, 2010, Fig. 1b).

Jonsson (2012) and Xu et al. (2016) infer that the tension fractures and faults at the surface were in zones as long as 14 km; in particular, Jonsson (2012) states that a normal fault on the western side of the 'graben' reaches this length. Presumably these authors interpret that strike dimension or length of the dyke as similar to this, or about 14 km. Xu et al. (2016) conclude that the depth to the dyke source was at least 20 km, and perhaps 35 km, so that the dyke dip dimension, while the dyke was continuously open, must, in their model, have been in this range. Their maximum dyke thickness is 2.3 m.

Our interpretation is that the dip dimension of the dyke is at least 20 km. The fact that the dyke continued to expand after it became arrested shows that the entire dip dimension was open at that time, and thus functioning as continuous fracture. For our modelling purposes it is enough to know that the dyke dip dimension is at least 20 km; this means that its dip dimension is larger than the strike dimension (given in a moment), so that the strike dimension is the 'controlling dimension', that is, the dimension that controls the thickness or opening of the dyke (Gudmundsson, 2011a). The strike dimension, based on the earthquake distribution (e.g. Baer and Hamiel, 2010), is most likely between 13 and 14 km (Fig. 8b). We take it as 14 km and conclude that the strike dimension is the controlling dimension.

To estimate the maximum opening or thickness of the dyke, in any layer or unit with a given Young's modulus and Poisson's ratio, we can either use the part-through crack model or the through-crack model.

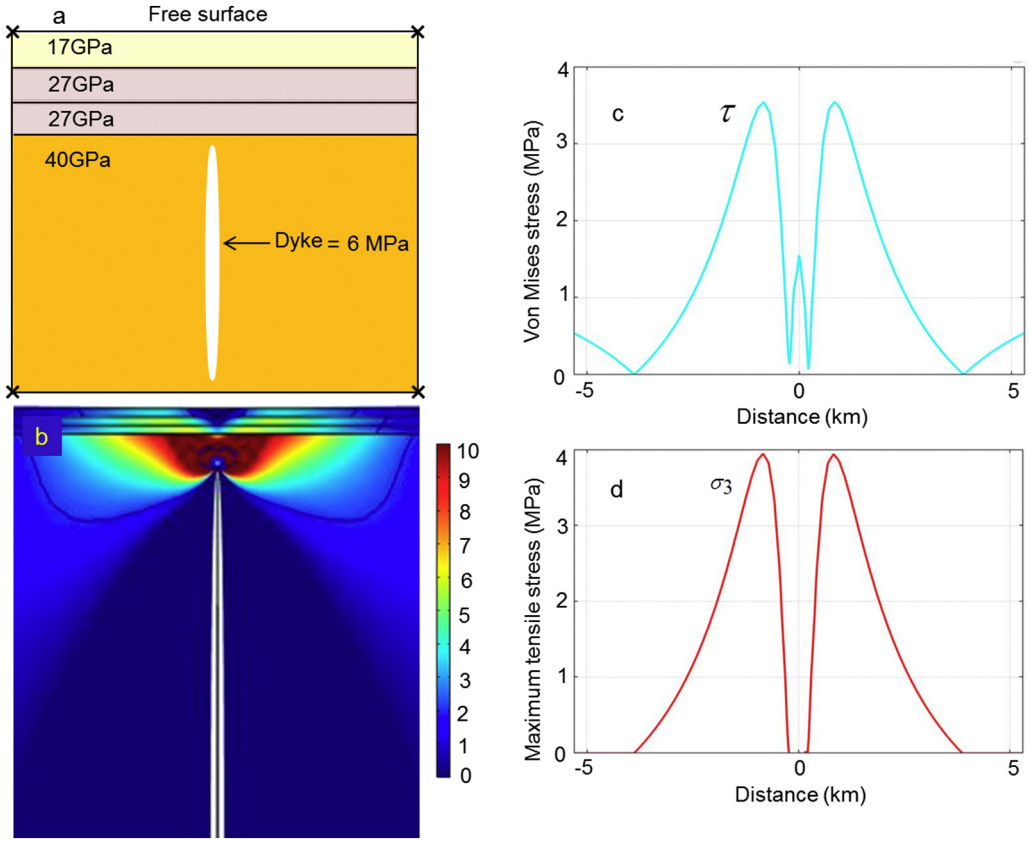

Fig. 17. Numerical model of a dyke arrested with a tip at the depth of 500 m below the Earth's surface. The magmatic overpressure is 6 MPa and Poisson's ratio of all the rock layers is 0.25. Each of the 3 top layers is 100 m thick. The surface layer has Young's modulus of 17 GPa, followed by two layers with a Young's modulus of 27 GPa. The unit or layer hosting the dyke has a Young's modulus of 40 GPa. a. Schematic setup of the model. The thickness of the layers and the height of the dyke are not to scale. b. Maximum principal tensile stress, σ_3, in mega-pascals (range shown 0–10 MPa). c. von Mises shear stress at the Earth's surface. d. Maximum principal tensile stress, σ_3, at the Earth's surface.

The part-through model is commonly used for non-feeder dykes (Gudmundsson, 2011a). However, in the present case the dyke presumably became arrested at a mechanically weak contact, perhaps partly an open contact – given that the contact of arrest may have been as shallow as 300 m below the surface. In such a case, the through-crack model is a good approximation, and we used it here. The maximum opening of the dyke, or thickness, Δu_l is then given by (Gudmundsson, 2011a):

$$\Delta u_l = \frac{2p_o(1-\nu^2)L}{E} \tag{8}$$

where p_o is the magmatic overpressure or driving pressure, ν is Poisson's ratio and E is Young's modulus of the layer/unit where the dyke thickness is to be determined, and L is the strike dimension or length of the dyke where the thickness/opening is determined.

Using the same values as in our numerical models, the main unit hosting the dyke has a Young's modulus of 40 GPa and a Poisson's ratio of 0.25. For a magmatic overpressure of 6 MPa and a dyke length or strike dimension of 14 km, the maximum thickness, from Eq. (8), would be about 3.9 m. At shallower depths, where the main layers have a Young's modulus of 27 GPa, the maximum opening or thickness of a dyke with the same length and overpressure would be about 5.8 m. And the dyke would be even thicker where hosted by very soft layers, such as 1 GPa in the model in Fig. 23. However, we believe that the dyke would tend to become arrested on meeting the very soft layers, so here we assume that the main uppermost part of the dyke would be in the layers with a stiffness of 27 GPa. As indicated above, these are dynamic stiffnesses, so that the static stiffness could easily be half this value or less (Gudmundsson, 2011a), yielding a dyke thickness of 11.6 m.

A maximum thickness of 5.8–11.6 m for a 14 km long dyke would yield a length/thickness ratio between about 2400 and 1200. This is similar to the measured length/thickness ratios of regional basaltic dykes in Iceland, which range from about 300 to about 2000 (Gudmundsson, 1986). The dykes in Iceland are exposed at depths of 500–1500 m below the original surface of the volcanic zones within which they were emplaced so, again, rather similar to the uppermost part of the 2009 dyke. The length/thickness ratios of dykes depend primarily on host-rock Young's modulus and magmatic overpressure, but measured dykes worldwide have commonly ratios similar to those reported for the Icelandic dykes (Rickwood, 1990).

Thus, in our interpretation, the 2009 dyke is much thicker than previous models would indicate. Elastic half-space models, such as dislocation models of dykes, tend to underestimate dyke thicknesses. This follows because, by definition, these models assume no layering or contacts in the crust, thereby ignoring any stress 'dissipation' and suppression that the layering normally gives rise to (Figs. 13–24). Consequently, the half-space dislocation models overestimate the surface stresses and displacements supposed to be generated by a dyke of a given thickness. Our interpretation of the dyke thickness in relation to its other dimensions is very plausible based on worldwide studies of length/thickness ratios of dykes, as indicated above.

9. Discussion

9.1. General implications

While the numerical models are here applied to the 2009 volcanotectonic episode at Harrat Lunayyir in Saudi Arabia, the results are completely general. Here we first discuss some of the general

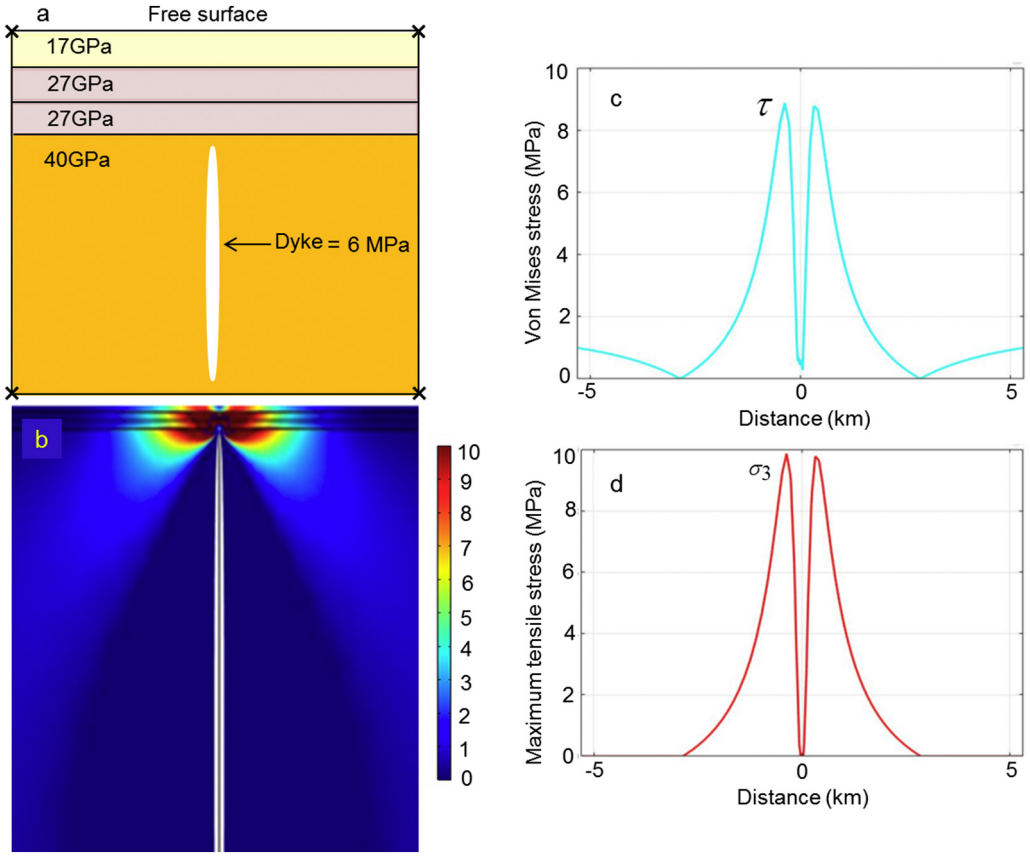

Fig. 18. Numerical model of a dyke arrested with a tip at the depth of 300 m below the Earth's surface. The magmatic overpressure is 6 MPa and Poisson's ratio of all the rock layers is 0.25. Each of the 3 top layers is 100 m thick. The surface layer has Young's modulus of 17 GPa, followed by two layers with a Young's modulus of 27 GPa. The unit or layer hosting the dyke has a Young's modulus of 40 GPa. a. Schematic setup of the model. The thickness of the layers and the height of the dyke are not to scale. b. Maximum principal tensile stress, σ_3, in mega-pascals (range shown 0–10 MPa). c. von Mises shear stress at the Earth's surface. d. Maximum principal tensile stress, σ_3, at the Earth's surface.

implications, and then those that apply particularly to the episode at Harrat Lunayyir. Some of the main results for dyke-induced stresses and surface deformation in an active volcanic zone may be summarised as follows:

- Unless there is great mechanical heterogeneity in the crustal segment within which the dyke is emplaced, the stresses and the related deformation should be symmetric. A highly asymmetric surface deformation, even in layered and anisotropic crust, is thus unlikely to be induced by a single dyke.
- The distance between the two surface-stress peaks, where dyke-induced fractures would be possible in case the maximum stresses reaches at least several mega-pascals, is similar to twice the depth to the top of the dyke below the surface. This is a well-known result from earlier studies, sometimes referred to as the 'graben rule' and confirmed by analytical and numerical studies (Figs. 13–24). The only exception to this rule is if the Gook-Gordon delamination occurs – a mechanism mostly limited to very shallow depths - so that the contact between layers opens up. Then the stresses at the surface normally peak above the lateral ends of the opened-up contact and would not have any correlation with the depth to the top of the dyke (Gudmundsson, 2003). In the present models, however, the contact is not weak enough to open up.
- It follows from the last point that, unless Cook-Gordon delamination operates, the half-width of a dyke-induced graben at the surface is similar to the depth to the top of the dyke. Thus, if a dyke-induced graben is 3 km wide, then the tip of the associated dyke would have to be at depth of close to 1.5 km. A dyke arrested at 1.5 km depth in an active volcanic zone would rarely induce large enough stresses at the surface to initiate fractures, major normal faults in particular. As we have seen in the models presented here, a crustal segment with one or several soft layers would commonly suppress any dyke-induced surface stresses to such an extent that only dykes arrested at very shallow depth – a few hundred metres or less – could possible trigger fracture formation at the surface.

9.2. Implications for the 2009 episode

The analytical and numerical models presented here do not support the suggestions that the entire surface-fracture formation and development during the 2009 episode was induced by an arrested dyke. The main reasons for this conclusion may be summarised as follows:

1. The graben in Fig. 8 is between 3 and 7 km wide. If we take an average width as 5 km, then that would imply that the dyke tip at the time of fracture formation was at a depth of >2 km (which is also the depth suggested by some of the authors of the cited papers). However, the numerical models presented here show that, for any reasonably layering, the surface stresses even at the depth of 1 km, let alone a depth of >2 km, would be too small to generate significant fractures. It is only when the tip reaches the shallow depth of 500 m, and, in particular, 300 m, that the surface stresses become large enough so as to generate significant fractures.
2. When the tip of the arrested dyke is at 300–500 m depth, clearly the graben that the dyke could initiate at the surface could not be wider than about 0.6–1 km. A graben of average width 5 km is simply too wide to be generated by the stresses induced by a dyke arrested at the depth of 300–500 m.
3. None of the main fractures coincide in strike with the inferred strike of the dyke and many strike very differently from that of the dyke

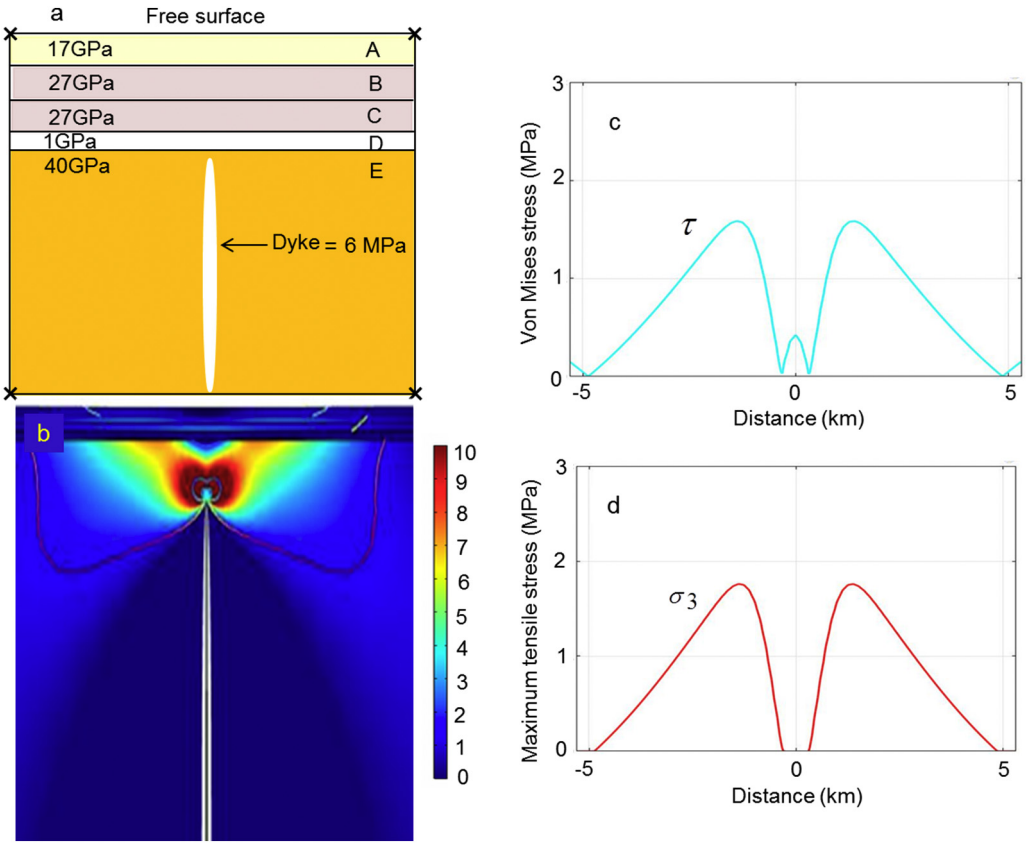

Fig. 19. Numerical model of a dyke arrested with a tip at the depth of 1000 m below the Earth's surface. The magmatic overpressure is 6 MPa and Poisson's ratio of all the rock layers is 0.25. Each of the 4 top layers is 100 m thick. The surface layer has Young's modulus of 17 GPa, followed by two layers with a Young's modulus of 27 GPa, and a fourth layer with a Young's modulus of 1 GPa. The unit or layer hosting the dyke has a Young's modulus of 40 GPa. a. Schematic setup of the model. The thickness of the layers and the height of the dyke are not to scale. b. Maximum principal tensile stress, σ_3, in mega-pascals (range shown 0–10 MPa). c. von Mises shear stress at the Earth's surfac. d. Maximum principal tensile stress, σ_3, at the Earth's surface.

(Fig. 8b). Furthermore, some of the fractures apparently dissect the dyke, when its strike is projected (as a broken line) to the surface.

4. Although we have followed the established tradition in the literature on this episode and referred to the structure as a graben, the general fracture pattern supposed to have been generated in the 2009 episode does not follow the geometry of a classical graben. In fact, the 'boundary fault' on the eastern side of the 'graben' is not a fault but rather a zone of tension fractures. The symmetry of the stress field induced by an arrested dyke would tend to generate a clear graben structures, with two normal boundary faults, but that is not what happened here.

While there have, apparently, been no previous numerical models applied to the 2009 episode (dislocation models of the dyke applied by many authors are, strictly, analytical models), some authors have used analogue models to explain the surface fracture pattern. Analogue models in structural geology and volcanotectonics, while always incorrect in detail (due to scaling problems of strength, gravity, grain size, and related aspects), often provide interesting suggestions and ideas that can then be tested by detailed field observations as well as analytical and/or (depending on the complexity of the problem) numerical models.

For the 2009 episode, Xu et al. (2016) provide an analogue model to explain some aspects of the evolving surface deformation induced by the inferred dyke emplacement. They use crushed silica powder as an analogue for the host rock layers of the dyke. The model is 15 cm wide, 25 cm long, and 12.5 cm thick. The thickness of the layer of crushed silica powder is such that 2.5 cm in the model corresponds to 1 km in the field. They do not explicitly state the depth of the dyke tip below the surface, but from their Fig. 5c one can infer that the dyke tip varies (as an 'arc') from a depth of about 3.6 km to, a minimum, of about 1 km below the surface. Xu et al. (2016) then gradually increase the opening, or thickness, of the dyke from 0 cm to a maximum of 0.6 cm and record the associated surface deformation.

Briefly, the main relevant results of the experiments are as follows. At dyke opening of 0.15 cm, there is still no surface faulting. The first faults at the surface appear when the dyke opening has reached 0.3 cm. The surface faults then continue to develop and link up into larger faults as the dyke opening is increased from 0.3 cm to 0.45 cm, and then to 0.6 cm.

These results are interesting, particularly when scaled to the corresponding dimensions in the field. Given that 2.5 cm in the model corresponds to 1 km, a dyke opening or thickness of 0.15 cm should correspond to 60 m. The first fault is seen when the dyke opening or thickness has reached 0.3 cm, which corresponds to a 120 m thick dyke. The final dyke opening of 0.6 cm in the model would correspond to 240 m thick dyke in the field.

That a 60 m thick dyke with a tip at a minimum depth of 1 km depth is unable to generate fractures at the surface is a remarkable result, as is the conclusion that the dyke thickness needs to reach 120 m for the first surface faults to form. These results suggest that only very thick intrusions, or thinner intrusions but very close to the surface, can induce surface fractures. In the paper by Xu et al. (2016) the dyke inferred to be emplaced during the 2009 episode has an opening of about 2 m, while Baer and Hamiel (2010) suggest a general dyke opening of 1–2 m and Pallister et al. (2010) an opening from <1 m to a maximum of 4 m. The dyke opening in the analogue model of Xu et al. (2016) at the time of first surface fault formation is thus 30–100 times greater than that of the dyke, as modelled from deformation data, and 10–20 times greater than the dyke thickness calculated in the present paper.

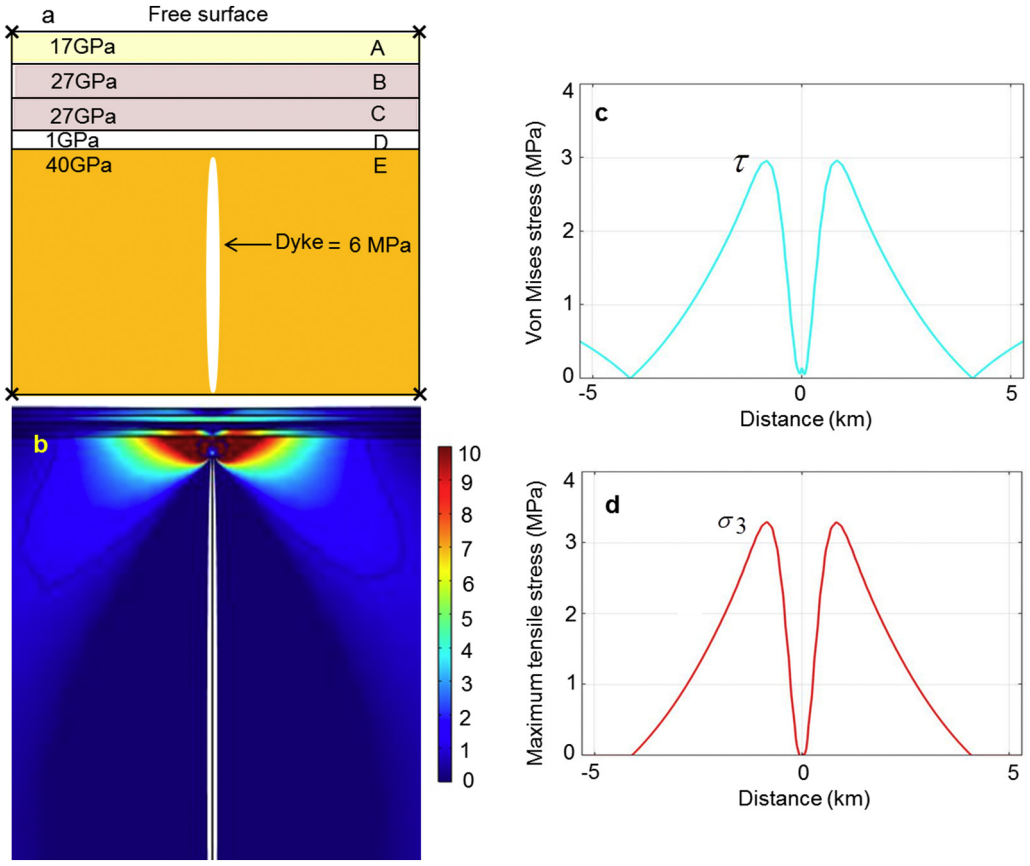

Fig. 20. Numerical model of a dyke arrested with a tip at the depth of 500 m below the Earth's surface. The magmatic overpressure is 6 MPa and Poisson's ratio of all the rock layers is 0.25. Each of the 4 top layers is 100 m thick. The surface layer has Young's modulus of 17 GPa, followed by two layers with a Young's modulus of 27 GPa, and a fourth and compliant layer with a Young's modulus of 1 GPa. The unit or layer hosting the dyke has a Young's modulus of 40 GPa. a. Schematic setup of the model. The thickness of the layers and the height of the dyke are not to scale. b. Maximum principal tensile stress, σ_3, in mega-pascals (range shown 0–10 MPa). c. von Mises shear stress at the Earth's surface. d. Maximum principal tensile stress, σ_3, at the Earth's surface.

The analogue models, even if they have little in common with the inferred dyke emplacement during the 2009 episode, illustrate well-known points from both field observations and numerical models. The first point is that there is normally little or no large-scale faulting observed at the tips of arrested dykes (Figs. 9–12; Gudmundsson, 2003). Many photographs of dyke tips reaching to depths of a few metres below the surface, such as from eruptions in Iceland and Hawaii, also fail to show large-scale grabens; well-known examples being the 2011 eruption in Kilauea and the 1980 eruption in the Krafla volcano in North Iceland. Some feeder-dykes and non-feeders, however, are associated with grabens; but the question remains whether the dyke-generated stresses induced the graben or whether the regional extension that is responsible for the dyke injection in the first place also generated the stresses suitable for graben formation. It is well known that most grabens worldwide, in sedimentary basins, in lava piles, and elsewhere are generated by stress fields that have nothing to do with dyke injections. Also, in volcanic areas such as Iceland, where grabens and normal faults are common, dykes are comparatively rare where normal faults are common, and vice versa (Forslund and Gudmundsson, 1991). The 'graben' in Harrat Lunayyir is located at the top of a regional dome, a ridge, which is 30 km wide and rises some 300 m above the surrounding areas (Baer and Hamiel, 2010). Thus, regional doming, presumably related to magma-pressure changes in a deep-seated reservoir beneath the area, may have contributed to the fracture formation during the 2009 episode, in addition to any contribution from the inferred dyke. Doming and general spreading in volcanic areas is a common reason for fracture formation, particularly the formation of tension fractures and normal faults (Gudmundsson, 1987; cf. Gudmundsson, 1999, 2017).

The second point is that most of the numerical models presented here indicate comparatively low surface stresses when there is any reasonable layering of the crust (Figs. 16–24). The only layered models that indicate high enough stresses so as to generate surface fractures are those where the dyke tip is arrested at a very shallow depth, namely at the depth of 300 m (Figs. 18 and 21). In many cases, to initiate surface fractures the dyke tip would have to be even shallower because the overpressure used here, 6 MPa, is comparatively high for a basaltic dyke at a shallow depth in a continental crust. Negative buoyancy (Eq. (2)) of basaltic magma in the uppermost kilometres of a continental crust may reduce the overpressure to a few mega-pascals. Also, layering may reduce the dyke-induced surface stresses, even for dyke tips at the shallow depth of 300 m, to very low values (Fig. 24).

As for the 2009 episode, the dyke continued to expand or inflate after it became arrested (Xu et al., 2016). This indicates that the dyke did not become arrested because of declining overpressure (driving pressure) or because of cooling of its front – mechanisms that are often proposed for dyke arrest – but rather though one of the three principal mechanisms discussed above. That is, the arrest of the dyke was most likely due to one, or a combination, of the following mechanisms: Cook-Gordon delamination, stress barrier, and elastic mismatch. All these mechanisms depend on the dyke tip meeting a contact where the arrest occurs – as is, indeed, the most commonly observed condition for dyke arrest in the field (Figs. 9–12; Gudmundsson, 2003, 2011b). Thus, because the mechanical conditions at and above the contact where the dyke becomes arrested do not allow the dyke to continue on its vertical path, irrespective of its overpressure, the dyke can expand and still stay arrested.

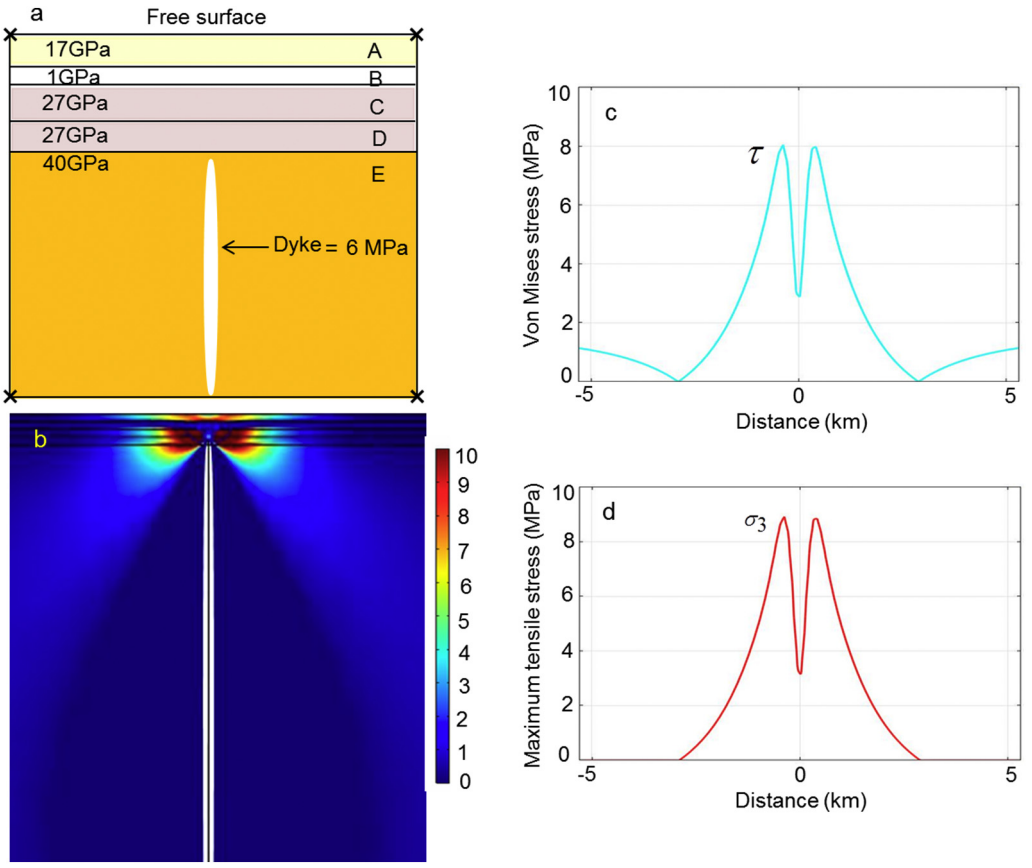

Fig. 21. Numerical model of a dyke arrested with a tip at the depth of 300 m below the Earth's surface. The magmatic overpressure is 6 MPa and Poisson's ratio of all the rock layers is 0.25. Each of the 4 top layers is 100 m thick. The surface layer has Young's modulus of 17 GPa, followed by a compliant layer with a Young's modulus of 1 GPa, and then two layers with a Young's modulus of 27 GPa. a. Schematic setup of the model. The thickness of the layers and the height of the dyke are not to scale. b. Maximum principal tensile stress, σ_3, in mega-pascals (range shown 0–10 MPa). c. von Mises shear stress at the Earth's surface. d. Maximum principal tensile stress, σ_3, at the Earth's surface.

Since the dyke continued to expand after it became arrested, it must have maintained its connection with its source reservoir. The depth to the source reservoir is not well constrained but thought to be somewhere between 20 km and 35 km (Xu et al., 2016). Despite the fact that the dyke must have extended to the depth of at least 20 km, and perhaps 35 km, elastic half-space dislocation modelling detects dyke opening primarily between the depth of 2 km and 7 km, with a maximum opening of 2.3 m, with little modelled opening below 7 km (Xu et al., 2016). Similarly, little opening was detected above 2 km, even if the top of the dyke, in that model, is assumed to have reached the depth of 1 km below the surface.

These results indicate that a dislocation in an elastic half space is a poor model for the dyke. Not only is it clear that the model captures basically only a part of the vertical dyke dimension (the uppermost part and the lower half or two-thirds are mostly missing from the model), but the model cannot explain why the dyke became arrested in the first place. Graben subsidence may contribute to dyke arrest (Gudmundsson, 2003), but in the 2009 episode there was no real graben subsidence because there were no major normal-fault slips at the eastern boundary of the 'graben', only tension fractures. For an overpressured dyke such as here, witness its continued expansion subsequent to arrest, the only known effective mechanisms of arrest are the three listed above, and all require mechanical layering with contacts in-between the layers. In the elastic half-space dislocation model there is absolutely no reason why the dyke should not have reached the surface. The fact that the dyke did not reach the surface clearly indicates a strong layering and local stresses that contributed to its arrest.

Some authors simulate the dyke geometry by dividing the dislocation model into 1 km × 1 km segments or patches, so as to allow for variation in dyke opening. That approach has been used for the dyke emplaced in Harrat Lunayyir in 2009 (Xu et al., 2016). Field measurements of regional dykes of these types, however, show that the thickness variations along strike is generally on the length scale of tens of metres (Delaney and Pollard, 1981; Gudmundsson et al., 2012). The tens-of-metre thickness variation along strike can sometimes been 'smoothed' to one to a few hundred metres (Delaney and Pollard, 1981), but we are not aware of any dykes that fit with the kilometre-scale thickness variation along strike. The measured strike variations in the examples cited above are mostly in mechanically similar host rocks (basaltic lava flows in Iceland and sedimentary rocks in the USA), so that the thickness variation is less than would be in case of greater heterogeneity in the mechanical properties of the host rock in the direction of strike. Variations on the scale of tens of metres in the opening and/or displacement on many kilometre long normal faults are also common and widely observed (Gudmundsson, 2011a). Such variations in displacements on fractures of any size are perhaps best analysed through Fourier series (Kusumoto and Gudmundsson, 2014).

The mechanical host-rock variations are normally much greater in the dip direction than in the strike direction. This follows because the host rock is layered, with great differences in stiffness between the layers (e.g., Figs. 9, 10, and 12). The real mechanical layering – primarily the variation in stiffness or Young's modulus – basically coincides with the natural layering of the rocks as seen in the field in young and highly active volcanic zones and fields - although in seismic layering, grouping together many similar rock layers is common. For a typical lava pile, the lava thicknesses are commonly 5–20 m and that would correspond to the main thickness variation in the dyke. Occasionally, there are thick pyroclastic or pahoehoe layers or intrusions, some of which may exceed one hundred metres in thickness, and the dykes could be of essentially uniform thickness inside some of those layers or units. Also, as a

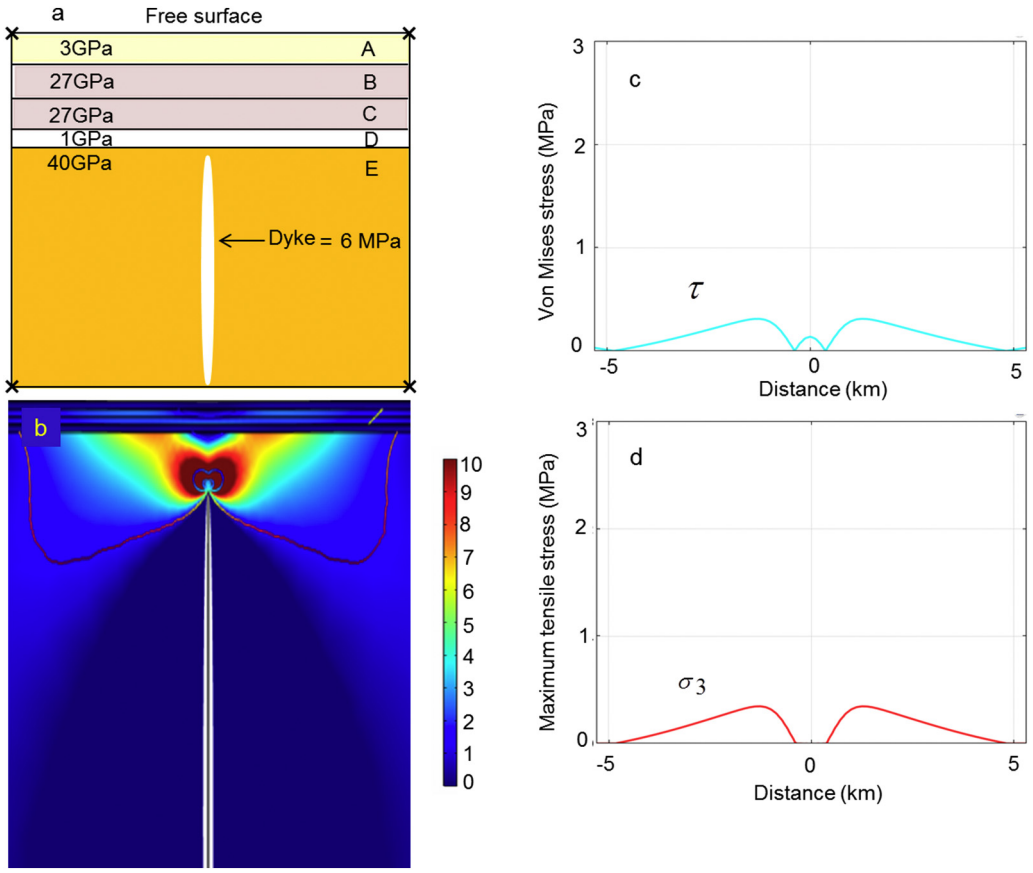

Fig. 22. Numerical model of a dyke arrested with a tip at the depth of 1000 m below the Earth's surface. The magmatic overpressure is 6 MPa and Poisson's ratio of all the rock layers is 0.25. Each of the 4 top layers is 100 m thick. The surface layer has Young's modulus of 3 GPa, followed by two layers each with a Young's modulus of 27 GPa, and then a compliant layer with a Young's modulus of 1 GPa. The unit or layer hosting the dyke has a Young's modulus of 40 GPa. a. Schematic setup of the model. The thickness of the layers and the height of the dyke are not to scale. b. Maximum principal tensile stress, σ_3, in mega-pascals (range shown 0–10 MPa). c. von Mises shear stress at the Earth's surface. d. Maximum principal tensile stress, σ_3, at the Earth's surface.

volcanic zone evolves, some mechanical layers or units may become thicker though mechanical homogenisation of the layers (Gudmundsson, 2011a), and dykes that dissect such layers/units may show little thickness variation in the dip direction for several hundred metres. But this applies to few and late-formed dykes in any given volcanic area – and primarily basaltic lava piles. Thus, normally, the thickness variation in the dip direction scales with the thicknesses of the layers that constitute the host rock, most commonly on the order of metres to one to a few tens of metres. Dividing dyke-dislocation models into patches of one square kilometre is thus normally not in harmony with the actual thickness variation of the dyke.

9.3. Interpretation of the 2009 episode

Based on the discussion above, as well as our field observations, analytical models, and numerical models, we interpret the 2009 Harrat Lunayyir episode as follows.

1. There was a regional dyke injection during the episode. The dyke had plenty of overpressure (driving pressure) so as to be potentially able to reach the surface, but became arrested at a shallow depth – most likely at a depth of a few hundred metres below the surface.
2. The arrest, almost certainly, occurred as the dyke tip met a contact between mechanically dissimilar layers. The detailed mechanism of arrest was one, or a combination, of the following: Cook-Gordon delamination, stress barrier, and elastic mismatch.
3. We estimate the dimensions of the dyke from seismic and geodetic data provided in the cited literature on this episode, combined with well-tested fracture-mechanics models and field studies of regional dykes. Our results as regards strike dimension (length) and dip dimension (height) are similar to those of earlier studies. We conclude that the strike dimension is about 14 km and the dip dimension at least 20 km. For the shallow depth of the dyke, the top parts, we estimate the maximum thickness in the range of 5.8–11.6 m or, given the inaccuracy in the estimated Young's moduli and overpressure, somewhere between 6 and 12 m. This is in contrast to the maximum thickness of 2–2.3 m obtained in earlier studies. However, our results fit much better with actual field measurements of the length/thickness ratios of regional dykes worldwide.
4. The tip of the dyke became arrested, not at a depth of 1–2 km, but rather at a depth of a few hundred metres. Our numerical and analytical results indicate that a dyke arrested at 1–2 km depth, as suggested in earlier studies, in a reasonably layered crust and with a typical magmatic overpressure could not induce significant fracture formation at the surface.
5. From the size and shape of the zone of fractures at the surface (Fig. 8) we conclude that a single dyke, whether its tip was arrested at 1 km or at 300 m depth, could not have induced all the fractures. This follows from the distance between the peaks of the surface stresses/surface deformation induced by a dyke – in the absence of an open contact - being roughly double the depth to the tip of the dyke (Figs. 12–24). This means that a dyke with an arrested tip at 1 km depth could explain a 2-km-wide fracture zone at the surface, and a dyke with a tip at 300 m depth could explain a 0.6-km-wide fracture zone. Since the 'graben' or fracture zone generated in the 2009 episode is 3 and 7 km wide, the dyke tip would have to be as deep as

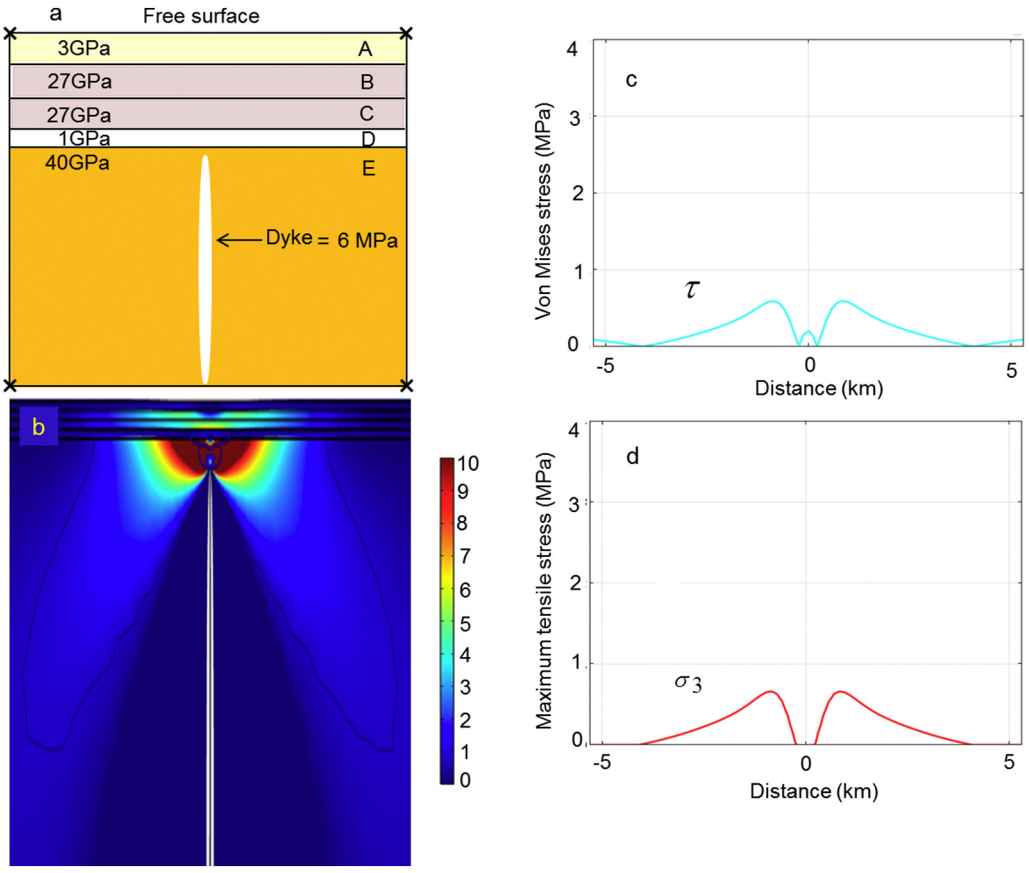

Fig. 23. Numerical model of a dyke arrested with a tip at the depth of 500 m below the Earth's surface. The magmatic overpressure is 6 MPa and Poisson's ratio of all the rock layers is 0.25. Each of the 4 top layers is 100 m thick. The surface layer has Young's modulus of 3 GPa, followed by two layers each with a Young's modulus of 27 GPa, and then a compliant layer with a Young's modulus of 1 GPa. The unit or layer hosting the dyke has a Young's modulus of 40 GPa. a. Schematic setup of the model. The thickness of the layers and the height of the dyke are not to scale. b. Maximum principal tensile stress, σ_3, in mega-pascals (range shown 0–10 MPa). c. von Mises shear stress at the Earth's surface. d. Maximum principal tensile stress, σ_3, at the Earth's surface.

3.5 km to generate it, and the stresses induced by such a deep dyke in a reasonably layered crust are simply far too low to generate the observed fractures.

6. Based on the inferred strike of the dyke, if not its inferred location (Fig. 8), we incline to the view that some of the fractures on the eastern side of the fracture zone or 'graben' were initiated by the dyke-induced stresses. Many of these are tension fractures, and their overall direction fits reasonably well with the inferred strike of the dyke. The projection of the dyke onto the surface, however, is likely to be in an error if this interpretation is correct, meaning that the real dyke was located somewhat further to the east. By contrast the directions of the fractures on the western side of the fracture zone fit poorly with the inferred strike of the dyke. The local direction of extension in the uppermost layers, above the dyke, may have been different from those in some or all the layers through which the dyke propagated. Rotations of the strike of the minimum principal stress σ_3 are common in layered rocks and well known from sedimentary basins and volcanic rift zones (Gudmundsson, 2011a). Such a rotation, if it occurred, would contribute to the condition for dyke arrest and also to the variation in the orientation of normal faults and tension fractures seen in Fig. 8.
7. One possibility that might be considered for the dyke to have induced all the fractures is a weak contact at shallow depths that opens up as the dyke approaches (basically the Cook-Gordon delamination). Then the stresses induced by the dyke concentrate at and above the lateral ends of the contact (Gudmundsson, 2003), so that, theoretically, the distance between the stress peaks could be anywhere between 3 km and 7 km (or wider or narrower depending on the lateral dimension of the open contact). However, for such conditions, the stress peaks at the surface are commonly narrow – a few hundred metres – and low in magnitude (Gudmundsson, 2003), and would thus not ideally fit with the 2–3 km wide zone of fracture formation on the eastern side of the fracture zone in Fig. 8.
8. In this interpretation, a considerable part of the surface fracturing relates to the tectonic stresses in the Harrat Lunayyir area. Relative tension due to some sort of spreading and/or doming (the fracture zone/graben is in the top of a 30 km wide volcanic ridge rising 300 m above its surroundings (Baer and Hamiel, 2010)), is normally a necessary condition for a dyke to form in the first place (Gudmundsson, 2011a). Thus, before the dyke was injected, there existed a local stress field in the area that favoured the formation of normal faults and tension fractures. As the dyke propagated to shallower depths, the local stresses became concentrated in the strip of land above the tip of the dyke. And these stresses are in addition to any stresses induced by the magmatic overpressure in the dyke. Depending on the layering and contacts above the dyke, these stresses could have generated normal faults and/or tension fractures, in additions to those directly induced by the magmatic overpressure of the dyke itself.

It is perhaps worth emphasising that in volcanotectonic rift zones, dyke intrusion, tension fracturing and normal faulting all connect to the same general loading; namely, horizontal extension across the rift zone. Thus, all these types of fractures occur in rift zones, and often simultaneously during volcanotectonic events, without one type of fracture necessarily triggering another type. It is worth remembering that the formation of most grabens, and normal faults in general, has nothing to do with dyke emplacement. Sedimentary basins are characterised by

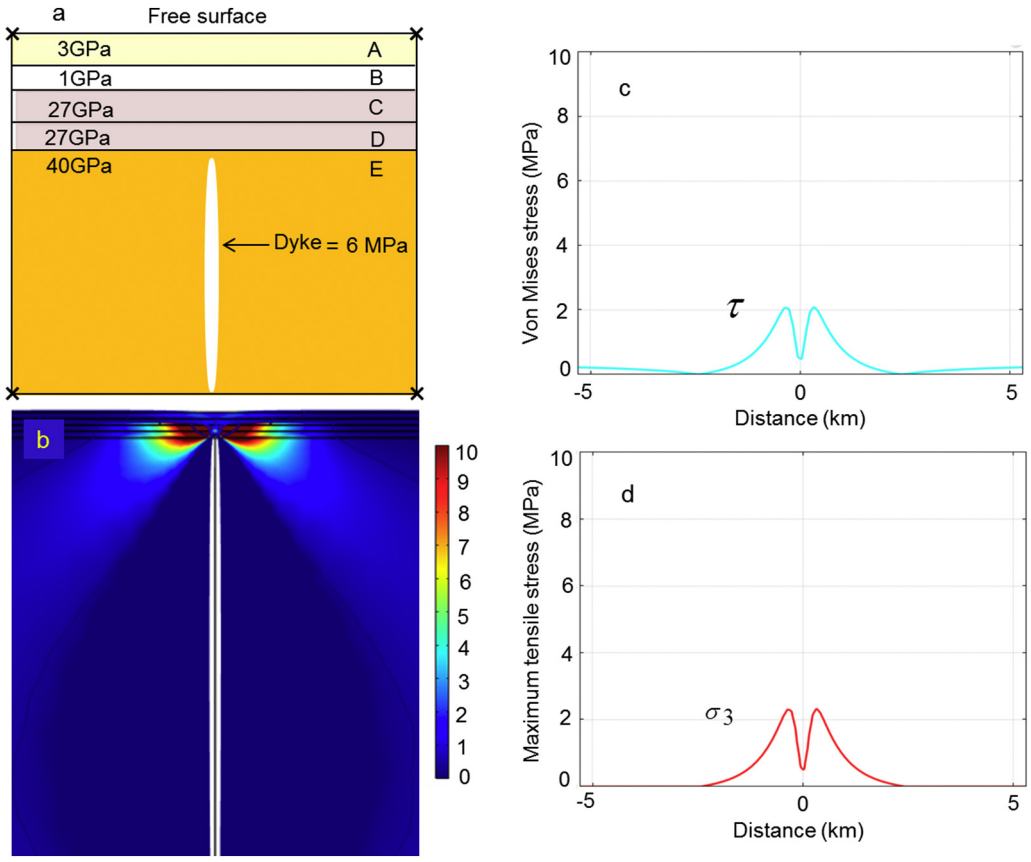

Fig. 24. Numerical model of a dyke arrested with a tip at the depth of 300 m below the Earth's surface. The magmatic overpressure is 6 MPa and Poisson's ratio of all the rock layers is 0.25. Each of the 4 top layers is 100 m thick. The surface layer has Young's modulus of 3 GPa, followed a compliant layer with a Young's modulus of 1 GPa, and then by two layers each with a Young's modulus of 27 GPa. The unit or layer hosting the dyke has a Young's modulus of 40 GPa. a. Schematic setup of the model. The thickness of the layers and the height of the dyke are not to scale. b. Maximum principal tensile stress, σ_3, in mega-pascals (range shown 0–10 MPa). c. von Mises shear stress at the Earth's surface. d. Maximum principal tensile stress, σ_3, at the Earth's surface.

normal faults and numerous grabens, few if any of which have anything to do with dykes. Thus, as indicated in point 9 above, normal faults, grabens, and dykes form partly due to loading through extension, either spreading of some sort or doming or both.

An additional point concerns the difference between half-space models and layered models. In this paper we show that the calculated surface stresses depend strongly on the assumed layering of the crust hosting the dyke. In particular, elastic half-space models, which assume that the crust is non-layered and thus use a uniform average Young's modulus, yield much higher tensile and shear stresses at the surface, for a given dyke overpressure or opening and depth, than models with a crust of alternating stiff and comparatively soft (compliant) layers.

One consequence of using elastic half-space models is that they tend to underestimate the thicknesses of the dykes supposed to induce the surface stresses and deformation. This follows because in half-space models the assumed uniform Young's modulus for the entire crustal segment hosting the dyke is normally much higher than that of the actual shallow layers close to the surface of an active volcanic zone or a volcano. Since there are no soft or compliant pyroclastic, sedimentary, or soil layers in the half-space model, there is no major stress dissipation; the models thus exaggerate the stresses transferred to the surface, and the associated deformation (cf. Figs. 13–15 and 22–24). Consequently, in a half-space model a thin dyke (normally a dyke with a low overpressure for its given dimensions) at a comparatively large depth can induce large stresses and deformation at the surface. Half-space models thus yield length/thickness or length/height (aspect) ratios of dykes that disagree with direct field studies of dykes as well as with standard fracture-mechanics models.

10. Summary and conclusions

The main conclusions may be summarised as follows.

- Mechanical layering has great effects on dyke-induced stresses and associated surface deformation. Even if the layering details are commonly unknown for volcanic areas, adding plausible general layering, using information from field observations of similar, well-exposed fossil volcanic zones, is likely to yield more realistic results as to surface stresses and deformation than non-layered models such as elastic half-space models.
- Half-space models, such as are commonly used for modelling arrested dykes, can be highly misleading, especially as regards dyke thicknesses. In particular, these models tend to (1) underestimate the dyke thickness so as to yield length (strike)/thickness ratios that are much larger than actually observed in the field and (2) overestimate the likely depth to the tip of a dyke that is supposed to induce a particular surface deformation.
- In the absence of mechanically weak (low tensile strength) or open contacts, the distance between the two dyke-induced surface stress peaks, tensile and shear stresses (and thus, normally, the main surface fractures, if formed) is roughly double the depth to the tip of the arrested dyke. In a reasonably layered volcanic zone/volcano, a typical dyke would rarely induce fractures (if at all) until its tip was as shallow as a few hundred metres or less. This means that any graben or fracture zone induced by the dyke would normally not be wider than several hundred metres.

- In case there is an open contact between layers of the host rock of the dyke, the depth to the dyke tip has no relation to the distance between the stress peaks or graben width at the surface.
- As for the 2009 Harrat Lunayyir episode, we conclude that both dyke emplacement and normal faulting were partly triggered by a regional extensional loading. Furthermore, part of the surface fracturing was the result of dyke-induced stresses. Based on inferred dyke orientation in relation to the fracture pattern, it is likely that primarily the fractures on the eastern side of the fracture zone/graben where thus formed.
- Based on numerical results, we infer that the dyke tip became arrested at a depth of only a few hundred metres. This means that the hazard during the 2009 episode was considerable since the dyke propagation halted only a few hundred metres below the surface. Most likely, the dyke became arrested at a contact between layers of widely different mechanical properties. This follows partly because the dyke thickness continued to increase after it became arrested, and yet the tip was not able to break through the arrester.
- From the inferred depth of the dyke dip it follows that the dyke-induced zone of fractures at the surface is most likely several hundred metres wide. We conclude that the dyke, on its own, could not have generated the entire 3–7 km wide fracture zone associated with the 2009 episode. Much of that fracturing must be directly related to the regional extension and/or doming in the area.
- Using analytical models, we estimate the thickness of the dyke at shallow depths as being in the range of 6–12 m. From seismic data we infer the strike dimension (length) of the dyke as 14 km and the dip dimension or depth as in excess of 20 km. From these results we calculate the length/thickness ratio of the dyke as between about 2400 and 1200, which is similar to the results of field measurement of the length/thickness ratios of dykes exposed at shallow depths in many palaeovolcanic zones.

Acknowledgements

AAS thanks Morayyea Al-Shahrani President of the General Commission of Survey for helpful suggestions and Zohair Nawab, President of Saudi Geological Survey, for help during her fieldwork in Harrat Lunayyir. She also thanks Adel Alsharif, Basim al Dahri, Hani Zahran for help with the field work. Abdullah Al-Amri, Sigurjón Jónsson, Abdullah AlRajehi, Mohammed Moufti, Nabil El-Masry, Maher Al Dahry, Basim Al Dahry, Talal Al Shafi, Yahya al Shehri, Mohammed al Farhan, Abdelsalam Elshaafi, and John Browning are thanked for various helpful suggestions and information in connection with this work. The authors thank Alessandro Tibaldi and an anonymous reviewer for helpful review comments.

References

Agustsdottir, T., Woods, J., Greenfield, T., Green, R.G., White, R.S., Winder, T., Brandsdottir, B., Steinthorsson, S., Soosalu, H., 2016. Strike-slip faulting during the 2014 Bardarbunga-Holuhraun dike intrusion, central Iceland. Geophys. Res. Lett. 43: 1495–1503. https://doi.org/10.1002/2015GL067423.

Al Amri, A., Fnais, M., 2009. Seismo-volcanic investigation of 2009 earthquake swarms at Harrat Lunayyir (Ash Shaqah), Western Saudi Arabia. Int. J. Earth Sci. Eng. (October issue), 1–18.

Al Amri, A., Fnais, M., Abdel-Rahma, K., Mogren, S., Al-Dabbagh, M., 2012. Geochronological dating and stratigraphic sequences of Harrat Lunayyir, NW Saudi Arabia. Int. J. Phys. Sci. 7, 2791–2805.

Al Damegh, K., Sandvol, E., Barazangi, M., 2005. Crustal structure of the Arabian plate: new constraints form the analysis of teleseismic receiver functions. Earth Planet. Sci. Lett. 231, 177–196.

Al-Amri, A.M., Al-Mogren, S.M., 2011. Seismo-volcanic Investigation of the Current Activity in Harrat Lunayyir, Al-Madinah Al-Munawwarah Area. Final Report. King Saud University, Riyadh, pp. 1–184.

Al-Zahrani, H., Al-Amri, A.M., Abdel-Rahman, K., Fnais, M., 2013. Aftershock sequence analysis of 19 May, 2009 earthquake of Lunayyir lava flow, northwest Saudi Arabia. Inter. J. Phys. Sci. 8, 277–285.

Baer, G., Hamiel, Y., 2010. Form and growth of an embryonic continental rift: InSAR observations and modelling of the 2009 western Arabia rifting episode. Geophys. J. Int. 182, 155–167.

Bailey, G., 2009. The Red Sea, coastal landscapes and hominin dispersals. In: Petraglia, M.D., Rose, J.I. (Eds.), The Evolution of Human Populations in Arabia. Springer, Dordrecht, pp. 15–37.

Barnett, Z.A., Gudmundsson, A., 2014. Numerical modelling of dykes deflected into sills to form a magma chamber. J. Volcanol. Geotherm. Res. 281, 1–11.

Becerril, L., Galindo, I., Gudmundsson, A., Morales, J.M., 2013. Depth of origin of magma in eruptions. Sci. Rep. 3:2762. https://doi.org/10.1038/srep02762.

Brown, G., Hedge, C., Marvin, R., 1978. Geochronologic Data for the Arabian Shield. Section 2. Tabulation of Rb-Sr and K-Ar Ages Given by Rocks of the Arabian Shield. US Geological Survey Saudi Arabian Project Report. 240-20.

Camp, E., Roobol, J., 1992. Upwelling asthenosphere beneath western Arabia and its regional implications. J. Geophys. Res. 97, 15,255–15,271.

Casagli, N., Tibaldi, A., Merri, A., Del Ventisette, C., Apuani, T., Guerri, L., Fortuny-Guasch, J., Tarchi, D., 2009. Deformation of Stromboli Volcano (Italy) during the 2007 eruption revealed by radar interferometry, numerical modelling and structural geological field data. J. Volcanol. Geotherm. Res. 182 (3–4), 182–200.

Cochrna, R., Karner, D., 2007. Constraints on the deformation and rupturing of continental lithosphere of the Red Sea: the transition from rifting to drifting. Geol. Soc. Lond. Spec. Publ. 282, 265–289.

Delaney, P.T., Pollard, D.D., 1981. Deformation of host rock and flow of magma during growth of minette dike and breccia-bearing intrusions near Ship Rock, New Mexico. U.S. Geol. Surv. Prof. Pap. 1202, 1–69.

Duncan, A., Al-Amri, M., 2013. Timing and composition of volcanic activity at Harrat Lunayyir, western Saudi Arabia. J. Volcanol. Geotherm. Res. 260, 103–116.

Dzurisin, D., 2006. Volcano Deformation. Springer Verlag, New York.

Forslund, T., Gudmundsson, A., 1991. Crustal spreading due to dikes and faults in southwest Iceland. J. Struct. Geol. 13, 443–457.

Galindo, I., Gudmundsson, A., 2012. Basaltic feeder dykes in rift zones: geometry, emplacement, and effusion rates. Nat. Hazards Earth Syst. Sci. 12, 3683–3700.

Garcia, A., Ortiz, R., Marrero, J.M., Sanchez, N., Tarraga, M., Vila, J., Correig, Macia, R., Sleeman, R., 2006. Monitoring the reawakening of Canary Islands' Teide Volcano. Eos 87, 61–72.

Genna, A., Nehilg, P., Le Goff, E., Guerrot, C., Shanti, M., 2002. Proterozoic tectonism of the Arabian Shield. Precambrian Res. 117, 21–40.

Gonnermann, H.M., Manga, M., 2013. Dynamics of magma ascent in the volcanic conduit. In: Fagents, S.A., Gregg, T.K.P., Lopes, R.M.C. (Eds.), Modeling Volcanic Processes. Cambridge University Press, Cambridge, pp. 55–84.

Gottsmann, J., Wooller, L., Marti, J., Fernandez, J., Camacho, A.G., Gonzalez, P.J., Garcia, A., Rymer, H., 2006. New evidence for the reawakening of Teide volcano. Geophys. Res. Lett. 33, L20311. https://doi.org/10.1029/2006GL027523.

Greenland, L.P., Rose, W.I., Stokes, J.B., 1985. An estimate of gas emissions and magmatic gas content from Kilauea volcano. Geochim. Cosmochim. Acta 49, 125–129.

Greenland, L.P., Okamura, A.T., Stokes, J.B., 1988. Constraints on the mechanics of the eruption. In: Wolfe, E.W. (Ed.), The Puu Oo Eurption of Kilauea Volcano, Hawaii: Episodes Through 20, January 3, 1983 Through June 8, 1984, US Geol. Survey Professional Paper, 1463, pp. 155–164.

Gudmundsson, A., 1986. Formation of crustal magma chambers in Iceland. Geology 14, 164–166.

Gudmundsson, A., 1987. Geometry, formation and development of tectonic fractures on the Reykjanes Peninsula, Southwest Iceland. Tectonophysics 139, 295–308.

Gudmundsson, A., 1999. Postglacial crustal doming, stresses and fracture formation with application to Norway. Tectonophysics 307, 407–419.

Gudmundsson, A., 2002. Emplacement and arrest of sheets and dykes in central volcanoes. J. Volcanol. Geotherm. Res. 116, 279–298.

Gudmundsson, A., 2003. Surface stresses associated with arrested dykes in rift zones. Bull. Volcanol. 65, 606–619.

Gudmundsson, A., 2011a. Rock Fractures in Geological Processes. Cambridge University Press, Cambridge.

Gudmundsson, A., 2011b. Deflection of dykes into sills at discontinuities and magma-chamber formation. Tectonophysics 500, 50–64.

Gudmundsson, A., 2012. Magma chambers: formation, local stresses, excess pressures and compartments. J. Volcanol. Geotherm. Res. 237–238, 19–41.

Gudmundsson, A., 2016. The mechanics of large volcanic eruptions. Earth Sci. Rev. 163, 72–93.

Gudmundsson, A., 2017. The Glorious Geology of Iceland's Golden Circle. Springer-Nature, Heidelberg.

Gudmundsson, A., Loetveit, I.F., 2005. Dyke emplacement in a layered and faulted rift zone. J. Volcanol. Geotherm. Res. 144, 311–328.

Gudmundsson, A., Philipp, L., 2006. How local stress fields prevent volcanic eruptions. J. Volcanol. Geotherm. Res. 158, 257–268.

Gudmundsson, A., Friese, N., Galindo, I., Philipp, S.L., 2008. Dike-induced reserve faulting in a graben. Geology 36:123–126. https://doi.org/10.1130/G24185A.

Gudmundsson, A., Kusumoto, S., Simmenes, T.H., Philipp, S.L., Larsen, B., Lotveit, I.F., 2012. Effects of overpressure variations on fracture apertures and fluid transport. Tectonophysics 581, 220–230.

Hansen, E., Puckett, E., Keller, R., Brueseke, E., Bulen, L., Mertzman, A., Finegan, A., McCleery, A., 2013a. Intra-plate magmatism related to opening of the southern Iapetus Ocean: Cambrian Wichita igneous province in the Southern Oklahoma rift zone. Lithos 174, 57–70.

Hansen, E., DeShon, R., Driskell, M., Al-Amri, M., 2013b. Investigating P-wave velocity structure beneath Harrat Lunayyir, northwestern Saudi Arabia, using double-difference tomography and earthquakes from the 2009 seismic swarm. J. Geophys. Res. 118:4814–4826. https://doi.org/10.1002/jgrb.50286.

He, M.Y., Hutchinson, J.W., 1989. Crack deflection at an interface between dissimilarelastic materials. Int. J. Solids Struct. 25, 1053–1067.

Hosny, A., Nyblade, A., 2014. Crustal structure in southeastern Egypt: symmetric thinning of the northern Red Sea rifted margins. Geology 42:219–222. https://doi.org/10.1130/G34726.1.

Hutchinson, J.W., 1996. Stresses and failure modes in thin films and multilayers. Notes for a Dcamm Course. Technical University of Denmark, Lyngby, pp. 1–45.

Jaeger, J.C., Cook, N.G.W., 1979. Fundamentals of Rock Mechanics. 3rd Ed. Methuen, London.

Johnson, P.R., Woldehaimanot, B., 2003. Development of the Arabian-Nubian Shield: perspectives on accretion and deformation in the northern East African Orogen and the assembly of Gondwana. In: Windley, M., Dasgupta, S. (Eds.), Proterozoic East Gondwana: Supercontinent Assembly and Breakup. Geol. Soc. Lond. Spec. Pub. 206, pp. 289–325.

Jonsson, S., 2012. Tensile rock mass strength estimated using InSAR. Geophys. Res. Lett. 39, L21305. https://doi.org/10.1029/2012GL053309.

Kavanagh, J., Menand, T., Sparks, R.S.J., 2006. An experimental investigation of sill formation and propagation in layered elastic media. Earth Planet. Sci. Lett. 245, 799–813.

Keir, D., Pagli, C., Bastow, I., Ayele, A., 2011. The magma-assisted removal of Arabia in Afar: evidence from dyke injection in the Ethiopian rift captured using InSAR and seismicity. Tectonics 30. https://doi.org/10.1029/2010TC002785.

Koulakov, I., El Khrepy, S., Al Arifi, N., Sychev, I., Kuznetsov, P., 2014. Evidence of magma activation beneath the Harrat Lunayyir basaltic field (Saudi Arabia) from attenuation tomography. Solid Earth 5, 873–882.

Kusumoto, S., Gudmundsson, A., 2014. Displacement and stress fields around rock fractures opened by irregular overpressure variations. Front. Earth Sci. 2. https://doi.org/10.3389/feart.2014.00007.

Moran, S.C., Newhall, C., Roman, D.C., 2011. Failed magmatic eruptions: late-stage cessation of magma ascent. Bull. Volcanol. 73:115–122. https://doi.org/10.1007/s00445-010-0444-x.

Mukhopadhyay, B., Mogren, S., Mykhopdadhyay, M., Dasgupta, S., 2013. Incipient status of dyke intrusion in top crust – evidences from the Al-Ays 2009 earthquake swarm, Harrat Lunayyir, SW Saudi Arabia. Geomat. Nat. Haz. Risk 4, 30–48.

Pallister, J., McCausland, W., Jónsson, S., Lu, Z., Zahran, H., El-Hadidy, S., Aburukbah, A., Stewart, I., Lundgern, P., White, R., Moufti, M., 2010. Broad accommodation of rift-related extension recorded by dyke intrusion in Saudi Arabia. Nat. Geosci. 8.

Pint, J., 2006. Vulcanospeleology in Saudi Arabia. UIS Commission on Volcanic Caves.

Powers, W., Ramirez, F., Redmond, D., Elberg, L., 1963. Geology of the Arabian Peninsula Sedimentary Geology of Saudi Arabia. U.S. Geological Survey.

Rickwood, P.C., 1990. The anatomy of a dyke and the determination of propagation and flow directions. In: Parker, A.J., Rickwood, P.C., Tucker, D.H. (Eds.), Mafic Dykes and Emplacement Mechanisms. Balkema, Rotterdam, pp. 81–100.

Rivalta, E., Taisne, B., Bunger, P., Katz, F., 2015. A review of mechanical models of dyke propagation: schools of thought, results and future directions. Sci. Direct, Tect. Phys. 638:1–42. https://doi.org/10.1016/j.tecto.2014.10.003.

Rodgers, J., Walter, R., Mellors, J., Al-Amri, M., 1999. Lithospheric structure of the Arabian Shield and Platform from complete regional waveform modelling and surface wave group velocities. Geophys. J. Int. 138, 871–878.

Segall, P., 2010. Earthquake and Volcano Deformation. Princeton University Press, Princeton.

Sigmundsson, F., Hreinsdottir, S., Hooper, A., Arnadottir, T., Pedersen, R., Roberts, M.J., Oskarsson, N., Auriac, A., Decriem, J., Einarsson, P., Geirsson, H., Hench, M., Ofeigsson, B.G., Sturkell, E., Sveinbjörnsson, H., Feigl, K.L., 2010. Intrusion triggering of the 2010 Eyjafjallajökull explosive eruption. Nature 468:426–430. https://doi.org/10.1038/nature09558.

Stern, J., 2008. Neoproterozoic crustal growth: the solid Earth system during a critical episode of Earth history. Gondwana Res. 14, 33–50.

Stern, R., Johnson, P., 2010. Continental lithosphere of the Arabian Plate; a geologic, petrologic, and geophysical synthesis. Earth-Sci. Rev. 101, 29–67.

Tibaldi, A., 2015. Structure of volcano plumbing systems: a review of multi-parametric effects. J. Volcanol. Geotherm. Res. 298, 85–135.

Tibaldi, A., Pasquarè, F., 2008. A new mode of inner volcano growth: the "flower intrusive structure". Earth Planet. Sci. Lett. 271, 202–208.

Townsend, M.R., Pollard, D.D., Smith, R.P., 2017. Mechanical models for dikes: a third school of thought. Tectonophysics 703-704, 98–118.

Waltham, T., 2005. Extension tectonics in the afar triangle. Geol. Today 2005. https://doi.org/10.1111/j.1365-2451.2005.00510.x.

Xu, W., Jonsson, S., Corbi, F., Rivalta, E., 2016. Graben formation and dike arrest during the 2009 Harrat Lunayyir dike intrusion in Saudi Arabia: insights from InSAR, stress calculations and analog experiments. J. Geophys. Res. 121. https://doi.org/10.1002/2015JB012505.

Zobin, V., Al-Amri, A., Fnais, M., 2013. Seismicity associated with active, new-born and reawakening basaltic volcanoes: case review and the possible scenarios for the Harrat volcanic provinces, Saudi Arabia. Arab. J. Geosci. 6, 529–541.

Chapter 6: Discussion, critical evaluation

6.1 Classify lava flows of Harrat Lunayyir using Landsat 8 satellite images.

Tarquini and Favalli (2011) observed that the most prominent representations of volcanic activities are those found in the flows of lava, and that this is a phenomenon that can be observed throughout all of the variegated surfaces of different planets. Michalski et al. (2006) reported that lava flows could be determined to be both scientific anomalies, capable of enthralling and arousing the interest of researchers, and natural phenomena, which could have an in-depth influence and impact on society. The simulation of flowing lava is associated with frontal movement simulation techniques. These techniques are utilised to considerably reduce the magnitude of the risks posed by the flow of lava from the uphill positions of the volcanic crater towards the densely inhabited regions that could be situated at the lower slopes of the volcanoes or at the foothills of such locations (Crisci et al., 2003; Favalli et al., 2009; Vicari et al., 2009). The nature of lava flows can be understood to be generally unstable, and the factors that influence such conditionality for streams of flowing lava are numerous. These factors may include the characteristic attributes of the magma after an eruption, the rate of discharge or effusion, the topographical contours of lava, and finally, the external environment in which the flow of lava takes place. This environment generally becomes responsible for diminishing the heat of the lava (Griffiths, 2000). Concerning the processes by which the extents and nature of geological hazards are evaluated, the history of previous volcanic magma eruptions, forecasting the lava flows in an active manner, and the available information regarding the manner in which lava streams behave are all dependent on the classification of lava flows. The data necessary to carry out these evaluations is derived from GIS and remote sensing satellites.

In Chapter 3 we have performed unsupervised classification of lava flows in Harrat Lunayyir, western Saudi Arabia, using remote sensing. The first step to study the

history of previous volcanic magma eruptions is to differentiate between lava flows of different ages. In this study we aimed at separating different ages lava flows of Harrat Lunayyir by using remote sensing technique. The remote sensing technique had been applied through the following steps:

- Classify the lava flow by using ISODATA unsupervised classification algorithm.
- Field check of the image classes and their boundaries.
- Sampling all the lava flow classes.
- Using ^{40}Ar-^{39}Ar to determine the age of incremental heating structures.
- Convert the Landsat image digital numbers (DNs) to radiance using the bias and gain values of the given Landsat image, then converts the radiance data to Top of the Atmosphere (TOA) reflectance.
- Using GIS to define the pure endmember (spectral signature) of each lava flow class out of the reflectance image data.
- Using the pure endmembers of all lava flow classes to build spectral library of lava flow classes Harrat Lunayyir.

6.1.1 Classify the lava flow by using ISODATA unsupervised classification algorithm

ISODATA unsupervised classification was used to classify the Landsat 8 image. The significant advantage of ISODATA is that the user need only provide an initial estimate of the number of clusters, and based on various heuristics the algorithm may alter the number of clusters by either deleting small clusters, merging nearby clusters, or splitting large diffuse clusters. However, ISODATA suffers from several limitations:

- First, the user has to have a feel for the necessary parameters. The critical distance parameter needs to be specified carefully to enable a satisfactory set of initial cluster centres to be established. The user often spends much analyst time on specifying input parameters by trial and error, particularly initial cluster centres and the maximum number of iterations.

- In addition, the user has to know how many standard deviations to use when assigning pixels in the second and subsequent lines of sample to existing clusters. With experience, those parameters can be estimated reasonably.

- Another limitation is the method's dependence on the first line of samples to initiate the clustering. Since it is only a one pass algorithm, and has no feedback checking mechanism by way of iteration, the final set of cluster centres can depend significantly on the character of the first line of samples.

The results are indicative of the most extensive value of reflectance that could be obtained from the old lava flows. This could be explained from the perspective of the existence of considerable weathering of the observed geological formations at 800-1600nm, with a rate of 12%. The outcomes of the ISODATA-based classification have been examined and found to be similar to those for TOA Reflectance. Moreover, the analysis of the samples can be effectively compared with the outcomes derived from the TOA Reflectance and ISODATA-based classification. These results can be presented in the following form: 15.1 ± 6.1 ka (4%), 15.0 ± 8.4 ka (6%), 14.6 ± 23.1 ka (10%).

However, the actual conditionalities which exist on the ground concerning the appropriation of the measurements of fields of lava and the associated reflectance spectra, could be outlined in the future through the application of ASD Field Spec 3 (Robertson et al., 2013). This would be significant regarding the collection of data from the region under study for the purpose of validation of the images derived from Landsat. This could be effective concerning the fields and terrains which are not rugged in appearance and have been formed by the flow of lava. Mafic flows of lava could be understood to be a common one. To this effect, the studies related to Volcanology have been consistently focusing on the Mafic lava flows over the previous years. Furthermore, the field based researches concerning the lava flows, both older ones and those which are active currently have been consistently impeded by various complications regarding accessing the information pertaining to the research derived from the field study. The flows which are active are mostly hot, on the other hand the flows of lava which are older in geological age could be identified from their undulated and irregular surface compositions which are harder to negotiate. This could be the reason of the Morphometric studies having been not able to achieve

the equal measure of research levels of those of the studies related to the behaviour of the lava flows.

To this effect, the progression and improvement of the technological applications have lead to the realisation of the possibilities of promoting the detailed and in-depth research studies regarding the flows of lava. This could be exemplified from the utilisation of the drone which could provide access to the hitherto inaccessible regions since most of the volcanic regions are replete with life threatening dangers for researchers to traverse. Apart from this, the cutting edge technologies could as well be permissive the research processes to extend the necessary coverage to a greater region which is beyond the scope of foot based research coverage. The drones could capture certain images which could provide the research scientists with the data which could be classified regarding the surfaces on which the lava flows could occur. Such data could be utilised to formulate digitised topographic maps which, are three dimensional, regarding the flows of lava. Such maps are also effective regarding the constitution of the estimation of the volumes and compositions of shapes of such lava flows.

6.2 Estimating relative changes in surface temperatures

In order to study complex occurrences, which lead to natural hazards and monitor volcanic activities, remote sensing has recently been used. Satellite images hold paramount importance when seeking to gain an understanding of volcanic behaviour, while investigating and observing thermal emissions from High Temperature Events. (Harris et al., 1997; Tralli et al, 2005; Barnie and Oppenheimer, 2015). Thermal infrared (TIR) remote sensing of land surface temperature has been used to monitor and explore magmatic processes and volcanic activity throughout the past 20 years. The fact that data is acquired remotely makes these processes relatively risk-free, therefore, enabling us to look for precursor signals of changing volcanic activity patterns. There have been many recent studies on the thermal properties of volcanoes using satellite data but for Lunayyir there is poor or we can say there is no any study about it. In chapter 4 we focuses on monitoring and estimating relative changes in

surface temperatures, as a means for detecting an impending eruption. With regards to the year 2009, the size of coverage has increased in the direction of the North of the Harrat Centre. We expect that there are several other parts of the dyke that take the same direction as the extinction fraction in 2009, but all these sectors have been arrested at different depths beneath the earth's surface.

The relationship between landscape pattern and land surface temperature is still a challenging task. There are a number of considerations that must be taken into account when acquiring and analyzing thermal imagery of volcanic activity:

1- Spatial resolution: The energy emitted by the earth is related to the temperature and emissivity of the objects or materials on the ground. The TIR band registers a range of wavelengths with lower energy content than the other remote sensing spectral bands, implying that a TIR image has a coarser spatial resolution. For instance, the TIR band (or band 6) of the ETM+ satellite sensor has a spatial resolution of 60 m, whereas the other 6 multispectral bands (bands 1, 2, 3, 4, 5 and 7) have a spatial resolution of 30 m and the panchromatic band (or band 8) has a spatial resolution of 15 m (Galiano et al, 2011). Spatial resolution relates to the smallest spatial unit of data that a sensor can collect, and in terms of remote sensing, it relates to the area on the Earth's surface that is imaged by one pixel (Blackett, 2017). It is to some extent a function of the altitude of the sensor, with the area imaged by one pixel being larger the further a sensor is from the surface. Major difficulty commonly encountered in evaluating the accuracy of thermal surveys is the disparity between the spatial scale of the remote sensing measurements and contemporaneous ground truth measurements. Aerial and orbital sensors are designed to measure the average radiance of a particular area. In comparison, ground truth determinations of kinetic surface temperature are generally point measurements. Areas 10m2 or larger in size can contain significant spatial variations in vegetation density, soil moisture, surface texture, etc. (Settle, 1980).

2- Atmospheric effects: All thermal remote sensing data, independent of the instrument used, is influenced by atmospheric conditions and radiative processes along the measurement path (Rybicki, 1996). In the TIR part of the electromagnetic spectrum, atmospheric effects that alter the radiance observed by the sensor include absorption and emission primarily induced by water vapour, carbon dioxide and ozone. These atmospheric effects can lead to temperature differences between true

surface temperature and remotely sensed values recorded by the sensor larger than 10K (Jacob et al., 2003).

Introduce additional complications in relating aerial or orbital measure· ments of surface radiance to actual surface temperatures. This is particularly true for space borne sensors with large fields of view which conduct regional surveys over ground swaths of hundreds of kilometres or more (Hammerle et al, 2017). Water vapour content, aerosol concentration, and thermal structure of the atmosphere can vary significantly over distances of several hundred kilometres. These atmospheric variations can contribute to areal or orbital measurements of surface radiance in ways which serve to camouflage the actual thermal energy being emitted at the earth's surface (Settle, 1980). Most infrared bands on sensors used to monitor volcanic activity have been strategically placed in 'atmospheric windows', or portions of the electromagnetic spectrum with high transmissivity and, hence, low atmospheric absorption . Even in these windows, however, a small proportion of the signal may be absorbed because volcanic gasses, including water vapour, strongly absorb certain wavelengths (Blackett, 2017).

3- Emissivity: This is the ratio of energy emitted from a particular body, to that radiated from a perfect emitter (a blackbody) at the same temperature and wavelength; in effect (Blackett, 2017).The energy emitted by the earth is related to the temperature and emissivity of the objects or materials within a pixel on the ground (Galiano et al, 2011) (Becker and Liand Li, 2009). Emissivity quantifies the radiating efficiency of a surface. An object with an emissivity of 1.0 is a perfect emitter, emitting radiation with 100% efficiency; all other objects emit with less efficiency with the effect that the apparent (or radiance) temperature of such objects, if measured remotely , is less than the true kinetic temperature of the object (Blackett, 2017).

It is an intrinsic material property and is independent of temperature, unless the material approaches near-molten temperatures. At such high temperatures the relationship between temperature and spectral emissivity of volcanic materials has been observed to vary (Abtahi et al., 2002). Spectral radiance is not an intrinsic material property; it depends on spectral emissivity and varies exponentially with temperature (Blackett, 2017). This means that to derive the true temperature of a volcanic, or indeed any surface, remotely, and then its emissivity must be known. The

emissivity of volcanic surfaces has been shown to vary widely depending on mineralogy, temperature and the waveband of observation (e.g., it has been shown to be 0.92 in the SWIR bands for cooled andesitic lava at Lascar in Chile and close to 1.0 for the active lava lake at Erta Ale in Ethiopia) we found also the emissivity rising systematically as the lava cools (Abtahi et al., 2002). Accurate emissivity values are essential, as errors in it have been shown to result in temperature retrieval discrepancies of over 125k (Blackett, 2017).

Future research objectives highlighted the need for a variety of activities, including:

- In situ field studies of the bulk emissivity and thermal inertia of surface cover materials.

- Empirical analysis of high spectral and spatial resolution imagery to evaluate the utility of thermal infrared measurements for mapping variations in the emissivity of natural surfaces (specifically, to evaluate tradeoffs between increased resolution and decreased signal-to-noise).

- Atmospheric effects can be accounted for within localized areas through the use of upward· viewing, ground based radiometers.

6.3 Surface stresses and arrested dykes

Volcanic eruptions occur when a magma-filled fracture is able to propagate from its source to the surface. Most dykes (and inclined sheets) do not reach the surface to erupt but rather become arrested (stop their propagation path, stall) at various depths in the crust (Gudmundsson, 2002, 2003; Moran et al., 2011; Rivalta et al., 2015; Townsend et al., 2017). The conditions for dyke arrest have been studied in the field (Gudmundsson, 2002, 2003; Gudmundsson and Philipp, 2006; Tibaldi, 2015) and through analogue models (Kavanagh et al., 2006), numerical models (Gudmundsson and Philipp, 2006; Barnett and Gudmundsson, 2014; Rivalta et al., 2015; Townsend et al., 2017), and analytical models (Gudmundsson, 2011a, 2011b). Understanding these

conditions is of fundamental importance in theoretical and applied volcanology when we study Harrat Lunayyir.

Most studies of volcano unrest in Harrat Lunayyir are concentrate on Interferometric Synthetic Aperture Radar (InSAR) measurements to evaluate the surface deformation associated with the event (Bear and Hamiel, 2010; Jónsson et al, 2010; Pallister et al, 2010), or studying Aftershock sequence analysis of 19 May, 2009 (Al-Zahrani et al, 2013), Evidence of magma activation beneath the Harrat Lunayyir basaltic field (Saudi Arabia) from attenuation tomography (Koulakov et al, 2014), study seismic activity recorded prior to some volcanic eruptions at active, new-born, and re-awakening basaltic volcanoes and associated with dike injections along rift zones is presented (Zobin et al, 2013). In chapter 5 (Alshehri and Gudmundsson, 2018) we present new and general results on dyke-induced stresses in crustal segments with contrasting mechanical properties. Here the focus is on new numerical models on dykes arrested with their tips at various crustal depths and hosted by rocks with mechanical properties that range from elastic half spaces (uniform properties) to those with alternating stiff (high Young's modulus) and soft (compliant, low Young's modulus) layers. The results are completely general, but are here applied to the 2009 volcano tectonic unrest period in Harrat Lunayyir in Saudi Arabia. The second, and main, aim is thus to use the numerical results, as well as some analytical models together with field observations of the associated surface deformation, to make new estimates of the dimensions, the depth to the tip at arrest, and contribution to surface deformation of the dyke inferred to have been emplaced during the 2009 episode. We also put the dyke propagation and arrest in Harrat Lunayyir into general context of arrested dykes, their dimensions, and aspect (length/thickness) ratios, as obtained in direct field studies. Furthermore, we explain the likely conditions for the 2009 dyke arrest in Harrat Lunayyir and the implications of the results for volcanic hazards. For understanding the 2009 episode, we first provide brief outline of the geological setting of the Harrat Lunayyir, as well as a short overview of its volcanic geology.

The qualitative nature of our final forecast model (Alshehri and Gudmundsson, 2018) means Mechanical layering has great effects on dyke-induced stresses and associated surface deformation. Even if the layering details are commonly unknown for volcanic areas, adding plausible general layering, using information from field observations of similar, well-exposed fossil volcanic zones, is likely to yield more realistic results as

to surface stresses and deformation than non-layer models such as elastic half-space models.

The models were created in a two-dimensional regime, as is standard for dyke modelling. Three-dimensional effects for long fractures such as dykes are primarily felt at the lateral ends of the dykes. Along the main part of the strike dimension of the dyke, two-dimensional models give very accurate results and three-dimensional modelling is not needed. Here we are only looking at the stresses induced by the dykes in vertical cross-sections, so that the segmentation is not generally of relevance. There exist, however, well-known analytical solutions for the interaction of mode I (dyke) fracture segments which show that when the lateral ends of the segments are close to each other when compared with the overall lengths of the segments, then the segmented fracture (here the dyke) functions as a single fracture – here a single dyke (Gudmundsson, 2011, Rock Fractures in Geological Processes, Chapter 13). There is no evidence for multiple dykes in the data analyzed and modeled for the 2009 volcanotectonic event. Most dykes are thought to grow as self-similar structures, so that even if there were multiple dyke injections, then as the dyke became thicker the surface effects would be similar to those in case of one original thick dyke.

In all of the models, the lower tip (bottom) of the dyke was at a depth of ~10 km. As was discussed by Al Shehri and Gudmundsson (2018), the dip dimension of the 2009 dyke might have been as large as 15–20 km but for the purpose of modelling effects of shallow layering on surface stresses, the dip dimension used here is appropriate. In all the models the only loading is internal magmatic overpressure (driving pressure) of 6MPa and we assume there is no any effect of the dyke on the depth of 20km because we have the same overpressure and it is the main factor to dyke emplacement.

More specifically, it should be emphasised that increasing the depth dimension of a tall dyke has little effect on the stress concentration around its upper tip, which is the stress concentration of concern here. Thus, even if the depth of the dyke were extended to 20 km, the modelling results as regards the local stresses in the layers above the upper tip (the top) of the dyke would remain very similar to those shown here.

Based on numerical results, we infer that the dyke tip became arrested at a depth of only a few hundred meters. This means that the hazard during the 2009 episode was

considerable since the dyke propagation halted only a few hundred meters below the surface. Most likely, the dyke became arrested at a contact between layers of widely different mechanical properties. This follows partly because the dyke thickness continued to increase after it became arrested, and yet the tip was not able to break through the arrester. Using analytical models, we estimate the thickness of the dyke at shallow depths as being in the range of 6–12 m. From seismic data we infer the strike dimension (length) of the dyke as 14 km and the dip dimension or depth as in excess of 20 km. From these results we calculate the length/thickness ratio of the dyke as between about 2400 and 1200, which is similar to the results of field measurement of the length/thickness ratios of dykes exposed at shallow depths in many palaeovolcanic zones.

The General Implications of our study on arrested dyke the simplicity of the analytical and numerical models presented here do not support the suggestions that the entire surface-fracture formation and development during the 2009 episode was induced by an arrested dyke.

1- The graben is between 3 and 7 km wide. If we take an average width as 5 km, then that would imply that the dyke tip at the time of fracture formation was at a depth of 2 km (which is also the depth suggested by some of the authors of the cited papers). However, the numerical models presented here show that, for any reasonably layering, the surface stresses even at the depth of 1 km, let alone a depth of N2 km, would be too small to generate significant fractures. It is only when the tip reaches the shallow depth of 500m, and, in particular, 300 m that the surface stresses become large enough so as to generate significant fractures.

2- When the tip of the arrested dyke is at 300–500m depth, clearly the graben that the dyke could initiate at the surface could not be wider than about 0.6–1 km. A graben of average width 5 km is simply too wide to be generated by the stresses induced by a dyke arrested at the depth of 300–500 m.

3- None of the main_fractures coincide in strike with the inferred strike of the dyke and many strikes very differently from that of the dyke. Furthermore, some of the fractures apparently dissect the dyke, when its strike is projected (as a broken line) to the surface.

4- Although we have followed the established tradition in the literature on this episode and referred to the structure as a graben, the general fracture pattern supposed to have been generated in the 2009 episode does not follow the geometry of a classical graben. In fact, the 'boundary fault' on the eastern side of the 'graben' is not a fault but rather a zone of tension fractures. The symmetry of the stress field induced by an arrested dyke would tend to generate a clear graben structures, with two normal boundary faults, but that is not what happened here.

6.3.1 Regional tectonics and relative contribution of the dyke

Before the dyke was injected, there existed a local stress field in the area that favoured the formation of normal faults and tension fractures. As the dyke propagated to shallower depths, its overpressure resulted in local stresses that became concentrated in the strip of land above the tip of the dyke. Depending on the layering and contacts above the dyke, these stresses could have generated normal faults and/or tension fractures.

It should be noted that the overpressure of the dyke, the pressure that generates the dyke-induced stresses, is by definition the total pressure minus the minimum principal compressive stress, σ3. It follows that for a given total pressure in the dyke, the lower the regional σ_3; the greater will be the effective overpressure. Thus any regional tension perpendicular to the dyke tends to reduce σ3 and thereby increase the effective overpressure. That increase, in turn, results in greater tensile and shear stress concentration above the tip of the dyke and, therefore, in more fracture formation. Thus, the regional stress contributes to the overpressure of the dyke, and since only the overpressure is inducing the stresses and the fractures in the area above the dyke, the effect of the total pressure and reduction in σ_3 cannot be distinguished. As we say in the paper, however, dyke-induced stresses at the surface are always local, and in the present case the fracturing occurred in such a wide area that a single dyke arrested at a shallow depth cannot have generated all the fractures .

No dykes form by 'passive' filling of existing fractures. All dykes form their own fractures through the rock being ruptured by the magmatic overpressure. Dykes are extension (mode I) fractures. Such fractures cannot form in the absence of fluid

pressure except in the uppermost several hundred metres of the crust. This result follows from the Griffith crack theory and is well-understood in terms of Mohr's circles. Below several hundred meters in the crust, extension in the absence of a fluid body always results in the formation of normal faults (shear fractures) – never in the formation of extension fractures. There are no large-scale tension fractures (where σ_3 is negative in the absence of a fluid body) at depths of many kilometres that magma can flow passively into – as is well established from field studies of fractures to crustal depths of 2km in Iceland and other similar deeply eroded areas (Gudmundsson, 2011). This is all well explained in Section 6, particularly Equation (7) of the paper by Al Shehri and Gudmundsson (2018) – Chapter 5 in the Thesis.

6.3.2 The effect of magma cooling and magma composition

Magma cooling has normally hardly any effects on dyke emplacement in most areas, and is therefore not considered here. Rate of cooling of magma is slow in comparison with the rate of propagation of dykes – the latter being commonly about 0.5 m/s. Thus during most propagation episodes of basaltic dykes cooling would have very little effect on the magma viscosity during dyke propagation. Only in the case of basaltic dykes propagating many tens or hundreds of kilometres would cooling be expected to have strong effect. Even if a part of a propagating dyke became solidified – say a small horn or particularly thin part of a dyke – the cooling as such would not be able to arrest the dyke. This follows because the solidified part of the dyke would have the same or lower tensile strength as the host rock. Thus, as long as there is any overpressure in the dyke, its magma would simply rupture the solidified part or, alternatively, find another path to bypass that solidified part.

Since almost all the erupted lavas in the studied areas are basaltic, we assume that the magma in the 2009 dyke was basaltic. We have no means of deciding which type of basalt was emplaced. The numerical results depend only on the geometry of the dyke, its overpressure (including effects of regional stresses), and the mechanical layering above the dyke tip. Magma composition is not of relevance for this type of modelling.

Chapter 7: Conclusion

In this thesis, the focus was on the volcanic processes related to the tectonic movements and shifts in the Harrat Lunayyir regions under consideration. The purpose is to improve the understanding of dyke emplacement in volcanoes and, specifically, the 2009 dyke emplacement in the Harrat Lunayyir region. The mechanical and aspects and thermal effects on the host rocks are considered.

In chapter 1.6 objectives statement the following objectives statement were formulated:

1. **To further assess the risks and hazards associated with the 2009 dyke emplacement in the research area. This assessment relies partly on the new estimates for the depth to the dyke tip when the dyke became arrested.**

The tip of the dyke became arrested, not at a depth of 1–2 km, but rather at a depth of a few hundred meters. Our numerical and analytical results indicate that a dyke arrested at 1–2 km depth, as suggested in earlier studies, in a reasonably layered crust and with a typical magmatic overpressure could not induce significant fracture formation at the surface.

2. **To estimate the general dimensions of the 2009 dyke.**

We estimate the dimensions of the dyke from seismic and geodetic data provided in the cited literature on this episode, combined with well-tested fracture-mechanics models and field studies of regional dykes. Our results as regards strike dimension (length) and dip dimension (height) are similar to those of earlier studies. We conclude that the strike dimension is about 14 km and the dip dimension at least 20 km. For the shallow depth of the dyke, the top parts, we estimate the maximum thickness in the range of 5.8–11.6 m or, given the inaccuracy in the estimated Young's moduli and overpressure, somewhere between 6 and 12 m. This is in

contrast to the maximum thickness of 2–2.3mobtained in earlier studies. However, our results fit much better with actual field measurements of the length/thickness ratios of regional dykes worldwide.

3. **To conduct a comprehensive numerical study of the dyke-induced surface stresses. In particular, to explore the effects of mechanical layering on the surface stresses and the resulting fracture pattern.**

Mechanical layering has great effects on dyke-induced stresses and associated surface deformation. Even if the layering details are commonly unknown for volcanic areas, adding plausible general layering, using information from field observations of similar, well-exposed fossil volcanic zones, is likely to yield more realistic results as to surface stresses and deformation than non-layered models such as elastic half-space models.

4. **To formulate, through the use of remote sensing technologies, a rigorous estimation of the surface temperature variations in relation to the 2009 dyke emplacement.**

We examined the relationship between the relative changes in surface temperatures ‘LST’ and seismic–tectonic activities and provided new insights into the spatiotemporal relationship between volcanic and tectonic processes in the area .

Through the employment of the methodology of thermal mapping and spatial density mapping of volcanic vents (primarily crater cones and small lava shields), the land surface temperature changes in the center of Harrat Lunayyir were recorded when the 2009 dyke was propagating toward the surface .

The obtained results are in agreement with previous research findings indicating the northwest–southeast direction of the dyke system and the normal fault formation.

5. To perform the unsupervised classification of the lava flows in Harrat Lunayyir through the use of remote sensing.

We employed the unsupervised classification of remote sensing inputs from Landsat 8, identifying different generations of lava flows in Harrat Lunayyir, western Saudi Arabia .

We have used numerical classification methods to identify the number of classes into which the data is separated for clustering within each land cover.

The utilization of ISODATA for the segmentation of the remote sensing data has also been made. The algorithm for performing unsupervised classification was obtained from the GIS package raster (Arc Info).

The characteristics of spectral reflectance regarding volcanic materials, which could be widely observed at the zone of analysis at Harrat Lunayyir, have been investigated, and the resultant classifications of the examined region have been spectrally classified .

The data was derived through an analysis involving the counting of the pixels of randomly selected regions. This suggests that the most elevated measures of reflectance value could be exhibited by the older flows of lava. The reason for this could be related to the weathering.

Bibliography

Al-Amri, A.m & Fnais, M., 2009. Seismo-volcanic investigation of 2009 earthquake swarms at Harrat Lunayyir (Ash Shaqah), Western Saudi Arabia. Int. J. Earth Sci. Eng., India.

Al-Amri, A., & Al-Mogren, S., 2011. Seismo-volcanic investigation of the current activity in Harrat Lunayyir, Al-Madinah Al-Munawwarah area. Final report. King Saud University, Riyadh, 184.

Al-Amri, A., Fnais, M., Abdel-Rahman, M., & Al-Dabbagh, M., 2012. Geochronological dating and stratigraphic sequences of Harrat Lunayyir, NW Saudi Arabia. International Journal of Physical Sciences, 7, 2791-2805.

Al Damegh, K., Sandvol, E., Barazangi, M., 2005. Crustal structure of the Arabian plate: new constraints form the analysis of teleseismic receiver functions. Earth Planet. Sci. Lett. 231, 177–196.

Al Shehri, A., Gudmundsson, A., 2018. Modelling of surface stresses and fracturing during dyke emplacement: Application to the 2009 episode at Harrat Lunayyir, Saudi Arabia. Volcanology and Geothermal Research. 356, 278-303.

Al-Zahrani, H., Fnais, M., Al-Amri, A., & Abdel-Rahman, K., 2013. Tectonic framework of Lunayyir area, northwest Saudi Arabia through aftershock sequence analysis of 19 May, 2009 earthquake and aeromagnetic data. Int. J. Phys. Sci, 7, 5821-5833.

Andrew, R., 2008. Volcano tectonic Evolution and Characteristic Volcanism of the Neovolcanic Zone of Iceland. PhD thesis, p. 130.

Baer, G., Hamiel, Y., 2010. Form and growth of an embryonic continental rift: InSAR observations and modelling of the 2009 western Arabia rifting episode. Geophysical Journal International, 182, 155-167.

Bailey, G., 2009. The Red Sea, coastal landscapes and hominin dispersals. In: Petraglia, M.D., Rose, J.I. (Eds.), the Evolution of Human Populations in Arabia. Springer, Dordrecht, pp. 15–37.

Barnett, Z., & Gudmundsson, A., 2014. Numerical modelling of dykes deflected into sills to form a magma chamber. Journal of Volcanolology Geothermal Research. 281, 1–11.

Barnie, T., Oppenheimer, C., 2015. Extracting high temperature event radiance from satellite images and correcting for saturation using Independent Component Analysis. Remote Sensing of Environment, 158, 56–68.

Bernard, B., 2013. Homemade ashmeter: a low-cost, high-efficiency solution to improve tephra field-data collection for contemporary explosive eruptions. Journal of Applied Volcanology, 2, 1-9.

Bonne, K., Cascone, M., Njome, S., Ranst, E., Suh, E., 2008. A new approach to assess long-term lava flow hazard and risk using GIS and low-cost remote sensing: the case of Mount Cameroon, West Africa. International Journal of Remote Sensing. 29, 6537–6562.

Brown, G., Hedge, C., Marvin, R., 1978. Geochronologic Data for the Arabian Shield. Section 2. Tabulation of Rb-Sr and K-Ar Ages Given by Rocks of the Arabian Shield. US Geological Survey Saudi Arabian Project Report. 240-20.

Brown, M., 1994. The generation, segregation, ascent and emplacement of granite magma: the migmatite-to-crustally-derived granite connection in thickened orogens. Earth Science, 36, 83-130.

Bryant, A., Johnson, F., Brazel, J., Balling, C., Hutchinson, F., Beck, R., 1990. Measuring the effect of overgrazing in the Sonoran Desert. Climatic Change, 17, 243-264.

Camp, E., Roobol, J., 1992. Upwelling asthenosphere beneath western Arabia and its regional implications. J. Geophys. Res. 97, 15,255–15,271.

Casagli, N., Tibaldi, A., Merri, A., Del Ventisette, C., Apuani, T., Guerri, L., Fortuny-Guasch, J., Tarchi, D., 2009. Deformation of Stromboli Volcano (Italy) during the 2007 eruption revealed by radar interferometry, numerical modelling and structural geological field data. J. Volcanol. Geotherm. Res. 182 (3–4), 182–200.

Cashman, K., Soule, S., Mackey, B., Deligne, N., Deardorff, N., Dietterich, H., 2013. How lava flows: New insights from applications of lidar technologies to lava flow studies. Geosphere. 9, 1664-1680.

Cayol, V., Cornet, F., 1998. Three-dimensional modeling of the 1983– 1984 eruption at Piton de la Fournaise Volcano, Reunion Island. Journal of Geophysical Research 103, 18025–18037.

Cochrna, R., Karner, D., 2007. Constraints on the deformation and rupturing of continental lithosphere of the Red Sea: the transition from rifting to drifting. Geol. Soc. Lond. Spec. Publ. 282, 265–289.

Colwell, R., 1966. Uses and Limitations of Multispectral Remote Sensing. In Proceedings of the Fourth Symposium on Remote Sensing of Environment. Ann Arbor: Institute of Science and Technology, University of Michigan, 71–100.

Colwell, R., 1983. Manual of Remote Sensing (2nd ed.). Falls Church, VA: American Society of Photogrammetry, 2.

Crown, A. & Ramsey, S., 2016. Morphologic and thermo physical characteristics of lava flows southwest of Arsia Mons, Mars. Journal of Volcanology and Geothermal Research, pp. 1-16.

D'Alessandro, W., 2006. Human fluorosis related to volcanic activity: a review. Environmental Toxicology Transaction: Biomedicine and Health, 10.

De Alwis, D., Easton, Z., Dahlke, H., Philpot, W., Steenhuis, T., 2007. Unsupervised classification of saturated areas using a time series of remotely sensed images. Hydrol. Earth Syst. Sci. 11, 1609–1620.

Duncan, R., & Al-Amri, A., 2013. Timing and composition of volcanic activity at Harrat Lunayyir, western Saudi Arabia. Journal of Volcanology and Geothermal Research, 260, 103-116.

Dzurisin, D., 2006. Volcano Deformation. Springer Verlag, New York.

Eidenshink, e., Haas, H., 1992. Analysing vegetation dynamics of land systems with satellite- data. Geocarto International, 1, 53-61.

Farrier, L., 2006. Influence of surface roughness on the specular reflectance of low gloss coatings using bidirectional reflectance measurements. Air Force Research Laboratory . thesis, OH 45433-7750.

Fischer, W., Hemphill, R., Kover, A., 1976. Progress in Remote Sensing. Photogrammetria, 32, 33–72.

Fowler, A., 1989. Generation and creep of magma in the Earth. SIAM Journal on Applied Mathematics, 49, 231-245.

Galindo, I., Gudmundsson, A., 2012. Basaltic feeder dykes in rift zones: geometry, emplacement, and effusion rates. Nat. Hazards Earth Syst. Sci. 12, 3683–3700.

Garcia, A., Ortiz, R., Marrero, J.M., Sanchez, N., Tarraga, M., Vila, J., Correig, Macia, R., Sleeman, R., 2006. Monitoring the reawakening of Canary Islands' Teide Volcano. Eos 87, 61–72.

Genna, A., Nehilg, P., Le Goff, E., Guerrot, C., Shanti, M., 2002. Proterozoic tectonism of the Arabian Shield. Precambrian Res. 117, 21–40.

Gonnermann, H.M., Manga, M., 2013. Dynamics of magma ascent in the volcanic conduit. In: Fagents, S.A., Gregg, T.K.P., Lopes, R.M.C. (Eds.), Modeling Volcanic Processes. Cambridge University Press, Cambridge, pp. 55–84.

Gottsmann, J., Wooller, L., Marti, J., Fernandez, J., Camacho, A.G., Gonzalez, P.J., Garcia, A., Rymer, H., 2006. New evidence for the reawakening of Teide volcano. Geophys. Res. Lett. 33, L20311. https://doi.org/10.1029/2006GL027523.

Greenland, L.P., Rose, W.I., Stokes, J.B., 1985. An estimate of gas emissions and magmatic gas content from Kilauea volcano. Geochim. Cosmochim. Acta 49, 125–129.

Greenland, L.P., Okamura, A.T., Stokes, J.B., 1988. Constraints on the mechanics of the eruption. In: Wolfe, E.W. (Ed.), The Puu Oo Eurption of Kilauea Volcano, Hawaii: Episodes Through 20, January 3, 1983 Through June 8, 1984, US Geol. Survey Professional Paper, 1463, pp. 155–164.

Gudmundsson, A., 1990. Emplacement of dikes, sills and crustal magma chambers at divergent plate boundaries. Tectono physics. 176, 257–275.

Gudmundsson, A., 2002. Emplacement and arrest of sheets and dykes in central volcanoes. Journal of Volcanology and Geothermal Research 116, 279–298.

Gudmundsson, A., 2003. Surface stresses associatedwith arrested dykes in rift zones. Bull. Volcanol. 65, 606–619.

Gudmundsson, A., 2006. How local stresses control magma-chamber ruptures, dyke injections, and eruptions in composite volcanoes. Earth Sci. Rev. 79, 1–31.

Gudmundsson, A., Philipp, L., 2006. How local stress fields prevent volcanic eruptions. J. Volcanol. Geotherm. Res. 158, 257–268.

Gudmundsson, A., 2011a. Rock Fractures in Geological Processes. Cambridge University Press, Cambridge.

Gudmundsson, A., 2011b. Deflection of dykes into sills at discontinuities and magma chamber formation. Tectono physics 500, 50–64.

Gudmundsson, A., 2012. Magma chambers: Formation, local stresses, excess pressures, and compartments. Journal of Volcanology and Geothermal Research, 237, 19-41.

Gudmundsson, A., Pasquarè, F. A., Tibaldi, A., 2014. Dykes, sills, laccoliths, and inclined sheets in Iceland. DOI: 10.1007/11157_2014_1.

Gudmundsson, A., 2017. The Glorious Geology of Iceland's Golden Circle. Springer International Publishing. DOI 10.1007/978-3-319-55152-4.

Gudmundsson, A., 2019. Volcanotectonics. Cambridge University Press, Cambridge.

Hansen, E., Puckett, E., Keller, R., Brueseke, E., Bulen, L., Mertzman, A., Finegan, A., McCleery, A., 2013a. Intra-plate magmatism related to opening of the southern Iapetus Ocean: Cambrian Wichita igneous province in the Southern Oklahoma rift zone. Lithos. 174, 57–70.

Hansen, S., DeShon, H., Moore-Driskell, M., & Al-Amri, A., 2013b. Investigating the P wave velocity structure beneath Harrat Lunayyir, northwestern Saudi Arabia, using double-difference tomography and earthquakes from the 2009 seismic swarm. Journal of Geophysical Research: Solid Earth, 118, 4814-4826.

Harris, L., Blake, S., Rothery, A., and Stevens, F., 1997. A chronology of the 199 to 1993 Etna eruption using AVHRR data: implications for real time thermal volcano monitoring. Journal of Geophysical Research. 102, 7985-8003.

Haselwimmer, C., Prakash, A., 2013. Thermal infrared remote sensing of geothermal systems. Remote sensing and digital image processing. 17, 453-473.

Haas, H., 1992. LANDSAT TM products for rangeland assessment Geocarto International, 1, 27-33.

Head, M., Maclean, L., & Carn, A., 2012. Mapping lava flows from Nyamuragira volcano (1967–2011) with satellite data and automated classification methods. Geomatics, Natural Hazards and Risk. 4, 119-144.

Hickey, J., Gottsmann, J., 2014. Benchmarking and developing numerical Finite Element models of volcanic deformation. Journal of Volcanology and Geothermal Research. 280, 126–130.

Huppert, H., Turner, J., Sparks, R., 1982. Replenished magma chambers: effects of compositional zonation. Earth and Planetary Science Letters, 57 , 345-357.

Huppert, H., Sparks, R., 1980. The Fluid Dynamics of a Basaltic Magma Chamber Replenished by Influx of Hot, Dense Ultrabasic Magma. Contrib Mineral Petrol, 75, 279 289.

Jaeger, J., Cook, N., 1979. Fundamentals of Rock Mechanics. 3rd Ed. Methuen, London.

Jain, A., Murty, M., Flynn, P., 1999. Data Clustering: A Review. ACM Computing Surveys. 31, 3.

Jensen, J., 2007. Remote Sensing of the Environment: An Earth Resource Perspective. 2nd Edition, Pearson Prentice Hall, Upper Saddle River.

Jellinek, A., DePaolo, D., 2003. A model for the origin of large silicic magma chambers: precursors of caldera-forming eruptions. Bull Volcanol, 65, 363-381.

Jónsson, S., Pallister, J., McCausland, W., El-Hadidy, S., 2010. Dyke Intrusion and Arrest in Harrat Lunayyir, western Saudi Arabia, in April-July 2009. Geophysical Research Abstracts, 12, 7704.

Johnson, D., Sigmundsson, F., Delaney, P., 2000. Comment on "Volume of magma accumulation or withdrawal estimated from surface uplift or subsidence, with application to the 1960 collapse of K¯ılaue volcano" by P. T. Delaney and D. F. McTigue. Bull Volcanol, 61, 491-493.

Johnson, P., Woldehaimanot, B., 2003. Development of the Arabian-Nubian Shield: perspectives on accretion and deformation in the northern East African Orogen and the assembly of Gondwana. In: Windley, M., Dasgupta, S. (Eds.), Proterozoic East Gondwana: Supercontinent Assembly and Breakup. Geol. Soc. Lond. Spec. Pub. 206, 289–325.

Joyce, K., Samsonov, S., Jolly, G., 2008. Satellite remote sensing of volcanic activity in New Zealand. Auckland. DOI: 10.1109/USEREST.2008.4740346, IEEE.

Kavanagh, J., Menand, T., Sparks, R.S.J., 2006. An experimental investigation of sill formation and propagation in layered elastic media. Earth Planet. Sci. Lett. 245, 799–813.

Kavanagh, J., Boutelier, D., Cruden, A., 2015. The mechanics of sill inception, propagation and growth: Experimental evidence for rapid reduction in magmatic overpressure. Earth and Planetary Science Letters. 421, 117-128.

Kavanagh, J., Burns, A., Hazim, S., Wood, E., Martin, S., Hignett, S., Dennis, D., 2018. Challenging dyke ascent models using novel laboratory experiments: Implications for reinterpreting evidence of magma ascent and volcanism. Volcanology and Geothermal Research. 354, 87-101.

Kenedi, L., Ruge, M., Mokhtar , T., Abdelwalhed , M., & Lindsay, J., 2013. The 1256 & 1999 Harrat Rahat and 2009 Lunayyir earthquake swarms: Implications for future volcano-seismic activity at Al-Madinah.

Koulakov, I., El Khrepy, S., Al-Arifi, N., Kuznetsov, P., & Kasatkina, E., 2015. Structural cause of a missed eruption in the Harrat Lunayyir basaltic field (Saudi Arabia) in 2009. Geology. 43, 395-398.

Koulakov, I., El Khrepy, S., Al-Arifi, N., Sychev, I., & Kuznetsov, P., 2014. Evidence of magma activation beneath the Harrat Lunayyir basaltic field (Saudi Arabia) from attenuation tomography. Solid Earth. 5, 873.

Logan, L., 2002. A First Course in the Finite Element Method. Brooks/ Cole, Pacific Grove, California, 720 pp.

Lwin, K., 2008. Fundamentals of Remote Sensing technology and its applications in Geographical Information Systems, Division of Spatial Information Science University of Tsukuba.

Maaloe, S., Scheie, A., 1982. The permeability-controlled accumulation of primary magma in a planetary mantle. Physics of the Earth and Planetary Interiors, 29, 344-353.

Macdonald, K., 1982. Mid-ocean ridges: Rne scale tectonic, volcanic and hydrothermal processes within the plate boundary zone. Annual Reviews of Earth and Planetary Science, 10, 155-190.

Marsh, D., 1989. Magma chambers. Annual Review of Earth and Planetary Sciences, **17**, 439-474.

Moor, G., 1979. What is a picture worth? A history of remote sensing. Hydrological Sciences Bulletin, 4, 477- 485, DOI: 10.1080/02626667909491887.

Moran, C., Newhall, C., Roman, C., 2011. Failed magmatic eruptions: late-stage cessation of magma ascent. Bulletin of Volcanology 73, 115–122.

Mukhopadhyay, B., Mogren, S., Mukhopadhyay, M., & Dasgupta, S., 2013. Incipient status of dyke intrusion in top crust–evidences from the Al-Ays 2009 earthquake

swarm, Harrat Lunayyir, SW Saudi Arabia. Geomatics, Natural Hazards and Risk. 4, 30-48.

Nicolas, S. T., Astrid, G., Minoru, U. & Zarah, S., 2008. Preliminary results of lava flow mapping using remote sensing in Piton de la Fournaise, La Réunion Island. s.l.:IEEE.

Nicholson, E., Davenport, L., Malo, R., 1990. A comparison of the vegetation response to rainfall in the Sahel and East Africa. using normalized difference vegetation index from NOAA-A VHRR. Climatic Change, 17, 209-241.

OSU, 2015. How do volcanoes affect the atmosphere and climate? [Online] Available at: http://volcano.oregonstate.edu/how-do-volcanoes-affect-atmosphere-and-climate.

Pallister, J., McCausland, W., Jónsson, S., Lu, Z., Zahran, H., El Hadidy, S., & Moufti, M., 2010. Broad accommodation of rift-related extension recorded by dyke intrusion in Saudi Arabia. Nature Geoscience. 3, 705.

Pint, J., 2006. Vulcanospeleology in Saudi Arabia. UIS Commission on Volcanic Caves.

Powers, W., Ramirez, F., Redmond, D., Elberg, L., 1963. Geology of the Arabian Peninsula Sedimentary Geology of Saudi Arabia. U.S. Geological Survey.

Realmuto, J., & Worden, M., 2000. The impact of atmospheric water vapor on the thermal infrared remote sensing of volcanic sulfur dioxide emissions: a case study from the Pu'u 'O'o vent of Kilauea Volcano, Hawaii. Journal of Geophysical Research. 21, 497–21.

Rivalta, E., Taisne, B., Bunger, P., Katz, F., 2015. A review of mechanical models of dyke propagation: schools of thought, results and future directions. Sci. Direct, Tect. Phys. 638:1–42. https://doi.org/10.1016/j.tecto.2014.10.003.

Robertson, K. M., Milliken, R. E., Ruff, S., Farmer, J., Shock, E., 2013. Can Vis-Nir Reflectance Spectra Be Used To Assess Formation Environments of Opaline Silica on Mars? In 44th Lunar and Planetary Science Conference 2–3. Texas.

Rodgers, J., Walter, R., Mellors, J., Al-Amri, M., 1999. Lithospheric structure of the Arabian Shield and Platform from complete regional waveform modelling and surface wave group velocities. Geophys. J. Int. 138, 871–878.

Segall, P., 2010. Earthquake and Volcano Deformation. Princeton University Press, Princeton.

Shen, C., Juang, C., & Tsai, L., 2008. Remote sensing stream flow and soil moisture by using reflected GPS Signals Li & L2 observation and Doppler shifts with an Integrated GPS Receiver. Taipei, s.n., pp. 181-189.

Sigmundsson, F., 2006. Magma does the splits. Nature 442, 251–252.

Sigmundsson, F., Hreinsdottir, S., Hooper, A., Arnadottir, T., Pedersen, R., Roberts, M.J., Oskarsson, N., Auriac, A., Decriem, J., Einarsson, P., Geirsson, H., Hench, M., Ofeigsson, B.G., Sturkell, E., Sveinbjörnsson, H., Feigl, K.L., 2010. Intrusion triggering of the 2010 Eyjafjallajökull explosive eruption. Nature 468:426–430. https://doi. org/10.1038/nature09558.

Stern, R., Johnson, P., 2010. Continental lithosphere of the Arabian Plate; a geologic, petrologic, and geophysical synthesis. Earth-Sci. Rev. 101, 29–67.

Tibaldi, A., 2015. Structure of volcano plumbing systems: a reviewofmulti-parametric effects. J. Volcanol. Geotherm. Res. 298, 85–135.

Tibaldi, A., Pasquarè, F., 2008. A new mode of inner volcano growth: the “flower intrusive structure”. Earth Planet. Sci. Lett. 271, 202–208.

Tralli, D., Blom, R., Zlotnicki, V., Donnellan, A., Evans, D., 2005. Satellite remote sensing of earthquake, volcano, flood, landslide and coastal inundation hazards. ISPRS Journal of Photogrammetry & Remote Sensing, 59, 185– 198.

Townsend, R., Pollard, D., Smith, P., 2017. Mechanical models for dikes: a third school of thought. Tectonophysics. 703-704, 98–118.

U.S. Geological Survey., 2008. Understanding volcano hazards and preventing volcanic disasters: A science strategy for the volcano hazards program. New York: USGS.

Vaughan, G., Hook, J., Ramsey, S., Realmuto, J., Schneider, J., 2005. Monitoring eruptive activity at Mount St. Helens with TIR image data. Geophysical Research Letters. 32, 1-4.

Xu, W., Jonsson, S., Corbi, F., Rivalta, E., 2016. Graben formation and dike arrest during the 2009 Harrat Lunayyir dike intrusion in Saudi Arabia: insights from InSAR, stress calculations and analog experiments. J. Geophys. Res. 121. https://doi.org/10.1002/ 2015JB012505.

Zanter, K., 2016. Landsat 8 (L8) data users handbook. Department of the Interior U.S. Geological Survey. Version 2.0.

Zobin, V., Al-Amri, A., Fnais, M., 2013. Seismicity associated with active, new-born, and re-awakening basaltic volcanoes: case review and the possible scenarios for the Harraat volcanic provinces, Saudi Arabia. Arabian Journal of Geosciences. 6, 529-541.